Hadron Production and Freeze-Out Dynamics at $\sqrt{s_{NN}} = 3.0$ GeV Au+Al and $\sqrt{s_{NN}} = 19.6$ GeV Au+Au Collisions as Measured at STAR

By

SAMANTHA GAIL BROVKO
B.S. (University of California, Davis) 2008
M.S. (University of California, Davis) 2010

DISSERTATION

Submitted in partial satisfaction of the requirements for the degree of

DOCTOR OF PHILOSOPHY

in

Physics

in the

OFFICE OF GRADUATE STUDIES

of the

UNIVERSITY OF CALIFORNIA

DAVIS

Approved:

Professor Daniel A. Cebra, Chair

Professor Manuel Calderón De La Barca Sánchez

Professor Ramona Vogt

Committee in Charge

2014

Samantha Gail Brovko
December 2014
Physics

Hadron Production and Freeze-Out Dynamics at $\sqrt{s_{NN}} = 3.0$ GeV Au+Al and $\sqrt{s_{NN}} = 19.6$ GeV Au+Au Collisions as Measured at STAR

Abstract

The Beam Energy Scan program at RHIC was commissioned to search for the critical point and the turn-off of QGP signatures. The program has completed collisions of Au+Au at energies from 7.7 to 62.4 GeV per nucleon pair in 2010 and 2011. The addition of a full-coverage Time-of-Flight detector at STAR extended the momentum range for clean particle identification. Mid-rapidity ($|y| < 0.5$) hadron spectra will be used to determine the freeze-out dynamics of the system. Particle spectra for π, K, p and $\bar{p}$ as a function of $m_T - m_0$ will be presented and these will be used to discuss in particular the source's Coulombic effect on soft pions, as well as three of the four signs of the onset of deconfinement: the "Kink," the "Horn," and the "Step." Comparisons will be made to $\sqrt{s_{NN}} = 7.7$ GeV, 11.5 GeV, 19.6 GeV (from 2001), 27 GeV, 39 GeV Au+Au data from STAR, and $\sqrt{s_{NN}} = 17.3$ GeV Pb+Pb data from the SPS heavy ion program. Collisions between gold ions in the RHIC beam with aluminum nuclei in the beam pipe allow us to analyze fixed-target interactions with the STAR detector at RHIC. These lower-energy fixed-target collisions may allow us to extend the low-energy reach of the RHIC beam energy scan and possibly improve the chance of finding the critical point of the hadronic to quark matter phase boundary. In this thesis, we will present preliminary results of spectra analyses for a fixed target collision system at $\sqrt{s_{NN}} = 3.0$ GeV and colliding beam system at $\sqrt{s_{NN}} = 19.6$ GeV . Also, the viability of doing fixed-target experiments with a collider detector will be discussed. Comparisons to simulation, using UrQMD, will also be made. The analysis provides a good reference to study excitation functions of strangeness production, net baryon number, and collective flow in heavy-ion collisions.

Dedication

This document is dedicated to my father.

Dad, you have always believed in me; look where I am now.

Acknowledgments

No one ever said writing a dissertation was easy. In fact, my dad always said it would take tears and coffee—lots and lots of coffee. He spoke truth. This document would still be left dangling and unfinished without the extensive support of my parents, Nicolai Brovko and Pamela Graves, my sisters, Julie Brovko and Christina Petruse, my best friends, Bonnie Coe and Amber Rammel, and my family. Thank you for always encouraging and pushing me and for your never-ending belief.

To Drs Liam Damewood, Owen Dix, and Colin Cunliff I owe great thanks for the Panera Bread and UCD library writing marathons, physics and C++ talks, coffee and lunch breaks, hikes, and sanity checks. Thank you for your willingness to share any and all knowledge in your extremely intelligent brains. And Thai Pizza.

Of course, none of this research would have been possible without the endless support of Professor Daniel Cebra and Professor Manuel Calderón De La Barca Sánchez. Both of you create the best of all possible work environments and I couldn't have asked for better research advisors, or better mentors. Thank you for everything.

Special thanks belongs to Colin Connors who, despite the difficulties, managed to help whenever I had need. Thank you for your C++ expertise, your patience, and your time.

Dr. Susan Brown, the Houghtby family, Sandy Rammel, Sharon Casey, Kiri Hamaker, Jack Wu, Kevin Sanford, Rosi Reed, Professor Sevil Salur, Terry Tarnowsky, Kolja Kauder, Dustin Readd, Scott Rammel, Alex Schmah, Patrick Huck, Laura Peterson, Craig and Laura Coe, and Professors Rena Zieve, Ramona Vogt, Richard Scalettar, Frank Geurts, and Bill Llope complete my network of support. Thank you all, I wouldn't have made it this far without each and every one of you.

Contents

List of Figures

List of Tables

Chapter 1

Introduction

1.1 Overview

This dissertation presents a summary of extensive analysis of charged light-particle production in 3.0 GeV per nucleon pair central Au+Al interactions as well as 19.6 GeV per nucleon pair Au+Au collisions of several centrality classes ($\sqrt{s_{NN}}$ = 3.0 GeV, and $\sqrt{s_{NN}}$ = 19.6 GeV respectively). The goal of this work is to analyze a particular energy between nominal SPS energies and nominal RHIC energies to search for interesting physics, including a possible phase transition, and to compare the systematics of RHIC and SPS for similar energies. By studying the interactions of the Au or Au-like nucleus with the Al nuclei in the beam-pipe material, we determine the feasibility of analyzing fixed target collisions with a center-of-mass designed detector. Knowing such an analysis is possible can further studies of the beam-energy dependence of the temperature and baryon chemical potential. By studying the collisions of two Au nuclei we obtain a particular temperature and baryon chemical potential for that collision characterizing some possible interesting physics and further understanding the nuclear matter phase diagram.

The dissertation is organized as follows: Chapter 1 presents a focused overview of the field of ultrarelativistic heavy ion physics and motivates the analysis; Chapter 2 provides a brief introduction to the necessary theory required to understand the analysis and the physics goals of the analysis; Chapter 3 describes in some detail the experimental setup and

an adequate description of the detector operation; Chapter 4 describes the analysis methods from initial data production to data refinement, particle identification and extraction of raw yields, as well as the corrections and systematic studies of the analysis; Chapter 5 concisely presents the results of the analysis and discusses the physical significance and relevance of those results by comparing to theoretical calculations and other world experiments; and finally in Chapter 6 a summary and conclusion are presented with future work in mind.

1.2 The States of Nuclear Matter

In ultrarelativistic heavy ion collisions a partonic state of matter is inferred from measurements made at energies of 200 GeV per nucleon pair. The Quark-Gluon Plasma (QGP) has been established based on two very important results [1]. First is the result describing the suppression of the away-side jet peak in central Au+Au collisions [2] [3]. The observed suppression indicates the existence of a dense medium in which hadrons interact strongly with the medium early in the collision history. The second important result being the result describing the hydrodynamic fit of the elliptic flow as a function of transverse momentum. Additionally, when scaling kinetic energy and elliptic flow by constituent-quark number, the separation of mesons from baryons disappears and all particles follow the same hydrodynamic curve. This property indicates that the underlying degrees of freedom when elliptic flow is established are consistent with being partonic, i.e. the flow of quarks rather than hadrons. These, and other signatures of the QGP, will be discussed in further detail in Section 2.2. Once the QGP was supported by these strong pieces of evidence, characterization of the medium and determination of the baryon chemical potentials and temperatures where the QGP could not exist became the next step.

The phase diagram of nuclear matter as it is today, see Fig. 1.1, is mostly a schematic with only two known points: nuclear matter at room temperature [5] and the transition temperature ($\sim$175 MeV) at μ_B of zero [6]. For reference, room temperature is $\frac{1}{40}$ eV. The

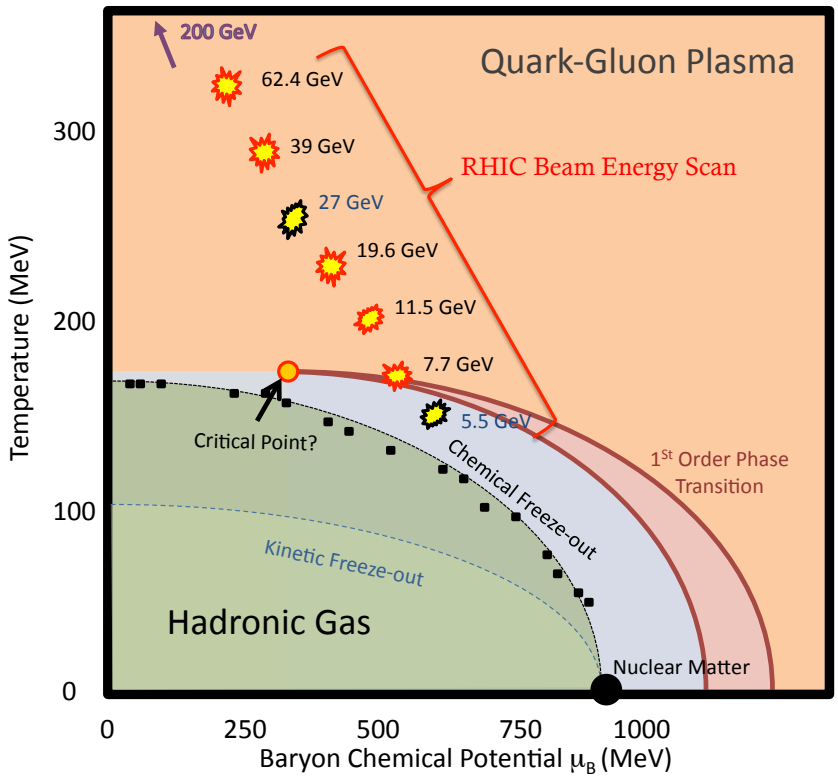

Figure 1.1: Nuclear matter phase diagram schematic with temperature versus baryon chemical potential μ_B. For reference, room temperature is $\frac{1}{40}$ eV. The large black dot represents the proton at room temperature. The muave/pink area wedged by thick dark red lines represents the possible region where the first order phase transition [4] may occur. The blue region represents the thermal production of hadrons before chemical freeze-out. The green regions represent elastic collisions above the kinetic freeze-out curve, and below the kinetic freeze-out curve, the final state of hadrons with fixed momenta. The peach region indicates the temperatures and baryon chemical potentials with a QGP phase. After chemical freeze-out, only particle decay contributes to changes in particle number. *D. Cebra via private communication.*

large black dot in the figure represents the proton at room temperature. The muave area wedged by thick dark red lines represents the possible region where the first order phase transition [4] may occur. The blue region represents the thermal production of hadrons before chemical freeze-out. The chemical freeze-out curve represents the temperature and baryon chemical potential at which the production of hadrons due to inelastic collisions has ceased [7]. After chemical freeze-out, only weak particle-decay contributes to changes in particle number. The kinetic freeze-out curve defines the temperatures and baryon chemical potentials at which elastic collisions and momentum transfer have ceased [7]. The green regions represent elastic collisions above the kinetic freeze-out curve, and below the kinetic freeze-out curve, the final state of hadrons with fixed momenta. It is expected that the chemical freeze-out temperatures are always greater than the kinetic freeze-out temperatures [7]. The diagram displays the temperature versus baryon chemical potential and qualitatively illustrates the trends we see from theoretical calculations of the various transition curves [4] and an approximate region for the location of the critical point [8] — the point where the cross-over phase transition is expected to change to first order — and onset of deconfinement (free quarks and gluons) [9]. The Beam Energy Scan's (see section 1.3) program of collision energies is aimed to create equilibrated systems whose initial states are near the T and μ_B of the onset of deconfinement; however, we are unable to measure directly these initial-state variables for the corresponding collision energies. The diagram will be better understood when the phase transition curve, the freeze-out curves and the critical point are determined.

1.3 The Beam Energy Scan Program

At the heart of ultra-relativistic heavy-ion physics is mapping the nuclear-matter phase diagram. And, at the forefront of current research in QCD theory and experiment is the search for evidence of a critical point and/or its associated first-order phase transition in the phase diagram. Though recent progress in lattice QCD and model calculations has been

great, an exact location of the phase boundaries between the QGP and a hadron gas as well as the postulated critical point are still unknown [10–12]. Observational evidence of these two features must then be found in heavy-ion experiments [13–16] such as those at the Relativistic Heavy Ion Collider (RHIC) because the wide collision-energy range of the facility corresponds to the prime QGP search region of the phase diagram.

Theory has predicted several signatures of a first-order phase transition and signatures for the critical point (for example [17–23] and Refs. therein). The majority of these predictions indicate an increase in fluctuations when the freeze-out trajectory passes through the critical point or some dependence of the fluctuations on center-of-mass energy near the range in μ_B where the critical point lies [23] [24]. Because the critical point may act as an attractor [25] (a phenomenon discussed in Ref. [26] in the context of nuclear liquid-gas transitions), as long as the thermalized initial conditions fall within a small range of μ_B the evolution of the system with time will pass through the critical point. Passing through the critical point would provide evidence for its existence without the problems precise theoretical calculations encounter (namely, Lattice calculations discussed in Sec. 2.1). Establishing the validity of the hypothesized critical point, or even bounding the region where it lies by proving the existence of both a crossover AND a first/second order transition, would begin to concretely define the phase diagram. This result would be arguably as groundbreaking as proving the formation of the QGP.

The nuclear matter phase diagram (see Fig. 1.1) is currently incomplete. Determining chemical freeze-out points, kinetic freeze-out points and the order of the phase transition all require multiple energies to be run with one given species of ion as well as running different species with similar energies [9] [27]. Experiments at facilities like the Super Proton Synchrotron (SPS) at CERN and the Alternating Gradient Synchrotron (AGS) at Brookhaven National Laboratory (BNL) were already running heavy-ion collisions at high μ_B. In RHIC, also at BNL, several species of ions are collided to determine the properties of the QGP and to look for its signatures in data with small μ_B.

In 2001 and 2008 test beams of lower center-of-mass energies of 19.6 GeV per nucleon pair and 9.2 GeV per nucleon pair, respectively, were run to demonstrate the capability of the RHIC detectors to collect data at these sub-injection energies. While neither of these runs were long enough to improve on the physics measurements reported by the SPS experiments, many checks were performed. With the results from these tests [28–30], a well-designed program suitable for both heavy-ion experiments at RHIC with the goals of mapping the phase diagram was created.

In 2009, the STAR Collaboration (Solenoidal Tracker At RHIC) proposed to run a beam-energy scan (BES) to find the energies where QGP signatures could no longer be observed, as well as to identify a softest point in the equation of state indicative of a first-order phase transition [31]. The BES program has three main goals and intends to achieve them by colliding Au beams in a range of energies from 5.5 GeV per nucleon pair (below the onset of deconfinement [9] and the supposed critical point) to 62.4 GeV per nucleon pair (above the supposed critical point) [31]. First, it will search for the turn-off of each of the signatures of the QGP discussed in Section 2.2. Second, it will search for a first-order phase transition and further map the kinetic and chemical freeze-out curves. And finally, it intends to search for evidence of a critical point [8].

In 2010, the majority of the proposed energies for Au+Au collisions were run (62.4, 39, 11.5, 7.7) with two energies (27, 19.6) postponed for the following year, 2011. A test of the 5.5 GeV beams was made in 2010 and, at the time, accelerator experts were unable to tune the beams for circulation in the RHIC rings, nor to bring them into collision at any interaction region. Thus the only proposed BES energy below the energy identified as the onset of deconfinement [9] could not be run, nor could data be collected. However, the STAR detector was able to record data from the beam halo (Au-like ions) colliding with the beam pipe (Al) with vertices within the geometry of the main detector, the Time Projection Chamber (TPC see section 3.2), during the 19.6, 11.5, and 7.7 GeV per nucleon pair beams. These beam-halo+pipe collisions have allowed the STAR collaboration to study

interactions with center-of-mass energies below the requested 5.5 GeV energy and to extend the low energy reach of the BES program. The STAR Collaboration can compare the beam-halo+pipe results with data from previous experimental programs, namely the fixed target heavy-ion program of the AGS.

1.4 Fixed Target Collisions Measured with the STAR Experiment

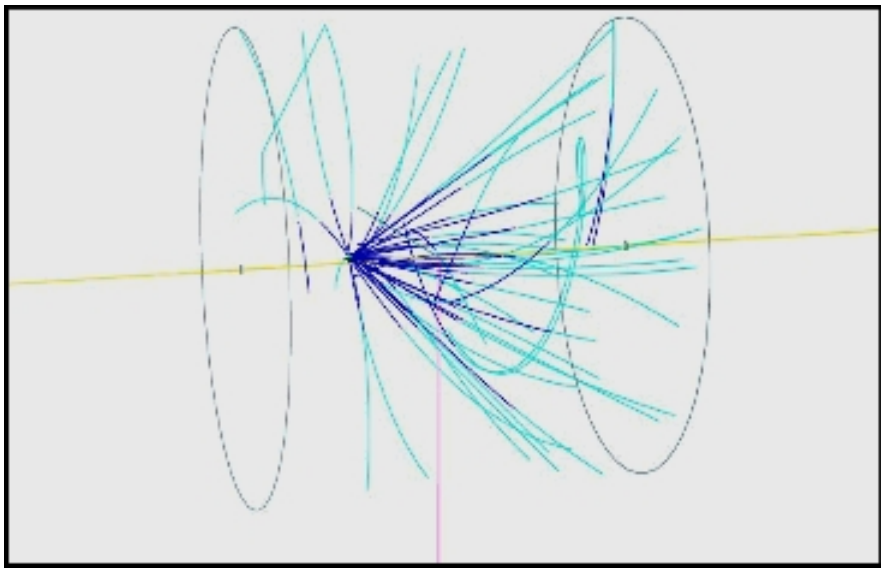

Figure 1.2: Fixed target interaction as reconstructed by the STAR detector. Note that the vertex is displaced from the beam axis (the yellow line) and also displaced from the center of the detector (denoted by the pink line). All of the tracks are to one side of the vertex (to the right) as would be expected from a projectile on a target at rest rather than being symmetric about the collision point, as is typical of collider events. (*A. Schmah via private communication.*)

During data collection of previous low-energy beam test runs at RHIC, the STAR collaboration found a large number of beam-halo+pipe interactions that were recorded in addition to the good Au+Au collisions. An example of a reconstructed fixed target interaction is shown in Fig. 1.2. The yellow line denotes the beam axis and the two black rings represent the z-location of the TPC endcaps. The pink line shows the center of the TPC. All of the tracks reconstruct and extrapolate to a point near the left TPC endcap where the

light blue portion indicates the part of a track that was reconstructed with hits and the dark blue portion indicates the extrapolation of that track to the vertex. A few attempts were made to exclude beam-halo+pipe collisions from data collection before the BES program began. However, those studies demonstrated the importance of recording data from these interactions. Further studies indicate the necessity of reconstructing the Au-like+Al vertices and tracks in addition to the Au+Au collisions for the entire BES program. By accurately reconstructing events like these, endusers could easily reject events of this type from their analyses without the risk of misassociated tracks to a vertex or "shadow vertices" (this is described in further detail in Sec. 4.2).

In the summer of 2010 the UCD group began in earnest to analyze the beam-halo+pipe events and to determine if physics extraction was possible. This required, among many other things, determining the energy at which the interactions occurred. The beam pipe 'target' (Al) is parallel to the Au ion beam axis and the Au-like projectile nucleus experiences energy loss while traveling through the metal of the pipe prior to experiencing a nuclear interaction. Additionally, considerations of the detector geometry to determine acceptance and efficiency of tracking were made. Careful evaluation of variables for determining collision centrality with comparisons to an analytic Glauber model [32] [33] (a model to estimate the number of particles produced based on the number of nucleons participating in an inelastic collision) as well as a Glauber Monte Carlo [34] was one of the largest challenges of the initial study. After diligent analysis of the data, described in Sec. 4.3, a determination of the collision energy and centrality definition allowed particle spectra to be produced.

Ultimately, being able to use STAR as a fixed target experiment as well as a colliding beam experiment has allowed the Beam Energy Scan (BES) to reach further into the high-baryon-chemical-potential and low-temperature region of the nuclear matter phase diagram than the program originally intended. Currently, a fixed-target program is under development to more accurately compare systematics between the colliding-beam energies and the fixed-target energies [35].

Chapter 2

Ultrarelativistic Heavy-Ion Physics

Systematic experimental studies with relativistic heavy ions began in the 1970's at laboratories in Berkeley, California, USA and Dubna, Russia. The early experiments broke ground with a better understanding of the strong force leading to a string of hypotheses requiring high temperatures and energy densities for the formation of a new phase, a quark-gluon plasma (QGP) [36–38]. This generated some excitement and momentum for experiments with higher energies per nucleon. The existence of a QGP required a phase transition and was expected to be characterized by free quarks and gluons. During these early years, quantum chromodynamics (QCD) was developed to investigate the strongly-interacting matter at said high energy densities and temperatures. This chapter will summarize the key concepts of QCD, highlight key features of the Quark-Gluon Plasma that can be experimentally quantified, discuss particle spectra analysis, and detail the Coulomb analysis to be presented in Chapter 5.

2.1 Introduction

The theory of quantum chromodynamics (QCD) was developed using the basis and methodology of quantum electrodynamics (QED). The success and precision of calculations in QED held promise for predictions in QCD. However, as QCD theory developed further (in particular the perturbative methods), key differences affected the ability to make as precise

predictions as the electromagnetic counterpart. In QED, the Lagrangian is:

$$\mathcal{L} = -\frac{1}{4}F_{\mu\nu}^2 \tag{2.1}$$

where,

$$F_{\mu\nu} = \partial_\mu A_\nu - \partial_\nu A_\mu \tag{2.2}$$

and A_μ describes the vector potential of the electromagnetic field. Diagrams that contain an increasing number of vertices will contain increasing powers of the coupling constant, $\alpha_s = \frac{1}{137}$, and thus the perturbative series will converge.

In QCD, the Lagrangian is:

$$\mathcal{L} = -\frac{1}{4}\sum_\alpha F_{\mu\nu}^\alpha F^{\mu\nu\ \alpha} + i\sum_q \bar{\psi}_q^i \gamma^\mu (D_\mu)_{ij}\psi_q^j - \sum_q m_q \bar{\psi}_q^i \psi_{q\ i} \tag{2.3}$$

where in the first term, the gluon-only term, $\alpha = 1, 2, \ldots, 8$ indicates the color indices of gluons, and the field tensor,

$$F_{\mu\nu}^\alpha = \partial_\mu A_\nu^\alpha - \partial_\nu A_\mu^\alpha + g_s[A_\mu, A_\nu]^\alpha \tag{2.4}$$

contains the eight 4-vector potentials, A_μ^α, of the gluon field, with g_s being the color charge. The last term in Eqn. (2.4) represents the self-interaction of gluons due to their non-zero color charge (very unlike photons in QED since photons have no electromagnetic charge). The second term in the Lagrangian describes the interaction of quarks with gluons where each of the ψ_q^i are four-component Dirac spinors of the quark fields with color i and flavor q, and the covariant derivative,

$$(D_\mu)_{ij} = \delta_{ij}\partial_\mu + i\frac{g_s}{2}\sum_\alpha \lambda_{i,j}^\alpha A_\mu^\alpha \qquad . \tag{2.5}$$

where the $\lambda_{i,j}$ in Eqn. (2.5) are 3×3 matrices and SU(3) group representations. The third

and last term in the Lagrangian describes the self-interaction of quarks. Finally, the coupling constant in QCD is:

$$\alpha_s(Q^2) = \frac{4\pi}{\beta_0 \ln(Q^2/\Lambda^2)}\big(1 + \text{higher logarithmic terms}\big) \qquad . \tag{2.6}$$

In equation 2.6, Λ is a scale constant, $\beta_0 = 11 - \frac{2}{3}n_f$ where n_f denotes the number of light quarks. Typically α_s is calculated at the mass of the Z^0 boson and $\alpha_s(m_{Z^0}) = 0.118 \pm 0.002$, giving $\Lambda = 217^{+25}_{-23}$ MeV [39]. For large values of Q^2, perturbative methods can be used in calculations. However, because the value of α_s is large at small Q^2, and goes to infinity if $Q^2 = \Lambda^2$, perturbative calculations do not always converge. Thus, more complex numerical methods are needed. Lattice QCD methodology was introduced in 1974 [40] and continues to be developed.

Lattice QCD relies on computational power and thus has pushed the development of parallel processing in computers. Because finite-temperature lattice QCD is beyond the scope of this thesis, only a brief discussion of the main findings will be presented here. An introduction to the theory can be found in Ref. [41] while more detailed information can be found in Refs. [42–47].

Calculations using lattice QCD begin with deconfinement starting with the Polyakov loop [48–50]

$$L(T) \sim \lim_{r\to\infty} e^{(-V(r)/T)} \tag{2.7}$$

where $V(r)$ is the potential between a static quark-antiquark ($q\bar{q}$) pair separated by distance r, and T is the temperature. The potential, $V(r) \sim \sigma r$, where σ is the string tension for pure gauge theory and, as $V(r) \to \infty$ (an infinite amount of energy required to separate a quark-antiquark pair), $L = 0$. Then $L(T)$ becomes similar to an order parameter because color screening causes the string to melt, forcing the potential to be finite and L to be nonvanishing. Thus for the temperature range $0 < T < T_c$, $L = 0$ and quarks are confined, but for temperatures $T > T_c$, L is finite and non-vanishing, meaning quarks are deconfined.

The temperature T_c is the temperature for the onset of deconfinement and an indicator of a first-order phase transition [41]. This rapid change in L is not as easily seen with light quark masses as it is with heavy quark masses [45].

The effective quark mass can be determined using lattice methods by calculating the expectation value of $\langle\bar{\psi}\psi\rangle(T)$, called the quark condensate. The quantity $\langle\bar{\psi}\psi\rangle(T)$ is the order parameter of the chirally-symmetric Lagrangian in the limit of vanishing current quark mass. Chiral symmetry is broken in the confined phase with finite constituent quark masses. It is expected that, at sufficiently high temperatures, the symmetry will be restored. At vanishing baryon number density, the shift from constituent quark mass to current quark mass and the onset of deconfinement are expected to occur simultaneously [51]. Physically, however, quark masses are neither infinite nor massless but rather have a finite current quark mass. Thus the symmetry is only approximate.

Next, lattice QCD characterizes the behavior of the energy density and the pressure at deconfinement. These bulk thermodynamic properties are indicative of the number of degrees of freedom in the system in the high-temperature limit. For example, pressure tends to the ideal gas value as the temperature becomes very high. The pressure of the ideal hadronic and deconfined systems are

$$\frac{P_\pi}{T^4} = \frac{3\pi^2}{90} \qquad T \to 0 \tag{2.8}$$

$$\frac{P_{\text{qgp}}}{T^4} = (16 + \frac{21}{2}n_f)\frac{\pi^2}{90} \qquad T \to \infty \tag{2.9}$$

when the baryon chemical potential, μ_B, is zero. Classically, the free energy density is calculated from the difference between two temperatures. In QCD this is approximated by

$$\epsilon \sim \frac{\partial(\ln(Z)/T^4)}{\partial T} \tag{2.10}$$

where Z is the QCD partition function. By taking the derivative with respect to the gauge coupling instead, Eqn. 2.10 becomes the difference between the expectation values of the Euclidean action,

$$\epsilon \sim N_\pi^4 \int_{\beta_0}^{\beta} d\beta' \Big(\langle \hat{S}_E \rangle - \langle \hat{S}_E(T=0) \rangle \Big) \qquad , \tag{2.11}$$

which is calculable on the lattice. An abrupt increase in the value of energy density is observed at the critical temperature when plotting ϵ/T^4 as a function of the temperature in units of the critical temperature, T/T_c. It increases from a small hadronic value to a large value approximately 10% below the value of a Stefan-Boltzmann ideal gas [52]. With some manipulation, one can obtain a value for P/T^4 which is indicative of the number of degrees of freedom in the system. The value of the transition temperature must be calculated by fixing other observables on the lattice, such as the proton or ρ-meson mass since there are no dimensions in the equations of QCD for massless quarks. Additionally, the value of the temperature depends on the number of quark flavors present in the theory, as well as the observable. For example, 2-flavor calculations yield $T_c = 173 \pm 4$ MeV while 3-flavor calculations obtain $T_c = 154 \pm 8$ MeV [45]; if using the ρ-meson mass as the point of reference, $T_c \sim 150$ MeV, or, if using the string tension, σ, then $T_c \sim 200$ MeV. All estimates, either using quark numbers or some particular observable, obtain $\epsilon = 1 - 2$ GeV/fm^3 for the energy density needed to reach the high-temperature phase, which we have called the Quark-Gluon Plasma phase.

Lattice calculations show that a transition from hadrons to a QGP does exist and that the transition coincides with chiral symmetry restoration. The calculations also demonstrate that the transition occurs at a crossover temperature and is observed when a sudden increase in the energy density occurs and shifts to a large value that is $\sim$10% lower than the Stefan-Boltzmann ideal gas value.

2.2 Signatures of the Quark-Gluon Plasma

Nucleus-nucleus collisions, $A+A$, have three main stages of evolution. Beginning at the point of collision, $t = 0$, a very hot, very energy dense region is created. The energy density of the initial collision can be estimated by the Björken formula, which is the rapidity-independent Lorentz formula:

$$\epsilon = \frac{1}{\tau_f S}\frac{dE_T}{dy} \simeq \frac{3}{2}\frac{\langle m_T \rangle}{\tau_f S}\frac{dN_{\rm ch}}{dy} \tag{2.12}$$

where ϵ is the initial energy density, τ_f the formation time, S the overlap region, dE_T/dy the transverse energy density, $\langle m_T \rangle$ the average transverse mass, and $dN_{\rm ch}/dy$ the density of charged particles. This stage is characterized by large momenta exchanges, prodicing jets and heavy quark pairs ($c\bar{c}$ and $b\bar{b}$) through parton-level interactions.

Next, the produced partons interact to achieve chemical and thermal equilibrium. This stage is characterized by a rapid expansion and cooling of the locally statistically-equilibrated system to the critical temperature, T_c [53]. Direct photons are produced and the start of collective flow begins at this stage. The quark-gluon plasma has an expected lifetime of between 1 to 10 fm/c and a size of at most a few femtometers in diameter. Equilibration of the QGP allows for further evolution to be calculable using relativistic hydrodynamics. Questions still remain in regard to the equilibration time: whether it occurs instantaneously [54] or on the same order as the lifetime [55] [56].

Finally, chemical freeze-out, kinetic freeze-out, and hadronization occur. In the subsequent hot hadronic gas phase following hadronization, global observables must be interpreted to determine, after the fact, the initial conditions of the collision. Utilizing observables, the signals of the quark-gluon plasma must be distinguished from the hadron background. Even these signals are modified by final-state interactions in the hadronic phase. Some of the key signatures are discussed in the following sections.

2.2.1 Strangeness Enhancement

A feature of the QGP is an enhancement of strangeness content compared to $p+p$ collisions. Typically in hadronic interactions, production of strangeness is suppressed due to the higher mass of the strange quark as compared to the up and down quarks. However, in the QGP environment, not only are quarks and gluons produced in abundance, but also the energy density and temperature are high (on the order of the strange quark mass $m_s = 101^{+29}_{-21}$ MeV [39]). As u and d quarks are the most easily produced and most abundant quarks in the initial stage of the QGP fireball, the available phase space is quickly filled; thus strangeness becomes more readily produced [57]. Furthermore, the u and d quarks annihilate with the $\bar{u}$ and $\bar{d}$ antiquarks, respectively, while $s\bar{s}$ annihilation occurs less frequently until the saturation of s and $\bar{s}$ abundances.

The two main production channels for $s\bar{s}$ pairs are $q\bar{q} \rightarrow s\bar{s}$ and $g\bar{g} \rightarrow s\bar{s}$. Considering production of $s\bar{s}$ pairs by only the $q\bar{q}$ channel, chemical equilibrium in strangeness would only be reached after about eight times the natural lifespan of the QGP fireball. One proposed idea is that the quark-antiquark pairs are created dominantly by the gluon-gluon fusion channel [57] [58] and this would be reflected in the enhancement of strange- and multi-strange baryons compared to purely hadronic interactions at the same temperature. However, a QCD calculation of heavy-quark production also explains that gg is more abundant than $q\bar{q}$ and thus gg dominance follows trivially.

Strangeness enhancement is experimentally defined as the yield per participating nucleon of a given type of strange particle in heavy ion collisions (at RHIC, Au+Au, for example) relative to the same strange particle yield in a lighter reference collision system ($p + p$, for example). Strangeness fugacity, γ_s, is introduced in thermo-chemical models to account for possible incomplete chemical equilibration of strangeness.

In contrast, other ideas illustrate that a difference between the use of micro-canonical versus grand canonical ensembles in hadronic ($p + p$) and heavy-ion collisions, respectively, accounts for the strangeness enhancement factor [59]. In fact, the difference in ensemble

utilization demonstrates that the enhancement in heavy-ion collisions compared to hadronic collisions decreases with collision energy [59] in agreement with experimental results.

2.2.2 J/ψ Suppression

In the presence of a QGP, the bound state of $c\bar{c}$, the J/ψ, will be suppressed with increasing temperature due to a weakening of the heavy-quark effective potential [60]. This is Debye screening of free color charges in the QGP. Gluon exchange explains the long-range Coulomb-type term in the effective potential. At small distances, the strong coupling constant $\alpha_s \sim Q^2$, the momentum transfer squared, while at large distances $\alpha_s \sim \infty$. This leads to the effective potential rising linearly with distance, r, and thus the effective potential between two heavy quarks is calculable on the lattice. This phenomenon adds the string-like term in the effective potential. The effective potential (also called "Cornell" potential) then looks like,

$$V(r) = \sigma r - \frac{\alpha}{r} \tag{2.13}$$

and describes the color interaction between c and $\bar{c}$ without the presence of a QGP medium (i.e. vacuum). This potential will turn into a short-range Yukawa-type

$$V(r) = \sigma r \frac{1 - e^{-\mu(T)r}}{\mu(T)r} - \frac{\alpha e^{-\mu(T)r}}{r} \tag{2.14}$$

interaction in the presence of a QGP medium (see Fig 2.1), with the range given by the Debye screening length, λ_D, related to the inverse of $\mu(T)$ the temperature dependent screening mass. This potential can be plugged into the Schrödinger equation, since it is non-relativistic, in order to determine the disassociating temperature of each state of J/ψ and Υ families.

The potentials mentioned above are rather simplified to what may actually occur during a heavy-ion collision. By looking at Fig 2.2 the magnitude of the observed suppression at both RHIC and SPS facilities indicates more than Debye screening as the dominant cause of suppression. The figure, taken from Ref. [62] shows the nuclear modification factor, R_{AA}, for

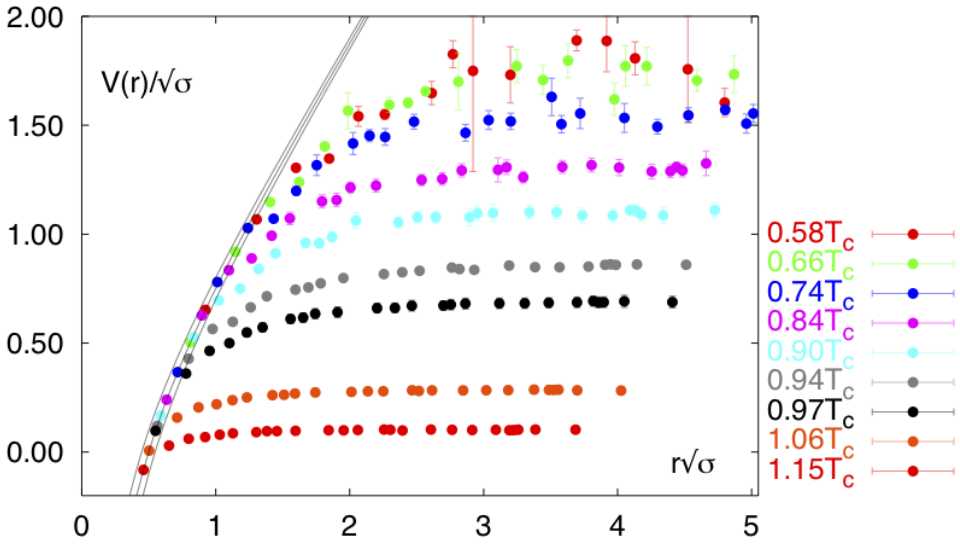

Figure 2.1: Taken from Ref. [61]. Temperature dependence of the heavy quark potential for three flavor QCD with a quark mass $m_q = 0.1$. The band of lines gives the Cornell-potential in units of the square root of the string tension, $V(r)/\sqrt{\sigma} = -(\alpha/r)\sqrt{\sigma} + r\sqrt{\alpha}$ with $\alpha = 0.25 \pm 0.05$. The gauge couplings corresponding to the different temperatures are $\beta = 3.25$, 3.30, 3.35, 3.40, 3.43, 3.45, 3.46, 3.50, 3.54. The string tension values used to set the scale are based on the interpolation formula given in Ref. [52]. The potentials have been normalized at short distances such that they agree with the zero temperature Cornell potential at $r = 1/4T$.

J/ψ's at midrapidity measured by PHENIX in Au+Au and Cu+Cu collisions as a function of the number of participants, N_{part}, in the initial collision. Also on the plot are similar results derived from measurements from other experiments with lower energies and different collision systems (Pb+Pb, In+In, S+U) at CERN. The nuclear modification factor (R_{AA} or R_{AB}) is again plotted as a function of the number of participants corresponding to the centrality bins made in each of the different analyses. The pattern showcased is similar for all colliding systems despite the colliding systems being in different energy (and therefore energy density and shadowing/antishadowing) regimes [62]. The original potential is too simplistic and we must look for additional modification factors such as those from cold nuclear matter effects to heavy quark suppression [62].

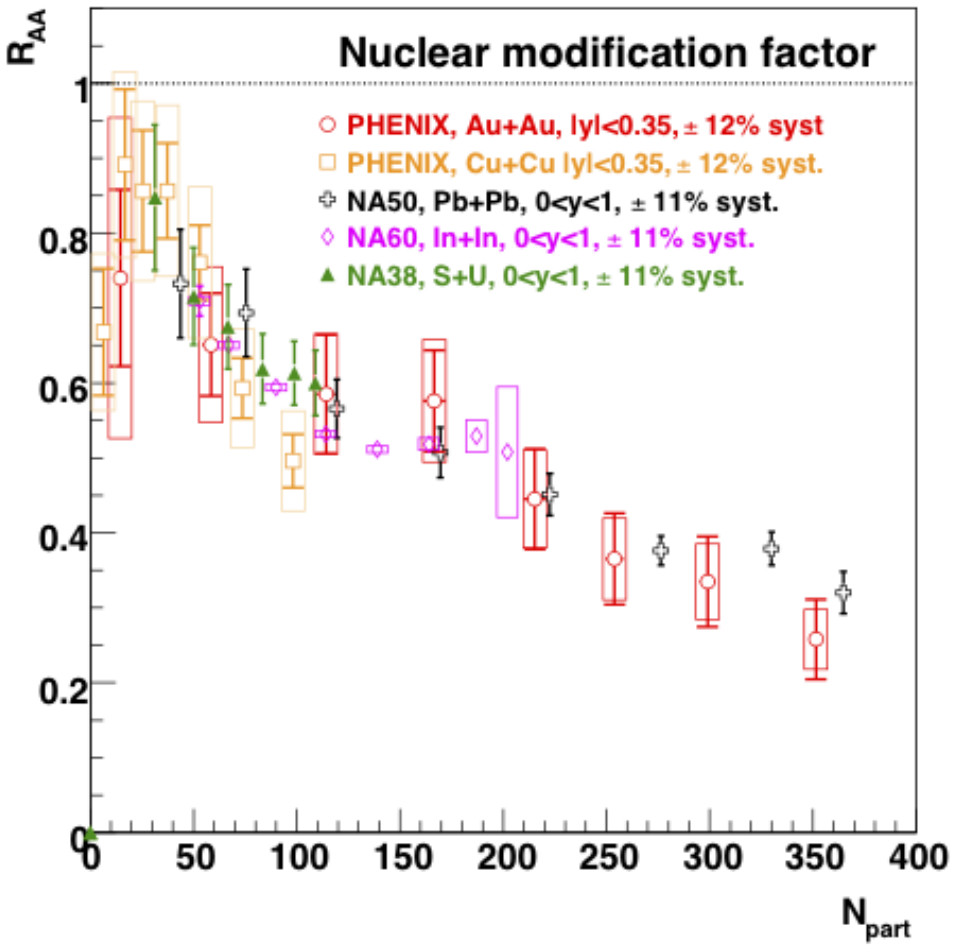

Figure 2.2: Taken from Ref. [62]. J/ψ nuclear modification factors for Au-Au, Pb-Pb, In-In and S-U colliding systems at their respective energies (200, 19 and 17.3 GeV) as a function of the number of participants, N_{part}.

2.2.3 Direct Photons and Dileptons

Two signals that can provide information about the earliest times of the collision without much interference from the colored medium are direct photon production and dilepton production. These two radiated signals are proposed as arguably the most promising and efficient signals for characterizing the initial state of a heavy ion collision.

Photons are produced at every stage of the fireball evolution, see Figure 2.3. Direct photons refer to photons that are produced from particle collisions. These photons have a large mean-free path compared to they system size (∼10 fm) and traverse the colored medium without participating in a collision or interaction since photons interact electromagnetically.

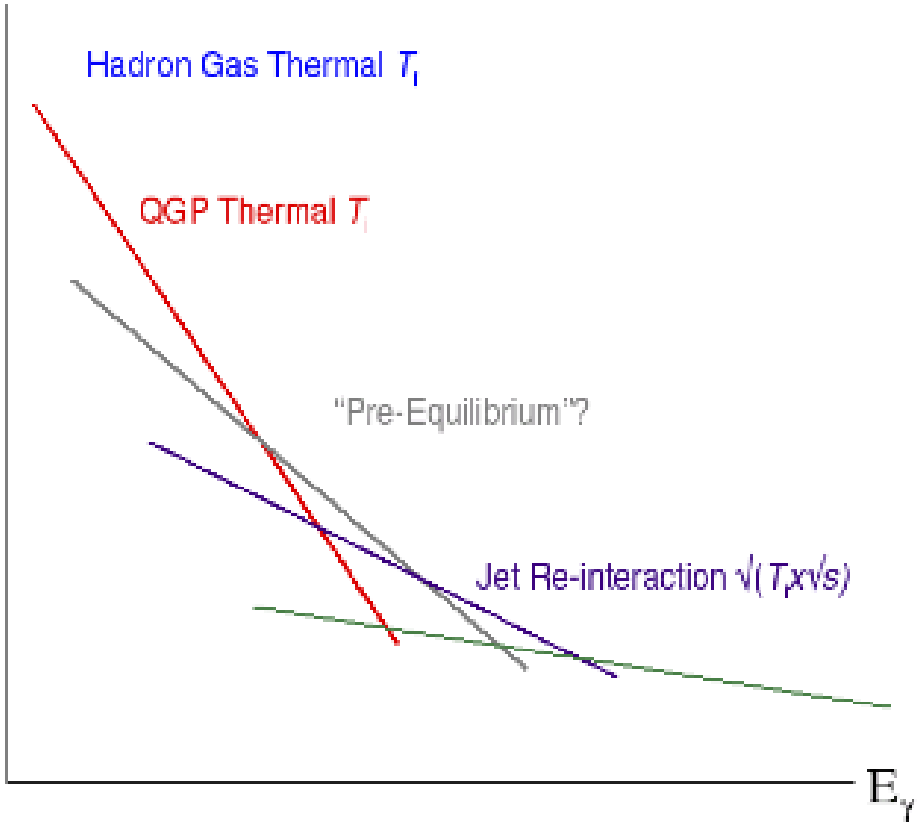

Figure 2.3: Schematic of expected sources of photons as a function of energy [63]. The red line is the contribution from QGP Thermal emission, the grey line represents the contribution from emission on pre-equilibrium, the purple line denotes contributions from jet re-interactions, the green line is not labeled but describes the photons emitted during the pQCD prompt $x\sqrt{s}$ phase, and the blue label for Hadron Gas Thermal is for contributions to the low energy side of emission which decreases rapidly as energy increases; it has a much steeper slope than thermal QGP emission.

Thus, direct photons can carry information about the QGP, like temperature at their production, and serve as a signal for QGP formation and early stages of the collision [64]. This broad category can be further subdivided by stages of the collision evolution into prompt photons, pre-equilibrium photons, thermal photons and jet conversion photons. Prompt photons are created in the early stages of the collision (initial hard scatterings) through gluon channels such as $q\bar{q} \rightarrow \gamma\bar{g}$, $g\bar{q} \rightarrow \gamma g$, or the dominant gluon-photon Compton Scattering process $gq \rightarrow \gamma q$. Pre-equilibrium photons are produced before the plasma is thermalized. Thermal photons are produced thermally from both hadronic reactions (certain types of Compton scatters like $\pi\rho \rightarrow \gamma\rho$ [65] [66]) and the QGP environment (the same production

channels as direct photons, only softer and much less abundant than decay photons). Jet conversion photons are produced from the passage of jets through the plasma [63].

Direct photon production, however, has a relatively small cross section in addition to the signal being washed out by the large number of additional sources of photons throughout the fireball lifetime. An example of other such sources of photons include hadronic decays (like pions $\pi^0 \rightarrow \gamma\gamma$). These backgrounds are typically subtracted using the invariant mass spectrum method established by the WA98 Collaboration [67] and then perfected by the PHENIX Collaboration [68].

Dileptons are massive, unlike the massless real direct photons, and allow for parameters like invariant mass and transverse momentum to be utilized to examine properties at each stage of the fireball [69]. Dileptons with high transverse momentum and/or high invariant mass are produced from hard scatters at earlier stages of the fireball whereas dileptons with low transverse momentum and/or small invariant mass are produced later. The dilepton production mechanism is $q\bar{q} \rightarrow \gamma^* \rightarrow l^+l^-$ during the QGP phase while in the hadronic phase mechanisms include decay particles like ρ, ω, ϕ, and J/ψ, interactions following $h^+h^- \rightarrow l^+l^-$ format as well as the Drell-Yan process (where a valence quark from one nucleus interacts with a sea quark from the other nucleus to produce a virtual photon which decays into a lepton pair) [63].

Dileptons can be subdivided into three rough categories corresponding to the invariant mass of the produced pair, see Figure 2.4. These categories are the low-mass region (LMR) where the invariant mass $M < M_\phi = 1.024$ GeV [39], the intermediate-mass region (IMR) where $M_\phi < M < M_{J/\psi} = 3.1$ GeV [39], and the high-mass region (HMR) where $M \geq M_{J/\psi}$. In the LMR, dilepton production is dominated by vector meson decays and the signal can illustrate the medium modification of vector mesons. Continuum radiation from the QGP dominates dilepton production in the IMR; thus they carry signatures of thermal radiation from the QGP. The HMR of dilepton invariant mass is dominated by heavy flavor decays from hadrons like Υ and J/ψ and carries valuable information regarding thermalization,

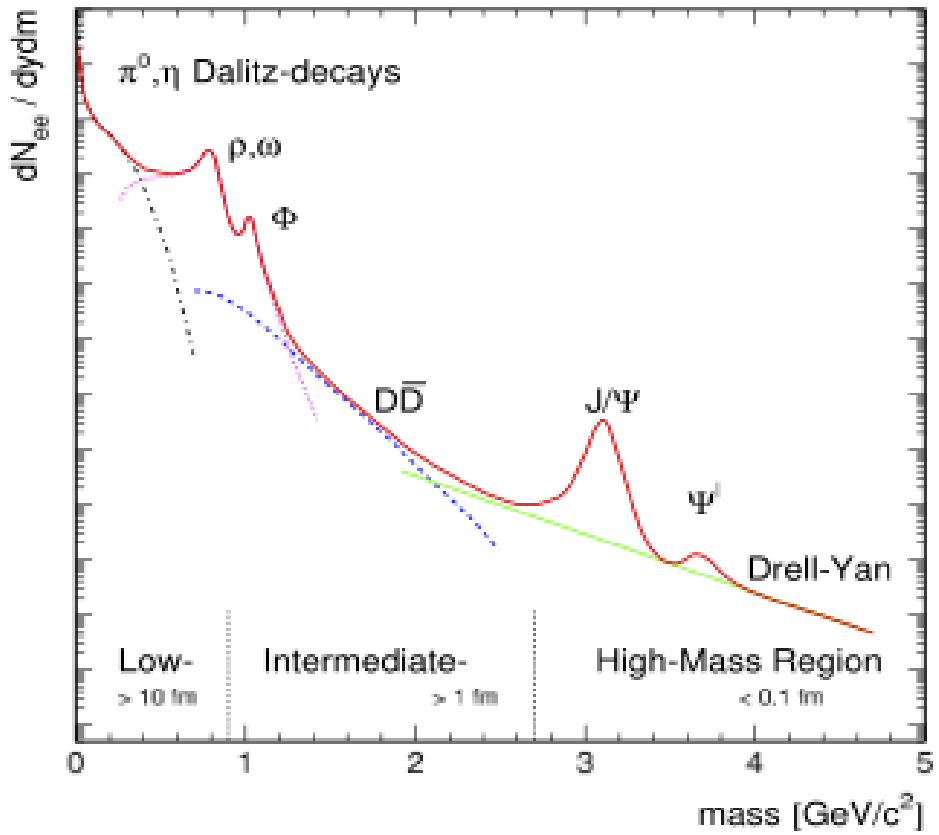

Figure 2.4: Schematic of expected sources of dileptons as a function of invariant mass [63]. The red line is the sum total of all contributions; the black dot-dashed line represents the contribution from Dalitz-decays of scalar mesons; the purple dotted curve is the ρ, ω, and ϕ vector mesons; the blue dashed line describes contributions from $c\bar{c}$; and the green line is the contribution from Drell-Yan processes.

elliptic flow, and energy loss of heavy quarks in the medium [63].

An example of an important confirmation of medium effects on particle decay is found when reviewing the history of the ρ meson and its production in heavy ion collisions. In the low-mass region, dilepton emission is mediated by the broad vector meson $\rho(770)$ since this meson couples strongly to the $\pi\pi$ channel and has a short lifetime. Hypotheses regarding the medium affecting the mass and/or width of mesons led to experiments, such as CERES [70]/NA45 [71] at the CERN SPS, to produce dilepton invariant mass distributions to determine the validity of those hypotheses. Both measurements found evidence that the invariant mass distribution was in excess below the ϕ meson mass and that $\pi\pi$ annihilation

could reproduce the data only if the intermediate ρ meson was modified [70] [71]. With the available statistics and resolution a differentiation between a larger width or change in mass was not possible and further studies by NA60 [72] with In+In definitively rules out models where the mass of the ρ meson was reduced, confirming a broadening of the width.

2.2.4 Azimuthal Anisotropy or Flow

Bulk behavior of the produced particles in a nucleus-nucleus collision can also relay information regarding early stages of evolution and the production of a QGP [73–77]. Particularly, when there is a non-central (not head-on) collision, the partons in the overlap region are subject to spatial anisotropy due to the random population of nucleons in the nucleus and the random orientation and magnitude of the impact parameter. The almond-shape of the overlap region is highlighted by the orange object in Fig. 2.5. The beam line is represented by the z-axis and the two blue-purple spheres are the spectator nucleons from the colliding nuclei. The grid bisecting the three objects denotes the reaction plane and is defined by the impact parameter along the x-axis and the beam line. The particles which are along the short axis of the ellipsoid are subject to a higher pressure gradient (all the arrows in the figure, where sizes denote the magnitude of the pressure gradient) as compared to particles along the long axis. As a result, the initial spatial anisotropy is converted into an anisotropy in momentum space. This momentum anisotropy will reflect the time evolution of pressure gradients generated in the system at early stages in the collision [79] [80].

The anisotropy in the momentum space can be calculated by looking at the azimuthal distribution of produced particles with respect to the reaction plane. The azimuthal distribution of the produced particles can be decomposed into the Fourier series [81],

$$E\frac{d^3N}{d^3\mathbf{p}} = \frac{1}{2\pi}\frac{d^2N}{p_T dp_T dy}\left(1 + 2\sum_{n=1}^{\infty} v_n \cos(n[\phi - \Psi_r])\right) \quad , \tag{2.15}$$

where E is the energy of the particle, $\mathbf{p}$ is the magnitude of the momentum, p_T is the

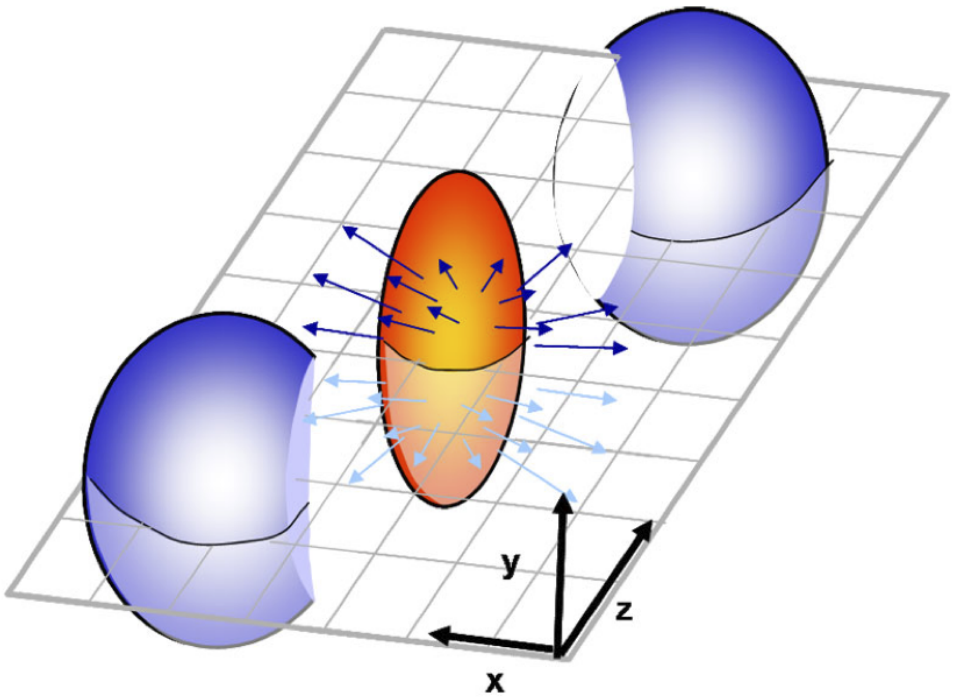

Figure 2.5: Cartoon of the overlap region in $A + A$ collisions from Ref. [78]. The beam line is represented by the z-axis and the two blue-purple spheres are the spectator nucleons from the colliding nuclei. The orange almond-shape defines the region of participating nucleons in the collision, with all the arrows sizes emphasizing the magnitude of the pressure gradients. The grid bisecting the three objects denotes the reaction plane and is defined by the impact parameter along the x-axis and the beam line.

transverse momentum, ϕ is the azimuthal angle, y is the rapidity, and Ψ_r is the reaction plane angle [82]. The sine terms in the expansion vanish due to the reflection symmetry of the collision with respect to the reaction plane. The coefficients can be calculated as average values

$$v_n = \langle \cos(n[\phi - \Psi_r]) \rangle \quad . \tag{2.16}$$

The first three harmonics hold some physical significance in heavy ion collisions; the first two are discussed in the following paragraphs while the third harmonic is discussed in more detail below. Higher-order harmonics (v_6 or v_8 for example) are currently under scrutiny to determine if physics can be deduced from their signals.

The 'zeroth' coefficient in the above Fourier decomposition represents radial flow, a completely isotropic emission of particles representing the uniform expansion of the fireball [53].

Radial flow gives information regarding the kinetic equilibrium of the system before its rapid expansion [83]. The momentum distribution of matter that has reached kinetic equilibrium will be isotropic while unequilibrated matter will have a Lorentz boosted momentum distribution [83]. There is an observed signal in the transverse momentum (p_T) spectra for heavier particles like the proton which can be measured roughly in experiment via the blast-wave model [84, 85] (described in Sec. 2.3.1): it is the shoulder in the low-p_T region of the spectra.

The first coefficient (v_1) represents directed flow. Directed flow describes the collective motion of produced particles from one nucleus being counterbalanced by the equal magnitude but opposite direction of produced particles from the other nucleus [53]. The directed flow signal is significant near beam rapidity, but vanishes near midrapidity at high energies. The loss of signal is due to the symmetry of the collision geometry [83]. Observing a minimum in the directed flow as a function of beam energy can mean a softening of the equation of state (EOS) [86–88]. Such softening may be a sign of QGP formation in the early stages of the collision [89].

Elliptic Flow

The second harmonic (v_2) represents elliptic flow and characterizes the ellipticity of the azimuthal distribution of produced particles. Elliptic flow arises due to the spatial anisotropy of the overlap region in the initial collision and develops early in the collision evolution. Final state interactions should lead to a positive value of v_2 [91] due to differing path lengths in the medium at different azimuthal angles. Elliptic flow is an advantageous signature of QGP formation due to its ease of measurement and high statistical accuracy: elliptic flow affects all final state particles.

Elliptic flow typically has its largest magnitude at midrapidity and falls off toward higher values of $|\eta|$. This pattern is found over a broad range of incident energies (and experiments) except for a study with Pb+Pb at the SPS [92] that demonstrates a flatter distribution.

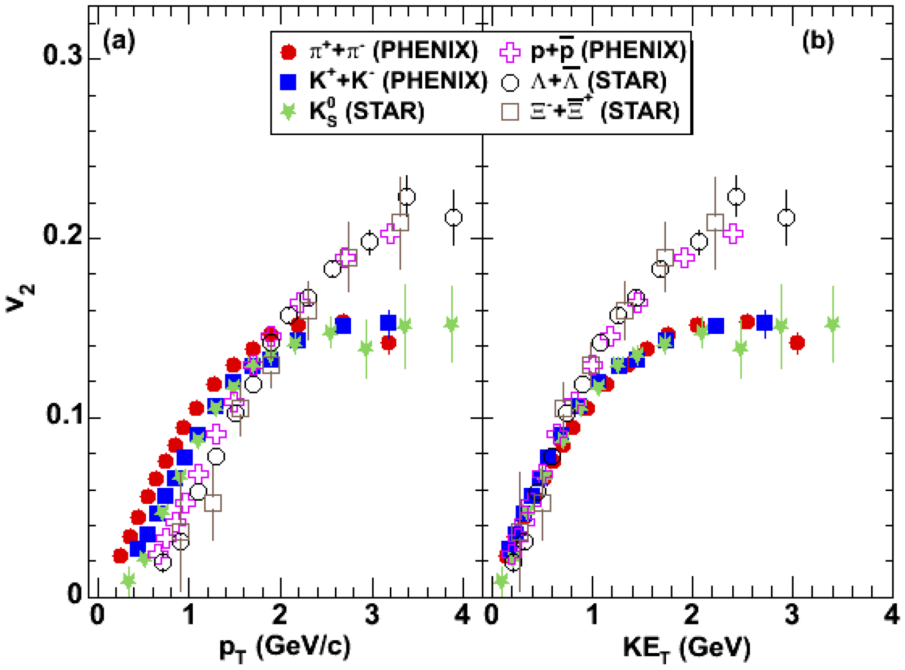

Figure 2.6: Second harmonic, v_2, plotted as a function of transverse momentum, p_T. Note that the baryons follow a different curve to mesons. From Ref. [90]

Results from the STAR experiment show that elliptic flow as a function of p_T follows two distinct curves separated by hadron type and a non-zero elliptic flow for strange hadrons [93, 94]. These findings were confirmed later by the PHENIX collaboration in Ref. [90] and shown in Fig. 2.6. Here, the second harmonic, v_2, is plotted as a function of transverse momentum, p_T , on the left panel and again as a function of transverse kinetic energy, KE_T, on the right panel. Clearly visible in both panels is the separation of mesons from baryons in two curves.

The PHENIX collaboration further found when scaling both axes by the number of constituent quarks (also called n_{cq} scaling) that all hadrons except for pions, fall on a common curve, see Fig. 2.7. Because multi-strange baryons are not as affected by the hadronic stage compared to lighter hadrons, combined with the evidence that elliptic flow develops early in the collision evolution, the large magnitude of v_2 suggests that the s quark flow is similar to

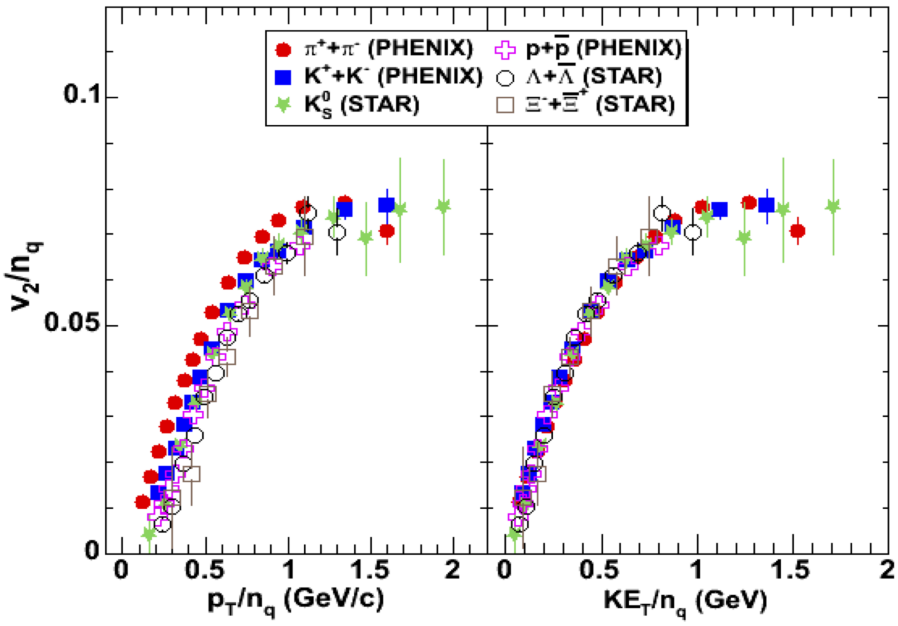

Figure 2.7: Number of quark (n_q) scaled v_2 as a function of scaled p_T on the left panel and scaled KE_T on the right panel. When each particle type is scaled by the number of constituent quarks (baryons by 3 and mesons by 2), all hadrons fall on the same curve. This is indicative of flow originating prior to hadronization. From Ref. [90]

u and d quarks [22, 95, 96]. Recent results from PHENIX on flow of non-photonic electrons (in this case, mainly from D-meson semileptonic decays) extend constituent quark scaling to the charm quark [97]. Quark coalescence (recombination) models show such common scaling with the number of constituent quarks, consistent with models utilizing partonic collectivity.

2.2.5 Jets, High p_T Probes

Hard-scattering processes produce highly-energetic particles. The manner in which these hard particles interact with the medium is a unique, direct probe of the environment without disturbing the medium itself. Dihadron azimuthal correlations at high p_T are a way to reconstruct jet interactions in the nuclear medium. For collisions like $p + p$, when reconstructing jets, the range or cone of the jet is narrow and fragments analagous to a charged particle through matter: via radiation or excitation of the medium. In QCD, gluon radiation

and quark pair production are the mechanisms by which a hard probe would lose energy. Once these hard-scatter particles are placed in the collision environment directly following a nucleus-nucleus interaction, one jet of the pair may have farther to traverse, or a longer interaction time with, before exiting the medium. Then, the away-side jet would lose energy as it traversed the hot and dense medium, possibly losing all of its energy along the way; this is called 'jet quenching'. Understanding the phenomenon of jet quenching helps to probe the color structure of QCD matter.

In Figure 2.8 correlations between high p_T hadrons for $p+p$, central d+Au and central Au+Au collisions (background subtracted) from STAR are shown [98]. The azimuthal distribution of hadrons have $p_T > 2$ GeV/c, with the angle measured relative to a trigger hadron with $p_{T\ \mathrm{trig}} > 4$ GeV/c. A hadron pair from the same jet will have an enhanced correlation strength at $\Delta\phi \approx 0$, seen in $p+p$, d+Au and Au+Au in the figure, with similar correlation strengths, widths and (not shown) charge-sign ordering (the correlation is stronger for oppositely charged hadron pairs [3]). A hadron pair from back-to-back dijets will have an enhanced correlation strength at $\Delta\phi \approx \pi$, as observed for $p+p$ and for d+Au with a slightly broader width than the near-side correlation peak. However, the back-to-back dihadron correlation is missing in central Au+Au collisions, while for peripheral Au+Au collisions the correlation appears quite similar to that seen in $p+p$ and d+Au. The results compared with $p+p$ and peripheral Au+Au collisions illustrate that the momentum-balancing hadrons azimuthally opposite a high-p_T trigger particle in central Au+Au collision are significantly softer, greater in number, and widely dispersed in azimuthal angle [98].

If the correlation can be attributed to jet fragmentation then the away-side peak suppression in Au+Au collisions is due to final-state interactions of hard-scattered partons in the dense medium [2]. We measure preferentially the hard hadrons from the partons which scatter outward toward the surface of the collision zone for a short duration in the dense medium. However, the dominant contribution of jet fragmentation must still be confirmed in the region with trigger particles higher than $p_{T\ \mathrm{trig}} > 6$ GeV/c where the meson and

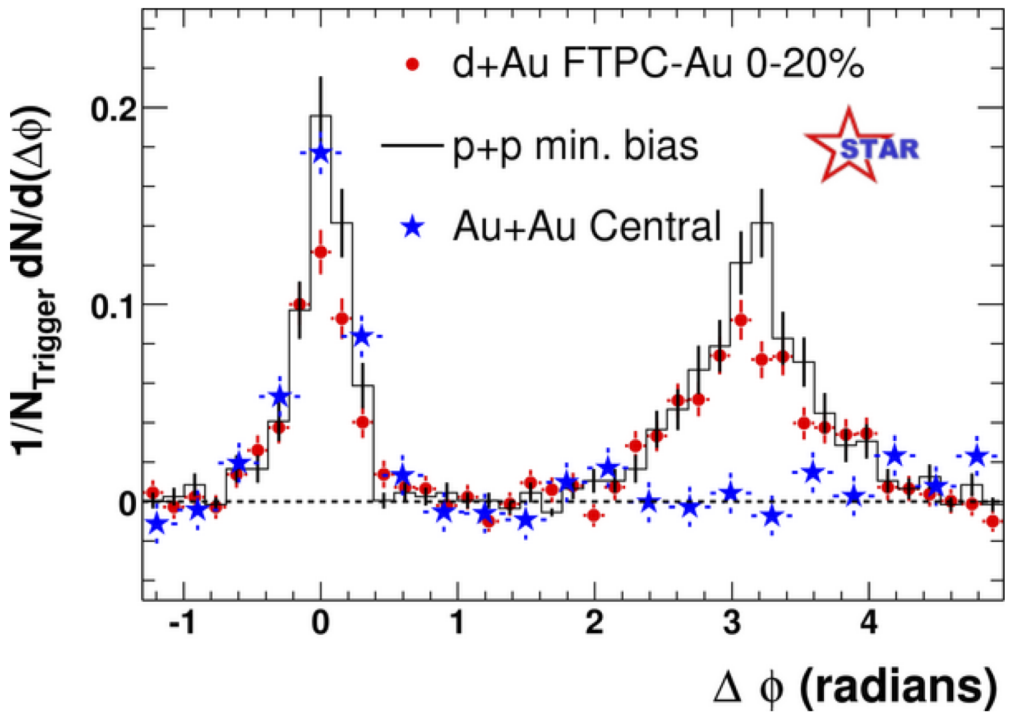

Figure 2.8: Dihadron azimuthal correlations at high p_T showing correlations for p+p, central d+Au and central Au+Au collisions (background subtracted). Indicative that higher-momentum fragments interact strongly with the medium as a final state effect. From Ref. [3, 98]

.

baryon yields are similar to those of jets fragmenting in vacuum in order to more accurately compare to $p+p$ and d+Au results. Studies of the azimuthal correlation with harder trigger particles show similar results to Fig. 2.8 [99] [100] and suggest that the peak structures are indeed due to jet quenching [98].

2.3 Particle Spectra

In order to have a different phase of matter, a phase transition is required where the new phase might consist of free quarks and gluons. Experiments currently are determining the nature of the phase transition, attempting to answer the question of a defined order transition or a cross-over transition. Analyzing particle spectra can help build a stronger case for a phase transition and describe some of its characteristics, though are not sufficient alone. Two types of spectra can be analyzed: transverse momentum or mass, p_T or m_T, and rapidity,

y, spectra. The rapidity spectra are distributions of particles in the longitudinal (beam) direction. Transverse momentum or mass spectra are distributions of particles perpendicular to the beam direction. Both types allow for a study of hadronic matter properties such as the energy density, ϵ, pressure, P, and entropy density, s, as a function of baryon chemical potential, μ_B, and temperature, T. Both are highly related to underlying collision dynamics though only transverse spectra will be explored in this thesis.

Hydrodynamics provides the model framework in which to analyze the particle spectra below $p_T < 2$ GeV. This model describes collective flow, expansion and other bulk matter phenomena of a collision. The basic equations of the model begin with conservation of energy-momentum ($\partial_\mu T^{\mu\nu} = 0$) and conservation of current ($\partial_\mu N_i^\mu = 0$). The energy-momentum tensor, $T^{\mu\nu}$, contains terms to include the energy density, hydrostatic and bulk pressure, energy/heat transfer, and the shear stress tensor. The set of conserved currents individually include a charge density and charge current for quantities like the net baryon current. In each of the conserved quantities, there are ideal terms and dissipative terms that define ideal hydrodynamics (excluding dissipative terms) and viscous hydrodynamics (including some number of dissipative terms) respectively.

In ideal hydrodynamics the energy density estimated via the Björken formula [101], assuming no work through $P\mathrm{d}V$, is

$$\epsilon_{Bj}(\tau) = \frac{\langle m_T \rangle}{\tau \pi R^2} \frac{dN}{dy} \qquad , \tag{2.17}$$

where τ is the proper time, $\langle m_T \rangle$ is the average transverse mass obtained via spectra analysis, R is the effective transverse radius and dN/dy is the number of particles per unit rapidity. One can also test the hypothesis of the matter in a collision coming to some chemical equilibrium by comparing the average number of particles of a given species, $\langle N_i \rangle$, to another in

order to cancel out the volume dependency of the $\langle N_i \rangle$ equation,

$$\langle N_i \rangle = V \left[n_i^{\text{th}}(T, \mu) + \sum_R \Gamma_{R \to i} n_R(T, \mu) \right] \quad , \tag{2.18}$$

where V is the volume, n_i^{th} is the number density of directly emitted particle i, n_R is the number density of resonance R, and $\Gamma_{R \to i}$ is the branching ratio of resonance R to particle species i. Since the average number of particles of a given species can be determined via particle spectra, and branching ratios from Ref. [39], the particle ratios depend on the remaining variables T and μ. The last check of ideal hydrodynamics is whether the matter reaches kinetic equilibrium. Kinetically equilibrated matter has an isotropic momentum distribution due to a pressure gradient leading to radial expansion. With a finite velocity, though, the distribution becomes Lorentz boosted and such distortions carry information regarding kinetic equilibrium of the system. The Blastwave Model [84, 85], discussed below, utilizes this framework to obtain a kinetic freeze-out temperature and radial flow velocity from particle spectra.

2.3.1 Blastwave Model

Expansion with some velocity, β_T, correlates with a linear increase in the apparent 'temperature' (slope parameter) with increasing particle mass. A "blast wave" model includes an expansion velocity that is assumed to increase with the radius, r,

$$\beta_T = \frac{\beta_s r}{R_G} \quad , \tag{2.19}$$

where β_s is the flow velocity at the surface and R_G is the outer radius of the expanding fireball [53]. More succinctly, a blastwave model describes identified particle transverse spectra with contributions from thermal emission and radial flow [53]. Below are descriptions of a few common blastwave models.

Siemens and Rasmussen developed a blastwave model [85] to describe particle production in Ne+NaF reactions. This model is characterized by a fast hydrodynamic expansion leading to quick hadronic decoupling and a 'finalized' momentum distribution where the only further effects on particle momenta come from collective expansion. Of utmost importance in this model is the spherically symmetric expansion of the shells (blast waves) with a constant radial velocity. The language used to describe the physical picture coined the term blast wave and brought such a model to heavy ion collisions [102]. The model, despite its motivation in hydrodynamics, developed from two freeze-out conditions — $t = t_0 + \beta_T r$ and $dt = \beta_T dr$ — and the Cooper-Frye formula,

$$E\frac{d^3N}{d^3p} = \frac{d^3N}{dyd^2p_T} = \int d^3\Sigma_\mu(x)p^\mu f(x,p) \qquad , \tag{2.20}$$

where E is the energy, $\Sigma_\mu(x)$ is the freeze-out hypersurface, p^μ is the four-momentum, and $f(x,p)$ is the phase-space distribution function. The model assumes the thermodynamic variables (T and μ) and the transverse velocity (β_T) to be constant. Hence the momentum distribution takes the form [85, 102]

$$\frac{dN}{d^3p} = \frac{e^{-\gamma E/T}}{2\pi^2}\left[\left(1+\frac{T}{\gamma E}\right)\frac{\sinh a}{a} - \frac{T}{\gamma E}\cosh a\right]\int_0^1 r^2(\zeta)\frac{dr}{d\zeta}d\zeta \tag{2.21}$$

where E is the hadron energy; T is the temperature of all shells of the fireball; γ is the Lorentz gamma factor with the velocity representing the collective radial flow; a is a dimensionless parameter defined as a function of transverse velocity, momentum, and temperature, $a = \gamma\beta_T p/T$; and r is the radius parameterized in ζ, which corresponds to the freeze-out times when the hadrons in the given blast shell (at radius r) cease interacting. The parameter ζ may always be restricted to the interval $0 \leq \zeta \leq 1$. Because this model assumes the aforementioned freeze-out conditions, shells which are further out from the center of the fireball will freeze-out later in time. Additionally, the hypersurface vector is parallel to the flow vector, another result of the freeze-out conditions.

The assumptions of Siemens and Rasmussen make the model appropriate for low-energy scattering processes where the expansion of the matter from colliding nuclei is largely isotropic. For higher energies, however, the expansion is known to be anisotropic [101], namely cylidrically symmetric. The blastwave model of Schnedermann, Sollfrank, and Heinz [84] modifies the Cooper-Frye formula to include a cylindrically symmetric hypersurface and boost-invariance in the freeze-out description as well as in the hydrodynamic and kinetic equations.

In the parameterization, $\zeta \rightarrow (t(\zeta), r(\zeta))$, ζ represents times when the cylindrical shells freeze-out and can be fully determined given one coordinate since for finite values, other freeze-out points can be obtained via Lorentz transformation. Assuming again a constant radial velocity and the freeze-out condition $dt/d\zeta = 0$, the Cooper-Frye formula simplifies to

$$\frac{dN}{dyd^2p_T} = (\text{const.})m_T K_1\left[\frac{m_T}{T}\cosh(\alpha_T)\right] I_0\left[\frac{p_T}{T}\sinh(\alpha_T)\right] \tag{2.22}$$

where m_T is the transverse mass, p_T is the transverse momentum, K_1 and I_0 are Bessel functions, T is the temperature, and α_T is the space-time transverse coordinate. This form of blastwave model has been used to describe various analyses of transverse spectra from SPS and RHIC energies [103]. Further modification to the boost-invariant blastwave model includes resonance decays which, at high energies, contribute heavily to light particle production. Inclusion of resonances is extremely important to calculating particle abundances and is essential to the success of any thermal model. Boost-invariance also implies that the values of thermodynamic variables on one freeze-out shell is the same for any other freeze-out shell, meaning the values are the same at any rapidity.

It is important to note that rapidity distributions at RHIC energies have a Gaussian shape with a dependence of thermodynamic variables on rapidity, both indicative that the system at these high energies is not boost invariant. There exists, however, a plateau region, $|y| < 1$, that does approximate boost-invariance and blastwave calculations performed over this region can be applied, to first-order, to any other value of rapidity in that region.

The final two blastwave models to be briefly discussed are the single-freeze-out model [104, 105] and the non-boost-invariant single-freeze-out model [102]. The single-freeze-out model applies the assumption of a constant proper time in Minkowski space, with the transverse size of the system defined by a maximum parameter, and finally a Hubble-like velocity field at freeze-out. These assumptions lead to a velocity-dependent volume element in the Cooper-Frye formula and also easily lead to the inclusion of resonance states. The non-boost-invariant single-freeze-out model modifies the system boundaries to include a dependence of the transverse size on the longitudinal coordinate. This last model compares well with pion and kaon spectra from BRAHMS but needs to incorporate the rapidity dependence of the baryon chemical potential to accurately model the protons [102].

2.4 Particle Ratios and the Coulomb Source

By looking at relative particle abundances of particular particles quite a bit of information regarding the environment of the expanding fireball can be determined. These aspects of the collision are important for understanding, for example, what production mechanisms dominate in that energy range, or when the available energy for particle production is high enough to erase initial-condition importance.

An antibaryon-to-baryon ratio as a function of center-of-mass energy, such as one found in Ref. [106], is indicative of the baryon chemical potential, μ_B, of the nuclear collision. The μ_B of the collision represents the amount of energy necessary to pair produce a baryon from the surrounding environment. As the available energy increases it becomes easier to pair produce, rather than transform one type of baryon to another. Higher energies allowing for pair production approach a baryon-free central region, as is expected [53].

Pion production in heavy ion collisions of nuclei where the number of neutrons is approximately equal to the number of protons ($N = Z$, up to about ^{40}Ca) is in equal proportions for π^+, π^-, and π^0 due to the isospin symmetry of the initial state. This property changes when

the number of neutrons begins to overwhelm the number of protons. Once $N > Z$ there is an excess of π^- due to the increased number of neutrons at the low energies of AGS and SPS experiments. However, once the available energy in a collision becomes high enough, as at RHIC energies, the disparity between charges begins to disappear. Taking a ratio of charged pions will place a particular collision energy in an isospin-dominated production regime or in an energy-dense environment rich with pair production.

Similarly, as energy of the collisions increases, heavier particles like kaons become easier to produce and are found more abundantly. Kaon production, namely K and $\bar{K}$, comes from two mechanisms similar to those for pions: associated production and pair production. Associated production ($N + N \rightarrow Y + K$) leads to a higher number of K^+ mesons along with hyperons like Λ, Σ, Ξ, and Ω. Pair production ($N + N \rightarrow N + N + K + \bar{K}$) is more costly energy-wise but produces K^+ and K^- in equal proportions. The production of kaons becomes more important as the collision energy increases due to fermi statistics, and the differences between the charged particle abundances decreases as the available energy for particle production increases.

Antiparticle-particle ratios in the context of a statistical-thermal model suggests chemical equilibrium in the final state [53]. A statistical-thermal model consists of two parameters, temperature T and baryon chemical potential μ_B, and usually involves a ratio similar to

$$\frac{\bar{p}}{p} = \frac{e^{-(E+\mu_B)/T}}{e^{-(E-\mu_B)/T}} = e^{-2\mu_B/T} \tag{2.23}$$

where the temperature T can be obtained from particle spectra, for example. A prediction of the temperature of the environment and the baryon chemical potential of the collision system can thus be made.

Particle ratios produced by the NA49 Collaboration as a function of center of mass energy show evidence for the onset of deconfinement [9, 107–109] resulting in the structures of the "Kink", the "Horn", the "Step", and the "Dale". Each of these structures are illustrated

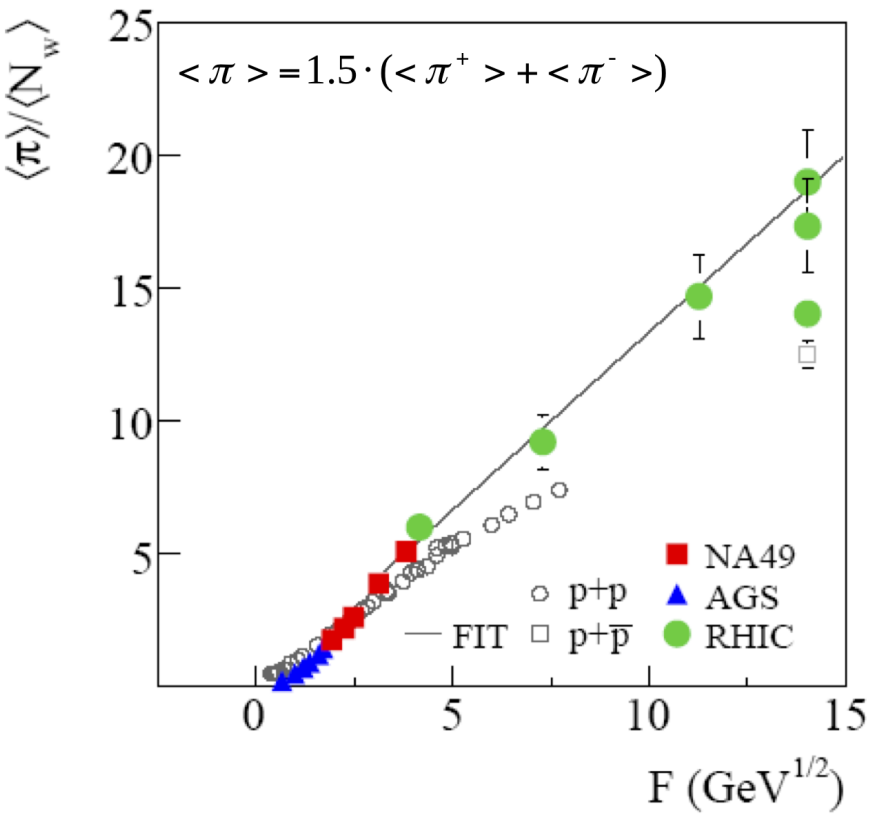

Figure 2.9: The Kink, taken from Ref. [9]. Energy dependence, $\sim (s_{NN})^{\frac{1}{4}}$, of the mean pion multiplicity per wounded nucleon measured in central Pb+Pb and Au+Au collisions (full symbols), compared with the corresponding results from $p + p(\bar{p})$ reactions (open symbols).

below. These structures are predicted in the statistical model for the early stage (SMES) of nucleus-nucleus collisions based on work by Fermi [110]. This model assumes the collision is either in a thermalized hadron gas—the confined phase—or in a thermalized QGP state—the deconfined phase. The model assumes a first-order phase transition between the two phases, constant entropy and strangeness during expansion, and uses Fermi-Landau initial conditions.

The Kink, in Fig. 2.9, is seen in the particle ratio of the average yield of pions to the average number of wounded nucleons in the collision plotted against Fermi's measure,

$$F = \left[\frac{(\sqrt{s_{NN}} - 2m_N)^3}{\sqrt{s_{NN}}} \right]^{\frac{1}{4}} \quad , \tag{2.24}$$

where $\sqrt{s_{NN}}$ is the center of mass energy per nucleon-nucleon pair, and m_N is the nucleon

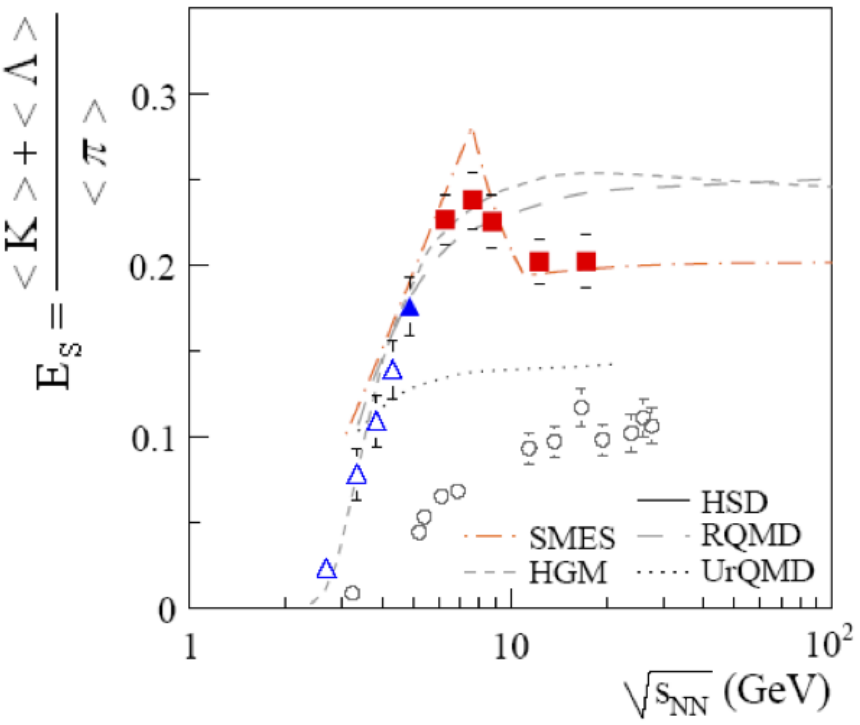

Figure 2.10: The Horn, taken from Ref. [9]. Energy dependence of the $(\langle K \rangle + \langle \Lambda \rangle)/\langle \pi \rangle$ ratio, an approximation of strangeness production, measured in central Pb+Pb and Au+Au collisions (full symbols) compared with the corresponding results from $p + p(\bar{p})$ reactions (open circles).

rest mass. It represents the sudden change in the number of pions per participating nucleon (wounded nucleon). Nucleus-nucleus collisions are plotted in solid symbols while $p + p$ data are plotted in open symbols. The fit to the data is parameterized by [9],

$$\frac{\langle \pi \rangle}{\langle N_w \rangle} = a + bF + cF^2 \qquad , \tag{2.25}$$

and the results of the fit indicate an increase in the slope parameter by 1.3 for collision systems with $F > 3.5$ GeV$^{\frac{1}{2}}$ from $F < 1.85$ GeV$^{\frac{1}{2}}$ [9]. Hence, there is a 'kink' in the slope parameter indicative of the onset of deconfinement [107, 111].

The Horn is a sharp and narrow peak in strangeness production, $E_s = (\langle K \rangle + \langle \Lambda \rangle)/\langle \pi \rangle$, or in particular the approximate strangeness ratio of $\langle K^+ \rangle / \langle \pi^+ \rangle$. In Figure 2.10 the steep increase followed by a turnover in the data is evident and is followed by a plateau at higher energies. The plateau is consistent with the onset of deconfinement from the SMES model

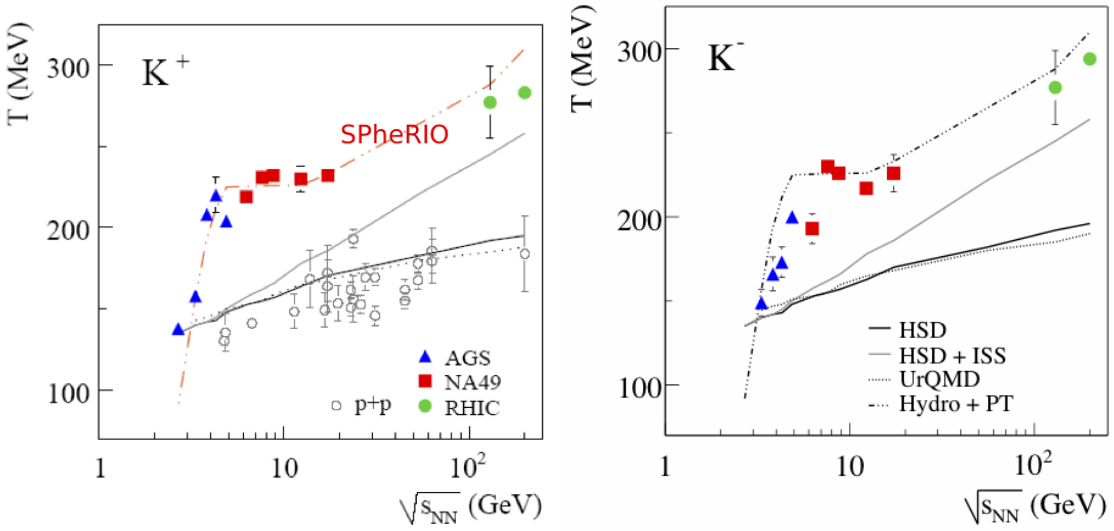

Figure 2.11: The Step, taken from Ref. [9]. Energy dependence of the inverse slope parameter T of the transverse mass spectra of K^+ (left) and K^- mesons (right) measured at mid-rapidity in central Pb+Pb and Au+Au collisions. The K^+ slope parameters are compared with those from $p+p(\bar{p})$ reactions in the left-hand plot (open circles). The curves represent predictions from various models described in the text.

[107, 111].

The Step, in Figure 2.11, is a plateau in the energy dependence of the inverse slope parameter, T, of the transverse mass, m_T, spectra for charged kaons. It arises from the assumption of a first-order phase transition in the model. In the mixed phase, the temperature and pressure are constant so the plateau is suggested to be caused by a softening of the equation of state. In the figure, energy versus the slope parameter of K^+ mesons is on the left and while for K^- mesons is on the right. The figure clearly shows a steep rise of T measured at the AGS to a plateau at SPS energies followed by the indication of a rise in T with the RHIC data. Although the scatter of data points is large, T appears to increase smoothly in $p + p(\bar{p})$ interactions.

A softening of the equation of state would also lead to a weakening of the collective expansion in the longitudinal direction. The Dale structure arises from the energy dependence of the calculated velocity of sound in the medium and is representative of the longitudinal expansion. In Figure 2.12 the Dale is illustrated in two ways. In the left-hand panel, the speed of sound is shown as a function of center-of-mass energy where blue triangles are data

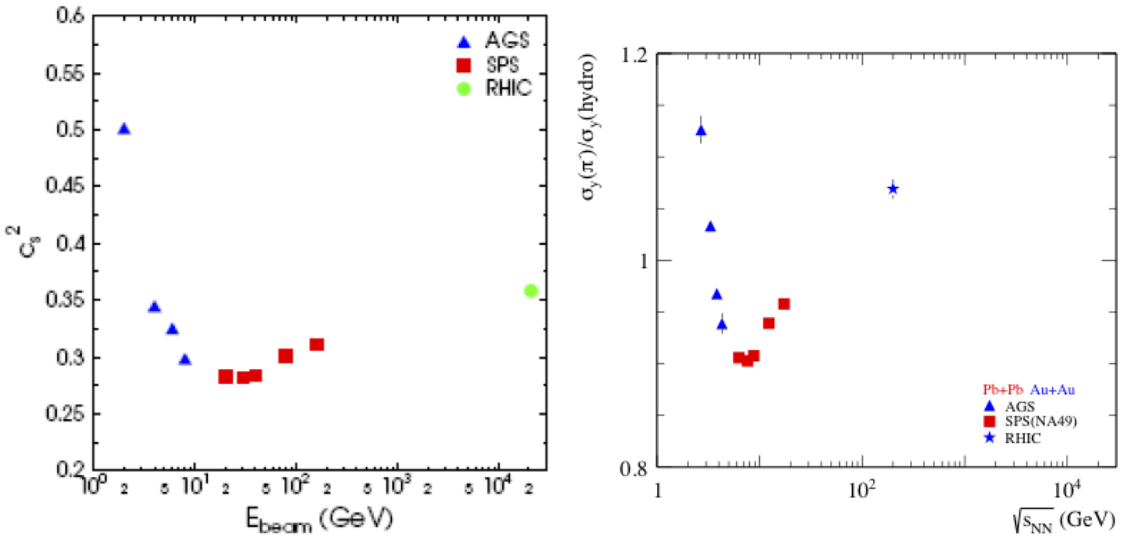

Figure 2.12: The Dale; left taken from Ref. [9], right taken from Ref. [112]. Left panel: Energy dependence of the speed of sound in the medium. Right Panel: Energy dependence of the ratio of the measured pion rapidity width to the value calculated according to Landau hydrodynamics, Eqn. 2.26.

from AGS experiments, red squares from SPS experiments and the green dot from a RHIC experiment. The right-hand panel illustrates the comparison of the measured pion rapidity width to the calculated width of the pion rapidity distribution according to the Landau hydrodynamical model [113, 114] equation,

$$\sigma_y^2(\text{hydro}) = \frac{8}{3}\frac{c_s^2}{1-c_s^4}\ln\left(\frac{\sqrt{s_{NN}}}{2m_N}\right) \tag{2.26}$$

where σ_y^2(hydro) is the pion rapidity distribution width, c_s is the speed of sound in the medium, $\sqrt{s_{NN}}$ is the center of mass energy per nucleon-nucleon pair, and m_N is the nucleon mass. The plot utilizes the value of $c_s = 1/3$ [112] to make the pion rapidity distribution width prediction. Both plots indicate a softening of the equation of state by the existence of a clear minimum as a function of the center-of-mass energy coupled with the step structure, as is predicted for the onset of deconfinement [112].

Three of these structures need some experimental observable associated with the pion or kaon spectra. Pions are extremely important for gathering information regarding the onset

of deconfinement, expansion temperature and the nature of the collision environment. One important aspect of a nucleus-nucleus collision environment at low-energies can be gained by studying the pion spectra, detailed below in Sec. 2.4.1.

2.4.1 The Coulomb-Source Effect

The Coulomb-source effect in ultrarelativistic heavy-ion collisions relies on the Coulomb force from the net-positive charge density of the expanding fireball on the formed pions emitted at the thermally-equilibrated freeze-out volume. The effect of the Coulomb interaction is greatest on the least massive particles, i.e. pions. Any positively-charged pion emitted will be slightly accelerated away from the positive source while any negatively charged pion will be marginally decelerated, leading to modifications in the momentum distribution of the final particle spectra. A ratio made from positive versus negative pions enhances these differences in the low-momentum region of the particle spectra and allows for a calculation of the Coulomb source potential, V_C, as well as the initial pion ratio, R_i [115]. This ratio studies the interaction region of nucleus-nucleus collisions by effectively determining the charge density of the source at freeze-out.

An enhancement in the ratio has been seen by experiments at the Bevelac [116–119] as well as the AGS [120, 121]. These results suggest the enhancement is due to the positive charge of the source. Theoretical contributions to these studies suggest that the source is a static Coulomb source. However a static source is not valid for heavy ion collisions since dominant charge-carrying protons are emitted alongside pions and expand in the fireball. Further investigations [122–124] show that the Coulomb potential in nucleus-nucleus collisions depends on the source radius and the charge of the system. These studies clearly indicate that with increasing center-of-mass energy (and hence more energy available for pion production) that the charged pion ratio approaches unity. In other words, as the pion ratio increases with center-of-mass energy, the Coulomb potential falls. Since the charge of the system is determined by the collision centrality and the potential decreases, it is the

source radius that increases, indicating an expanding freeze-out surface.

The modification of the pion spectra by the Coulomb potential occurs after freeze-out, on the 'initial' pion spectra, resulting in the measured, 'final', spectra. The final energy, E_f, of the pion becomes

$$E_f = E_i \pm V_C \tag{2.27}$$

where E_i is the initial energy, V_C is the Coulomb potential, and the addition or subtraction depends on the charge of the pion. Consequently, the final pion ratio, R_f, becomes energy dependent,

$$R_f(E_f) = \frac{E_f - V_C}{E_f + V_C} \frac{\sqrt{(E_f - V_C)^2 - m^2}}{\sqrt{(E_f + V_C)^2 - m^2}} \frac{n^+(E_f - V_C)}{n^-(E_f + V_C)} \tag{2.28}$$

where the first two terms are the charge appropriate Jacobian for a static spherical source, $J = (E_f \pm V_C)\sqrt{(E_f \pm V_C)^2 - m^2}$ [115], and $n^{\pm}(E)$ is the pion emission function of the initial pion spectrum, typically best following a Bose-Einstein distribution:

$$n^{\pm}(E_f \mp V_C) = A^{\pm}(e^{(E_f \pm V_C)/T_\pi} - 1) \tag{2.29}$$

where T_π is the slope parameter for the initial pion distribution. Note that the initial pion ratio, R_i, is defined to be $R_i = A^+/A^-$. Recall that the Coulomb source is also expanding with the pions and the source potential is further modified to incorporate the reduced magnitude of the potential. The effective potential can be calculated as a function of pion momentum by integrating the proton emission function up to the maximum kinetic energy corresponding to the selected pion velocity,

$$E_{\max} = \sqrt{(m_p p_\pi / m_\pi)^2 + m_p^2} - m_p \tag{2.30}$$

to obtain,

$$V_{\text{eff}} = V_C(1 - e^{-E_{\max}/T_p}) \tag{2.31}$$

where T_p is the slope parameter for the Maxwell-Boltzmann-like proton distribution. In this analysis, the effective Coulomb potential, V_{eff}, and total yield pion ratio, R_f, are the free parameters while the rapidity window, pion slope parameter and proton slope parameter are held fixed. Further details can be found in Chapter 4.

Chapter 3

The STAR Experiment

3.1 Introduction to the STAR Experiment

STAR is an acronym for the Solenoidal Tracker At RHIC (Relativistic Heavy Ion Collider). The detector consists of several subsystems designed to track and measure the momentum, energy, velocity, and position of thousands of particles at the top RHIC energy of 200 GeV per nucleon pair for Au+Au collisions [125–142]. At the time of construction, STAR had the largest time-projection chamber in the world [140].

Though always improving, STAR has subsystems like an electromagnetic calorimeter and shower maximum detector surrounding the barrel and one end of the cylindrical time-projection chamber, a resistance plate time-of-flight system, muon telescope detectors, beam-beam counters, a vertex position detector, time-projection chambers for the forward region and a powerful iron magnet surrounding the three-story facility, see Fig. 3.1. The TPC acts like a digital camera capturing an image of a collision a few nanoseconds following a collision. The following chapter will discuss in detail some of these subsystems from theory and design to application.

3.2 The Time Projection Chamber

This subsystem identifies emitted charged particles based on ionization energy loss and measures the full track position to obtain a momentum for each of these particles. STAR's

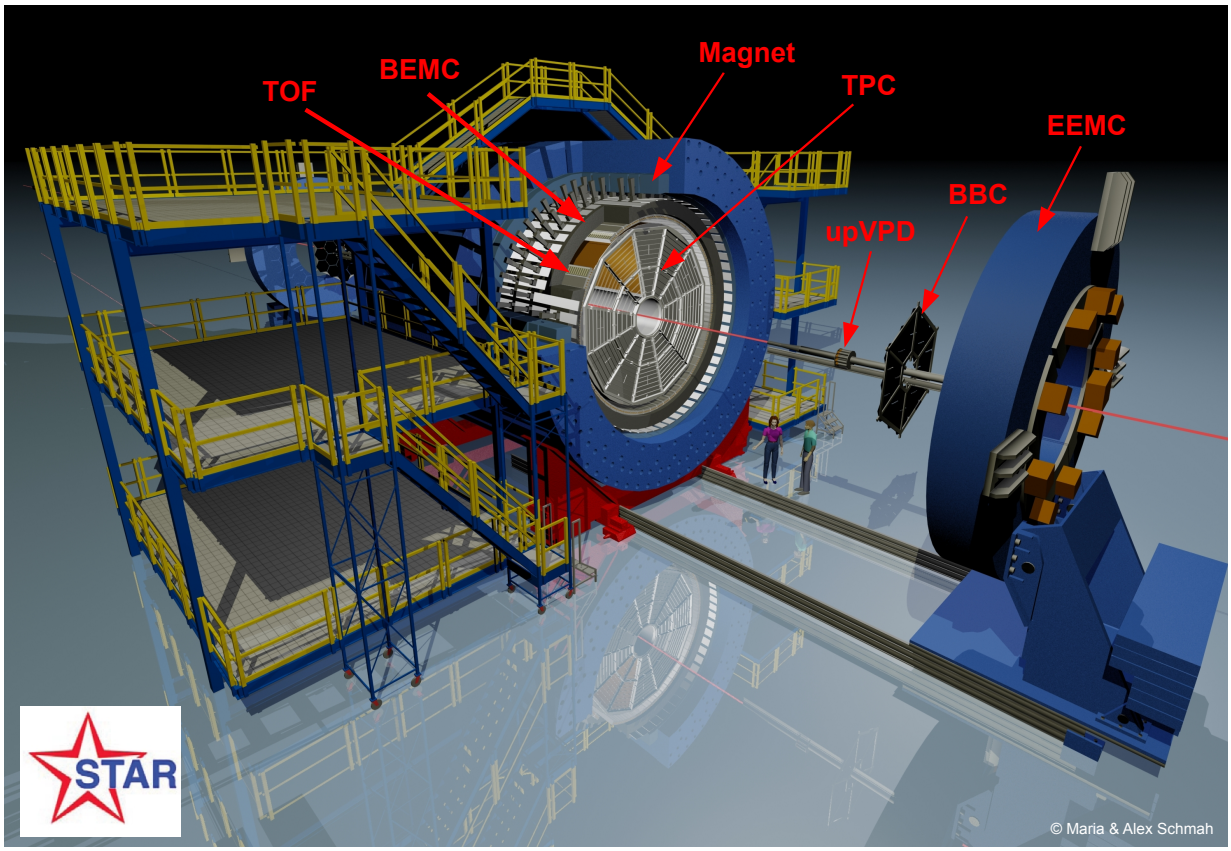

Figure 3.1: An illustration of the full STAR experiment. The two people at the bottom right near the bare electronics platforms are for scale. Most of the detector subsystems are included for the 2011 configuration of the experiment, including the: Time Projection Chamber (TPC), Barrel Electromagnetic Calorimeter (BEMC), End-cap Electromagnetic Calorimeter (EEMC), Time of Flight and Vertex Position Detector (TOF and upVPD), Beam-Beam Counter (BBC), and Magnet [143].

Time Projection Chamber, or TPC, is a cylindrical cavity filled with P-10 gas (90% Argon and 10% Methane) and has a well-known drift velocity of 5.1 cm/μs. Either end of the cylinder has high-voltage anodes in multi-wire proportional counters for read-out. At the center of the chamber is a 70 μm thin membrane cathode made of carbon loaded Kapton film. A schematic is shown in Fig. 3.2 below.

The TPC has a pseudorapidity coverage from $|\eta| < 1.8$ with full 2π azimuthal coverage in the center-of-mass frame. It measures 2.0 m in radius and 4.2 m in length. The central membrane (CM, labeled "high voltage membrane" in the figure) cathode, held at -28 kV, separates the two main sections of gas volume, and straddles the center of one concentric field

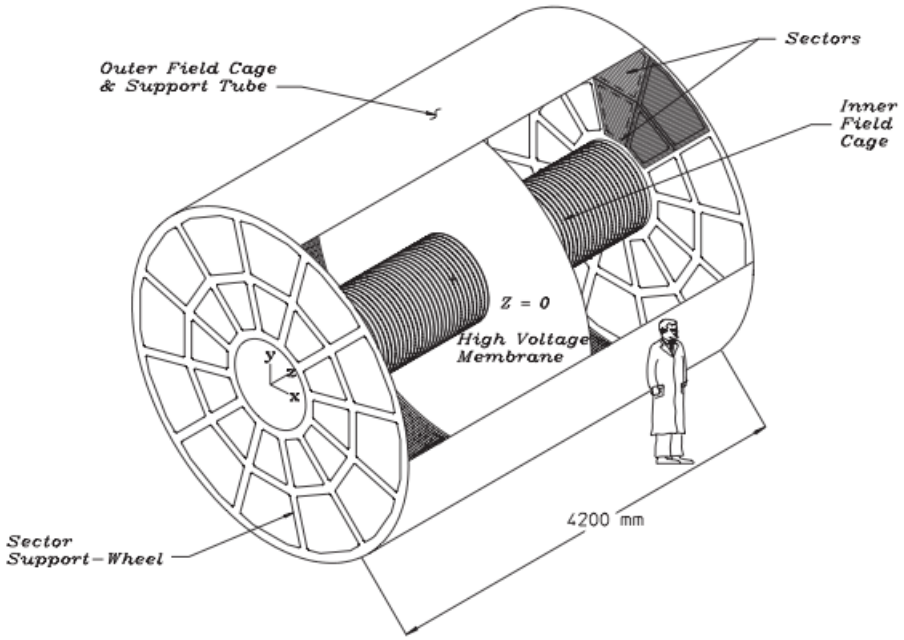

Figure 3.2: The time-projection chamber. A schematic picture of the TPC at STAR from Ref. [140].

cage cylinder. The field cage ensures the uniformity of the electric field, a critical component to ensure a constant drift velocity, from the CM to the grounded plane of wires at the end caps. At both ends are Multi-Wire Proportional Counters (MWPCs) which consist of anode wires, each 1390 kV for outer sectors and 1170 kV for inner sectors, a plane of grounded wires and a gating grid of wires.

STAR's MWPC (see Fig. 3.3) is like a typical MWPC: anode wires are protected by the gated grid of wires and are oriented to obtain the maximum resolution for higher-momentum tracks. Drifting electrons avalanche quickly near the anode wires with a uniform avalanche distance to induce an image charge on cathode pads. The pad plane is designed so that the maximum induced charge from the anode wires covers up to three pads. This allows for a three-point Gaussian fit or weighted mean and good determination of the centroid, thus a better resolution of the primary ionization position. Distances between the anode plane and pad plane are optimized to match the diffusion width of the drifting electrons in order to

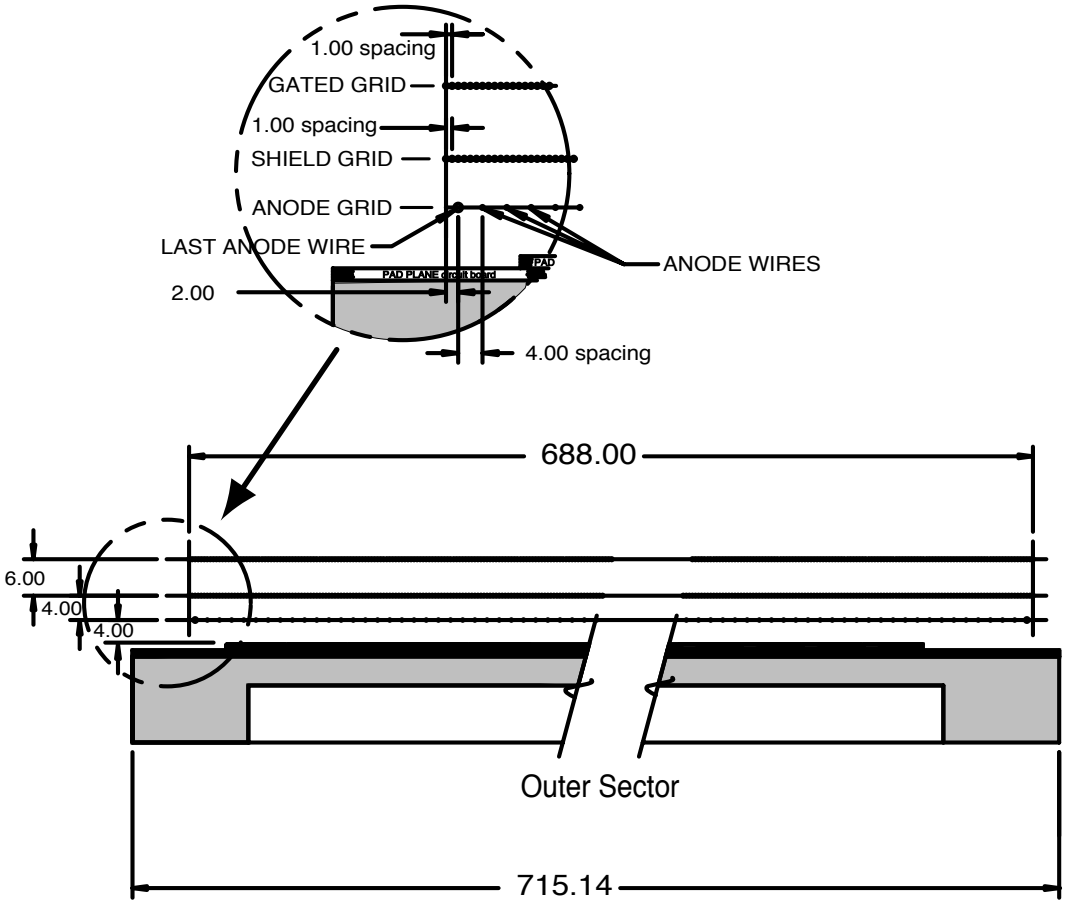

Figure 3.3: The time-projection chamber MWPC from Ref. [140]. A cutaway view of an outer sub-sector pad plane. The cut is taken along a radial line from the center of the TPC to the outer field cage so the center of the detector is towards the right hand side of the figure. The figures shows the spacing of the anode wires relative to the pad plane, the ground shield grid, and the gated grid. The bubble diagram shows additional detail about the wire spacing. The inner sub-sector pad plane has the same layout except the spacing around the anode plane is 2 mm instead of the 4 mm shown here. All dimensions are in millimeters.

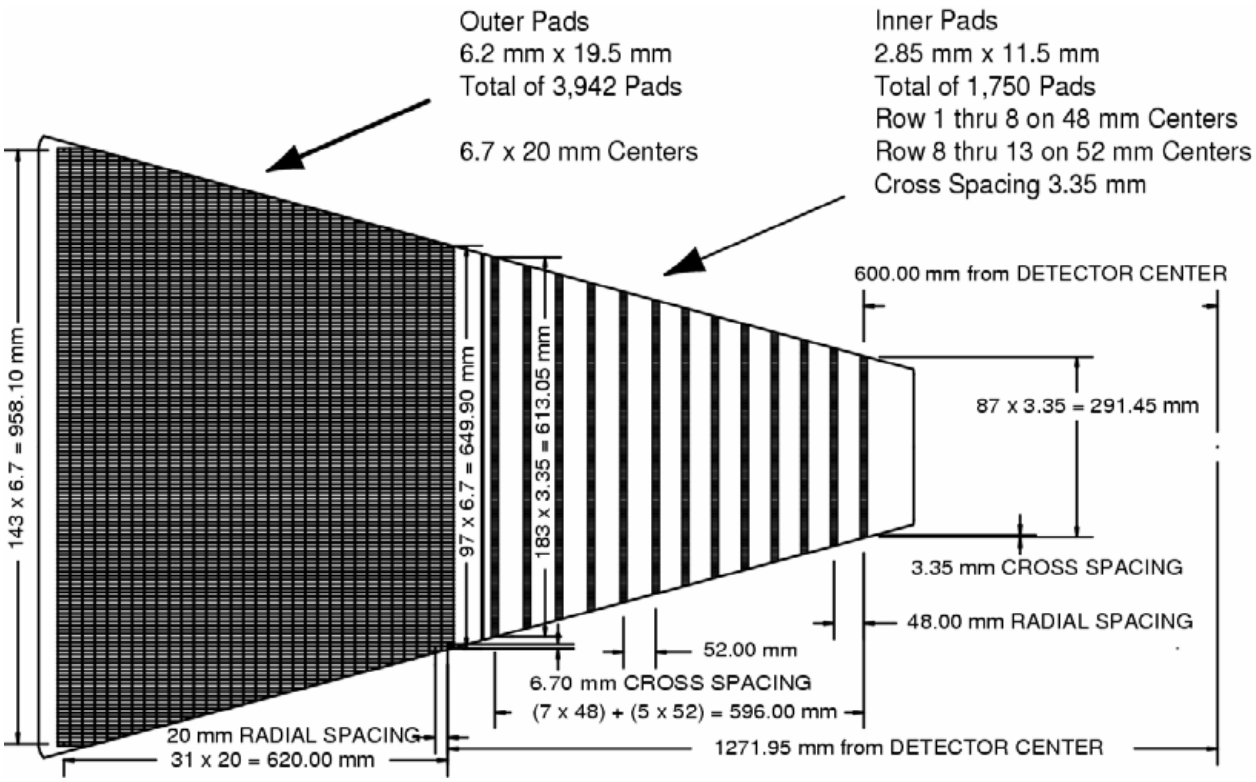

Figure 3.4: The time-projection chamber sector diagram from Ref. [140]. The anode pad plane with one full sector shown. The inner sub-sector is on the right and it has small pads arranged in widely spaced rows. The outer sub-sector is on the left and it is densely packed with larger pads.

give the best signal-to-noise ratio without compromising two-track resolution.

Inner sectors are specifically designed for the optimum two-hit determination–small pads arranged in widely spaced rows–while outer sectors are designed to best define the dE/dx resolution–the densely packed larger pads. A full sector is illustrated in Fig. 3.4 where the inner sector is the right-hand side of the figure and the outer sector is the left-hand side of the figure. All measurements are in millimeters.

Since the ionization electrons must traverse a 2.1 m drift volume, minimal diffusion is necessary for spatial precision measurements. The magnetic field plays two roles; aiding in minimal diffusion is one of them. The second role for the magnetic field is to bend charged particle tracks for momentum measurements. For a more detailed discussion of the magnet see Ref. [142]. Momentum measurements rely on the uniform field of a solenoid magnet to track a particle's curvature through the gas-filled chamber. At full-field, the magnetic field

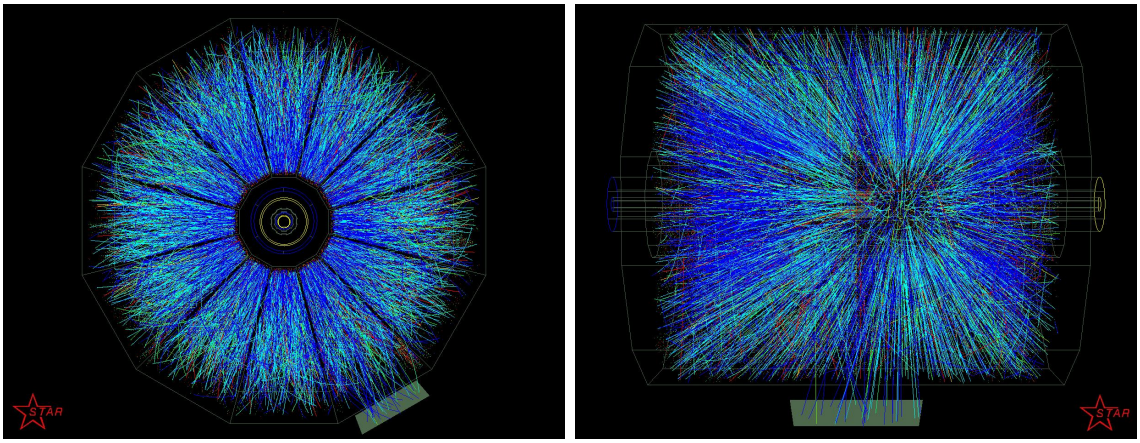

Figure 3.5: An example of event reconstruction using the STAR TPC from a central Au+Au collision during the first run at RHIC [144]. The left-hand panel illustrates a view looking down the beam line (the z-direction going into the page). One can clearly see the sectors of the TPC as well as the inner field cage dimension. The light-color shaded box is one RICH detector module installed at the time. The right-hand panel is a side view of the same event where the beam line is the horizontal. Again, the light-color shaded box is the RICH module. Track color represents the particle's energy loss with dark blue being smallest and red being largest.

measures 0.5 T and allows for measurements with transverse momentum $p_T > 100$ MeV/c.

3.2.1 Event Reconstruction

The TPC read-out system obtains electron ionization cluster information in 512 time buckets (which with a weighted average yields the z-position) and by the charge measured on adjacent pads in a single pad row (yielding the x- and y-position). In this way, measuring energy loss and tracking position, the TPC acts like a digital camera, capturing the trajectories of thousands of particles at once (up to 1,000 particles per unit of pseudorapidity at full RHIC energy of $\sqrt{s_{NN}} = 200$ GeV). At the very first stages of data acquisition after amplification, shaping and digitization, ADC and TDC values are converted to hits. From hits to global tracks, any reconstructed track that happened to be read-out in the TPC at the time of triggering, an algorithm spins over the hit information many times; first it creates tracklets (small track segments of only a few hits each) as candidates for a track and then fits again with an algorithm that keeps —or rejects — hits depending on their position with respect to the overall fitted track. At this point, a pion mass is assumed and Coulomb scattering as

well as energy loss are corrected for when creating these tracks. At the end of the tracking algorithm, all global tracks have information regarding their position and 3-momenta defined and stored. An example of event reconstruction using the STAR TPC from a central Au+Au collision during the first run at RHIC can be seen in Fig. 3.5. The left-hand panel illustrates a view looking down the beam line (the z-direction going into the page). One can clearly see the sectors of the TPC as well as the inner field cage dimension. The light-color shaded box is one Ring Imaging Cherenkov (RICH) module installed at the time. The right-hand panel is a side view of the same event where the beam line is the horizontal. Again, the light-color shaded box is the RICH module. Track color represents the particle's energy loss with dark blue being smallest and red being largest. At this point, tracks are used to find vertex candidates with the Vertexer, or vertexing algorithm, which nominally looks for at least five tracks within a 1.5 cm radial and 3 cm long cylinder to converge. With a ranking system in the Vertexer, the tracks are utilized to find probable collision vertices, or primary vertices.

For the BES energies, possible vertices are formed from two tracks rather than five and global tracks are associated with primary vertices when its helical trajectory distance in the z-direction is within 6 cm and its radial distance is within 6 cm of the vertex location (these values are modified from the full energy values of 3 cm and 1.5 cm respectively) which will be discussed in Section 4.2. Once a global track has been associated with a primary vertex, the track is re-fit with the additional point of the primary vertex on the helix to obtain a "new" momentum. By including the vertex position in the fit for primary tracks the resolution of the momentum is highly improved [145]. These new helices are then dubbed primary tracks and all their information is stored in the primary track collection of the event's container. As expected, the vertex resolution decreases with the number of tracks used in the calculation and the vertex resolution is 350 μm when there are at least 1,000 tracks associated with that vertex.

Often there are many primary vertices found in a given "event" and the Vertexer algo-

rithm ranks the found vertices by likelihood that that vertex is the one which satisfied the trigger requirements and caused the readout of all the detector subsystems. Additional discussion of the Vertexer and its performance during the BES data acquisition will be discussed in Section 4.2.

3.2.2 Particle Identification (PID) of the TPC via dE/dx

Particle identification (PID) in the TPC is based upon the energy that particle has lost in the active gas volume. Energy loss for particles with low momentum is highly correlated with mass, but the differentiation between particle species (mass dependence of energy loss) blurs as the particle's momentum increases to $v > 0.7c$. The energy loss of a particle traversing a medium is characterized by the Bethe-Bloch formula [39],

$$-\frac{dE}{dx} = Kz^2\frac{Z}{A}\frac{1}{\beta^2}\Big[\frac{1}{2}\ln\Big(\frac{2m_e c^2\beta^2\gamma^2 T_{\max}}{I}\Big) - \beta^2 - \frac{\delta^2}{2}\Big] \tag{3.1}$$

where K is a constant, z the intrinsic particle charge, Z the charge of the medium, A the atomic mass of the medium, $\beta\gamma = p/mc$ with p the momentum c the speed of light in vacuum and m the mass of the particle, m_e the electron mass, $T_{\max}$ the maximum kinetic energy that can be given to a free electron in an interaction, I the average ionization energy of the material, and δ is a correction based on the electron density. The energy loss of a particle as it traverses the active volume of the STAR detector is specifically characterized and parameterized with the Bichsel functions [146] [147] which are used in this analysis. Equation (3.1) illustrates the mass and momentum dependence of the energy loss as charged particles traverse any medium while the equations in references [146] and [147] are extensions of the Bethe-Bloch formula specific to the STAR detector.

With the design of the TPC sectors, a particle traversing the entire gas volume of the TPC would obtain 45 pad-row hits for energy loss measurements. The mean of the measured charge clusters is highly sensitive to the fluctuations in the tail of the distribution. Thus, only

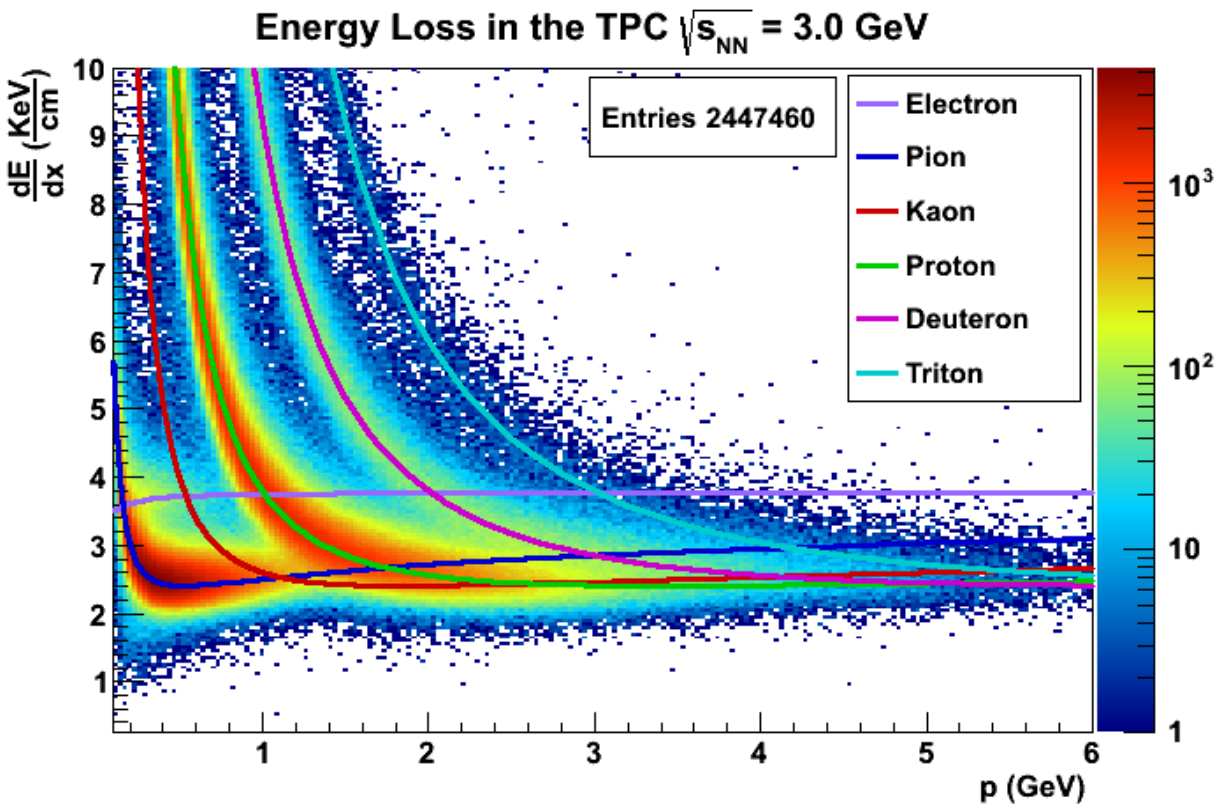

Figure 3.6: Ionization energy loss as a function of momentum. Colored lines are the theoretical predictions of the specified particle's Bichsel function while the scatterplot bands represent the actual measured dE/dx values.

70% of each track's charge distribution is used for defining the average ionization energy loss for data analysis. Particle distributions for dE/dx as a function of momentum is illustrated in Fig. 3.6. Clear particle separation can be seen for pions and kaons up to approximately 750 MeV/c while protons and antiprotons can be identified up to about 1.0 GeV/c. The colored lines represent the theoretical predictions of the Bichsel functions while the scatterplot bands represent the actual measured dE/dx values. Proton and deuteron bands also have contributions from interactions with the beam pipe and other inner material of the experiment. Decays of pions and kaons contribute to the muon band. Additionally, common neutral particles, such as the K^0_S and Λ, also decay to contribute to the pion and/or proton bands.

3.3 The Time Of Flight Detector

The Time Of Flight (TOF) detector is a set of multi-gap resistive plate chambers (MRPC), and two standard scintillation detectors. Its purpose is to extend the direct particle identification capabilities of STAR out to 1.9 GeV/c for pions and 3.1 GeV/c for protons. The 120 trays of MRPCs cover the full azimuth of STAR and have a pseudorapidity coverage of $-1 < \eta < 1$.

The scintillation detectors, called pseudo-Vertex Position Detectors (pVPD) sit outside the STAR magnet on the east and west ends of the detector arrangement, as shown in Fig. 3.7. These instruments are very close to the beampipe and serve the purpose of detecting the very high-energy, very forward emitted photons from particle collisions. The fast pulse these photons produce in the pVPD effectively serve as the "start time" of the TOF detector with an overall resolution of 24 ps (58 ps resolution for the pVPD single detector) for $p+p$ collisions and 140 ps for Au+Au collisions.

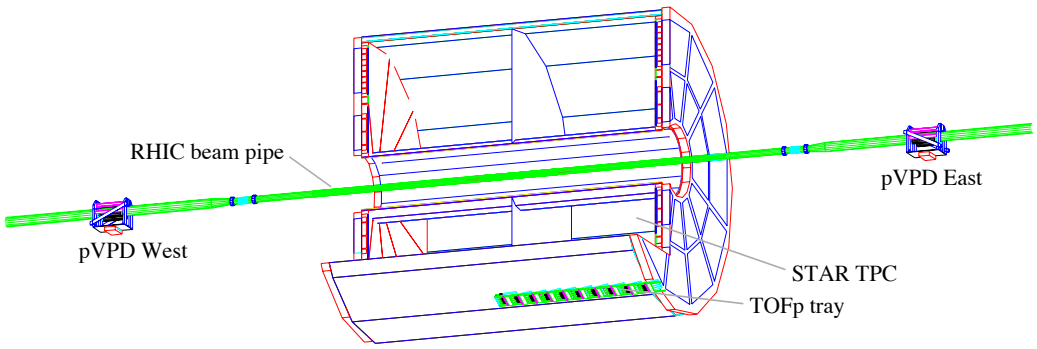

Figure 3.7: The pVPD position from Ref. [148]. A cut-out of the STAR detector identifying the position of the pVPD portion of the time-of-flight detector subsystem. Both pVPD devices are identical in construction and occupy positions near the beampipe at approximately 5.6 m from the interaction region.

Each of the six pVPD assemblies are constructed with a front "cap" of magnetic shield, an air gap, an approximately 1 cm-thick layer of lead (∼1 radiation length), a 1/4"-thick layer of scintillator, a PMT, and a linear resistive base, very reminiscent of a flashlight design [148]. Fig. 3.8 illustrates the assembly construction where a particle would be incident on the left and electronic read-out would occur on the right. Three of these assemblies are arranged

as in Fig. 3.9 and attached very near the beam pipe at ±5.6 m from the defined detector center. The configuration in Fig. 3.9 covers approximately 19% of the pseudorapidity inverval $4.43 < \eta < 4.94$.

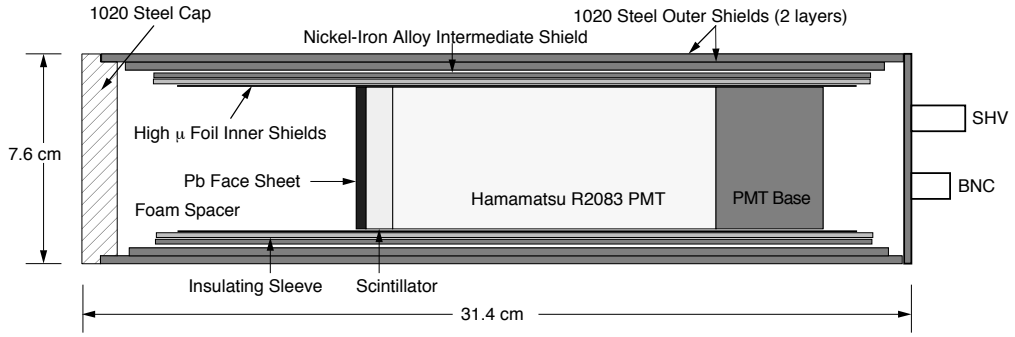

Figure 3.8: The pVPD construction. A cutaway of the detector assembly for the pVPD from Ref. [148]. This design construction was used for all six modules.

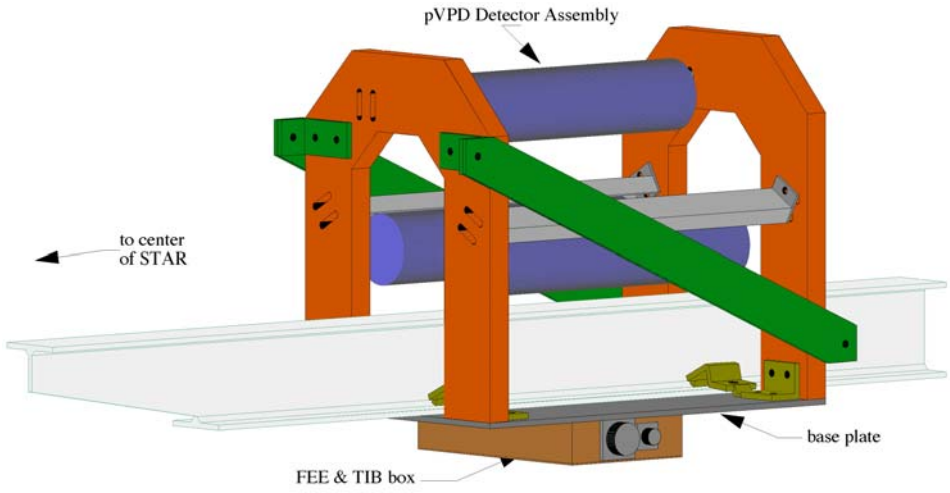

Figure 3.9: The pVPD full assembly from Ref. [148]. A schematic of the pVPD attachment to the beam pipe. This construction is identical for both pVPDs on the east and west sides.

Typical resistive plate chambers (RPC) consist of parallel plates in a gaseous mixture with resistive electrodes. The resistive electrodes serve to quench streamers (the ionized region brought about by the strong field of the avalanche electrons) so that they do not initiate a spark breakdown and thus allows RPCs to operate at much higher gains in avalanche mode. Because RPCs could first be used inexpensively for muon detection capabilities with large-area coverage, the technology was expanded to extend their application to a time-of-

flight system [149] [150]. At first, the size of the gap between plates was expanded from 2 mm, the typical gap size, to 6 or 8 mm. With the larger gap, gap tolerance is less critical; additionally a light gas can be used instead of a highly electronegative gas like freon. The advantage to using light gases is the elimination of high charges (ionic currents) produced in the gas gap allowing for an increase in the firing rate. Unfortunately, with the larger gap, there is worsening of timing resolution. The next incarnation of RPCs was a multi-gap system where the outer plates have the electrodes attached and the inner plates create small 2 to 3 mm gaps. In this way, we obtain all the advantages given by the wide-gap RPC with the timing resolution of the small gap RPC.

A through-going particle produces individual and separate clusters of primary ionization; each of these clusters will start an avalanche and the final signal will be the sum of all the avalanches. In the MRPC there is a strong feedback mechanism that forces the gas gain to be equal in all subgaps. The sheets of resistive material, electrically floating and transparent to the fast signals generated by the avalanches, allow the simultaneous readout of many subgaps so that the signal is truly the sum of independent avalanches (the charge spectrum has a Γ shape, similar to a Landau distribution). The avalanches occur in independent subgaps. Then each avalanche — at least one per subgap, depending on the gas mixture — accumulates the same charge.

At STAR, the MRPC, or TOFr, consists of a stack of resistive glass plates arranged in parallel with the uppermost and lowermost plates extending further in width than the intermediate plates, see the lower schematic in Fig. 3.10. Attached to the outer plates are electrodes which, when a high voltage is applied, produce a strong electric field between all the intermediate plates. The intermediate plates create a series of gas gaps by initially obtaining the voltage as defined by electrostatics, but are kept at the correct voltage by the flow of electrons and ions produced in the gas via avalanches. We operate these devices in avalanche mode, with a non-flammable gas mixture which contains 90% of tetrafluoro-ethane ($C_2H_2F_4$); 5% of isobutane and 5% of SF_6 [151].

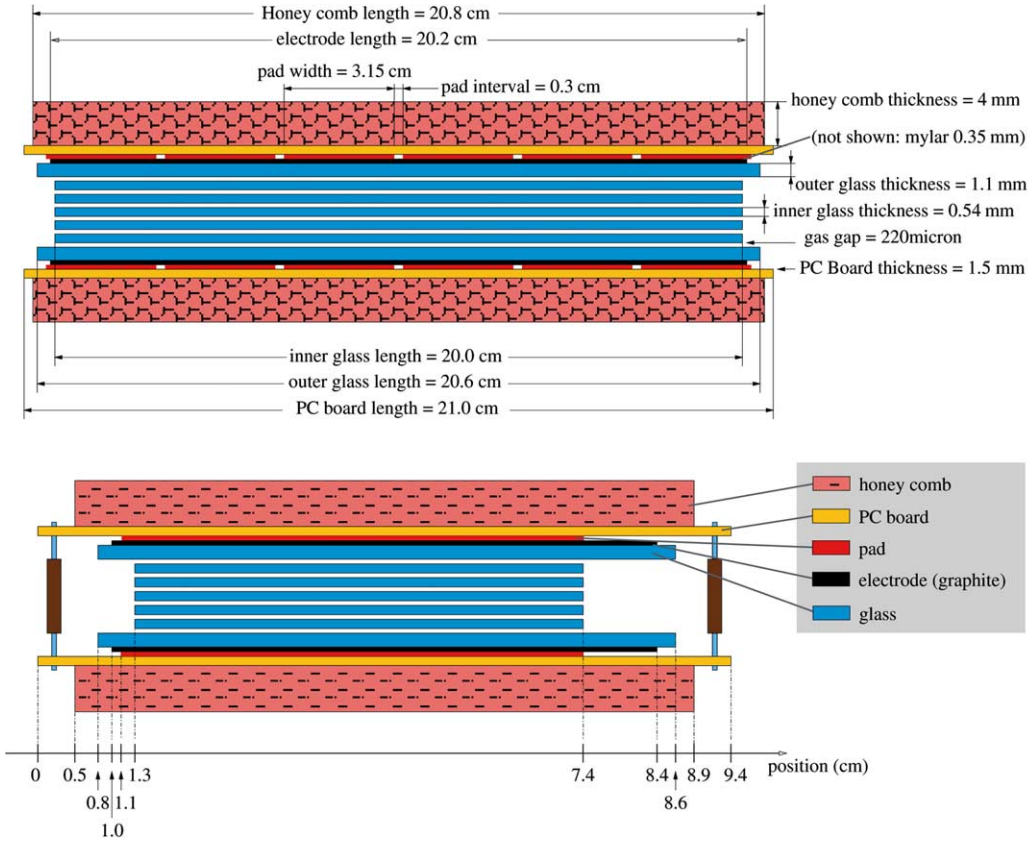

Figure 3.10: Detailed cut-out of TOFr trays. A schematic picture from Ref. [151] of the TOFr tray assembly where the upper picture depicts the length of the tray and the lower picture depicts the width of the tray. These pictures are not of the same scale.

3.3.1 Particle Identification (PID) of the TOF via $1/\beta$

Timing information from the pVPD (the "Start" time) and the TOFr trays (the "Stop" time) in addition to information about the track length from the TPC allows for the calculation of the velocity of the particles,

$$\beta = \frac{L}{tc} \qquad .$$

With this velocity and the momentum measurement, also from the TPC, a calculation of the square of the mass, m^2, of each particle can be made,

$$m^2 = p^2(\frac{1}{\beta^2} - 1) \qquad .$$

This method is the direct identification of hadrons via the calculation of the mass that the TOF detector allows us to make. Fig. 3.11 shows the $1/\beta$ distribution from TOFr measurements as a function of momentum, p, as calculated by the TPC tracking algorithm. The small plot in the upper right indicates the Gaussian-like distribution of particles in m^2 in a given transverse momentum region, $1.2 < p_T < 1.4$ GeV/c. Raw yields of identified hadrons are obtained from Gaussian fits to these distributions in $1/\beta$ for each p_T bin. Calibration of each MRPC's timing is completed first by correcting for differing cable lengths for different read-out channels and then using a pure pion sample selected from a well-separated region of energy loss, $dE/dx < 0.028 \times 10^{-4}$ GeV/cm in the momentum range $0.3 < p < 0.6$ GeV/c in order to shift the mean value of the overall distribution to zero, channel by channel, assuming that every particle was a pion. Following this, a slewing correction is made to correct for a correlation between the timing and signal amplitude of the electronics. Finally a z-position correction is made since there is a transmission timing dependence on the position of hits on the read-out strip [152].

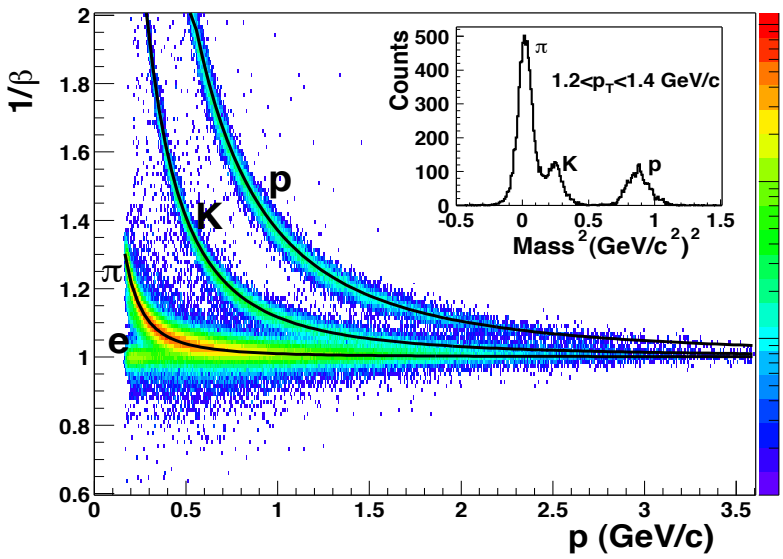

Figure 3.11: Particle Identification using TOF from Ref. [31]. The $1/\beta$ distribution from TOFr measurements as a function of momentum, p, as calculated by the TPC tracking algorithm. The inset in the upper right indicates the Gaussian-like distribution of particles in m^2 in a given transverse momentum region, $1.2 < p_T < 1.4$ GeV/c.

3.4 The Trigger Detectors

3.4.1 Beam–Beam Counters

The BBCs were designed to be the triggering system for $p + p$ collisions but also have use in other areas. Specifically, they can reject beam+gas events, measure absolute luminosity with 15% precision, and measure relative luminosities of different proton spin orientations with high precision. The timing difference between the east BBC and west BBC can also be used to measure the primary vertex position. Additionally, the small tiles in the array illustrated in Fig. 3.12 and described below are used to reconstruct the first-order event plane for directed-flow analyses.

The BBCs are scintillator annuli mounted around the beam pipe outside the pole tips of the STAR magnet, about 3.75 m from the center of the detector. The BBCs consist of small and large scintillator tiles arranged as in Fig. 3.12. The array of small hexagonal tiles complete a ring around the beam pipe with a 9.6 cm inner- and 48 cm outer diameter, covering a pseudorapidity range of $3.4 < |\eta| < 5.0$. In the center of this ring, marked B in

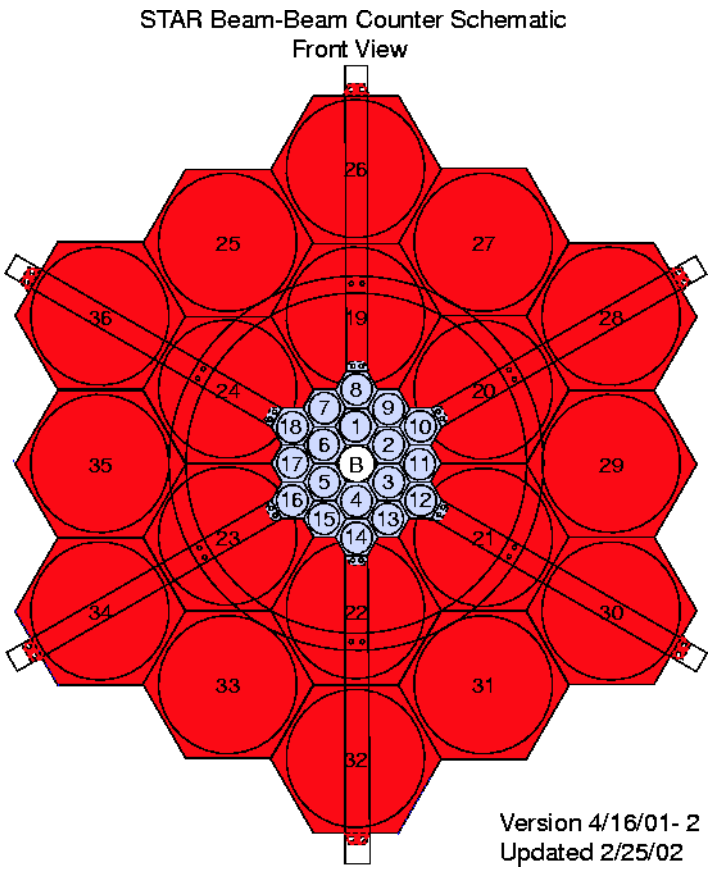

Figure 3.12: The BBC scintillator array from Ref. [153]. Diagram of the BBC scintillator array.

Fig. 3.12 is the beam pipe. Completing a ring around the small tile array is an array of large hexagonal tiles with an inner diameter of 38 cm and an outer diameter of 193 cm covering a pseudorapidity range of $2.1 < |\eta| < 3.6$. Each scintillator tile has four wavelength shifting optical fibers inside of grooves which were inscribed onto the hexagonal scintillator. Charged particles traversing through the BBCs produce light in the tiles and these fibers collect the scintillation light. Both BBCs were required to fire to trigger minimum bias $p+p$ collisions.

3.4.2 Zero Degree Calorimeter

Placed far to the east and west of the main STAR detector assembly, at ± 18 m from the detector center and at 2 milliradians relative to the beam axis, are the Zero Degree Calorimeters (ZDCs). The purpose of the ZDCs is to detect neutrons emitted within this cone along

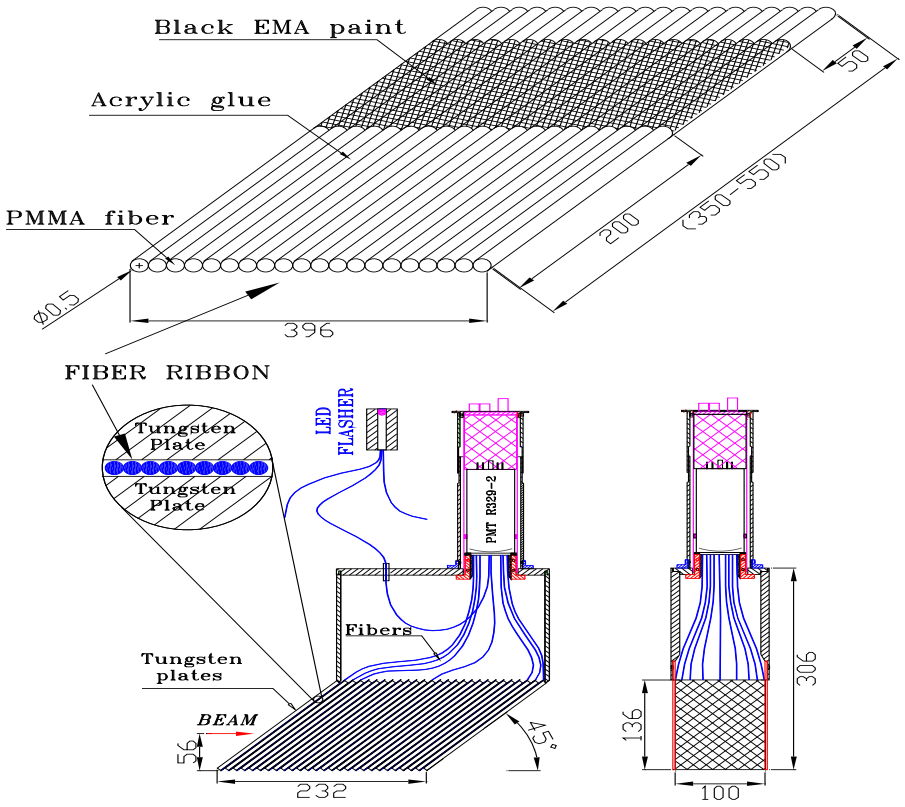

Figure 3.13: ZDC module construction from Ref. [154]. Mechanical design of the production Tungsten Modules. All dimensions are in mm.

both beam directions and measure their total energy (from which we can calculate multiplicity) [154]. These detectors are hadronic calorimeters designed to measure very far forward neutrons that did not participate in the nuclear collision, also called spectator particles. Since the dipole magnets of RHIC, just upstream along the beam line, will bend the charged spectator fragments away from the ZDCs, the neutral fragments are what the detectors measure; these are neutrons.

Both ZDCs are comprised of three identical 50 radiation-lengths long hadronic calorimeter modules, see Fig. 3.13. Each module consists of a series of tungsten plates alternating with layers of wavelength-shifting fibers which are connected to a PMT. Additionally, each module has a Shower Maximum Detector (SMD) consisting of two layers of scintillator planes, one in the horizontal direction and the other in the vertical direction. The SMD mainly identifies the position of the neutral particles that initiate hadronic showers. These ZDC modules

were designed to minimize the loss in energy resolution due to shower leakage [154].

The ZDCs provide centrality determination as well as triggering. The ZDC coincidence of the two beam directions is a minimum bias selection of heavy ion collisions. This makes it useful as an event trigger and a luminosity monitor [155]. For this reason identical detectors were built for all four RHIC experiments. The neutron multiplicity is also known to be correlated with event geometry [156] and will be used to measure collision centrality in mutual beam interactions [154].

3.5 Software and Detector Acceptance and Efficiency

3.5.1 TPC Tracking Efficiency

The tracking efficiency is highly dependent on the acceptance of the TPC since tracking is completed with information from the TPC alone. Spatial gaps in the active region — creating dead zones — as well as electronic efficiency and two-hit resolution all contribute to the inefficiency of measuring tracks in the detector. Additionally, any software cuts implemented also reduce the efficiency of detecting tracks in the active zones. The dead zones of the TPC, like gaps between sectors where wires must pass or isolation gaps between pads to distinguish them, are necessary features for data collection and its accuracy, in some cases. These physical gaps contribute $\sim$4% to the overall inefficiency of the TPC tracking. Software cuts that neglect the leading edge of an induced charge on the outermost two pad rows as well as dead channels and number of hit requirements on tracks contribute to the inefficiency. Since a leading edge falling on either of the two outermost pad rows would not have the symmetry of additional pad rows to complete a three-point Gaussian weighted fit, they are only used for constructing hits when the symmetry is present. This contributes a $\sim$2% loss in tracking efficiency. Software cuts on hit number prevent broken tracks from being included in the track count but sacrifice tracks with a small angle with respect to the beam axis as well as low-momentum tracks that spatially curl too much inside the TPC, due

to the strong magnetic field, to obtain more than a few hits.

Dead channels may arise during data collection that cannot be reconfigured, mended or replaced until after the full run time of the RHIC accelerator. These issues may be caused by bad hardware, a blown soldering joint, loose cables, software loss of communication or a number of other issues that do not allow experts to easily bring sections of a detector back online. The number of dead channels is a dynamic aspect of the detector but usually contributes no more than $\sim$1% loss to the tracking efficiency.

Analyses attempt to correct for these inefficiencies by the embedding process. By taking simulated tracks and embedding them in real events and then sending these events through the reconstruction software we quantify a tracking efficiency based on the qualities of a real event. The qualities that may affect this efficiency include ionization, the inner material budget, track density, electron drift, gas gain, signal collection, dead channels, electronic amplification and noise. Specific energy and centrality efficiencies for this analysis will be discussed in Sec. 4.3 and Sec. 4.4.

3.5.2 TOF Matching Efficiency

A key aspect of utilizing the TOF information is to ensure that a hit in the TOFr trays matches with a track in the outer edges of the TPC active volume. Making this match allows for the momentum of the particle to be associated with a flight time and thus to obtain its $1/\beta$ or the particle mass. Without matching a TOFr tray hit to a track in the TPC, these track variables cannot be determined. Each of the trays has a series of pick-up pads, approximately six per tray, see Fig. 3.14, to which a track may be associated. Three types of associations are possible: one TPC track to one TOFr hit, multiple TPC tracks to one TOFr hit, and one TPC track to multiple TOFr hits. Only TPC tracks with associations of the first and last type are considered in this analysis. This selection leads to additional efficiency losses since not only are we including the efficiency of finding a track in the TPC, but also if that track falls in the acceptance of the TOF and if it can be substantially associated with

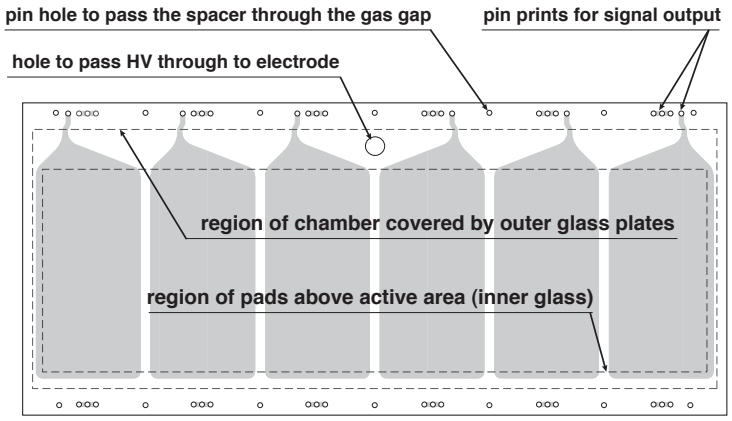

Figure 3.14: TOFr tray pick-up pad layout from Ref. [152]. Note the shape of each of the six read-out strips, or pick-up pads, for each MRPC.

the proper tray hit. There are differences in matching efficiency as a function of momentum and particle species but the overall peak efficiency is around $\sim 60\%$. Further discussion of TOF matching efficiency for specific particle species, centrality and energy can be found in Sec. 4.3 and Sec. 4.4.

Chapter 4

Analysis Methods

4.1 Introduction

Utilizing the RHIC ring during the Beam Energy Scan (BES) pushed the accelerator into energy regimes for which it was not designed. Many modifications to run-time operations as well as data processing were made to allow for the accurate recording of data. One important change to a major component of data processing—vertex analysis and the algorithm to find vertices in recorded events—is discussed in this chapter followed by the unique definition of the STAR detector geometry and collision geometry for fixed-target analysis. Lastly, methods for analyzing traditional Au+Au events at $\sqrt{s_{NN}} = 19.6$ GeV are presented.

4.2 Modifications to the STAR Vertexing Algorithm

An accurate primary-vertex location is necessary for the determination of many physics variables in collisions of any species. It is important to reconstruct a vertex in a given event which corresponds to the collision(s) that caused the read-out of all detectors (fire the trigger) associated with that event, in order both to properly analyze the results and to determine the integrated luminosity for the triggers. The challenge is that a high luminosity environment and a long detector read-out time between bunch crossings will cause many pile-up vertices to be recorded in each event.

There are three different types of pile-up that may occur with a long detector read-out

time. First is within-bucket pile-up, meaning any collision which occurs during the same bunch crossing as the event that fired the trigger. Second and third are pre-crossing pile-up and post-crossing pile-up where the collisions that are recorded with the collision that fired the trigger are either typically one to two bunch crossing(s) before or one to two bunch crossing(s) after the collision. A cartoon illustration can be seen in Fig. 4.1. In each case, the vertex in blue is constructed from the collision that fired the trigger, while the vertex in red is a pile-up vertex. The pile-up collision in the left-hand panel of Fig. 4.1 occurred after the triggered collision (post-crossing), meaning that the tracks associated with the triggered collision had already drifted away from the TPC Central Membrane. When this event is reconstructed, these tracks are connected properly but the tracks from the post-crossing vertex have discontinuities at the Central Membrane. In the right-hand panel of Fig. 4.1, the pile-up collision happened before the triggered collision so that the tracks from that collision had already started to drift down the TPC when the trigger was fired [157].

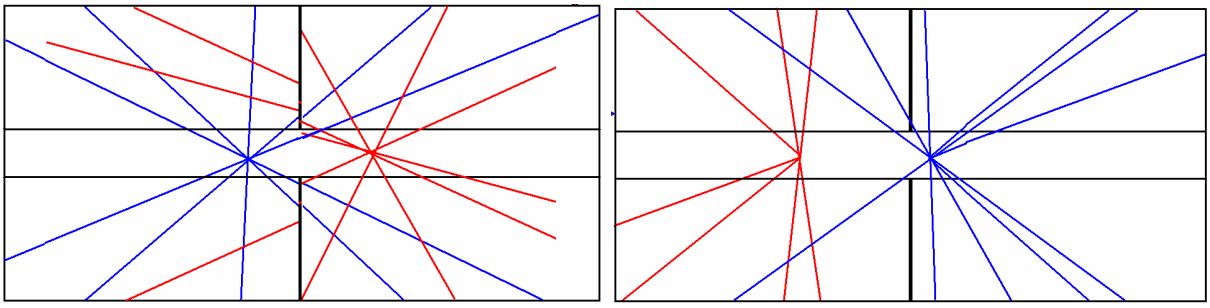

Figure 4.1: Cartoon events showing the way the two different types of pile-up will be reconstructed for a particular event. In each case, the vertex in blue is constructed from the collision that fired the trigger, while the vertex in red is a pile-up vertex. The pile-up collision for the left-hand panel occurred after the triggered collision (post-crossing). In the right-hand panel the pile-up collision happened before the triggered collision so that the tracks from that collision had already started to drift down the TPC when the trigger was fired [157].

The STAR vertexing algorithm for ion collisions uses a Minuit minimization technique to find the most probable vertex that fired the trigger. Tracks are used to find vertex candidates with the Vertexer which nominally looks for at least five tracks (N) within a 1.5 cm radius (R) of a 3 cm long (Z) cylinder to converge. It then calculates the z-position of this vertex and runs in a loop to find additional tracks within a new cylinder centered around this vertex

position. When a track has a DCA (distance of closest approach) within the cylinder, the vertexer associates this new track with this vertex, removes outlier tracks, and recalculates the z-position to go through the loop again. The algorithm uses several variables to rank vertices: the number of tracks crossing the central membrane, the number of track matches to the Barrel Calorimeter (BEMC), and a comparison to an estimate of the average dip angle for vertices with a similar z-location. The dip angle of a track is the angle between that track and the z-axis. The BEMC track matches are used because this detector is a "fast" detector, meaning its data read-out occurs quickly and can be interpreted by logic quickly. A collision that is near the edge of the detector will have a number of outgoing particles that do not have reconstructed tracks in the TPC because the tracks will not leave enough hits in the TPC. The vertices constructed from these collisions will have an average dip angle that is skewed when compared to a vertex constructed for a similar collision in the center of the detector. The primary vertex is the vertex with the highest rank. All other vertices are saved in order of their vertex rank [157].

For the BES energies, however, the detector systems were bombarded with stray particles from collisions of gold ions upstream with different parts of the accelerator: the beampipe, gas, bending magnets, flanges, etc. Random coincidences (random pile-up) of these stray particles would sometimes satisfy trigger requirements and cause the read-out of all detectors. The beam halo was large enough and populated enough to have collisions at a measurably high rate, see Fig. 4.2. The top plots are vertex distributions far zoomed out, while the bottom set is the same but zoomed in the x- and y-dimensions.

With such a high pile-up environment, it became necessary to study the performance of the traditional vertexer in these even more demanding conditions. Noted during fast offline production—a sneak peak using the calibrations from the previous year to interpret the data being taken during the current run—were some strange features in well-known distributions like multiplicity and average dip angle. From the studies of the vertexer, we were able to discover that, with the tight cuts of the full-energy minimization, some tracks from the halo

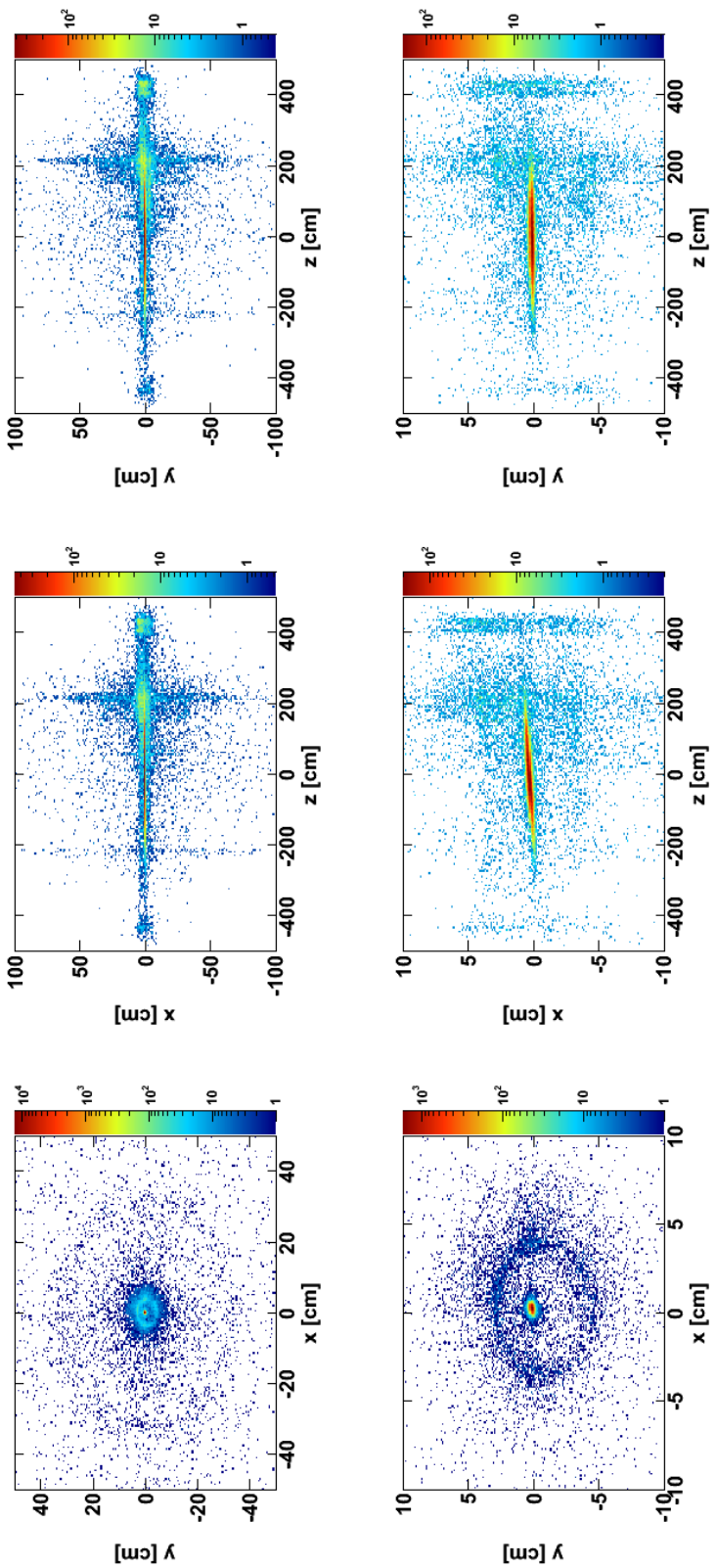

Figure 4.2: Reconstructed Vertex Locations for two tracks in a cylinder of dimensions 6 cm×6 cm or (R, Z, N) = (6, 6, 2). The left-hand column/top plots are vertex distributions far zoomed out ($|x| < 100$ cm), while the bottom set is the same but zoomed in the x and y dimensions.

collisions with the aluminum beampipe were being pulled into good Au+Au vertices, see Fig. 4.3. This pulling of tracks and displacing of the beam-on-beampipe vertex, or shadow vertex, was skewing the multiplicity, lowering the vertex rank (for having incorrect values of BEMC matches and CM crossers) and displacing the vertex location causing incorrect recalculations of track momentum.

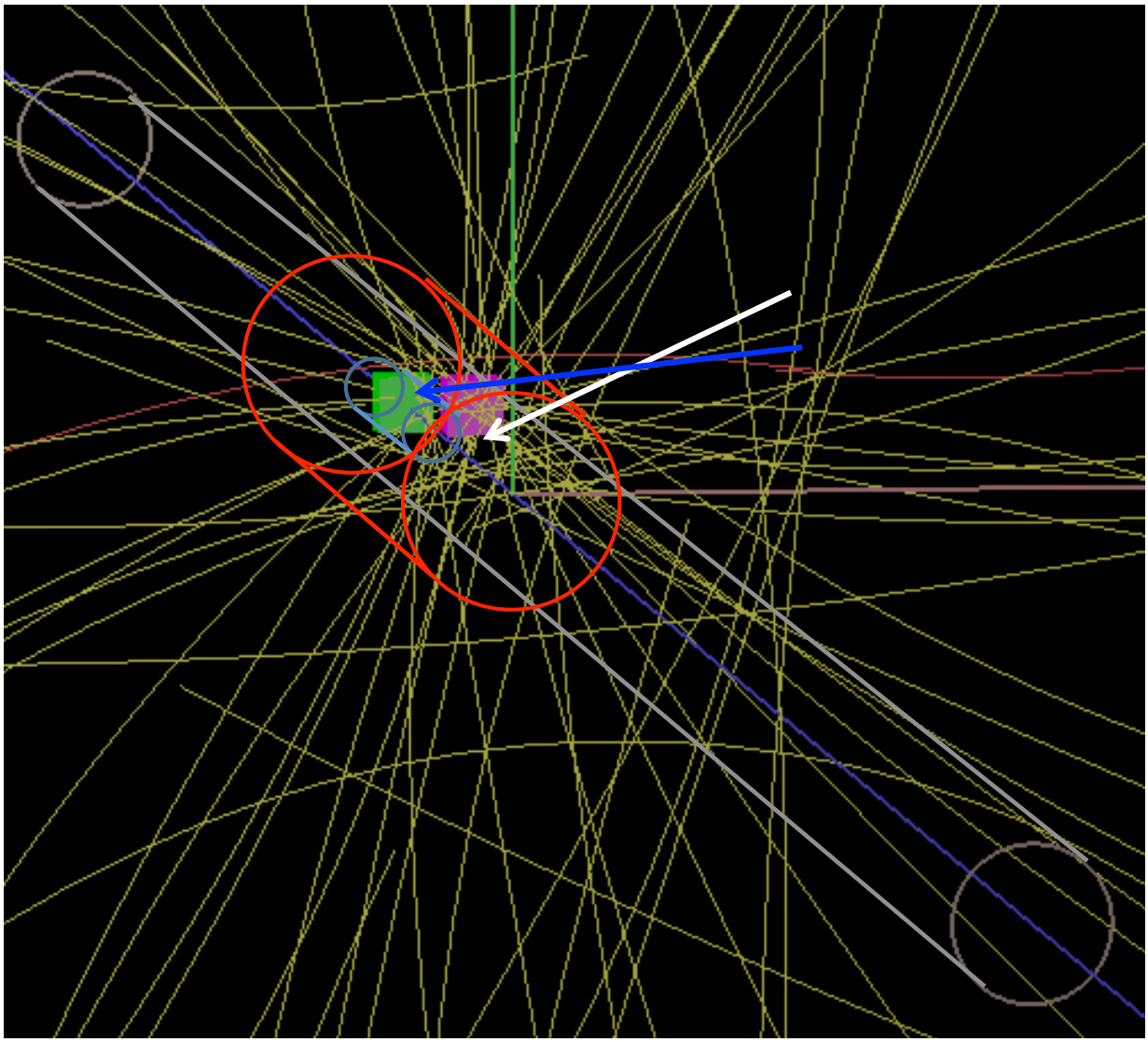

Figure 4.3: A reconstructed event with two vertices. The blue arrow points to the good Au+Au event. The white arrow points to the Au+Al , beam on beampipe, vertex which has been pulled close to the beamline by the default vertexer parameters: a shadow vertex. Grey illustrates the beam pipe, sea-green the central membrane, the red cylinder the expanded (R, Z, N) = (6, 6, 2) parameter cuts, the smaller light-blue cylinder the default parameters, and the indigo line represents the beamline. All deep yellow lines are reconstructed tracks.

(R, Z, N) (cm,cm,)	Number of Vertices	Number of Good Vertices	Index 0	Index 1	Index 2	Index 3	Index 4
1.5, 3, 5	198/3841	75	75	0	0	0	0
6, 6, 5	909/3841	103	88	4	7	2	1
6, 6, 2	1417/3841	139	96	15	17	7	8

Table 4.1: Comparing the three vertexing parameter sets investigated for data production. The radial parameter is indicated first describing the maximum radial distance away from the beam line the vertexer will loop over tracks; then the z-parameter describing how far along the beam line in the positive and negative direction the vertexer will look for tracks; and finally the N parameter describing the minimum number of tracks required to make a vertex. A total number of 3841events were analyzed for vertices. A "good" vertex is defined as having a radial position within 2 cm of the nominal beam line and a z-position within 30 cm of the center of the detector. Each vertex in a collision is ranked and given an index number determined by the likelihood that collision fired the trigger.

Specifically, the default vertexer loops over tracks within ± 3 cm from the estimated z-vertex position and within a radius of 1.5 cm. Additionally, a minimum of 5 tracks must be present in order for a vertex to be formed. We first studied six separate parameter changes to these cuts by expanding the cylinder up to the geometrical location of the beam pipe and reducing the number of tracks necessary to create a vertex. Labels for each of the studies were by their parameters: R—radial distance (1.5 cm for default, or 3 cm, or 6 cm), Z—beam line distance (3 cm for default, or 6 cm), N—number of tracks needed to create a vertex (5 for default, or 2). After a preliminary study, only two settings made a significant difference to the default parameters: (R, Z, N) of (6, 6, 5) and (R, Z, N) of (6, 6, 2).

By including the beampipe in the cylinder to find vertices, the extra tracks that the default vertexer was assigning to good Au+Au collisions could be properly placed with vertices located on the beam pipe. Additionally, the lower track requirement allowed the vertexer to find additional vertices along the beam line that the default settings would not.

A summary of vertex finding efficiency is found in Table 4.1 where the total number of events analyzed for vertices was 3841 and a "good" vertex is defined as having a radial position within 2 cm of the nominal beam line and a z-position within 30 cm of the center of the detector. The "wide open" cuts (R, Z, N) of (6, 6, 2) are more efficient at finding good Au+Au vertices and placing knock-out events on the beam pipe. Thus, for production of the Beam Energy Scan (BES) data, all global tracks are associated with primary vertices when the helical trajectory's distance of closest approach (DCA) is within 6 cm of the vertex location in the $\pm z$-direction and out to a radial distance of 6 cm from the nominal beam line.

4.3 Fixed-Target Interactions

With the vertexing parameters expanded to place vertices on the beam pipe, data analyses of these collisions—of the Au-like ion beam on the Al beam pipe—could be performed. Ultimately being able to use STAR as a fixed-target experiment as well as a colliding-beam experiment has allowed the Beam Energy Scan (BES) to reach further into the high baryon-chemical-potential and low-temperature region of the nuclear-matter phase diagram.

4.3.1 A Fixed-Target Geometry

STAR was built to measure symmetric collisions of separate particle beams, but never intended to measure collisions with fixed targets. By analyzing the data from the ion beam on the beampipe material, Al, we are pushing the absolute limits of STAR's capability. An example of a reconstructed fixed-target collision is illustrated in Fig. 4.4. The black rings denote the endcaps of the TPC, the yellow horizontal line represents the beam line, the red vertical line illustrates the position of the central membrane and all the blue and cyan lines are reconstructed tracks where the darker shade represents the part of the track which is extrapolated from the helical fit to the hit points (the lighter shade). All of the tracks are

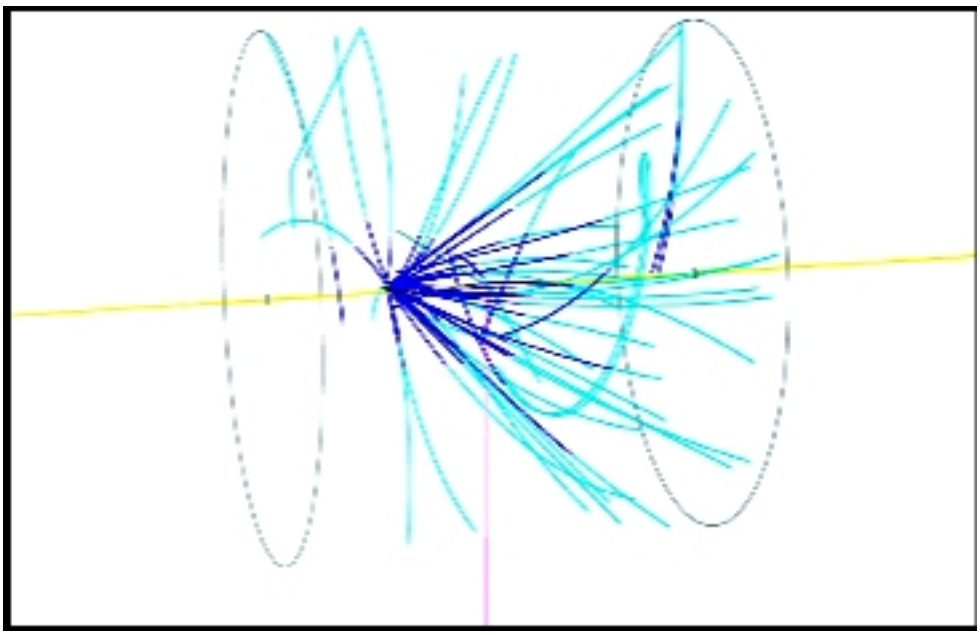

Figure 4.4: An example of a fixed-target collision as measured in the STAR detector. The black rings denote the endcaps of the TPC, the yellow horizontal line represents the beam line, the red vertical line illustrates the position of the central membrane and all the blue and cyan lines are reconstructed tracks where the darker shade represents the part of the track which is extrapolated from the helical fit to the hit points (the lighter shade). (*A. Schmah via private communication.*)

directed asymmetrically to one side of the detector, not distributed evenly to the forward and backward regions, as one would expect for a colliding-beam event.

In order to ensure that tracks are long and obtain plenty of hit points for decent resolution and dE/dx measurements we need to look at a z-vertex position, V_z, displaced from the center of the detector in the region from 150 cm $< |V_z| <$ 200 cm. When we select for events with this displaced vertex position we have a different geometry for detector acceptance. This geometry is illustrated in Fig. 4.5. All detector subsystems are labeled in the diagram, as well as the Al portions of the beam pipe in green and the Be portion in blue. Also in green are sample tracks that illustrate the pseudorapidity acceptance of the TPC and TOF for an event with a vertex at the very edge of the detector.

For the BES energies where a significant number of events can be analyzed to obtain particle spectra, the highest mid-rapidity we have is $y_{\rm mid} = 1.5$ for the $\sqrt{s_{NN}} = 4.5$ GeV fixed-target energy collected during the $\sqrt{s_{NN}} = 19.6$ GeV collider-energy run. It is important

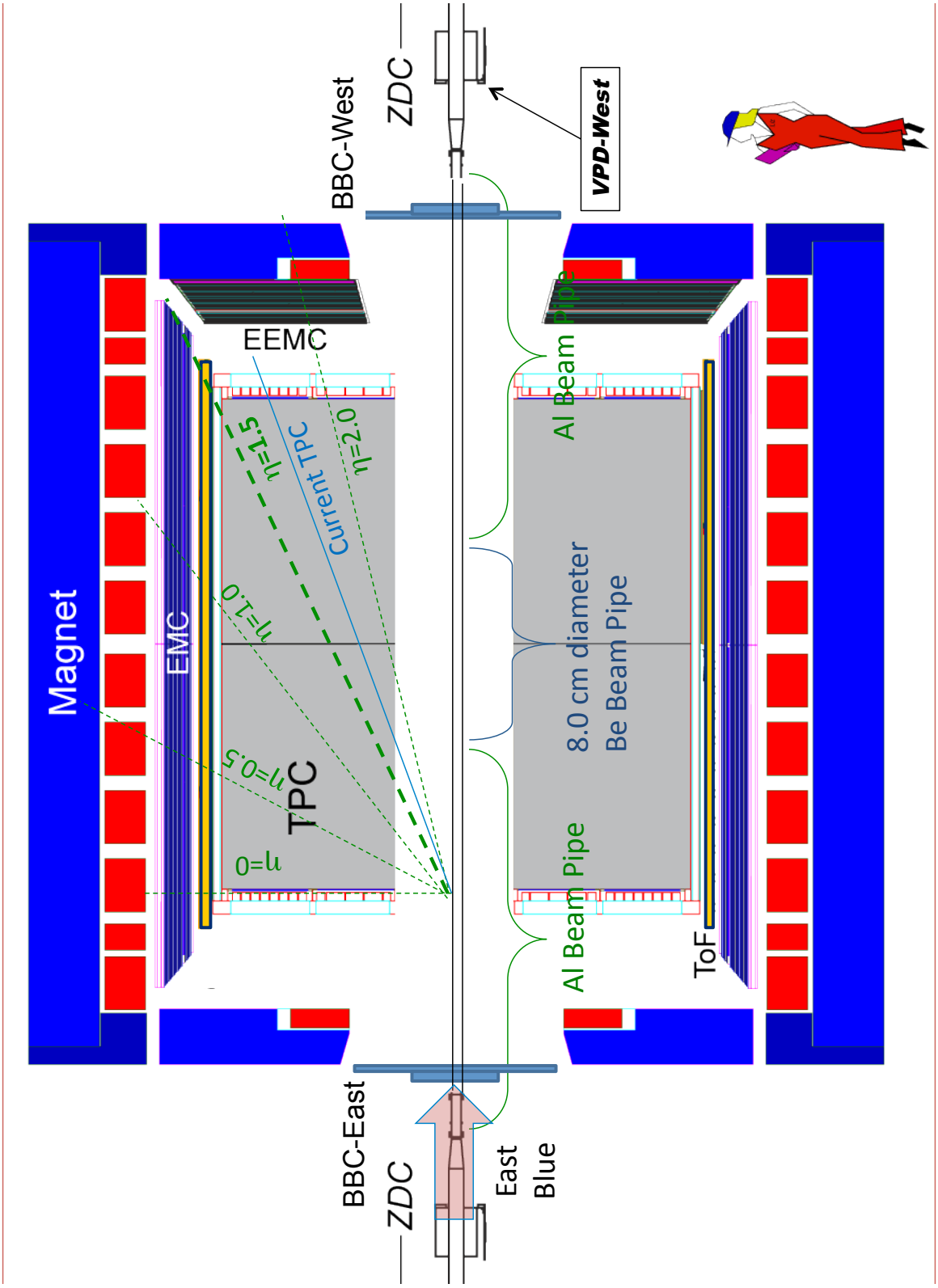

Figure 4.5: The STAR fixed-target geometry where all detector subsystems are labeled appropriately, as well as the Al portions of the beam pipe in green and the Be portion in blue. Also in green are sample tracks that illustrate the pseudorapidity acceptance of the TPC and TOF for an event with a vertex at the very edge of the detector. (*D. Cebra via private communication.*)

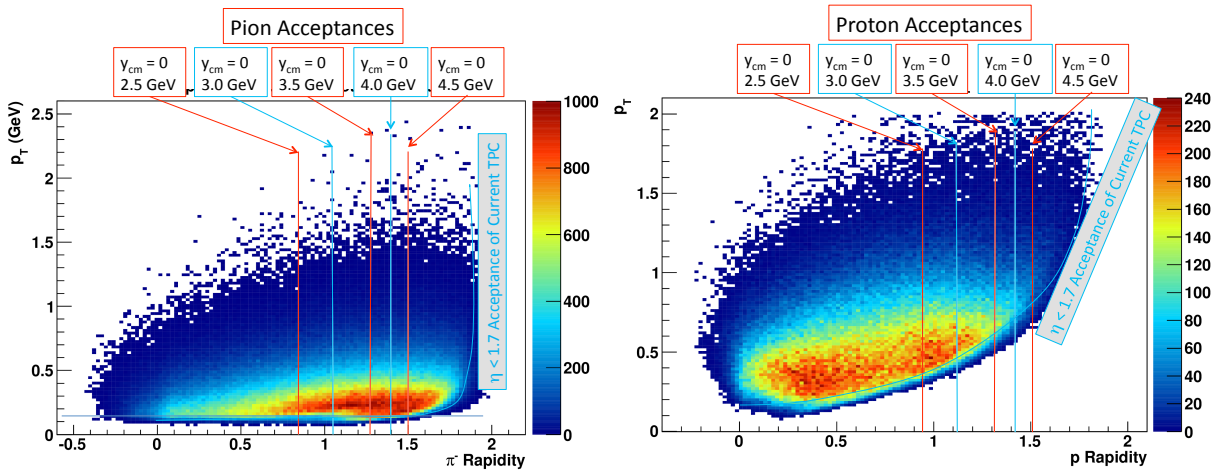

Figure 4.6: Pion (left) and proton (right) acceptance for the STAR fixed-target geometry. Note that as the energy of the beam changes, so does midrapidity and thus the acceptance of the detector. Pions have relatively uniform acceptance in this geometry. However, protons have a high cut-in that depends on the beam energy. This efficiency loss will affect the ability to obtain a spectrum in the low momentum region.

to note that, for the highest energy, we begin losing acceptance in the forward region but have full acceptance from beam rapidity back to target rapidity. For the other energies, we have some acceptance in the forward region but full acceptance from beam rapidity back to target rapidity.

When changing beam energy in the accelerator, the acceptance of the detector changes as well. This is a feature of a fixed-target experiment. Particle acceptances can be seen in Fig. 4.6 with pions on the left and protons on the right. Note that as the energy of the beam changes, so does midrapidity and thus the acceptance of the detector. Pions have relatively uniform acceptance in this geometry. However, protons have a high cut-in that depends on the beam energy. This efficiency loss will affect the ability to obtain a spectrum in the low-momentum region.

4.3.2 Understanding Centrality and Event Selection

Another challenge of the fixed-target collisions appears when attempting to determine centrality of Au+Al to compare to other spectra. Recall that Al has 27 nucleons while Au has

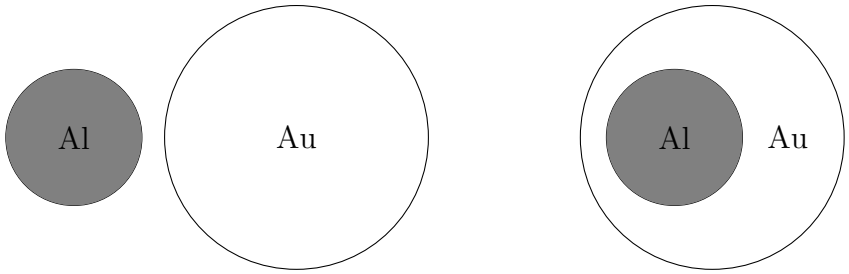

Figure 4.7: For comparative size, in (a) the Au nucleus on the right has a diameter which is approximately twice as large as the Al nucleus on the left. When the Au collides with the Al nucleus, there is a range of impact parameters where the Al is completely absorbed, as in (b).

197, and the nucleon density of the nucleus is uniform [158]. We can thus estimate the radius of the nucleus from its volume and nucleon number,

$$R = R_0 A^{1/3} \quad ,$$

where $R_0 \simeq 1.2$ fm and A is of course the number of nucleons. The gold nucleus has a radius of 6.97 fm while aluminum has a radius of 3.6 fm, see Fig. 4.7. This leads to a range of impact parameters where the Al nucleus is completely absorbed by the Au ion. We had to determine what "most central" would mean for this type of collision. It largely depended on the number of participating Au nucleons. Since Au is nearly spherical and relativistically flattened, the number of nucleons that can collide in a given small cylindrical volume with an axis parallel to the beam axis is higher toward the center of the Au nucleus than at the edges. Figure 4.8 shows Woods-Saxon populated Au (blue) and Al (red) nuclei. The dark blue nucleons have participated in the collision—are participants—while the light blue have not—are spectators. The impact parameter here is small enough that all the Al nucleons are participants.

We also needed a variable to approximate the impact parameter and define centrality. By utilizing simulations from UrQMD [159] [160] we looked for highly correlated variables, simi-

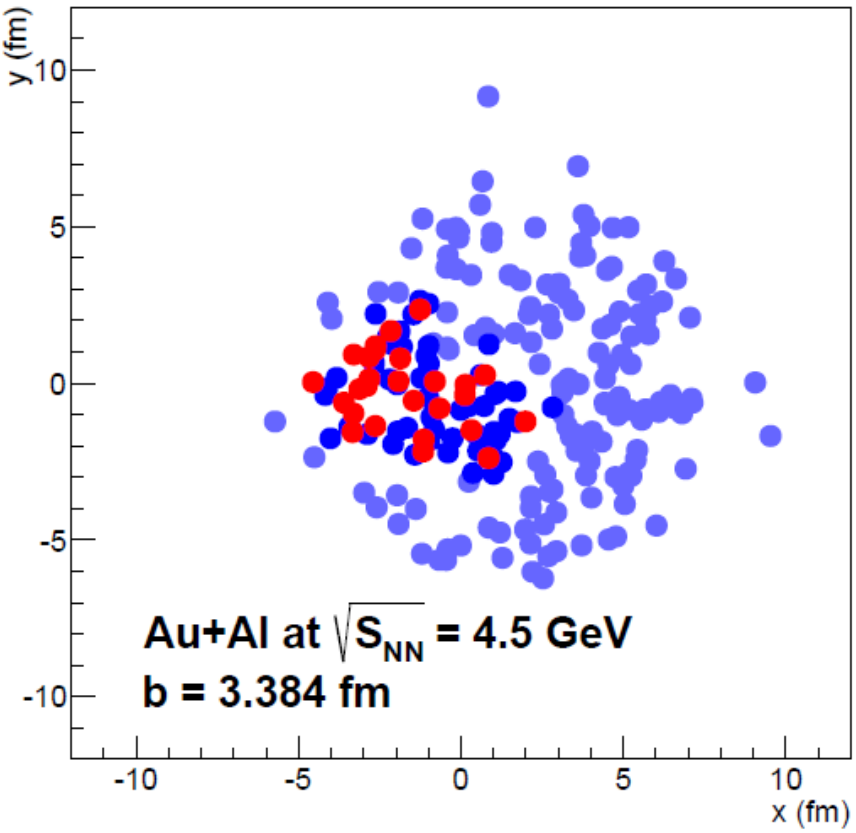

Figure 4.8: An illustration of Woods-Saxon populated nuclei for Au (blue) and Al (red). The dark blue nucleons have participated in the collision (participants), while the light blue have not (spectators). The impact parameter here is small enough that all the Al nucleons are participants.

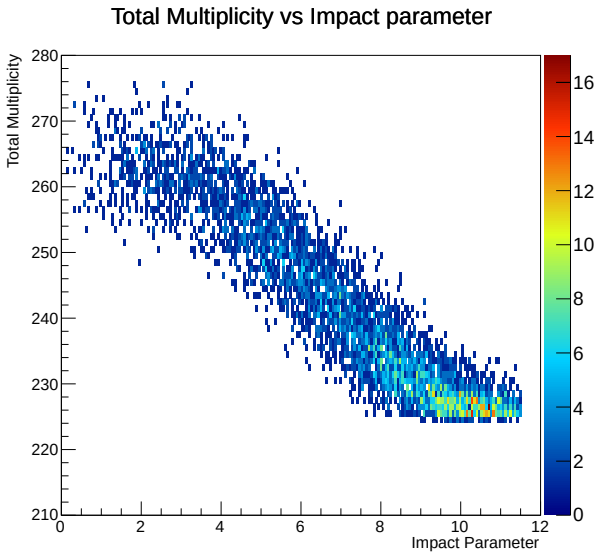

Figure 4.9: This plot illustrates the strong correlation between the total multiplicity of an event, including all spectators and produced particles over the entire rapidity range versus impact parameter.

lar to the use of reference multiplicity for nominal Au+Au collisions, with impact parameters for the Au+Al $\sqrt{s_{NN}} = 3.0$ GeV collision system. Total multiplicity versus impact parameter can be seen in Fig. 4.9. Total multiplicity is defined as all spectators and produced particles over the entire rapidity range. This type of strong correlation is what we want to reproduce using the measurable variables (of which total multiplicity is not experimentally observable) available with the STAR detector. Pion multiplicity as a function of impact parameter and a crude detector model for the TPC acceptance, called TPC multiplicity in the figure, versus impact parameter can be seen in Fig. 4.10. The pion multiplicity comes from counting charged pions produced in the simulated collision that fall within a crude detector model of the TPC acceptance: $-0.5 < \eta < 1.96$. The correlation between these two variables—pion multiplicity and impact parameter—is good. And, with the crude detector model, the shape of the correlation is very similar despite the inclusion of protons in the total multiplicity of Fig. 4.9. This is indicative that the majority of particles in the TPC acceptance are charged pions. The total proton multiplicity and proton multiplicity at midrapidity are shown in Fig. 4.11. Recall that for the Au+Al $\sqrt{s_{NN}} = 3.0$ GeV collision system mid-rapidity is

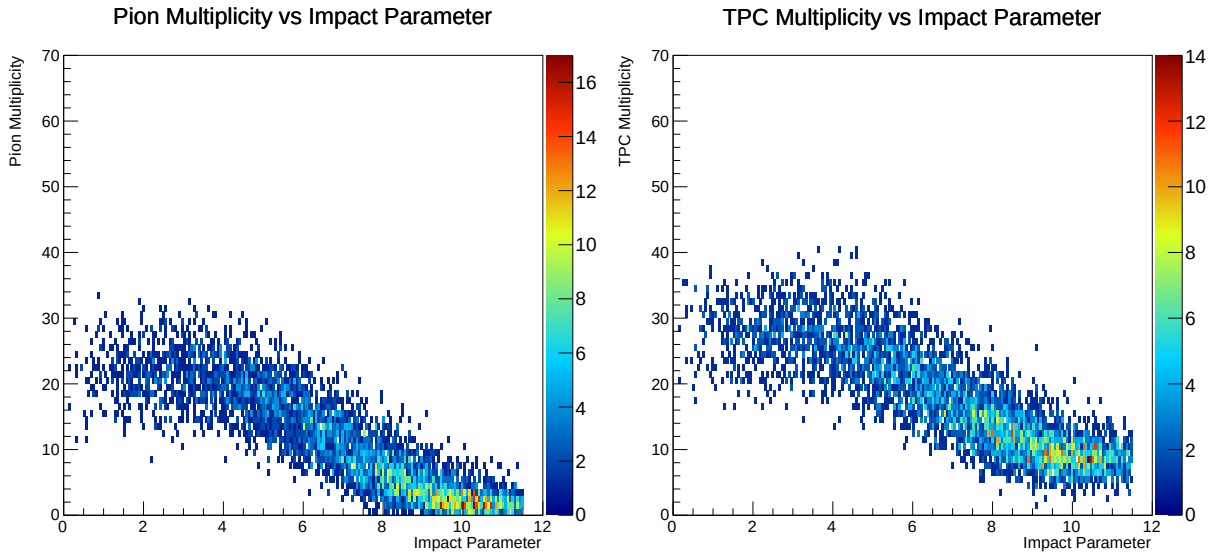

Figure 4.10: On the left-hand panel is the pion multiplicity versus impact parameter. The correlation between the two variables can clearly be seen. On the right-hand panel is the charged particle multiplicity found in the pseudorapidity of the TPC range for the adjusted fixed-target geometry.

$y_{\text{mid}} = 1.05$ and mid-rapidity protons are more reference-multiplicity like in that they fall within $0.55 < y_{\text{proton}} < 1.55$ and cover a full unit of rapidity. Unfortunately, protons do

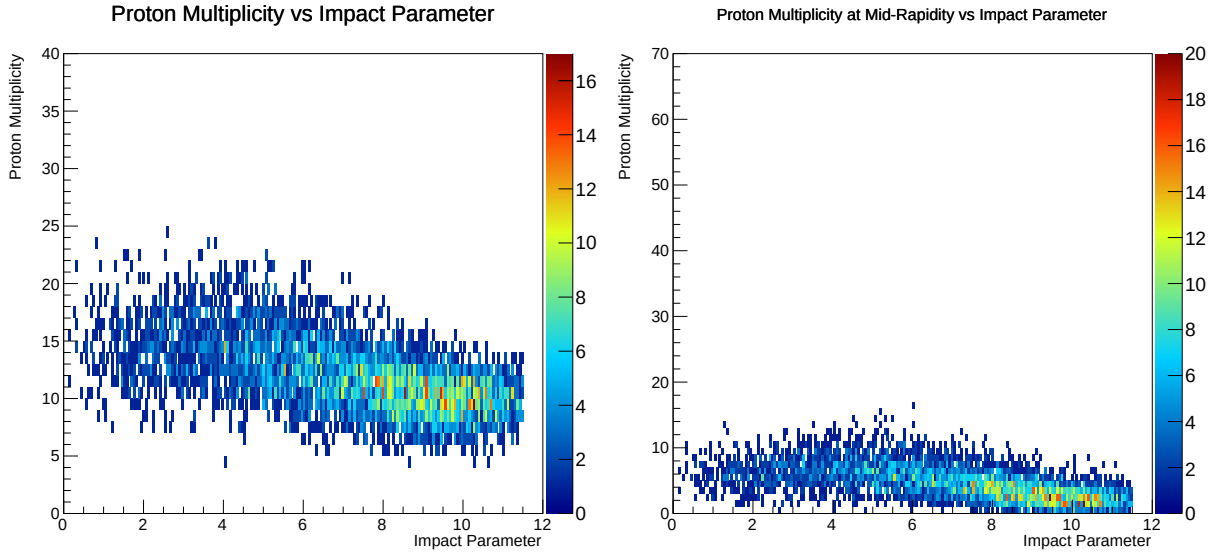

Figure 4.11: On the left-hand panel is the total proton multiplicity versus impact parameter. The proton multiplicity distribution is found in a similar way to the pion distribution. Because the event is simulated, as long as the identified proton falls within the crude TPC model, it is counted in the multiplicity. On the right-hand panel is the proton multiplicity around mid-rapidity versus impact parameter. In neither case is a clear and strong correlation between the variables seen.

not present a strong correlation with impact parameter. Even attempting to ensure that the protons we count are coming from the nucleus collisions, in the midrapidity proton plot (Fig. 4.11) the correlation becomes even weaker. Protons, in this case, prove incapable of representing collision centrality.

Since pion multiplicity is shown to be indicative of the collision impact parameter, a fit to this distribution with a Glauber Monte Carlo to define centrality classes is next. In the model, nucleons are randomly scattered according to a Woods-Saxon distribution for each nucleus, again as in Fig. 4.8. Then, an impact parameter is arbitrarily selected for the collision and the transverse position with respect to the impact parameter of each of the nucleons is computed. Any nucleons within the overlap region are counted as participants, N_{coll}, while the number of binary collisions, N_{coll}, is counted by any nucleon overlapping the two dimensional area (cross section) of a nucleon from the opposing nucleus. For each Au+Al collision, a Negative Binomial Distribution is utilized N_{part} times to determine the number of pions produced for that event. The parameters for the Negative Binomial Distribution, n and p, are determined by performing a grid search of various combinations and determining the suitability of the parameters by a χ^2 test to the data. The pion multiplicity is found by selecting measured events with some preliminary cuts in the z- and radial vertex position as well as ensuring the collisions sprayed particles into the TPC rather than out of it. The number of pions is determined by making a mass assumption and comparing the energy loss of the particle to the STAR-adapted Bethe-Bloch function in the Bichsel class [146]. If the particle energy loss fell within 2σ of the Gaussian-like distribution around the pion Bichsel line, that particle was counted as a pion. No cuts to eliminate the anomalous low multiplicity are made, but, the low multiplicity spike is understood to include collisions of fragments like α particles on the Al bream pipe. The pion multiplicity distribution is plotted in Fig. 4.12. The red stars are data fit with the Glauber Monte Carlo (blue histogram); the fit parameters with the best goodness of fit, $\chi^2 = 3.8$, are $n = 2.0$ and $p = 0.058$. The green histogram is the same Glauber Monte Carlo for collisions with an impact parameter $b \leq 3.416$ fm only.

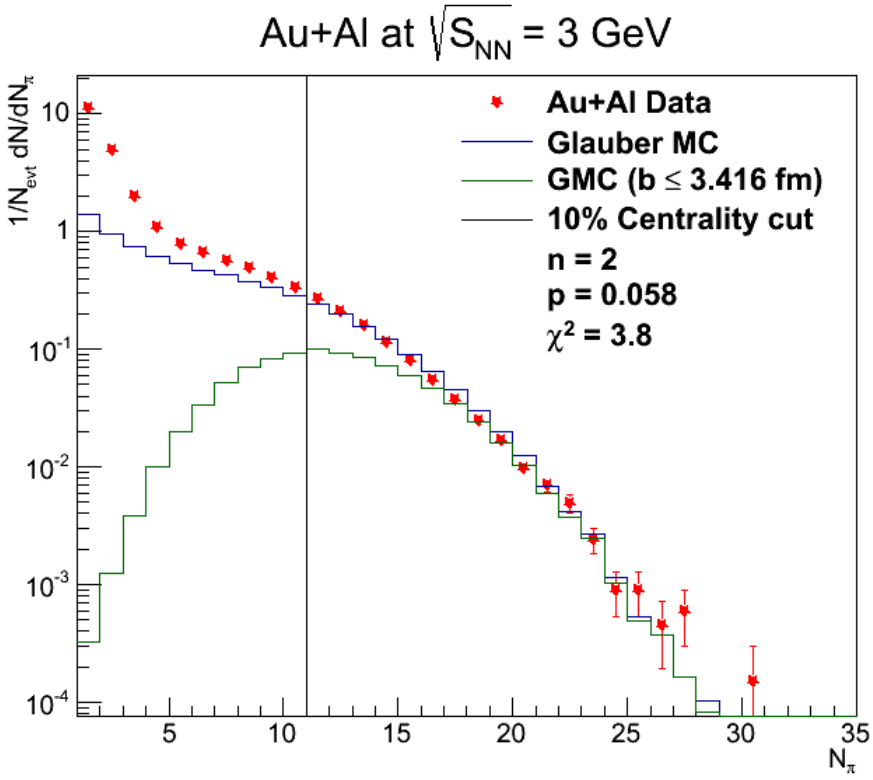

Figure 4.12: This figure shows the experimental pion multiplicity (red stars) fit with a Glauber Monte Carlo (blue histogram) for pion multiplicity; the fit parameters and goodness of fit are stated on the plot. The green histogram is the same Glauber Monte Carlo for collisions with an impact parameter $b \leq 3.416$ fm only. This allowed us to determine the number of pions which would give us the top 10% of centrality.

This distribution was integrated to find the pion multiplicity corresponding to the top 10% of centrality. For Au+Al collisions at $\sqrt{s_{NN}} = 3.0$ GeV the number of pions indicative of the top 10% central events is $M_\pi > 11$.

Event selection for fixed-target spectra analysis requires few cuts, four in total: two geometric vertex requirements, one dynamic requirement, and one centrality requirement. These are summarized in Table 4.2. Since these collisions were preferentially selected against being recorded, and all data were collected via random coincidence, no trigger requirements are needed for minimum bias. Distributions in the z-vertex position and the x-y-vertex position before any cuts are applied are shown in Fig. 4.13. In the left-hand panel, the number of events distributed in z-vertex position allows us to see the inner material budget from the

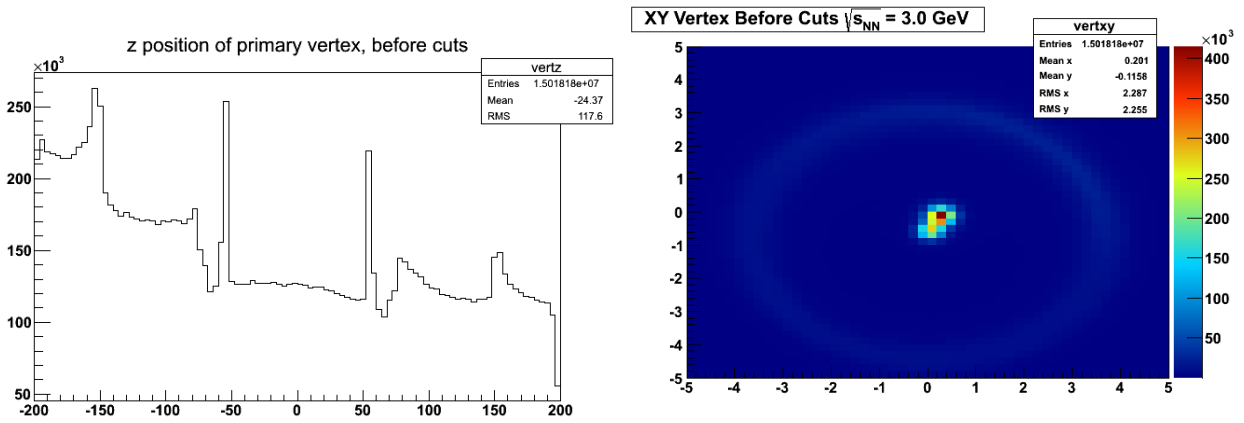

Figure 4.13: On the left-hand panel, the number of events versus the z-vertex position allows us to see the inner material budget by the peaks at the faces of the FTPC detectors located at approximately ± 150 cm in the STAR coordinate system and additional peaks at approximately ± 50 cm which are the remainders of the old Silicon Vertex Tracker (SVT) detector supports. The feature at approximately ± 75 cm is the switch from an Al beam pipe material to a Be beam pipe material. The right-hand panel shows the x-y-vertex position for all vertices, with most collisions occurring in the beam spot in the approximate center.

peaks at the faces of the FTPC detectors located at approximately ± 150 cm in the STAR coordinate system and additional peaks at approximately ± 50 cm which are the remainders of the old Silicon Vertex Tracker (SVT) detector supports. The feature at approximately ± 75 cm is the switch from an Al beam pipe material to a Be beampipe material. The right-hand panel of Fig. 4.13 illustrates the x-y-vertex position for all vertices, with most collisions occurring at the beam spot in the approximate center. The two geometric cuts applied are a z-vertex position at the edge of the TPC, -200 cm $< V_z < -150$ cm, and radial vertex position on the beam pipe, 2 cm $< V_r <$ 5 cm. The upper limit on the radial position is to eliminate any events recorded as a result of a collision with the face of the FTPC detectors.

Additionally, to ensure that the collisions sprayed particles into the TPC rather than out of it, the dynamic requirement relies on the total momentum of the collision multiplied by the z-vertex position to be less than zero: $(p_{\mathrm{Tot}} \times V_z) < 0$. To get a better idea of this, take a fixed-target collision at the center of the detector and suppose all of the particles spray in the $+z$-direction. In order to measure long tracks, we really want this vertex to be displaced in the $-z$-direction and as close to the edge of the TPC as possible. Thus, for collisions that

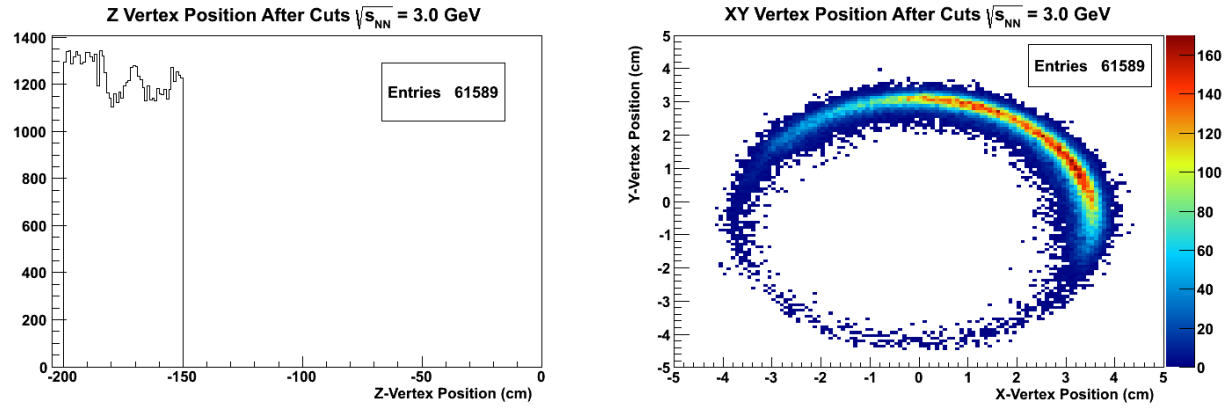

Figure 4.14: On the left-hand panel is the number of events versus the z-vertex position after all geometric, dynamic and centrality cuts are applied. Only events from the West side of the detector (spraying to the East) are analyzed. On the right-hand panel is the x-y-vertex position after all geometric, dynamic and centrality cuts are applied. These cuts select the shape of the beam pipe very well.

z-Vertex Position	x-y-Vertex Position	Total Momentum	Centrality	Spray Direction
-200 cm $< V_z < -150$ cm	2 cm $< V_r <$ 5 cm	$p_{\mathrm{Tot}} > 0$	$\mathrm{M}_\pi = 11$	$(p_{\mathrm{Tot}} \times V_z) < 0$

Table 4.2: A summary of the analysis event cuts for the fixed-target data.

spray into the detector, the total momentum will point in the direction opposite the sign of the z-vertex position and the product of the two values will always be negative. Lastly, only the top 10%, the most central, events are analyzed. These are selected using the number of pions in the event, $\mathrm{M}_\pi = 11$. Figure 4.14 illustrates the z-vertex position and the x-y-vertex position after all cuts are applied. On the left-hand panel of Fig. 4.14, the number of events versus the z-vertex position after all geometric, dynamic and centrality cuts are applied is shown. Only events from the West side of the detector (spraying to the East) are analyzed. On the right-hand panel of Fig. 4.14 is the x-y-vertex position after all geometric, dynamic and centrality cuts are applied. These cuts select the shape of the beam pipe very well.

4.3.3 Fitting Methods

Event information and track information for events satisfying the cuts detailed in Table 4.2 are collected from the full data set. From the curvature of a particle-track inside the solenoidal magnetic field, B, the transverse momentum, p_T, is calculated knowing that it is perpendicular to the magnetic field, $p_T \perp B_z$, and assuming the magnitude of the particle charge is $1e$. To extract the pion yield in a particular region of transverse mass, $m_T - m_0$, and rapidity, y, both of which have a mass dependence, a pion mass assumption, m_π, is made for every track and used with p_T to obtain $m_T - m_\pi$ and y. Recall

$$m_T = \sqrt{E_{\mathrm{TOT}}^2 - p_z^2} = \sqrt{m_0^2 + p_T^2} \tag{4.1}$$

and

$$y = \frac{1}{2} \ln \left(\frac{E_{\mathrm{TOT}} + p_z}{E_{\mathrm{TOT}} - p_z} \right) \tag{4.2}$$

where E_{TOT} is the particle total energy, and p_z is the longitudinal or z-component of the momentum—along the direction of the beam line and magnetic field. The analysis identified particles by the ionization energy loss of each track in the active gas volume, or dE/dx. The energy loss of each track as it traverses the TPC (dE/dx) is plotted as a function of the track momentum in Fig. 4.15. The colored lines are the Bichsel functions for a given particle species as indicated in the legend. It is clear from the dE/dx distributions that particle identification, PID, is relatively clean and possible in the fixed-target configuration using the TPC.

The $n\sigma$ variable is defined as the distance between the dE/dx of a track and the Bichsel curve of the particle of interest in units of σ,

$$n\sigma_X = \frac{\log(dE/dx) - \log(B_X)}{\sigma_X} \tag{4.3}$$

where X is the particle of interest, B_X the expected mean value from the Bichsel parame-

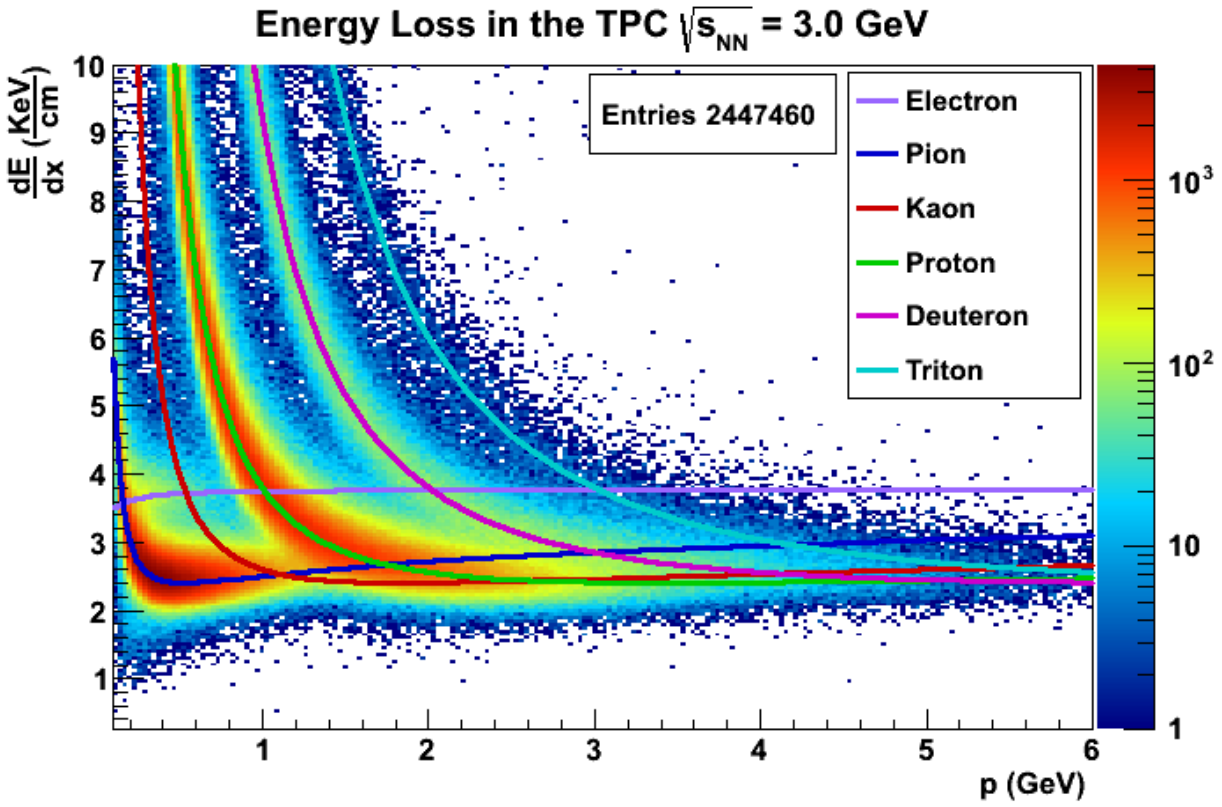

Figure 4.15: The energy loss of each track as it traverses the TPC, dE/dx, is plotted as a function of the track momentum. The colored lines are the Bichsel functions for a given particle species as indicated in the legend. It is clear from the dE/dx distributions that PID is possible in the fixed-target configuration using the TPC.

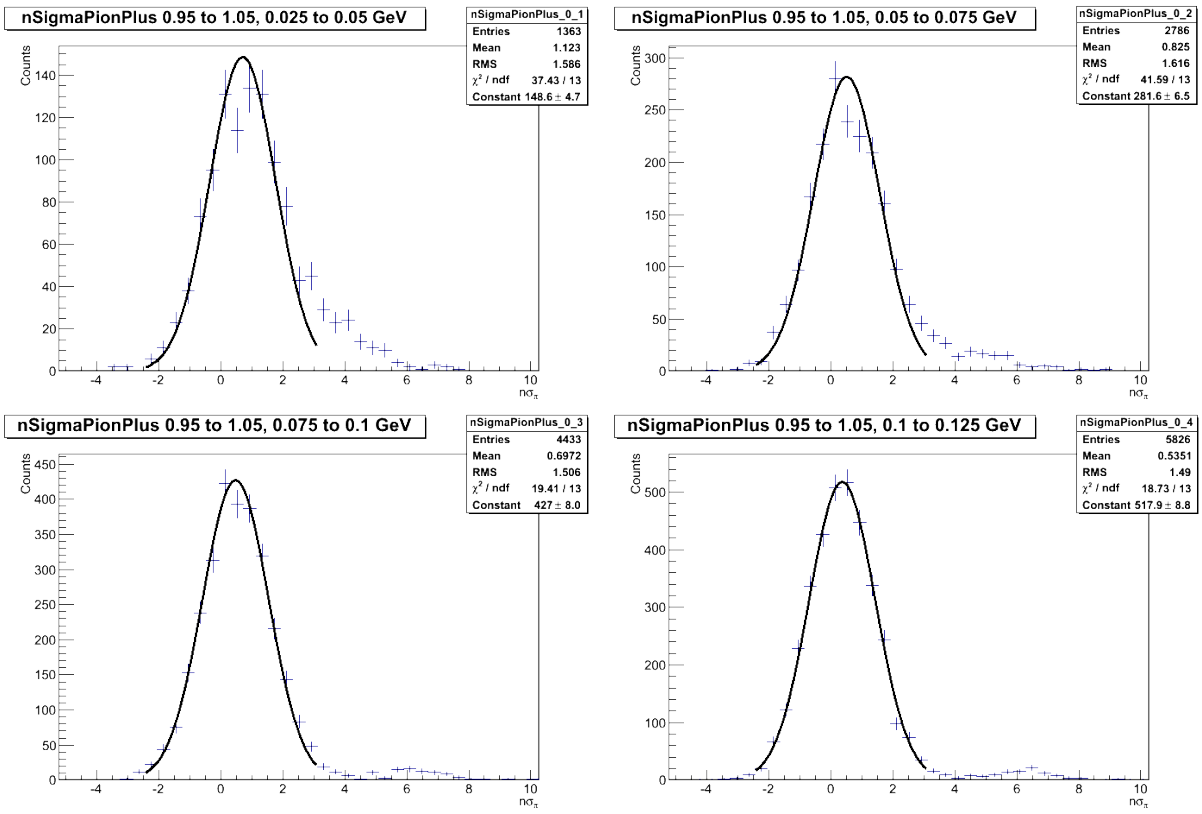

Figure 4.16: Positive pion fits for Au+Al $\sqrt{s_{NN}} = 3.0$ GeV. These are organized in 25 MeV bins in $m_T - m_0$ in a rapidity window of 0.1 units from $0.95 < y < 1.05$. The Gaussian fits, drawn in black, are in $n\sigma_\pi$ and are of the $m_T - m_0 = 0$ to 0.125 GeV/c^2 range. The track data are the blue crosses.

terization, and σ_X the dE/dx resolution of the TPC which is a function of the track length. The mean of the $n\sigma$ distribution is zero for the particle of interest. Because energy loss in the TPC is a random process, we expect to see Gaussian distributions for each particle species in $n\sigma$ space.

The tracks are divided into 25 MeV transverse mass bins and their $n\sigma$ values are histogrammed. Only tracks within ± 0.05 units of rapidity from mid-rapidity are considered. The histograms are then fit with a single Gaussian,

$$N = N_0 \exp\left[-\frac{1}{2}\left(\frac{f(dE/dx) - \mu)}{\sigma}\right)\right] \tag{4.4}$$

where N is the yield, N_0 the amplitude, μ the centroid, and σ the width. The mean, width,

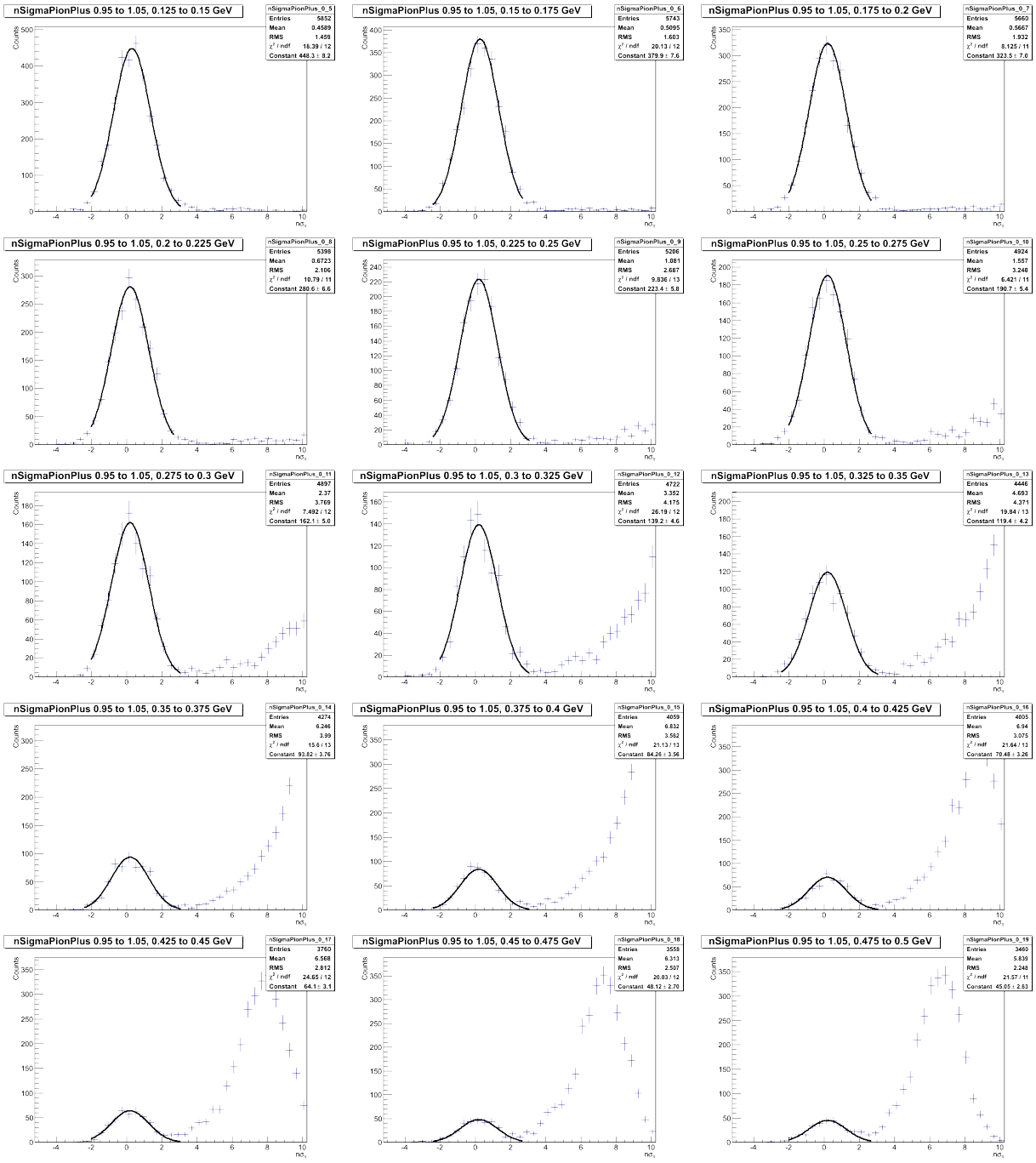

Figure 4.17: Positive pion fits for Au+Al $\sqrt{s_{NN}} = 3.0$ GeV. These are organized in 25 MeV bins in $m_T - m_0$ in a rapidity window of 0.1 units from $0.95 < y < 1.05$. The Gaussian fits, drawn in black, are in $n\sigma_\pi$ and are of the $m_T - m_0 = 0.125$ to 0.500 GeV/c^2 range. The track data are the blue crosses.

and fit range are fixed so that the amplitude (labeled as constant in the figures) is the only permitted floating parameter. The mean, width, and fit range are fixed to values which

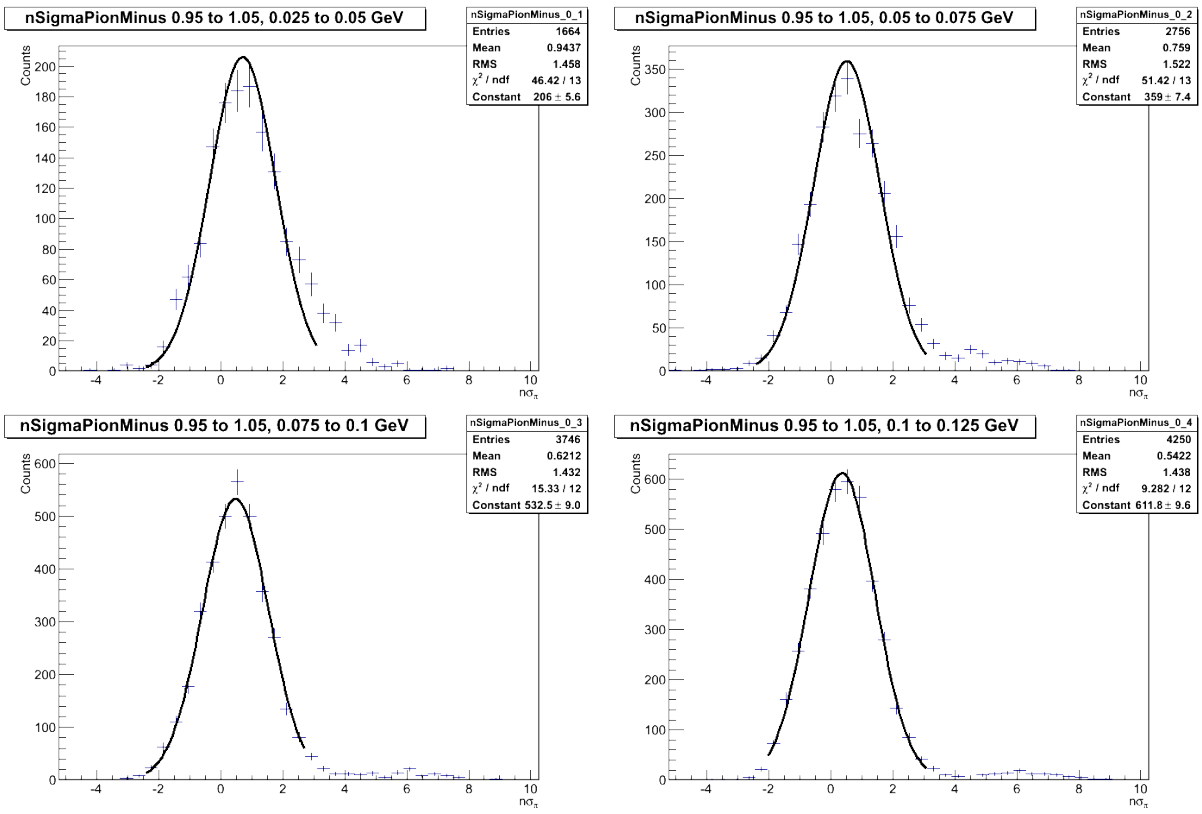

Figure 4.18: Negative pion fits for Au+Al $\sqrt{s_{NN}} = 3.0$ GeV. These are organized in 25 MeV bins in $m_T - m_0$ in a rapidity window of 0.1 units from $0.95 < y < 1.05$. The Gaussian fits, drawn in black, are in $n\sigma_\pi$ and are of the $m_T - m_0 = 0$ to 0.125 GeV/c^2 range. The track data are the blue crosses.

result in the best χ^2/ndf value. The Gaussians are then integrated to find the raw yields of the particles of interest.

Positive and negative pion fits for Au+Al $\sqrt{s_{NN}} = 3.0$ GeV are illustrated in Figures 4.16, 4.17, 4.18, and 4.19. These are organized in 25 MeV bins in $m_T - m_0$ in a rapidity window of 0.1 units from $0.95 < y < 1.05$. The Gaussian fits are in $n\sigma_\pi$, drawn in black, and are in the range $m_T - m_0 = 0$ to 0.500 GeV/c^2. The track data are the blue crosses.

4.3.4 Corrections, Systematics and Errors

For fixed-target collisions, the normal correction methods utilized by STAR end users had to be modified to take into account the differing geometry and symmetries in the events of interest. Normally, an analysis would request for embedding. Embedding is the pro-

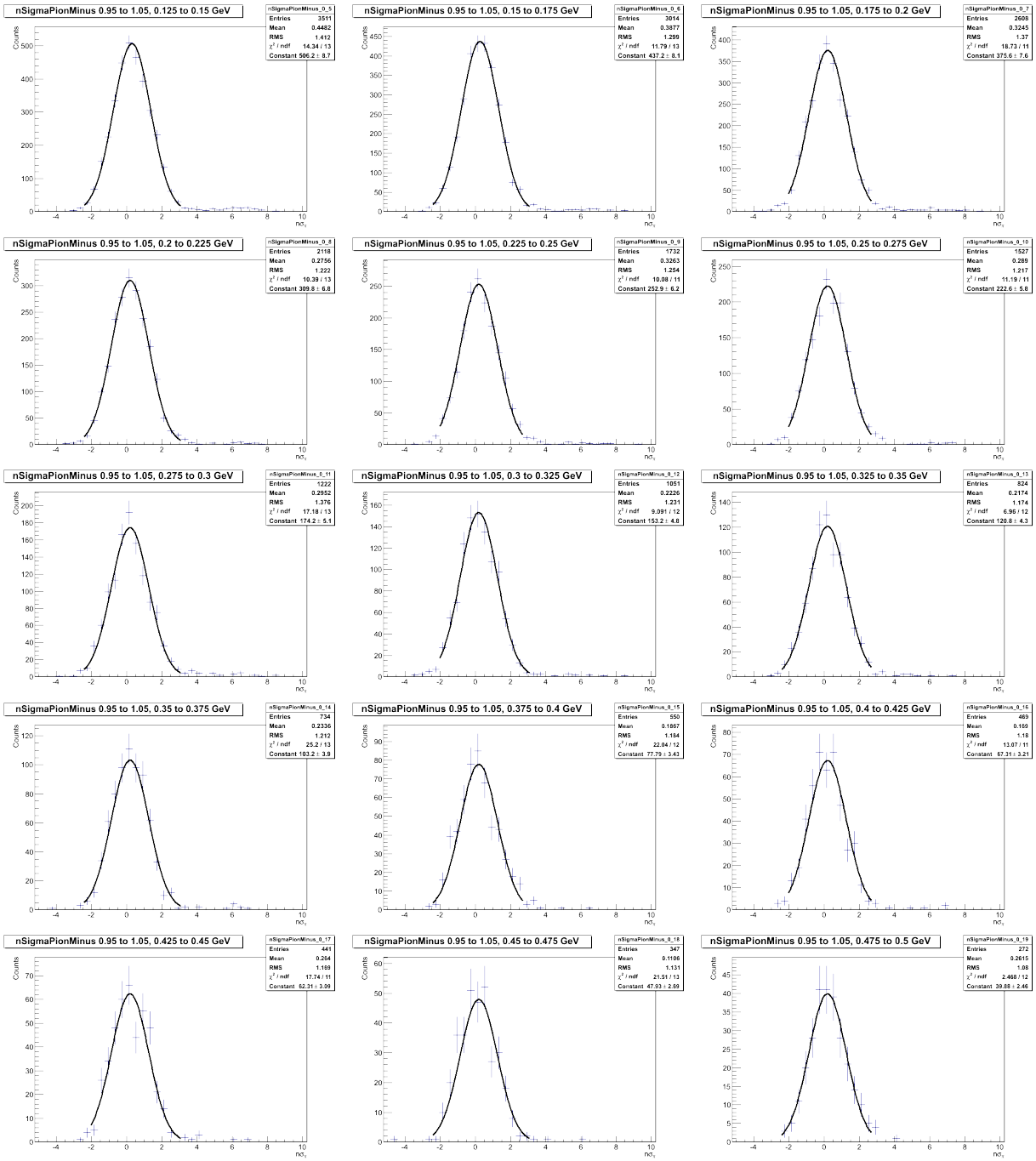

Figure 4.19: Negative pion fits for Au+Al $\sqrt{s_{NN}} = 3.0$ GeV. These are organized in 25 MeV bins in $m_T - m_0$ in a rapidity window of 0.1 units from $0.95 < y < 1.05$. The Gaussian fits, drawn in black, are in $n\sigma_\pi$ and are of the $m_T - m_0 = 0.125$ to 0.500 GeV/c^2 range. The track data are the blue crosses.

cess of creating simulated Monte Carlo tracks of a given momentum range, species set and rapidity/pseudo-rapidity range, inserting these tracks into real raw data events, and simulat-

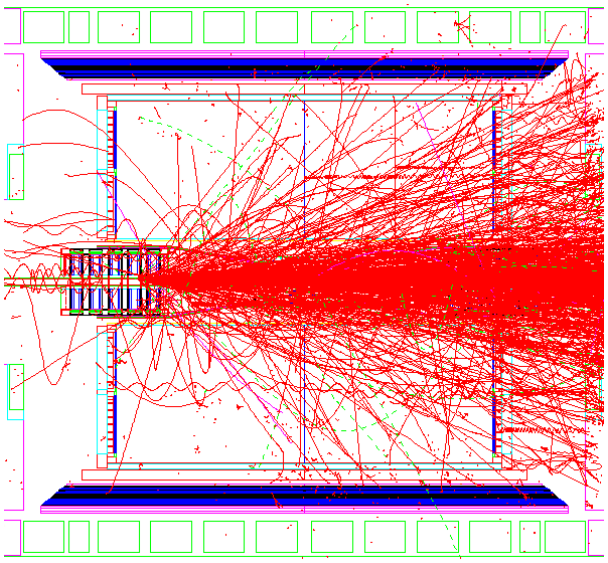

Figure 4.20: An example of a completely simulated (UrQMD) Au+Al event processed through STARSim, offline software that uses GEANT to simulate a detector response.

ing response of the subsystems utilizing the GEANT model of the STAR detector, STARSim. Embedding allows the end user to calculate efficiencies of particle detection and account for detector acceptance, the two major correction factors for any particle spectra. With the special circumstances of fixed-target interactions and the small number of overall tracks in the TPC from these interactions, fully simulated events from UrQMD [160] are in the process of running through STARSim. An example of a completely simulated (UrQMD) Au+Al event processed through STARSim is illustrated in Fig. 4.20. The key with embedding is to determine if a simulated particle is the reconstructed with the correct values of all its track information: momentum, rapidity, energy, mass, etc. When the track is detected, the spectra can be corrected for detector acceptance. If the track values are correct, then the spectra can be corrected for efficiency. Since all efficiency studies for fixed-target are underway, the remaining analysis will not be efficiency corrected.

Additionally, despite our best efforts, a conclusive determination of the projectile species cannot be made. All physics results indicate a Au or very nearly Au-like projectile but without calculations that demonstrate a relatively large and finite probability of a beam-

halo Au nucleus straying from the beam line and colliding with the beam pipe material, evidence that the projectile is Au is incomplete.

4.4 Beam–Beam Collisions

Beam-beam collisions are the traditional collision type measured at STAR. As part of the Beam Energy Scan (BES) program at RHIC, the $\sqrt{s_{NN}} = 19.6$ GeV Au+Au collision system ran during 2011, completing the first set of collision energies in the program. This is the type of collision that STAR was designed to record: symmetric particle production with full azimuthal angle coverage in the TPC and TOF (see Sections 3.2 and 3.3 for more details). The only specialty in this collision system (compared to $\sqrt{s_{NN}} = 200$ GeV Au+Au) is that the beams are not accelerated in the RHIC rings, but rather 'stored' until brought into collision.

4.4.1 Trigger Requirements

The trigger at STAR is divided into three aptly named levels: level 0 (L0), level 1 (L1), and level 3 (L3). The L0 system receives digitized data from the fast "trigger" detectors (like the BEMC or TOF) for every bunch crossing (every ∼107 ns) to indicate if the event at the very basic level (i.e. multiplicity) is interesting. The subsequent levels perform some amount of data processing to determine just how interesting an event is up to L1 when the TPC is finally read out. The L3 pool performs fast tracking and event reconstruction with a dedicated CPU farm which allows the online display to draw events during run time for quality assurance and detector performance.

The trigger supplies a unique identification number, or token, consisting of 12 bits attached to detector information to the DAQ buffer system while the logic determines if an event is interesting. The token is, and must be, unique since any combination of detectors may be live at any given time and cause detector read-out for a given bunch crossing. Thus

z-Vertex Position	x-y-Vertex Position	Trigger ID Number	DCA Radial	DCA Longitudinal
$\|V_z\| < 30.0$ cm	$\|V_r\| < 2.0$ cm	340001, 340011, 340021	$\|\mathrm{DCA_R}\| < 2.0$ cm	$\|\mathrm{DCA_L}\| < 2.0$ cm
Rapidity Window	Total Hit Number	Track Momentum	Track Flag	Fit Points Fraction
$\|y\| < 0.05$	$\mathrm{N_{Hits}} > 25$	$p > 0.1$ GeV	$0 <$ Flag < 1000	Fit/Possible > 0.52

Table 4.3: A summary of the analysis event (first three cells of the top row) and track (last two cells of the top row and all cells of the bottom row) cuts for the beam-beam collision data.

all data from each detector per event is associated with the unique 12 bit token until all the data is recorded for that event, at which time the token is recycled and able to be used again [161].

The trigger requirements for this analysis were those of the minimum-bias selection. Traditionally, minimum-bias in higher energy Au+Au collisions means a coincidence between the east and west BBC detectors as well as a requirement for the pVPD vertex position measurement. However, this particular minimum bias requirement, for the BES program as a whole, differed from traditional minimum bias in that the logic required to record an event was an 'OR' between the ZDC coincidence, pVPD coincidence, and BBC coincidence. This title trigger attempts to include as little bias as possible into the dataset while still recording data. The logic labels a minimum-bias event as interesting by determining that a collision did occur.

4.4.2 Event and Track Selection

Standard STAR event selection criteria for this analysis were used. The trigger detectors are optimized to preferentially select events which occur closest to the center of the detector. Thus most of the event cuts used are to ensure uniform coverage in the forward and backward

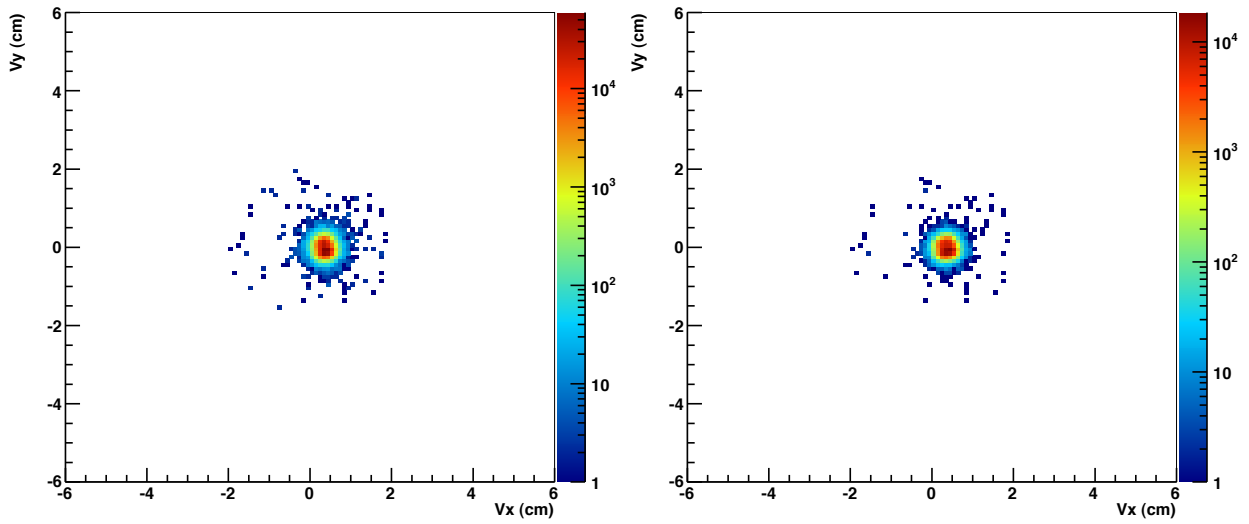

Figure 4.21: On the left-hand side is the x-y-vertex position before all event geometric cuts are applied. On the right-hand side is the x-y-vertex position after all event geometric cuts are applied. These cuts select the shape of the beam spot and illustrate the beam profile very well.

directions and to be symmetric around midrapidity, $y = 0$. The number of cuts to select on good events and then, within that event, to select high-quality tracks are many. A summary of the basic event and track cuts is given in Table 4.3.

Since the data set, unlike the fixed-target set, had a specified trigger defining 'minimum-bias' events, the trigger identification numbers (explicitly stated in the top row's third column) were utilized to select events that came from the minimum-bias set. To ensure uniform coverage with the TPC and TOF detectors (as well as the BEMC and others not used in this analysis), a vertex position cut in the longitudinal direction of $|V_z| < 30.0$ cm was used. Additionally, to exclude many beam+gas or beam+beampipe collisions, a radial vertex cut of $|V_r| < 2.0$ cm is also enforced. Because the beam profile for the 19.6 GeV data set is slightly larger, the nominal radial cut of $|V_r| < 1.5$ cm was too strict and removed good Au+Au events from the data set (see Section 4.2 for more details). These cuts all apply to the event on the whole. The remaining cuts in the Table refer to individual tracks in an event and are further discussed below.

The distance of closest approach (DCA), detailed in Section 4.2, was further restricted

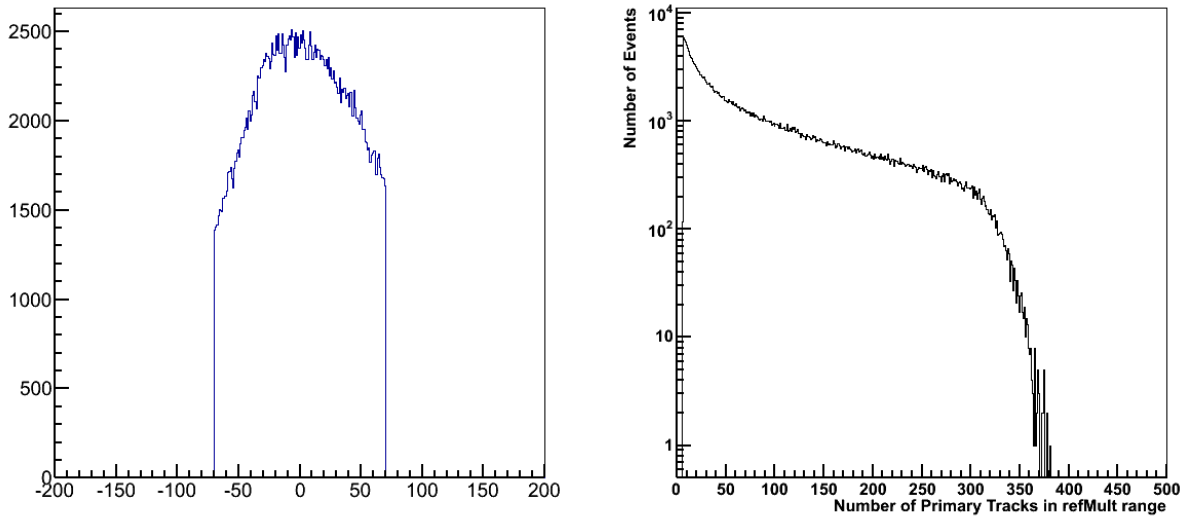

Figure 4.22: On the left-hand panel is the z-vertex position after all event geometric cuts are applied. On the right-hand panel is the reference multiplicty distribution: the number of events given the number of particles with $|\eta| < 0.5$.

from the nominal value used in the vertexer algorithm. The purpose of the vertexer method of associating a track with a larger DCA window ensured that tracks were associated with the proper vertex, whether that vertex is in the beam-line or on the beampipe. To ensure that an individual track is a good track, it should closely approach the vertex position both radially, $\mathrm{DCA_R} < 2.0$ cm, as well as longitudinally, $\mathrm{DCA_L} < 2.0$ cm.

A feature of the strength of the magnetic field when the data were taken means that any track with a momentum below a certain value will not travel into the TPC detector. Additionally, it would be near impossible to tell if the track could be firmly associated with the vertex of the collision of interest. Therefore, a cut on the momentum of $p > 0.1$ GeV is made to ensure the track travels into the TPC.

The geometry of a track in the TPC allows for a different number of TPC pad row hits to be available per track. The maximum number of hits possible for a given track is 45. To ensure that a track was not accidentally split in its reconstruction, a ratio of the number of pad row hits that were used to fit the track's trajectory (as well as calculate its momentum) compared to the possible number of hits the track could have had if that track

cleanly traversed the available length of the TPC was formed. Tracks with ratios with less than 50% were cut out to exclude split tracks. Meaning, included tracks all have a ratio Fit/Possible > 0.52.

Additionally, long tracks are better for such an analysis since the calculation of the momentum is more precise. The number of hits that are associated with a track correlates to how long the track is in the TPC. A cut on the number of hits, NHits > 25, was made to ensure long tracks in the analysis. Long tracks typically also coincide with a good track flag, or coded number, indicating the likelihood that a track was recorded at the proper time (indicating if it is a pile-up track, or an in-time track) along with which detectors have data on that track and the quality of the fit. Any negative track flag indicates that the fit of that track was bad in some way (too many fit iterations, not enough points to fit or outlier removal eliminated too many points, for example). A track with a flag number in the 1000's indicated that the track is a pile-up track, out-of-time. So, a track flag cut of $0 <$ Flag < 1000 is included to select well-fit, in-time tracks. Finally, a cut on the rapidity is made to analyze midrapidity tracks since this is a midrapidity analysis.

4.4.3 Fitting Methods

Event information and track information for events satisfying the cuts detailed in Table 4.3 are collected from the full dataset. It is important to note that more stringent track requirements are made for the beam–beam collision analysis than the fixed-target analysis. With more energy, a copious number of particles for each species is produced and tracks of good quality can be selected without the risk of increasing statistical error. Additionally, a larger number of events of this particular type are recorded supporting more stringent requirements on track quality.

In the same process as fixed-target, the transverse momentum, p_T, is calculated from the curvature of a particle track inside the solenoidal magnetic field, B, knowing that it is perpendicular to the magnetic field, $p_T \perp B_z$, and assuming the magnitude of its charge

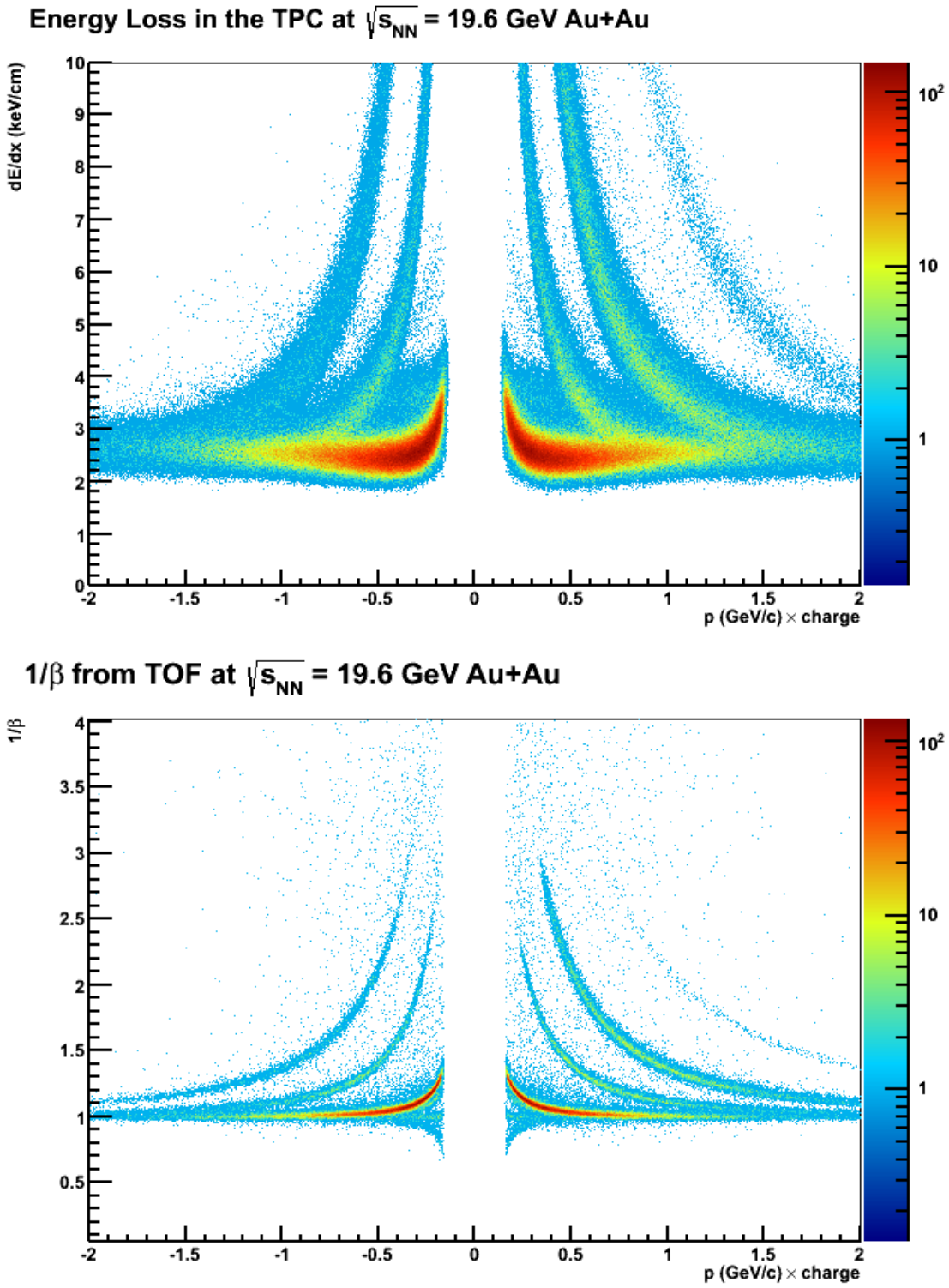

Figure 4.23: The energy loss of each track as it traverses the TPC (dE/dx) is plotted in the top panel as a function of the rigidity: track momentum × charge. $1/\beta$ as measured with the TOF is plotted as a function of the rigidity in the bottom panel.

is the same as the electron, $e = 1.602 \times 10^{-19}$ C, or 1 in the detector system units. To extract the particle yield in a particular region of transverse mass, $m_T - m_0$, and rapidity, y, both of which have a mass dependence, a mass assumption, m_0, is made for every track and used with p_T to obtain $m_T - m_0$ and y. Recall Equations 4.1 and 4.2 for transverse mass and rapidity. Since the particles of interest are pions, kaons, protons and antiprotons, their respective masses are used in each of the equations for their respective particle yield extractions.

For a given m_0, only the yield of the particle with that mass is extracted. First, the range in $m_T - m_0$ between 0 and 1.0 GeV/c^2 is divided evenly into 40 bins, resulting in bins of size $\Delta(m_T - m_0) = 0.025$ GeV/c^2. Next, the rapidity range between $|y| < 0.05$, or 0.1 units around midrapidity, $y_{\rm cm} = 0$ is selected. The analysis identified particles by the energy loss of each track in the active gas volume, or dE/dx, as well as by the $1/\beta$ measurement from the TOF. The energy loss of each track as it traverses the TPC (dE/dx) is plotted as a function of the track rigidity (momentum $\times$ charge) in the top panel of Fig. 4.23. In the bottom panel of Fig. 4.23, $1/\beta$ is plotted as a function of rigidity. Clear particle separation can be seen in the TPC for low momentum: pions can be cleanly identified up to ~0.8 GeV/c, kaons can be identified to about ~0.7 GeV/c and protons can be identified up to ~1.0 GeV/c. When particle species begin to overlap in dE/dx, the TOF continues to have clear particle separation. The combination of the information from the two detectors allows for an extensive momentum range to be analyzed.

Each bin in centrality, particle species, rapidity window and $m_T - m_0$ is then fit with a quadruple-Gaussian,

$$N = A_1 \exp\left[-\frac{1}{2}\Big(\frac{f_1(dE/dx) - \mu_1)}{\sigma}\Big)\right] + A_2 \exp\left[-\frac{1}{2}\Big(\frac{f_2(dE/dx) - \mu_2)}{\sigma}\Big)\right] + A_3 \exp\left[-\frac{1}{2}\Big(\frac{f_3(dE/dx) - \mu_3)}{\sigma}\Big)\right] + A_4 \exp\left[-\frac{1}{2}\Big(\frac{f_4(dE/dx) - \mu_4)}{\sigma}\Big)\right] \quad (4.5)$$

where the mean μ_n comes from the Bichsel parameterization [146] of energy loss in the TPC

with modifications due to detector calibration, and the width σ_n is related to the resolution of the TPC and is a function of track length. Means, widths, and fit ranges are fixed when fitting and only the amplitudes are permitted to float. The Gaussian corresponding to the particle of interest in the particular bin is then integrated to find the raw yield of the particle. As there are significantly more particle species and centrality bins in this analysis, all fits are shown in Appendix A.

Electrons present the most common contamination as their particle band in dE/dx passes under each particle species. When the electrons are completely engulfed by a particular particle, the electron amplitudes are estimated and fixed by a fit function to the regions where the electrons are clearly separated from the other particle distributions. This happens most notably with fitting the kaons. The kaon band obscures the electron band from 0.175 GeV/c to 0.65 GeV/c; this region has fixed electron amplitudes in the fit. The mean, width, and fit range are fixed to values which result in the best χ^2/ndf value.

4.4.4 Corrections, Systematics, and Errors

Recall from Sec. 4.3 that the two important correction factors that need to be implemented are for detector acceptance and efficiency; these factors are calculated via the embedding process where simulated Monte Carlo tracks of a given momentum range, species set, and rapidity/pseudorapidity range are embedded into real raw-data events and STARSim simulates the detector response. The key with embedding is to determine if a simulated particle is reconstructed with the correct values of all its track information: momentum, rapidity, energy, mass, etc. A match between the distributions of reconstructed, embedded tracks and real data tracks for quantities reflecting track quality, and used in track selection, allows for an accurate calculation of the overall efficiency and acceptance.

The ratio of the distribution of reconstructed and simulated Monte Carlo tracks as a function of $m_T - m_0$ gives the acceptance $\times$ efficiency correction factor for the rapidity window studied. Specific values for the acceptance $\times$ efficiency correction factors for the 5%

most central collisions for $\pi^{\pm}$, $K^{\pm}$, p, and $\bar{p}$ are illustrated in Figures 4.24, 4.25, and 4.26, respectively.

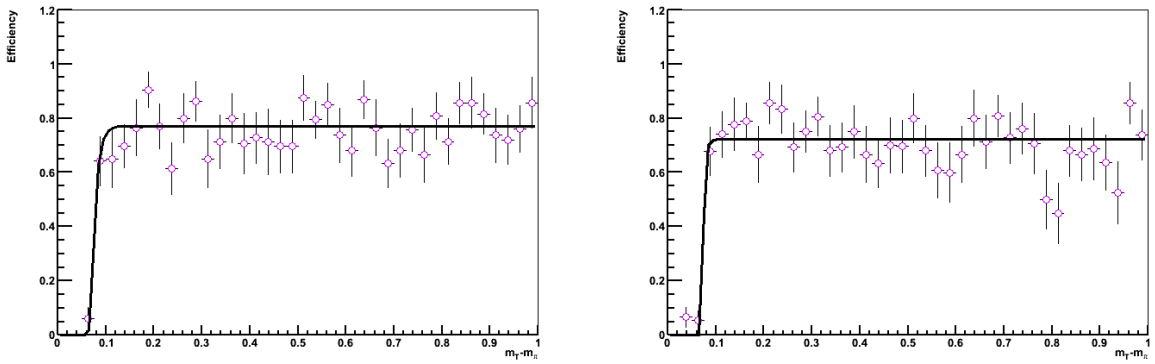

Figure 4.24: Efficiency for $\pi^{\pm}$ in Au+Au $\sqrt{s_{NN}} = 19.6$ GeV as measured by a GEANT simulation of particle tracks through the STAR detector compared to the original Monte Carlo generated tracks.

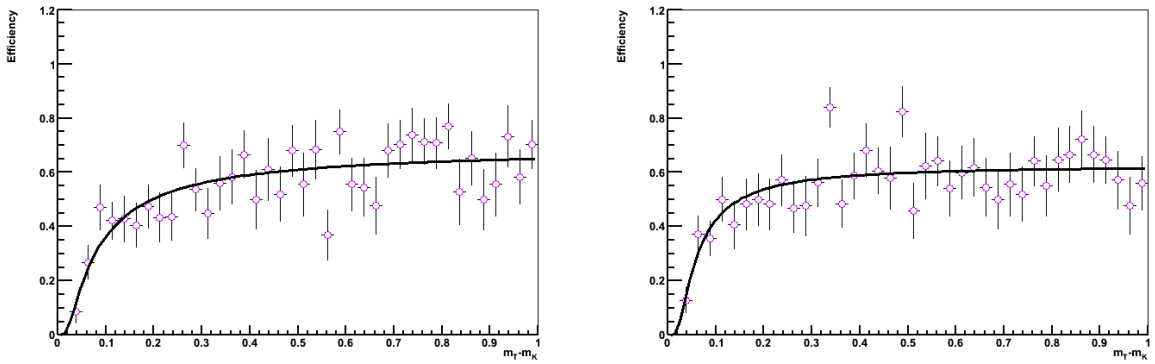

Figure 4.25: Efficiency for $K^{\pm}$ in Au+Au $\sqrt{s_{NN}} = 19.6$ GeV as measured by a GEANT simulation of particle tracks through the STAR detector compared to the original Monte Carlo generated tracks.

Each of these histograms is fit with an exponential of the form,

$$\text{Efficiency} = Ae^{(-B/(m_T - m_0))^C} \tag{4.6}$$

where the fit parameters do not have particular physical meaning but allow for a good parameterization. The efficiency depends on the particle mass and transverse momentum as well as the event centrality. Particles with shorter lifetimes will be harder to detect. Particles

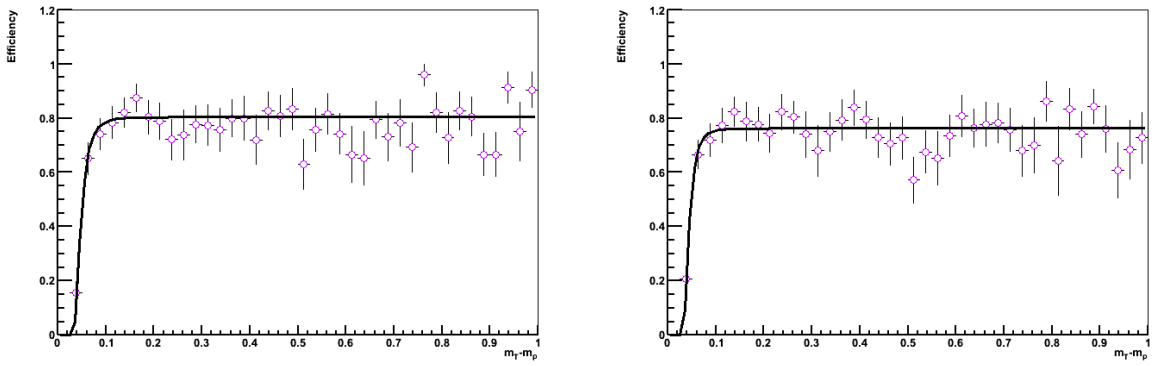

Figure 4.26: Efficiency for p on the left and $\bar{p}$ on the right in Au+Au $\sqrt{s_{NN}}$ = 19.6 GeV as measured by a GEANT simulation of particle tracks through the STAR detector compared to the original Monte Carlo generated tracks.

produced in more central collisions are in an environment of densely packed tracks, lowering the tracking efficiency. The efficiency drops sharply below $m_T - m_0 \approx 0.3$ GeV/c due to the tight curl of low-momentum particles in the magnetic field, greatly influencing the TPC acceptance.

The efficiency also depends on the analysis cuts applied. For example, reducing the number of fit points required for a track to be included in the analysis would increase the efficiency. The embedding study was done for all six particle species ($\pi^{\pm}$, $K^{\pm}$, p, and $\bar{p}$) and the function extracted from the fit utilized to correct the spectra. Overall, the systematic error for the efficiency is estimated to be 8%.

As particles traverse the detector material they will lose energy, and a correction is made for Coulomb scattering and energy loss at reconstruction assuming all particles are pions. However, not all produced particles are pions and further corrections must be made for the heavier particles ($K^{\pm}$, p, and $\bar{p}$). The momentum bins in $m_T - m_0$ must be shifted by subtracting the shift correction value from the bin center value. These shift corrections come from the embedding process, described at the beginning of this section, where the difference in $m_T - m_0$ between a reconstructed track and its corresponding simulated track is plotted as a function of $m_T - m_0$ of the simulated (embedded) track. Fig. 4.27 illustrates the energy loss as function of p_T for kaons and protons respectively. The distribution is fit with the

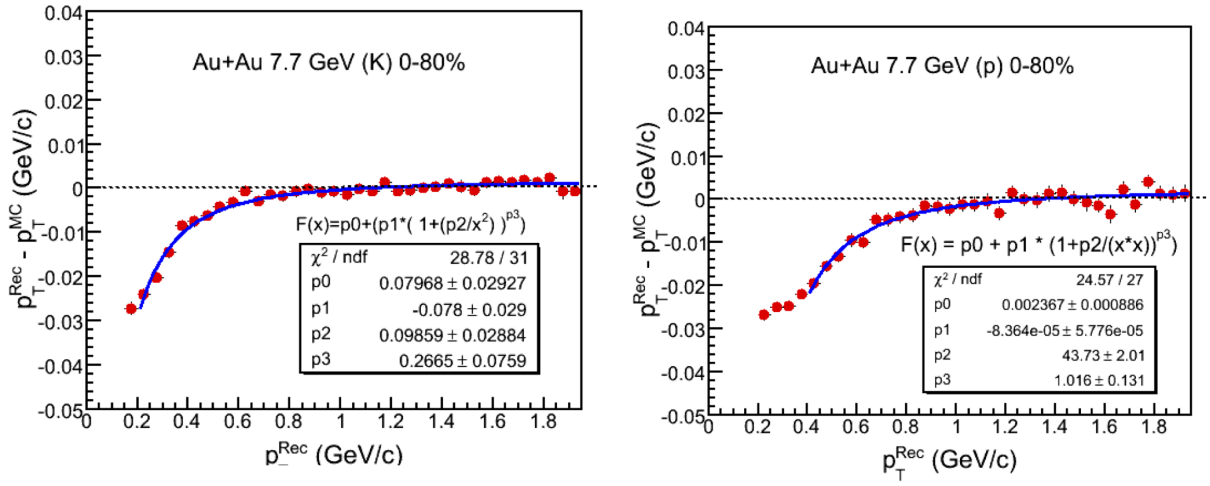

Figure 4.27: The difference between the reconstructed momentum and simulated momentum plotted as a function of the simulated momentum. The function is a parameterization of the difference and the value is utilized for the energy loss correction of kaons (on the left) and protons (on the right).

functional form,

$$f(p_T) = A + B\big(1 + \frac{C}{p_T^2}\big)^D \quad , \tag{4.7}$$

shown in blue where A, B, C, and D are the fit parameters $p0$, $p1$, $p2$, and $p3$ in the figure legend, respectively. The energy loss also affects the bin width in $m_T - m_0$ and is a multiplicative correction with a stronger effect at lower momentum.

The track matching efficiency of the TOF software is determined by comparing the number of tracks found in the TPC with the number of matched hits in the TOF detector as a function of momentum $(m_T - m_0)$. Identified particle plots of these ratios are shown in Fig. 4.28. The tracks are identified through dE/dx in the TPC when the energy loss is within 1σ of the predicted Bichsel [146] parameterization. These represent a pure particle sample and each track is then tested for a match in the TOF detector. In the figure, black markers indicate positive particles while magenta markers indicate negative particles. This distribution is fit with the function,

$$\text{MatchingEfficiency} = Ae^{(-B/(m_T-m_0))^C} \tag{4.8}$$

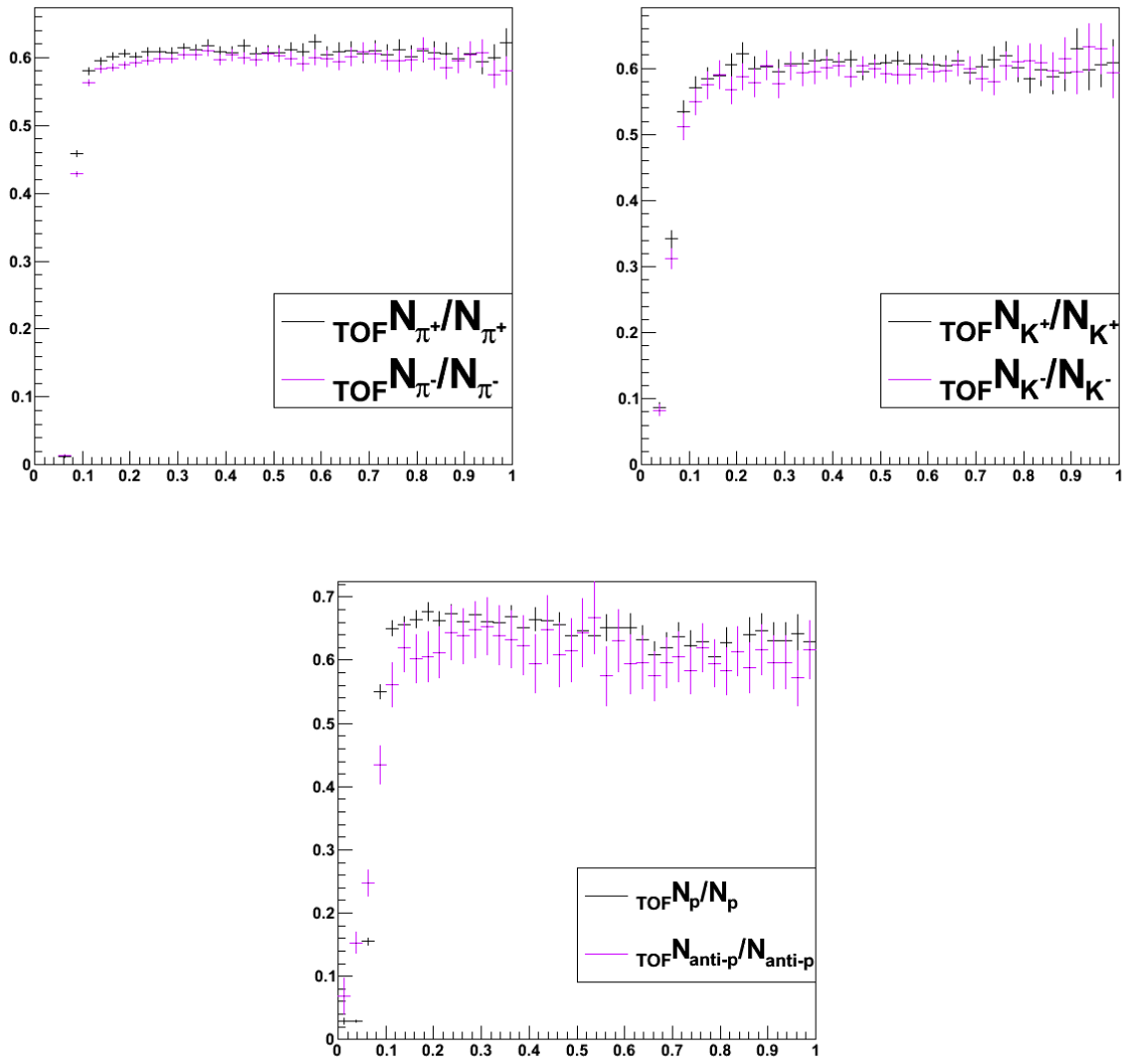

Figure 4.28: The track matching efficiency between the TPC and TOF detectors. Black markers indicate the positive particles, while magenta markers indicate negative particles.

where A, B, and C are fit parameters. Yields from the TOF detector are corrected by the function evaluated at the value of $m_T - m_0$.

Systematic uncertainties for the spectra are estimated in two ways. First, varying the analysis cuts found in Table 4.3 and then assessing the purity of the identified hadron samples in dE/dx measurements provides a rough estimate of the systematic error. Second, varying the values of Gaussian fit parameters and fit ranges gives the final estimate for the systematic uncertainty. Utilizing these techniques, the systematic error sources are summarized in

Hadron	V_Z	Track Cuts	Energy Loss Correction	Fit Parameters
π	3%	3.2%	5%	5%
K	3%	6.2%	5%	10%
p	3%	5.4%	5%	4%

Table 4.4: A summary of the systematic errors on produced particle yields for the beam-beam data.

Table 4.4.

Chapter 5

Results and Discussion

First, fixed target results are presented, followed by beam-beam results. All results shown include uncertainties discussed in Sec. 4.3 and Sec. 4.4, respectively. Comparisons to STAR data as well as world data are made in the respective results sections.

5.1 Fixed-Target Interactions

Utilizing the analysis methods of Chapter 4, $\pi^{\pm}$ and $p/\bar{p}$ spectra have been extracted and are presented along with Coulomb results and comparisons to previous experiments.

Pion spectra for the 10% most central events for three energies: Au-like+Al at $\sqrt{s_{NN}} =$ 3.0 GeV, $\sqrt{s_{NN}} = 3.5$ GeV and $\sqrt{s_{NN}} = 4.5$ GeV, are shown in Fig. 5.1. Plotted as a function of $m_T - m_\pi$, open stars represent π^- while solid stars represent π^+. In green symbols are $\pi^{\pm}$ from $\sqrt{s_{NN}} = 3.0$ GeV, in blue symbols are $\pi^{\pm}$ from $\sqrt{s_{NN}} = 3.5$ GeV, and in red symbols are $\pi^{\pm}$ from $\sqrt{s_{NN}} = 4.5$ GeV. The drop-off at low $m_T - m_\pi$ is due to the efficiency and acceptance of the STAR detector as a fixed target experiment. Further studies with GEANT may prove useful to correct these spectra and describe what portion of these low-momentum pions can actually be measured with the detector. The limited reach in momentum is due to the detector acceptance discussed in Sec. 4.3.1. The spectra from each energy is fit with a linear function to guide the eye rather than to imply physics.

Proton spectra are represented by solid stars, given as a function of $m_T - m_p$ for three energies: Au-like+Al at $\sqrt{s_{NN}} = 3.0$ GeV, $\sqrt{s_{NN}} = 3.5$ GeV and $\sqrt{s_{NN}} = 4.5$ GeV, in

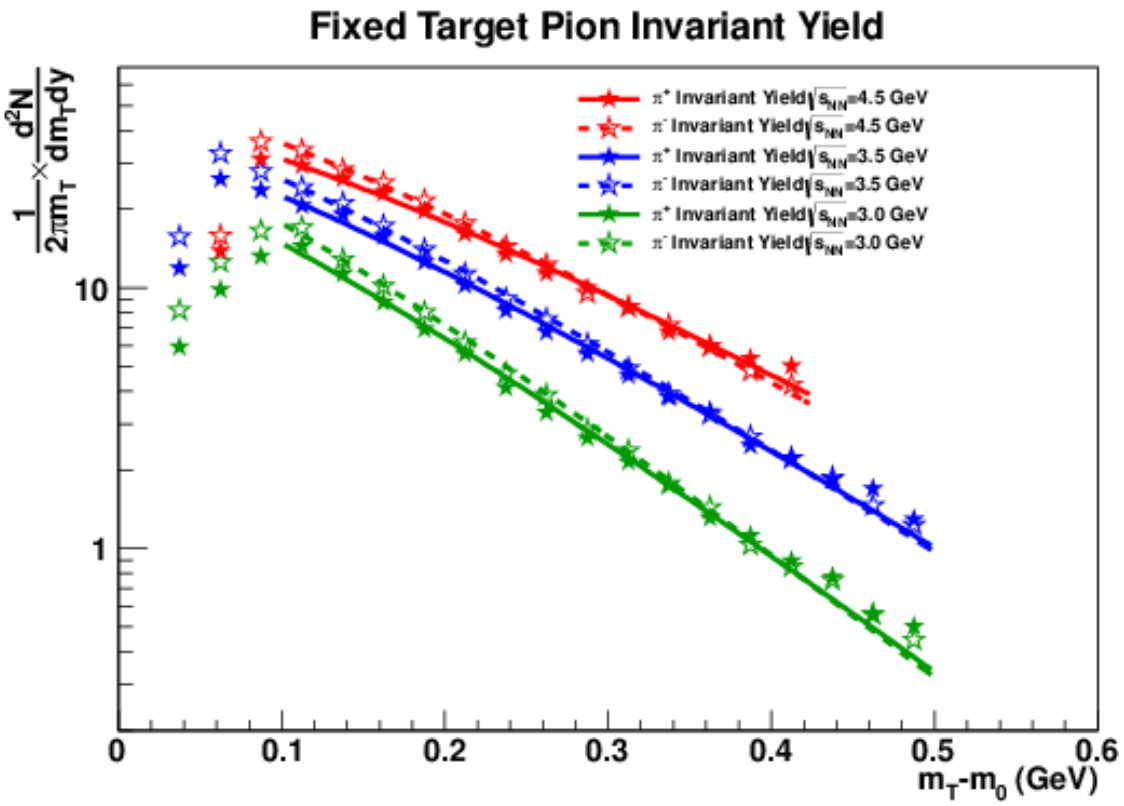

Figure 5.1: Pion spectra are plotted as a function of $m_T - m_\pi$. Open stars represent π^- while solid stars represent π^+. The fixed target energy of $\sqrt{s_{NN}} = 3.0$ GeV in green is compared with the fixed target Au-like+Al energies of $\sqrt{s_{NN}} = 3.5$ GeV in blue and $\sqrt{s_{NN}} = 4.5$ GeV in red.

Fig. 5.2. In green are p from $\sqrt{s_{NN}} = 3.0$ GeV, in blue are p from $\sqrt{s_{NN}} = 3.5$ GeV, and in red are p from $\sqrt{s_{NN}} = 4.5$ GeV. The drop-off at low $m_T - m_p$ is due to the efficiency and acceptance of the STAR detector as a fixed target experiment discussed in Sec. 4.3.1. Again, studies with GEANT may prove useful to correct these spectra at low momentum. Each of the spectra are fit with a linear function to guide the eye rather than to imply physics. At these energies, $\bar{p}$ production is limited if not energetically impossible.

Figure 5.3 shows the π^+/π^- ratios as a function of $m_T - m_\pi$ for three fixed-target data sets from STAR for Au-like+Al collisions at $\sqrt{s_{NN}} = 3.0$, 3.5, and 4.5 GeV all utilizing the top 10% of central events. These pion ratio data are fit with the Coulomb model described in Sec. 2.4.1 which assumes similar initial spectra that are then modified by the Coulomb potential after emission from the nuclear source. The energy $\sqrt{s_{NN}} = 3.0$ GeV in green

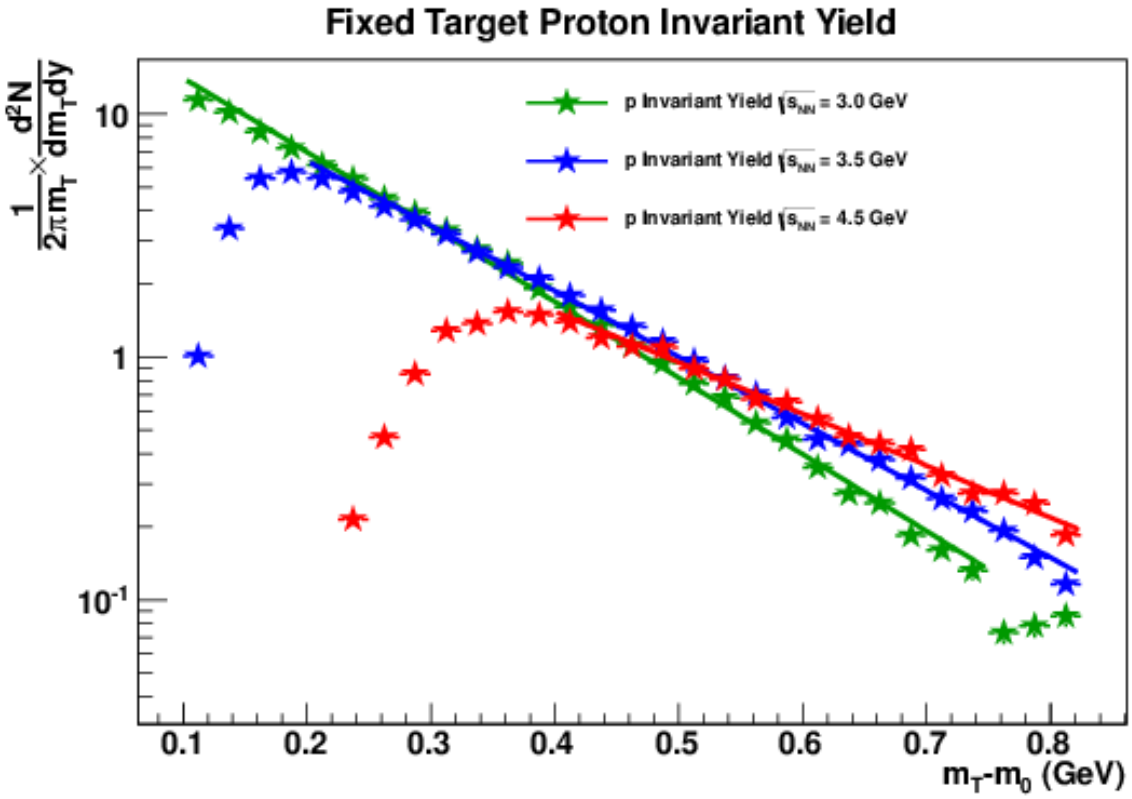

Figure 5.2: Proton spectra are plotted as a function of $m_T - m_p$. The fixed target energy of $\sqrt{s_{NN}} = 3.0$ GeV in green is compared with the fixed target Au-like+Al energies of $\sqrt{s_{NN}} = 3.5$ GeV in blue and $\sqrt{s_{NN}} = 4.5$ GeV in red.

is compared with the fixed target Au-like+Al energies of $\sqrt{s_{NN}} = 3.5$ GeV in blue and $\sqrt{s_{NN}} = 4.5$ GeV in red. Comparisons are also made to other experiments and a BES collision energy measured with STAR.

The Coulomb potential and $p(\bar{p})$ yield are shown in Fig. 5.4 in red with the right-hand red y-axis and $p(\bar{p})$ yield in magenta(cyan) utilizing the left-hand y-axis (respectively) as a function of center of mass energy. Comparisons to other world data and some BES collision energies measured with STAR also appear in the figure. Fixed-target data from the current measurement are in solid red stars. Displaying these two sets of data together highlights their similarity in shape with collision energy. This is not unexpected since the Coulomb potential is related to the net charge of the source and the bulk of that net charge is due to stopped protons.

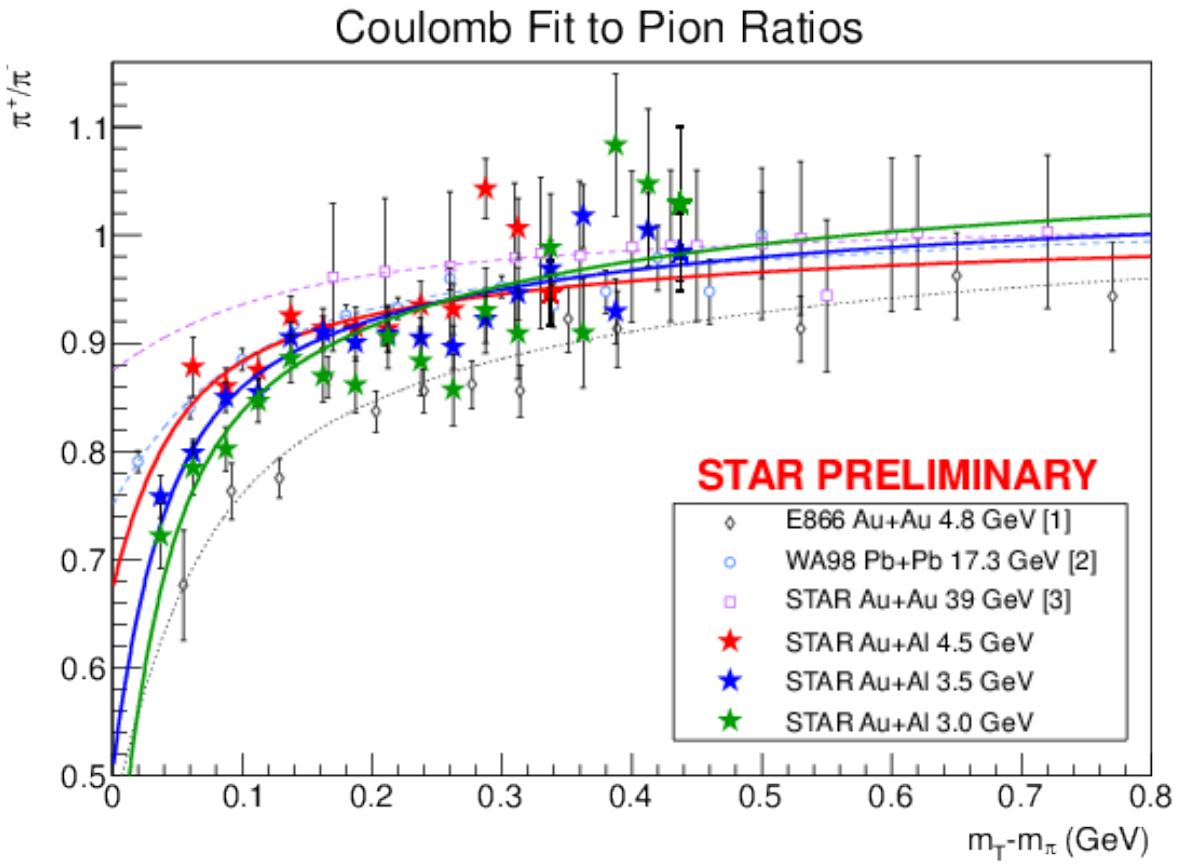

Figure 5.3: Pion ratios, π^+/π^-, are plotted as a function of $m_T - m_\pi$ and fit with the Coulomb Source Potential described in Chapter 2. The fixed target energy of $\sqrt{s_{NN}} = 3.0$ GeV in green is compared with the fixed target Au-like+Al energies of $\sqrt{s_{NN}} = 3.5$ GeV in blue and $\sqrt{s_{NN}} = 4.5$ GeV in red. Comparisons are also made to other world experiments and a collision energy from the BES measured with STAR.

Naively, one would expect that $V_C = Q/4\pi\epsilon_0 r$, where Q is the net charge of the source and r is the pion emission radius. The emission radius can be estimated to be 3.06 $\pm$ 0.47, 3.39 $\pm$ 0.23, and 3.06 $\pm$ 0.28 fm for the 4.5, 3.5, and 3.0 GeV systems respectively. By comparison, the radius of the overlap region is estimated to be 3.4 fm from the Glauber Monte Carlo for the 10% most central collisions. The fact that the estimated emission radius is similar in size to the overlap radius suggests that there is not much expansion, implying a short source lifetime.

Figure 5.5 shows the midrapidity charged pion dN/dy values scaled by the number of participants for the Au-like+Al data at the three energies studied. The yields are determined

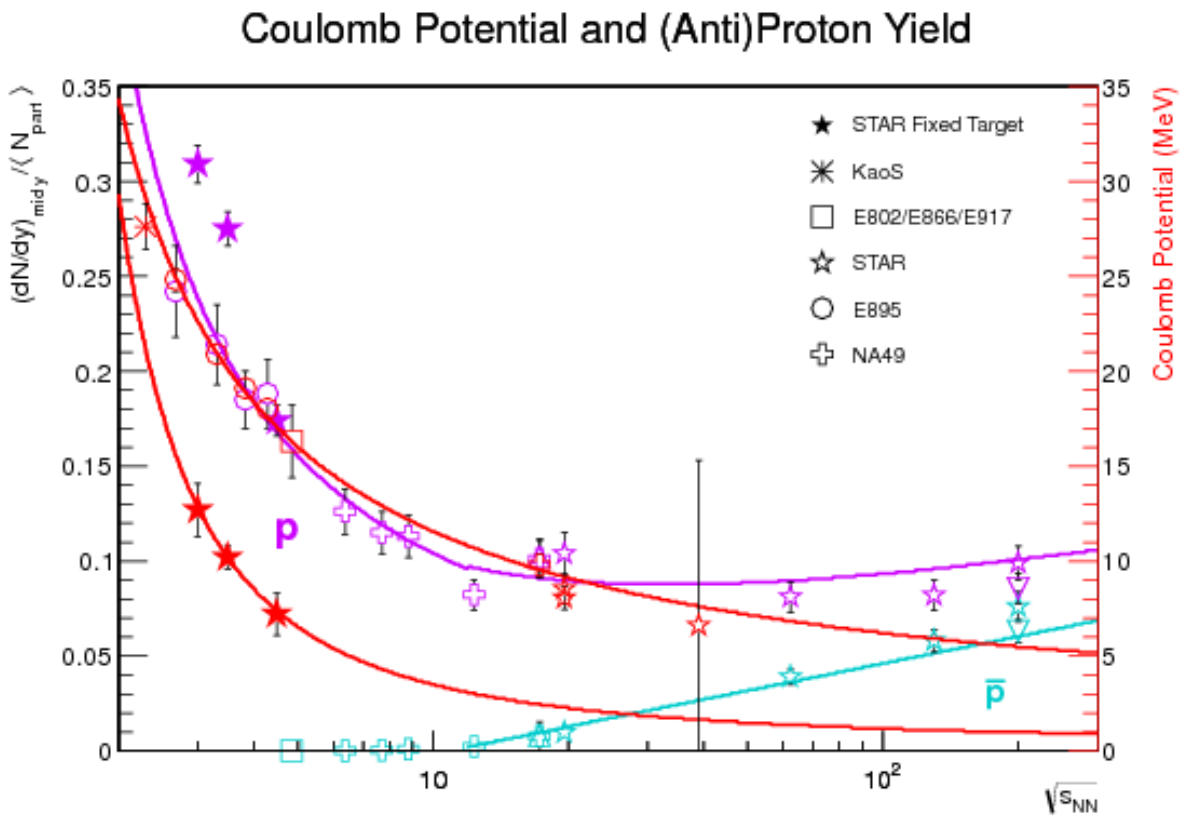

Figure 5.4: The Coulomb potential (V_C) in solid red stars with the right-hand red y-axis and midrapidity dN/dy (anti)proton yield in solid (cyan)magenta stars utilizing the left-hand y-axis are plotted as a function of center of mass energy. Comparisons are also made to other world experiments and some collision energies from the BES measured with STAR. Fixed target data are in solid stars. For comparison, scaled midrapidity proton yields (open magenta symbols) and Coulomb potentials (open red symbols) are also shown for Au+Au collisions at 1.0 AGeV (KaoS [162]), at 2, 4, 6, and 8 AGeV (E895 [163,164]), and at 2, 4, 6, 8, and 10.8 AGeV (E866 [122,165]). Yields and potentials also are shown for central Pb+Pb collisions at 20, 30, 40, 60, 80, and 158 AGeV (NA44 [166,167], and NA49 [9,168]). Additional data from Refs. [30,123,169–174] are also included. The proton yields are fit with a falling exponential function to guide the eye.

by integrating the Bose-Einstein fit functions for all $m_T - m_0$. The average number of participants comes from a Monte Carlo Glauber model estimated for the top 10% centrality for Au-like+Al. This method yields an estimate of 88 participating nucleons for each of the three energies. By comparison, the midrapidity scaled dN/dy values are also shown for central Au+Au and Pb+Pb data from several other experiments across a broad range of collisions energies. For these comparison data, the estimated number of participants is determined using either the values stated by the collaborations or from Glauber model

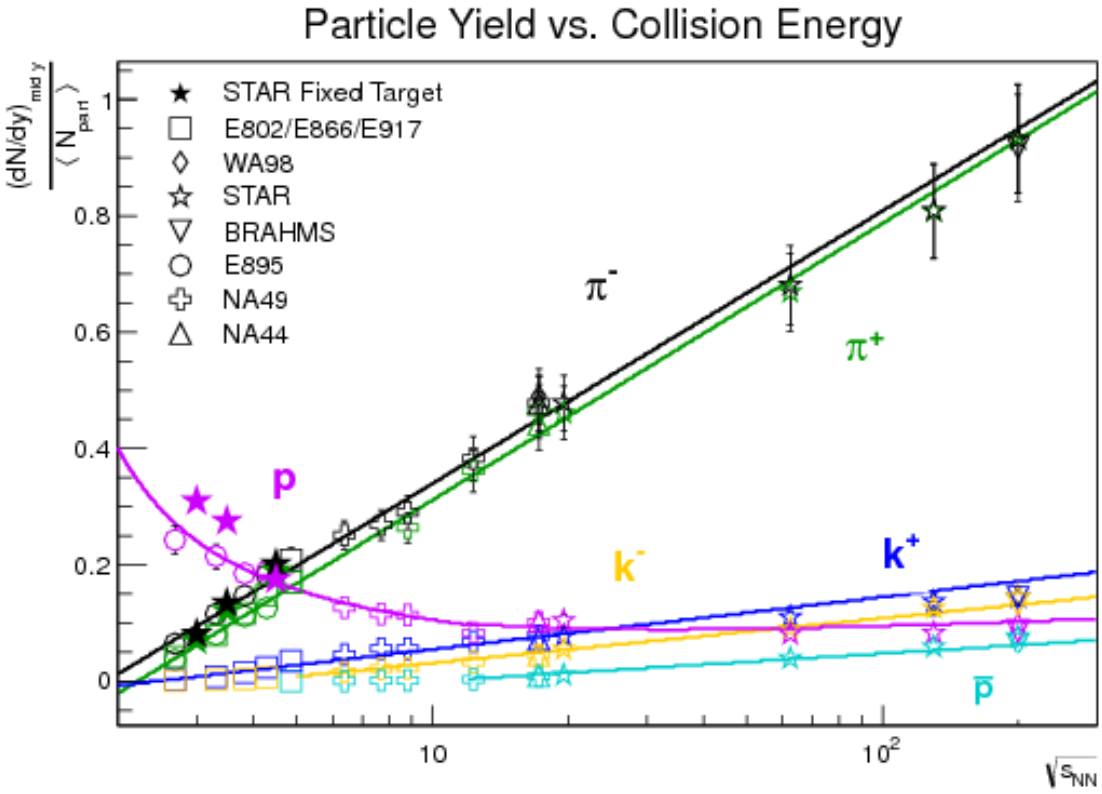

Figure 5.5: The midrapidity ($|y - y_{cm}| < 0.1$) dN/dy yields scaled by the average number of participants are shown for negative (solid stars) and positive (open stars) pions from central (top 10%) Au-like+Al collisions at the three collision energies ($\sqrt{s_{NN}}$ = 3.0, 3.5, 4.5 GeV). For comparison, scaled midrapidity pion yields are also shown for Au+Au collisions at 1.0 AGeV (KaoS [162]), at 2, 4, 6, and 8 AGeV (E895 [163, 164]), and at 2, 4, 6, 8, and 10.8 AGeV (E866 [122, 165]). Yields and potentials also are shown for central Pb+Pb collisions at 20, 30, 40, 60, 80, and 158 AGeV (NA44 [166,167], and NA49 [9,168]). Additional data from Refs. [30,123,169–174] are also included. The pion yields are fit with a linear function to guide the eye.

estimates using the centrality selection of the collaborations. The published data are fit with a simple linear function which is meant to guide the eye rather than to imply physics. Note that the extracted scaled pion yields from the new Au-like+Al data are consistent with trends previously seen in central data from heavy symmetric systems. Of additional import is the enhancement of the π^- yields with respect to that of the π^+ in the Au-like+Al data, as has been seen in Au+Au data at similar energies. This enhancement is expected as the neutron-to-proton ratio is closer to unity in aluminum than in either gold or lead.

5.2 Beam–Beam Collisions

With the analysis methods described in Chapter 4, identified particle spectra have been extracted and are presented along with the Coulomb potential and some signs of the onset of deconfinement. In Fig. 5.6, particle spectra are plotted as a function of $m_T - m_0$. Open

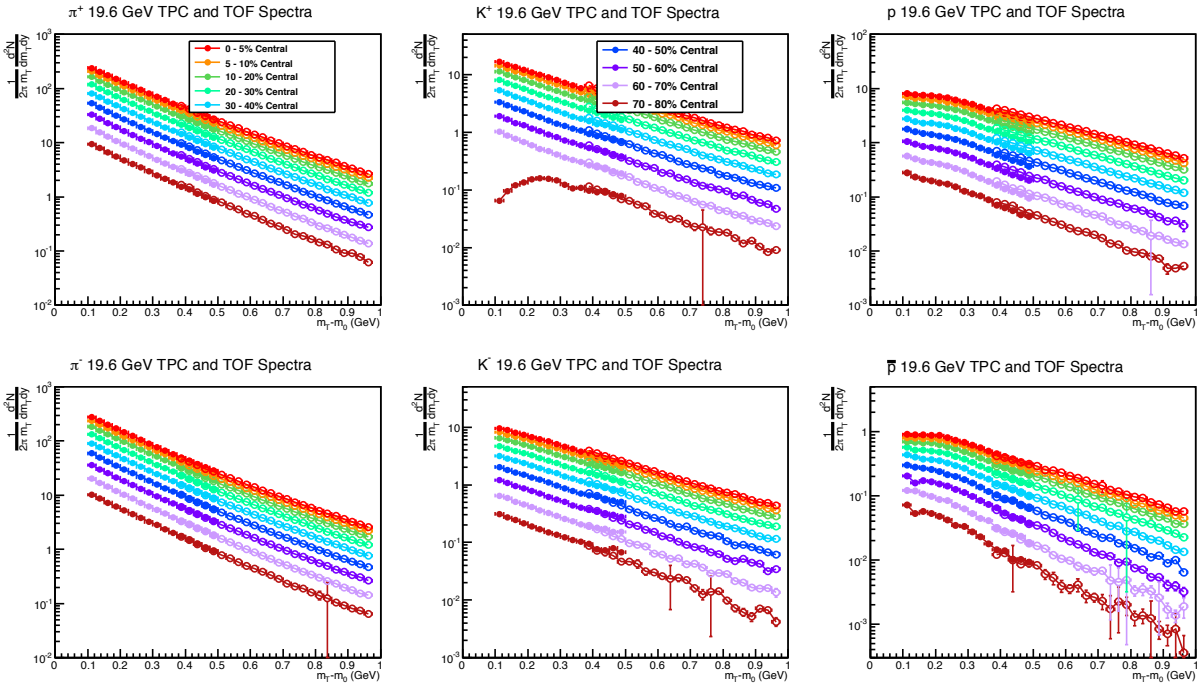

Figure 5.6: Particle spectra are plotted as a function of $m_T - m_0$. Open symbols represent identified particles with the TOF detector while solid symbols represent particles identified with the TPC detector at the energy of $\sqrt{s_{NN}} = 19.6$ GeV. Each color represents a different centrality with the most central on top an the most peripheral on bottom. Statistical and systematic errors are included. Pions are on the left, kaons in the center and protons are on the right. All positive particles are in the top row and negative particles are in the bottom row.

symbols represent particles identified with the TOF detector while solid symbols represent particles identified with the TPC detector at the energy of $\sqrt{s_{NN}} = 19.6$ GeV for Au+Au collisions. Each color represents a different collision centrality with the most central on top and the most peripheral on bottom. Statistical and systematic errors are included. Pions are on the left, kaons in the center, and protons on the right. All positively charged particles are in the top row while negatively charged particles are in the bottom row. The main corrections applied to these spectra are acceptance, efficiency, momenta, matching efficiency

(in the case for the TOF identified particles), and energy loss.

As expected, pions are the majority of produced particles since they are lightest hadrons and also have the largest interaction cross section. Positively charged kaons are next most numerous, which is expected due to their light mass. Protons and negatively charged kaons follow next while the smallest contribution to produced particles is from antiprotons.

The number of (anti-)protons produced per unit of rapidity normalized to the number of participating nucleons versus the center of mass energy is shown in Fig. 5.7. Results for Au+Au at $\sqrt{s_{NN}} = 19.6$ GeV are displayed in solid red stars. Scaled comparisons to other world data are also shown for Refs. [9, 30, 122, 123, 162–174] and are in additional figures to follow. The proton yields are fit with a falling exponential function of the form,

$$\frac{dN}{dy}/N_{\rm part} = A \exp\left(-\log(\sqrt{s})/B \right) \quad , \tag{5.1}$$

and anti-protons are fit with a function of the form,

$$\frac{dN}{dy}/N_{\rm part} = \frac{A \exp\big(-\log(\sqrt{s}/B)\big) + C}{A \exp\big(-\log(\sqrt{s}/B)\big) + 1} \quad , \tag{5.2}$$

to guide the eye only.

Proton dN/dy is calculated using a fitted Fermi-Dirac distribution giving a value of $dN/dy_p = 35.02 \pm 0.39$ while the anti-proton dN/dy fit uses an exponential in p_T [2] resulting in $dN/dy_{\bar{p}} = 3.89 \pm 0.14$. The average number of participants in Au+Au at $\sqrt{s_{NN}} = 19.6$ GeV is $N_{\rm part} = 353$. Thus the values in Fig. 5.7 are $dN/dy_p = 0.09921 \pm 0.0011$ for protons and $dN/dy_{\bar{p}} = 0.1103 \pm 0.0004$ for anti-protons.

In Fig. 5.8, the Coulomb potential (V_C) in open red stars with the right-hand red y-axis and midrapidity dN/dy (anti)proton yield in solid (cyan)magenta stars utilizing the left-hand y-axis are plotted as a function of center of mass energy. Displaying these two sets of data together highlight their similarity in shape with collision energy. This is not unexpected since the Coulomb potential is related to the net charge of the source and the bulk of that

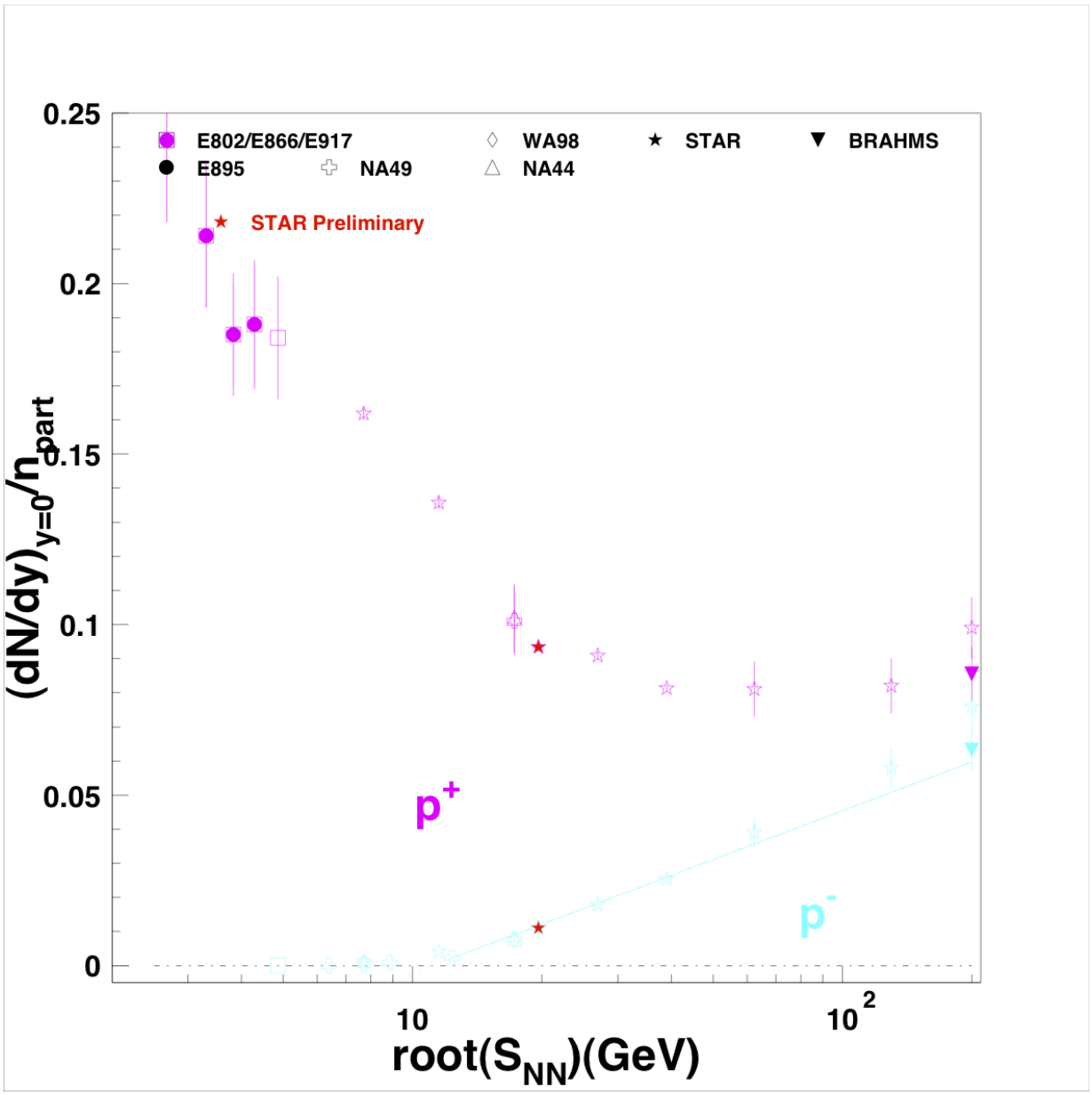

Figure 5.7: The number of (anti-)protons produced per unit of rapidity normalized to the number of participating nucleons versus the center of mass energy. Results for Au+Au at $\sqrt{s_{NN}} = 19.6$ GeV are shown in solid red stars. Scaled comparisons to other world data are also shown for Au+Au collisions at 1.0 AGeV (KaoS [162]), at 2, 4, 6, and 8 AGeV (E895 [163, 164]), and at 2, 4, 6, 8, and 10.8 AGeV (E866 [122, 165]). Yields and potentials also are shown for central Pb+Pb collisions at 20, 30, 40, 60, 80, and 158 AGeV (NA44 [166, 167], and NA49 [9, 168]). Additional data from Refs. [30, 123, 169–174] are also included. The proton yields are fit with a falling exponential function to guide the eye.

net charge is due to stopped protons. Also highlighted in the figure are the fixed-target data in open black stars. The Coulomb potential for $\sqrt{s_{NN}} = 19.6$ GeV is $V_C = 8.07 \pm 0.61$ V

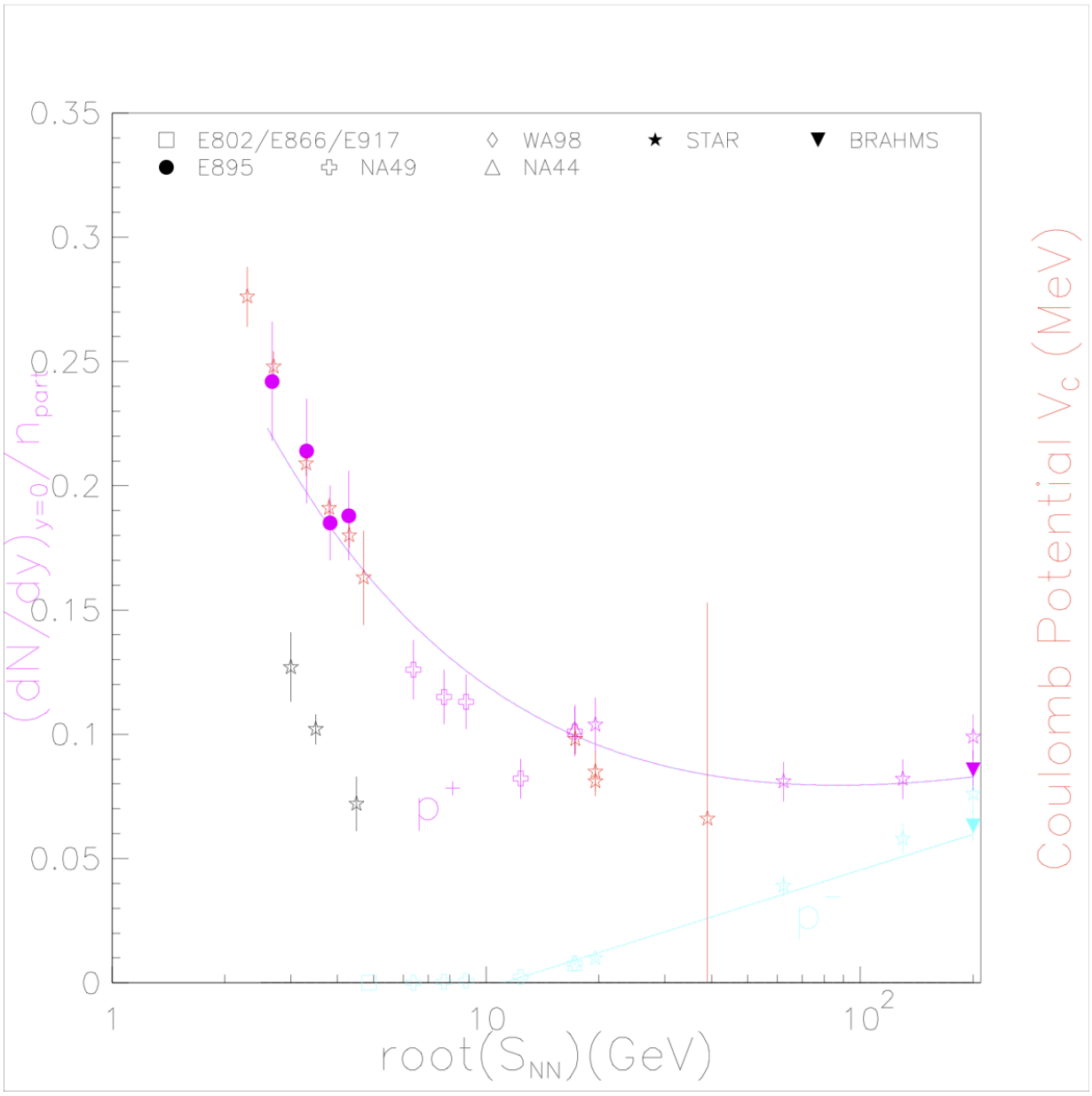

Figure 5.8: The Coulomb potential (V_C) in open red stars with the right-hand red y-axis and midrapidity dN/dy (anti)proton yield in solid (cyan)magenta stars utilizing the left-hand y-axis are plotted as a function of center of mass energy. Comparisons are also made to other world experiments and some collision energies from the BES measured with STAR. Fixed target data are in open black stars. For comparison, scaled midrapidity proton yields (open magenta symbols) and Coulomb potentials (open red symbols) are also shown for Au+Au collisions at 1.0 AGeV (KaoS [162]), at 2, 4, 6, and 8 AGeV (E895 [163,164]), and at 2, 4, 6, 8, and 10.8 AGeV (E866 [122,165]). Yields and potentials also are shown for central Pb+Pb collisions at 20, 30, 40, 60, 80, and 158 AGeV (NA44 [166,167], and NA49 [9,168]). Additional data from Refs. [30,123,169–174] are also included. Note the proton yields are fit with a falling exponential function to guide the eye.

with an initial pion ratio of $R_i = \pi^+/\pi^- = 0.953 \pm 0.002$ utilizing the Coulomb fit discussed in Sec. 2.4 on the Coulomb potential. This calculated Coulomb potential follows the world trend while the pion ratio falls well within world data and is comparable to similar SPS energies.

Figure 5.9 illustrates the number of pions produced per unit of rapidity normalized to the number of participating nucleons as a function of center-of-mass energy. Results for Au+Au at $\sqrt{s_{NN}} = 19.6$ GeV are displayed in solid red stars. Pion distributions were fit with a Bose-Einstein distribution for values $dN/dy_{\pi^+} = 160.615 \pm 1.765$ for π^+ and for π^- the fit obtains $dN/dy_{\pi^-} = 167.675 \pm 1.765$. Normalizing to the number of participants, we obtain the values $dN/dy_{\pi^+} = 0.455 \pm 0.005$ and $dN/dy_{\pi^-} = 0.475 \pm 0.005$, respectively, for the values in the figure.

Figure 5.10 illustrates the Kink discussed in Sec. 2.4 where the number of pions produced per unit of rapidity normalized to the number of participating nucleons is plotted against Fermi's measure, $F = \left[(\sqrt{s_{NN}} - 2m_N)^3/\sqrt{s_{NN}}\right]^{\frac{1}{4}}$. Results for Au+Au at $\sqrt{s_{NN}} = 19.6$ GeV are displayed in open red squares. Pion dN/dy is calculated as above, using a Bose-Einstein exponential and Fermi's measure for the 19.6 GeV data is $F = 4.1077$. Again, the pion values fall within world trends and further display the "kink" in the fitted slope and adds to the indication for the onset of deconfinement.

Figure 5.11 illustrates the Horn discussed in Sec. 2.4 where the number of kaons produced per unit of rapidity normalized to the number of participant nucleons is plotted as a function of center-of-mass energy. Results for Au+Au at $\sqrt{s_{NN}} = 19.6$ GeV are displayed in solid red stars. Kaon distributions were fit with a Bose-Einstein distribution, obtaining values $dN/dy_{K^+} = 28.2047 \pm 0.6707$ for K^+ and $dN/dy_{K^-} = 18.3207 \pm 0.6001$for K^-. Normalizing to the average number of participants, we obtain $dN/dy_{K^+} = 0.0799 \pm 0.0019$ and $dN/dy_{K^-} = 0.0519 \pm 0.0017$, respectively, which are the values plotted in the figure. These results are in line with world data and contribute to the prominence of the "horn" feature.

The Step in Fig. 5.12, discussed in Sec. 2.4, where the positively charged kaon temperature

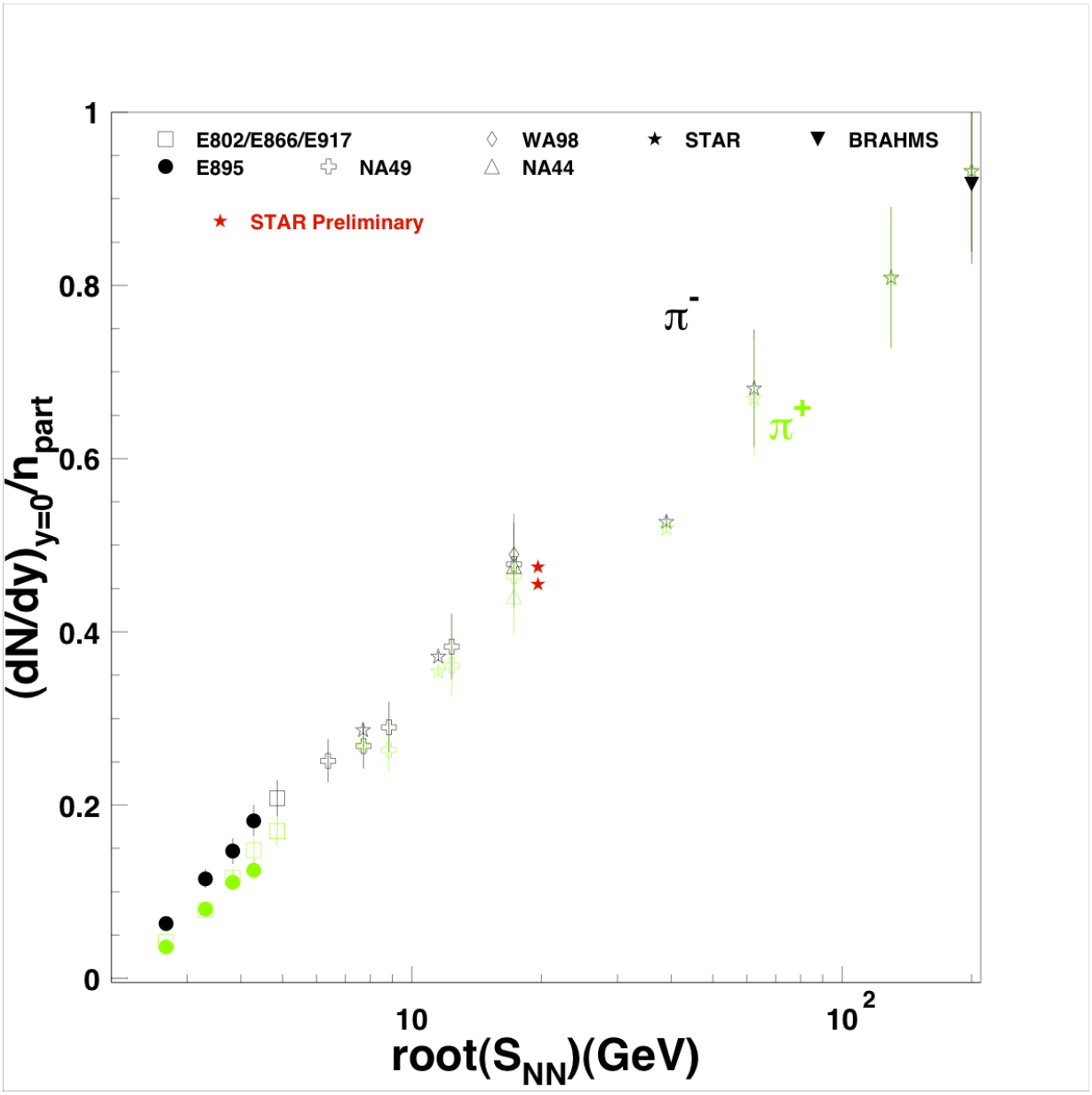

Figure 5.9: The number of pions produced per unit of rapidity normalized to the number of participating nucleons versus center of mass energy. Results for Au+Au at $\sqrt{s_{NN}} = 19.6$ GeV are displayed in solid red stars. Scaled comparisons to other world data are also shown for Au+Au collisions at 1.0 AGeV (KaoS [162]), at 2, 4, 6, and 8 AGeV (E895 [163,164]), and at 2, 4, 6, 8, and 10.8 AGeV (E866 [122, 165]). Yields and potentials also are shown for central Pb+Pb collisions at 20, 30, 40, 60, 80, and 158 AGeV (NA44 [166, 167], and NA49 [9, 168]). Additional data from Refs. [30, 123, 169–174] are also included.

is plotted against center-of-mass energy, with the addition of STAR data in solid red stars can be more readily seen. Data from collision energies of Au+Au at $\sqrt{s_{NN}} = 7.7, 11.5, 19.6$ and 39 GeV are in the figure. All temperatures are obtained from a Bose-Einstein fit to the

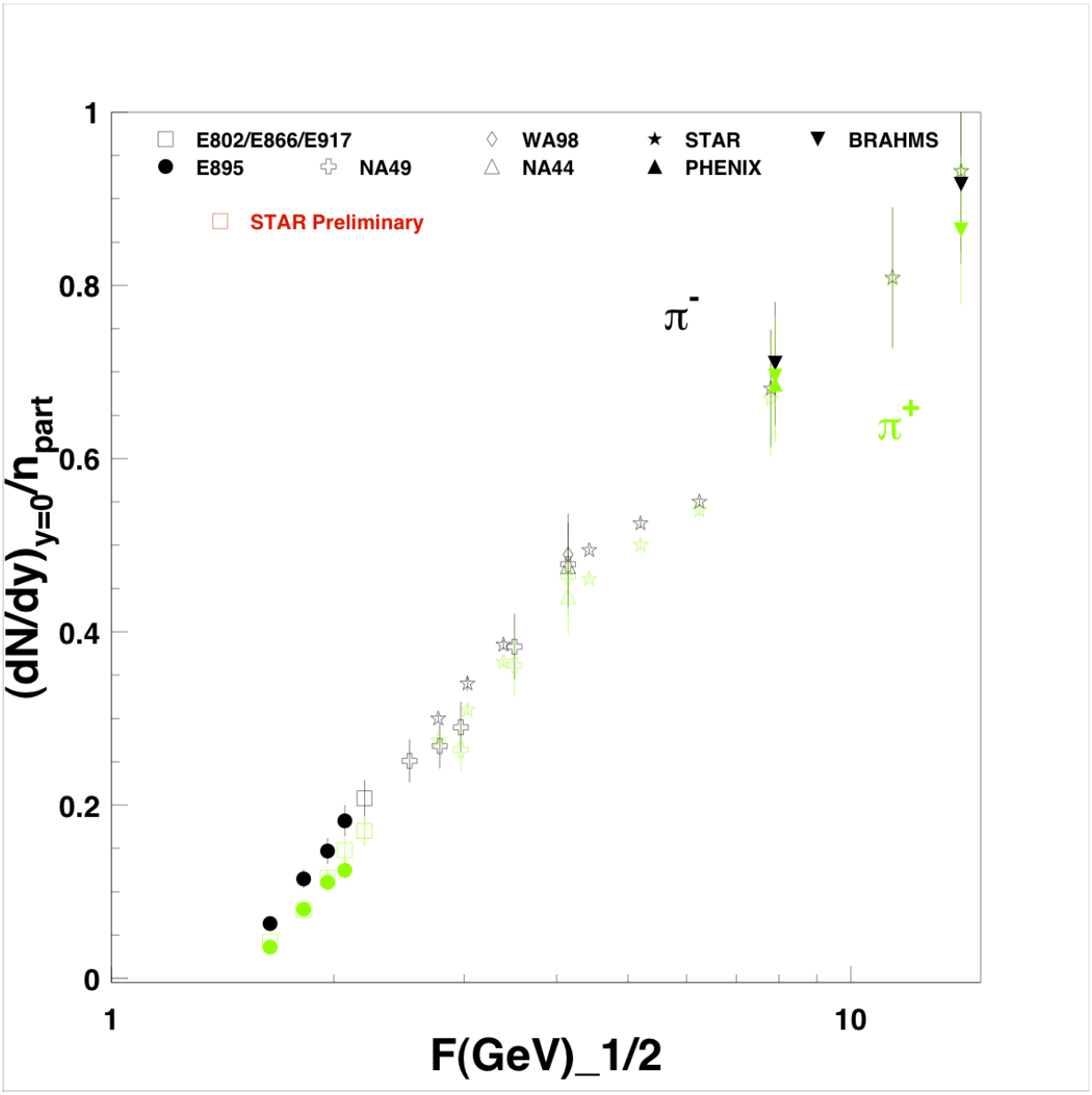

Figure 5.10: The Kink: the number of pions produced per unit of rapidity normalized to the number of participating nucleons versus Fermi's measure. Results for Au+Au at $\sqrt{s_{NN}} = 19.6$ GeV are displayed in open red squares. Scaled comparisons to other world data are also shown for Au+Au collisions at 1.0 AGeV (KaoS [162]), at 2, 4, 6, and 8 AGeV (E895 [163, 164]), and at 2, 4, 6, 8, and 10.8 AGeV (E866 [122, 165]). Yields and potentials also are shown for central Pb+Pb collisions at 20, 30, 40, 60, 80, and 158 AGeV (NA44 [166, 167], and NA49 [9, 168]). Additional data from Refs. [30, 123, 169–174] are also included.

spectra. Particularly, the temperature at $\sqrt{s_{NN}} = 19.6$ GeV for positively charged kaons is $T_{K^+} = 190.2 \pm 1.1$ MeV. This value for the temperature falls along trends of world data and further solidifies the idea of a softening of the equation of state, or the "step" structure of

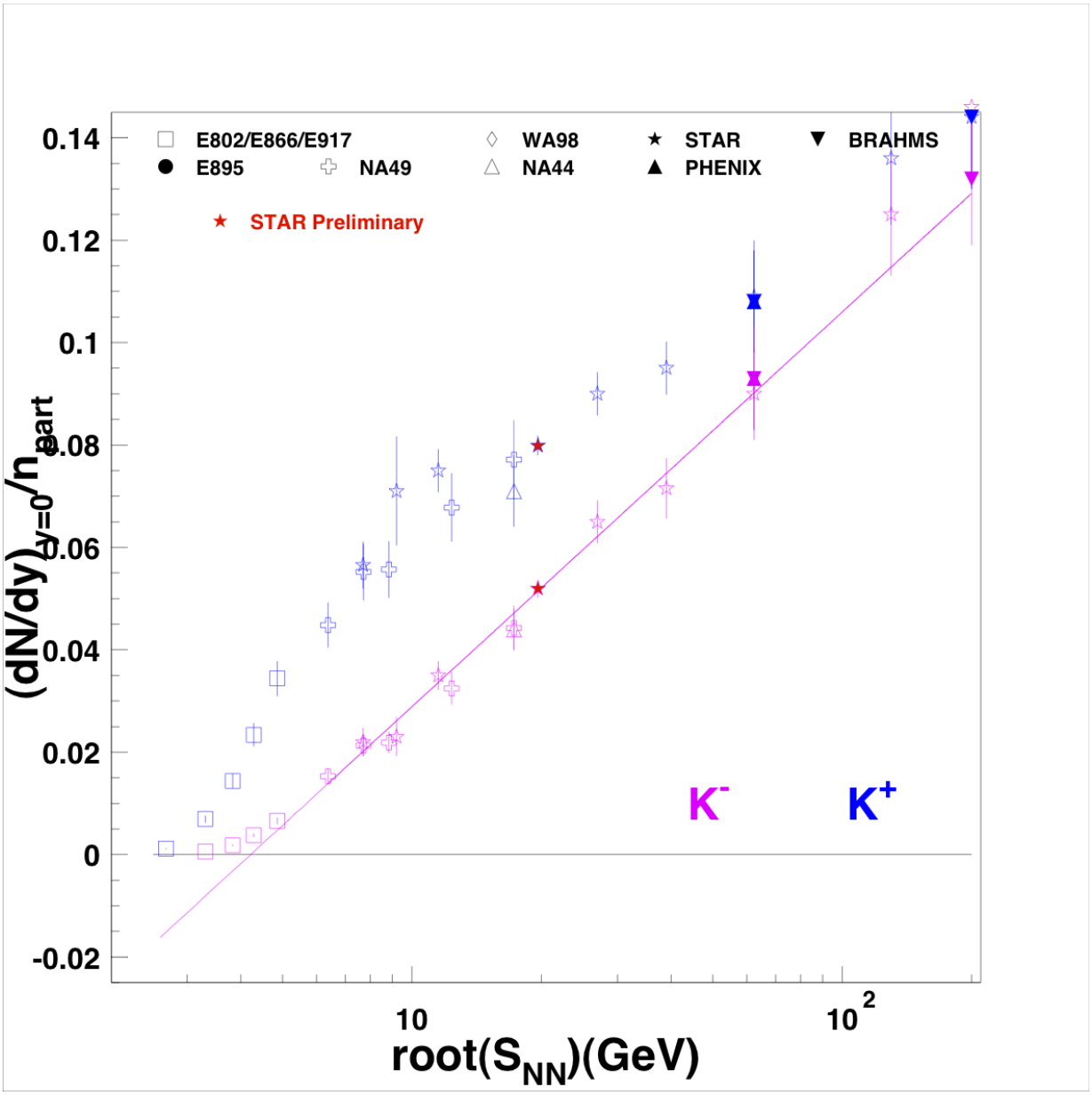

Figure 5.11: The Horn: the number of kaons produced per unit of rapidity normalized to the number of participating nucleons versus center-of-mass energy. Results for Au+Au at $\sqrt{s_{NN}} = 19.6$ GeV are displayed in solid red stars. Scaled comparisons to other world data are also shown for Au+Au collisions at 1.0 AGeV (KaoS [162]), at 2, 4, 6, and 8 AGeV (E895 [163, 164]), and at 2, 4, 6, 8, and 10.8 AGeV (E866 [122, 165]). Yields and potentials also are shown for central Pb+Pb collisions at 20, 30, 40, 60, 80, and 158 AGeV (NA44 [166, 167], and NA49 [9, 168]). Additional data from Refs. [30, 123, 169–174] are also included.

the plot.

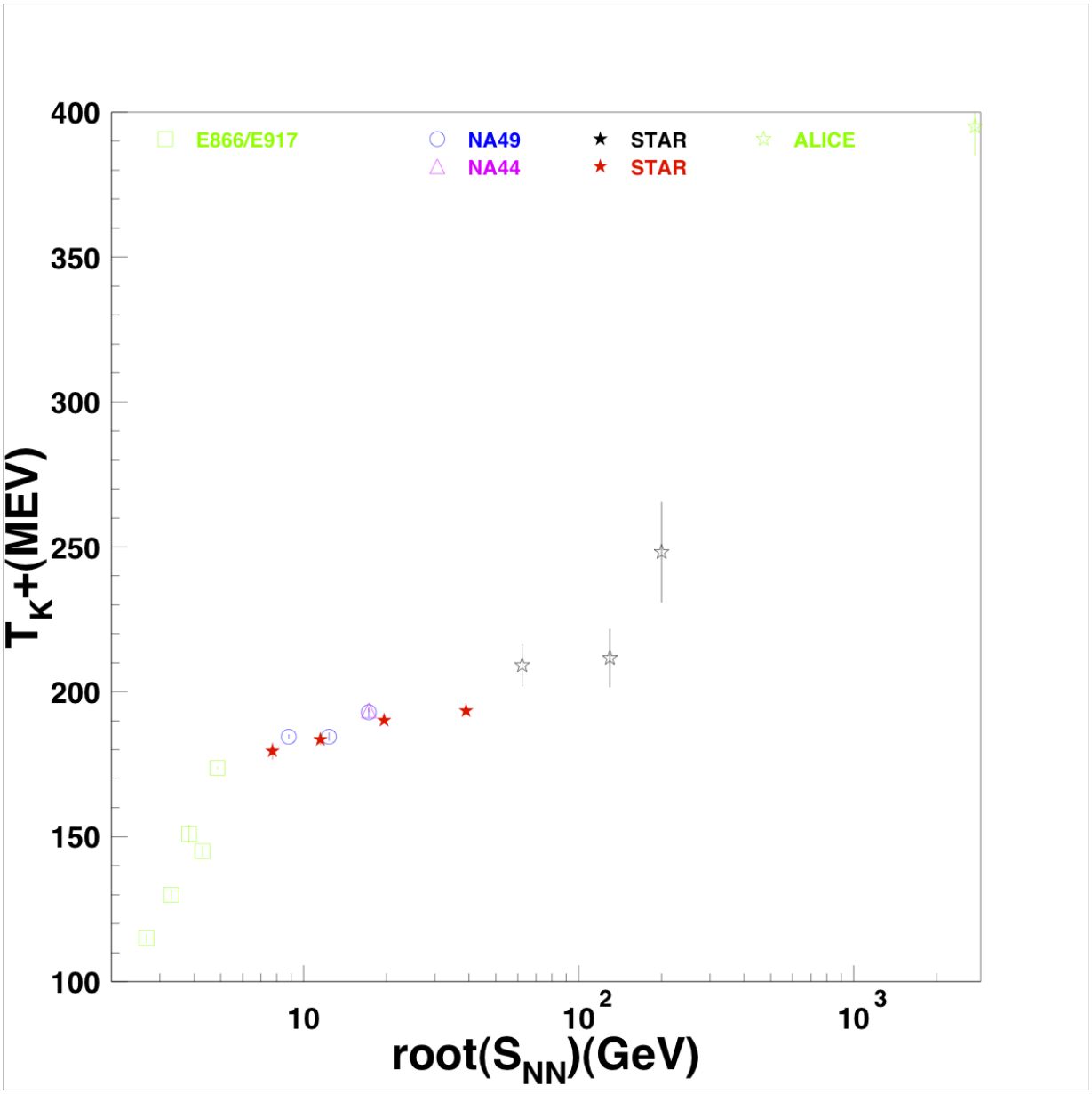

Figure 5.12: The Step, discussed in Sec. 2.4, where the positively charged kaon temperature is plotted against center-of-mass energy. Results for Au+Au at $\sqrt{s_{NN}} = 19.6$ GeV are displayed in solid red stars along with other BES energies. Scaled comparisons to other world data are also shown for Au+Au collisions at 1.0 AGeV (KaoS [162]), at 2, 4, 6, and 8 AGeV (E895 [163, 164]), and at 2, 4, 6, 8, and 10.8 AGeV (E866 [122, 165]). Yields and potentials also are shown for central Pb+Pb collisions at 20, 30, 40, 60, 80, and 158 AGeV (NA44 [166, 167], and NA49 [9, 168]). Additional data from Refs. [30, 123, 169–174] are also included.

Chapter 6

Conclusion

Although RHIC is a collider facility, it is possible to study fixed-target collisions using ions from the halo of the injected beam as the projectile and aluminum nuclei in the beam pipe as the target. The beam halo is likely comprised of heavy forward projectile fragments resulting from Au+H beam-gas interactions in the warm bore between the D0 and DX dipole magnets or from $^{+78}$Au ions resulting from electron capture off of He atoms in the cold bore of the main arc dipole magnets of RHIC.

Using the beam energies developed for the RHIC beam energy scan, STAR is able to study Au-like+ Al collisions at center-of-mass energies of 3.0, 3.5 and 4.5 GeV per nucleon pair. The STAR detector has been demonstrated to have good acceptance and particle identification capabilities at midrapidity for fixed-target collisions at these energies. The midrapidity pion and proton spectra have been measured and the slope parameters have been compared to previously published data at similar energies.

The shape of the ratios of positive to negative pions at low transverse mass has used to extract the Coulomb potential of the emission source. This Coulomb potential is created by the participating protons from the projectile and target which are transported to midrapidity during the collision. Comparisons of the Coulomb potential and the proton dN/dy can shed light of the emission radius and the lifetime of the source. Details of the pion ratios at low transverse mass allow for a better integration of the total emission ratio. This ratio helps clarify the production process which is expected to be dominated by the Delta resonance at

the lowest collisions energies and by pion-pair production at higher energies.

For nominal Au+Au collisions at the center-of-mass energy of 19.6 GeV per nucleon pair, pion, kaon and proton spectra have been measured and utilized to compare dN/dy values in previously-published data at center-of-mass energies ranging from 1 GeV to 200 GeV per nucleon pair. Detailed comparisons of spectra, rapidity densities, particles ratios, and slope parameters have been made to the previously-published data. The recent STAR analysis is consistent with previous results at the SPS. The rapidity densities are consistent with world trends for all species studied. Most species increase with collision energy; the exception is the protons, which decrease with collision energy as stopping is reduced in this energy range. The slope parameter of the positive kaons is seen to flatten across the energy range from 7 to 40 GeV. This has previously been interpreted as evidence of the onset of deconfinement. The recent STAR results further refine this measurement.

In conclusion, it has been demonstrated that the STAR detector has good capabilities for fixed-target collisions. Data from these collisions can be used to extend the search for the critical point and the onset of deconfinement at STAR for energies below 7.7 GeV.

Appendices

Appendix A

$\sqrt{s_{NN}} = 19.6$ GeV Au+Au Gaussian Fits

The following pages show the Gaussian fits ordered first by centrality bin, then by particle type, then by charge and finally by the detector type used to make the identification. Pions will always come first in each section, followed by kaons and then protons.

A.1 The 70%-80% Centrality Class

This is the most peripheral bin of all centrality classes. All figures have a legend which tells of the fit parameters in the upper left corner. Axes are explained in the figure captions.

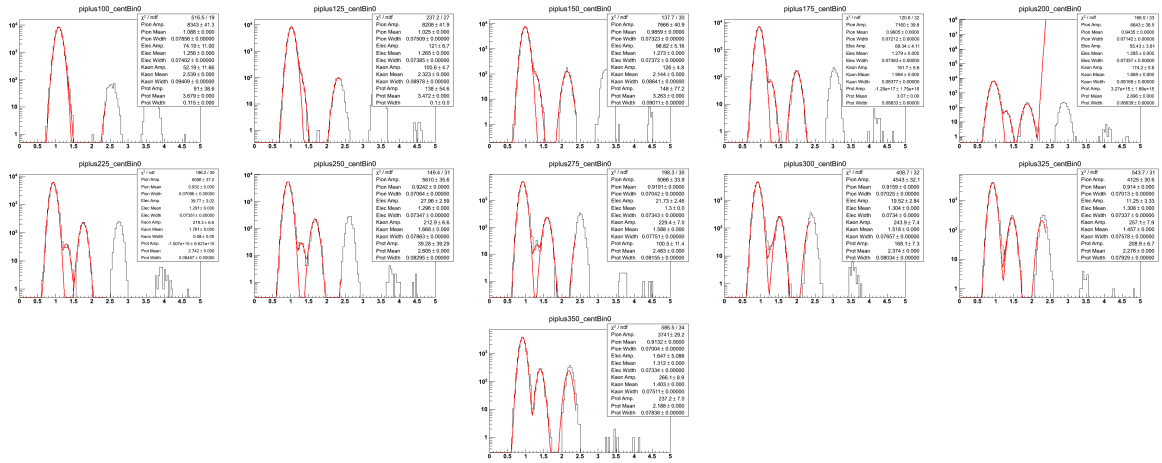

Figure A.1: Positive pion TPC fits for 70%-80% central events Au+Au $\sqrt{s_{NN}} = 19.6$ GeV. These are organized in 25 MeV bins in $m_T - m_\pi$ in a rapidity window of 0.1 units around mid-rapidity, $|y| < 0.05$. The Gaussian fits, drawn in red, are in $\log(10^6 \times dE/dx)$ and are of the $m_T - m_\pi =$ 0.100 to 0.500 GeV/c^2 range. The track data are represented in the black histogram.

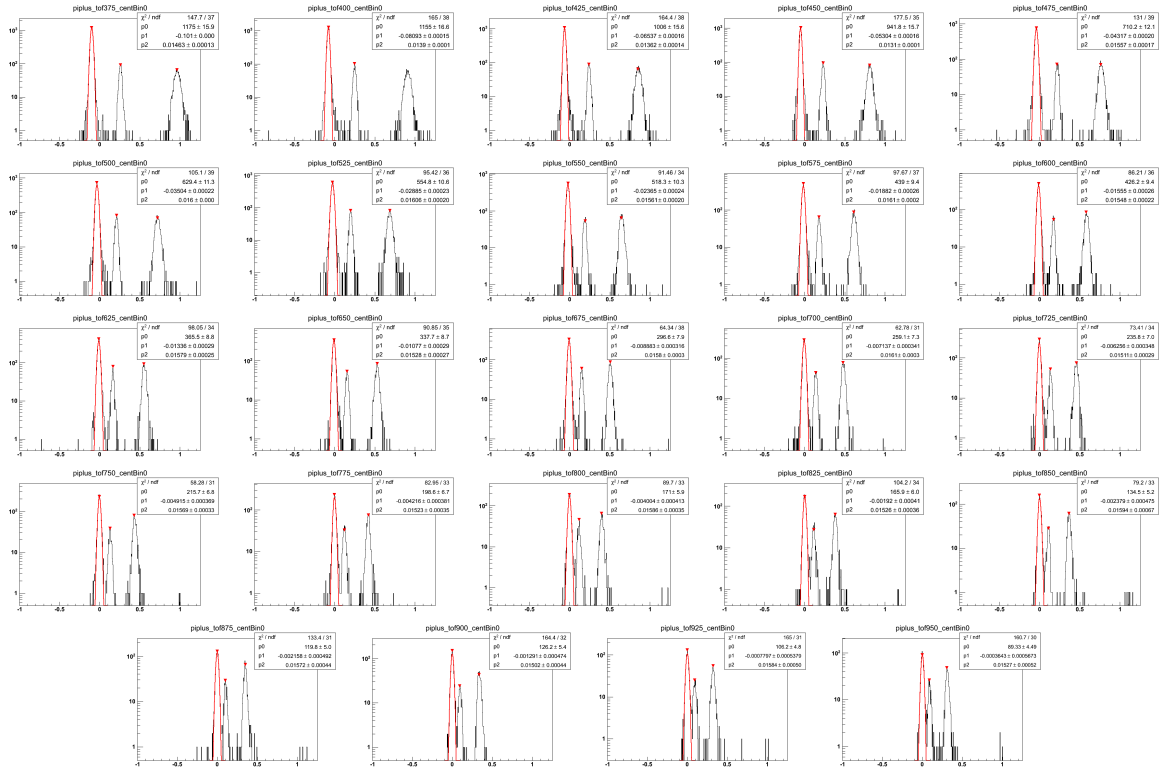

Figure A.2: Positive pion TOF fits for 70%-80% central events Au+Au $\sqrt{s_{NN}} = 19.6$ GeV. These are organized in 25 MeV bins in $m_T - m_\pi$ in a rapidity window of 0.1 units around mid-rapidity, $|y| < 0.05$. The Gaussian fits, drawn in red, are in $\beta^{-1}_{\text{expected}} - \beta^{-1}_{\text{measured}}$ and are of the $m_T - m_\pi =$ 0.350 to 1.0 GeV/c^2 range. The track data are represented in the black histogram.

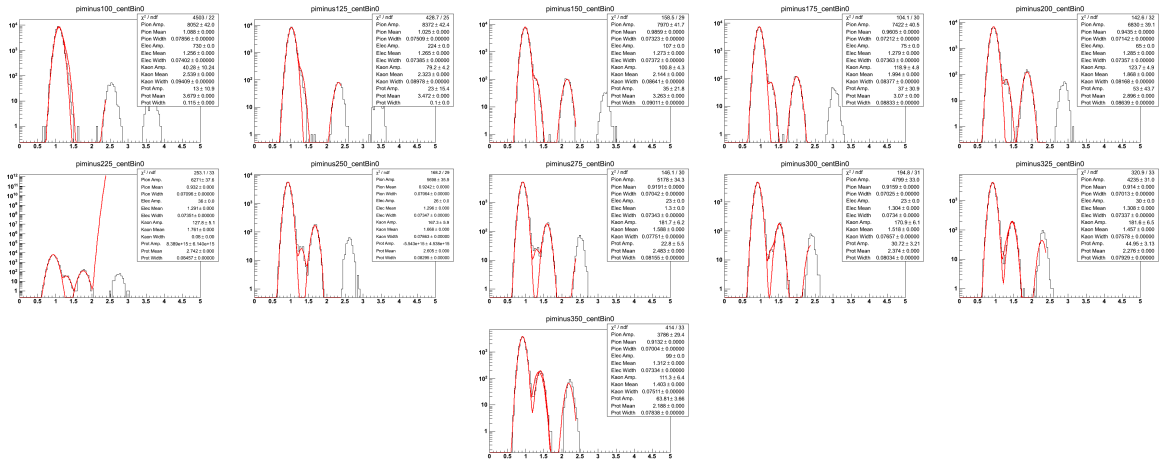

Figure A.3: Negative pion TPC fits for 70%-80% central events Au+Au $\sqrt{s_{NN}} = 19.6$ GeV. These are organized in 25 MeV bins in $m_T - m_\pi$ in a rapidity window of 0.1 units around mid-rapidity, $|y| < 0.05$. The Gaussian fits, drawn in red, are in $\log(10^6 \times dE/dx)$ and are of the $m_T - m_\pi =$ 0.100 to 0.500 GeV/c^2 range. The track data are represented in the black histogram.

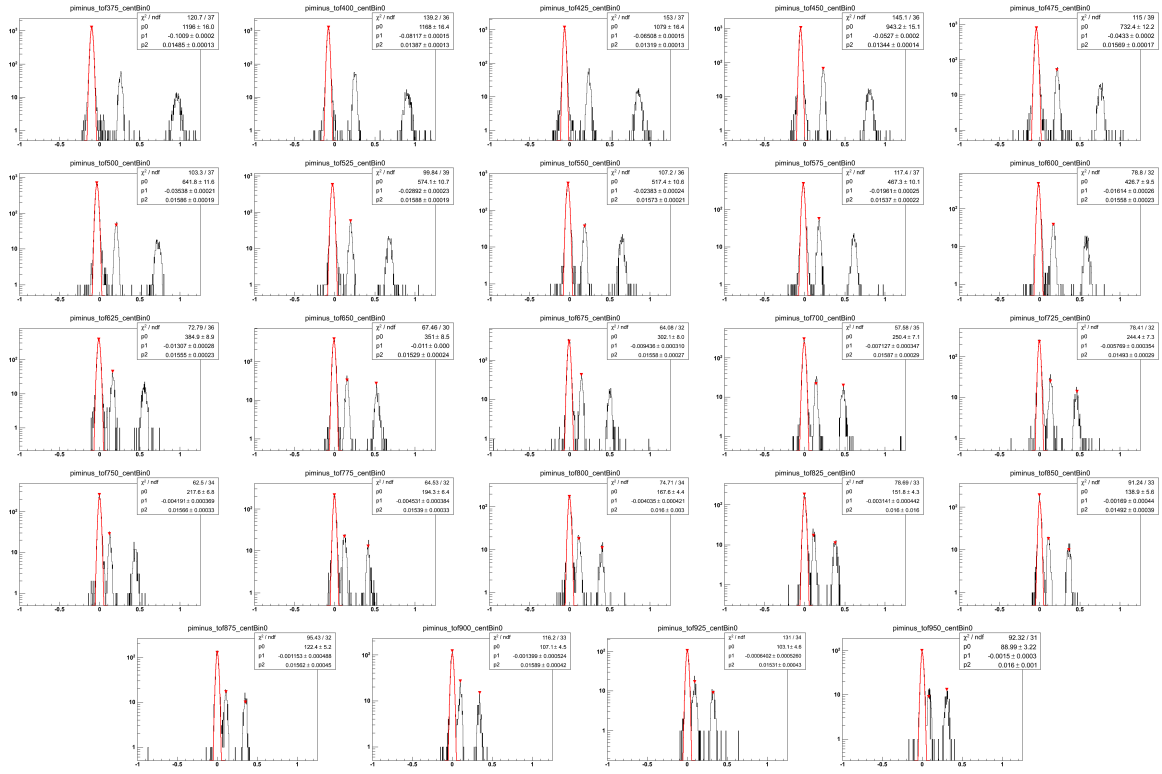

Figure A.4: Negative pion TOF fits for 70%-80% central events Au+Au $\sqrt{s_{NN}} = 19.6$ GeV. These are organized in 25 MeV bins in $m_T - m_\pi$ in a rapidity window of 0.1 units around mid-rapidity, $|y| < 0.05$. The Gaussian fits, drawn in red, are in $\beta^{-1}_{\text{expected}} - \beta^{-1}_{\text{measured}}$ and are of the $m_T - m_\pi =$ 0.350 to 1.0 GeV/c^2 range. The track data are represented in the black histogram.

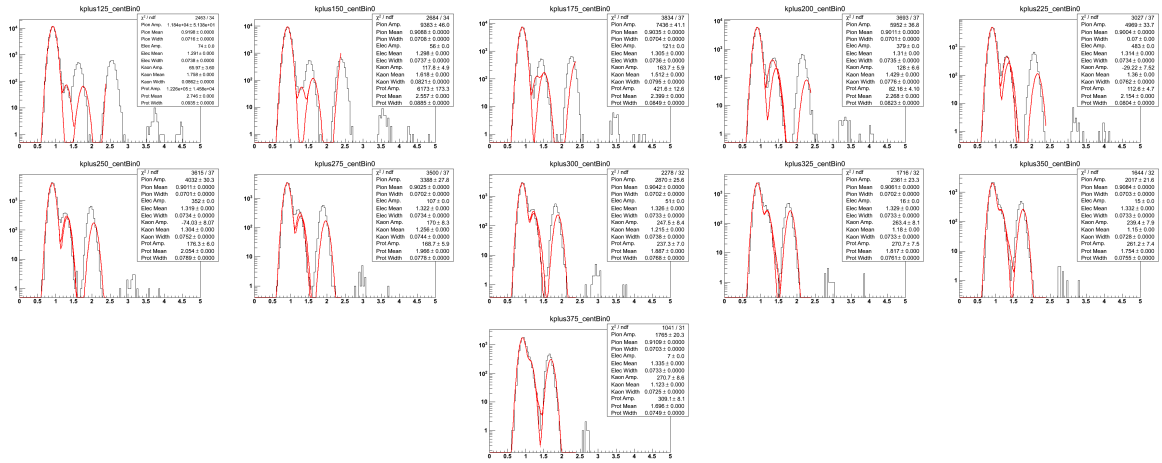

Figure A.5: Positive kaon TPC fits for 70%-80% central events Au+Au $\sqrt{s_{NN}} = 19.6$ GeV. These are organized in 25 MeV bins in $m_T - m_K$ in a rapidity window of 0.1 units around mid-rapidity, $|y| < 0.05$. The Gaussian fits, drawn in red, are in $\log(10^6 \times dE/dx)$ and are of the $m_T - m_K =$ 0.100 to 0.500 GeV/c^2 range. The track data are represented in the black histogram.

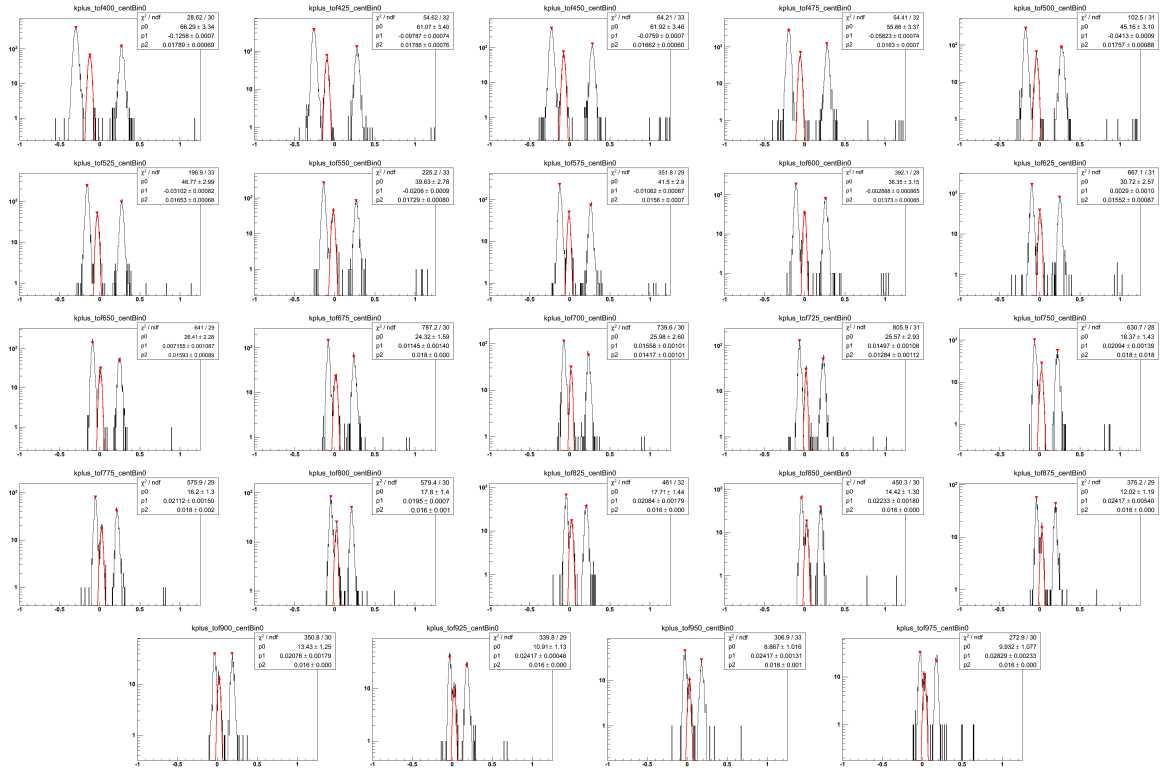

Figure A.6: Positive kaon TOF fits for 70%-80% central events Au+Au $\sqrt{s_{NN}} = 19.6$ GeV. These are organized in 25 MeV bins in $m_T - m_K$ in a rapidity window of 0.1 units around mid-rapidity, $|y| < 0.05$. The Gaussian fits, drawn in red, are in $\beta^{-1}_{\text{expected}} - \beta^{-1}_{\text{measured}}$ and are of the $m_T - m_K =$ 0.350 to 1.0 GeV/c^2 range. The track data are represented in the black histogram.

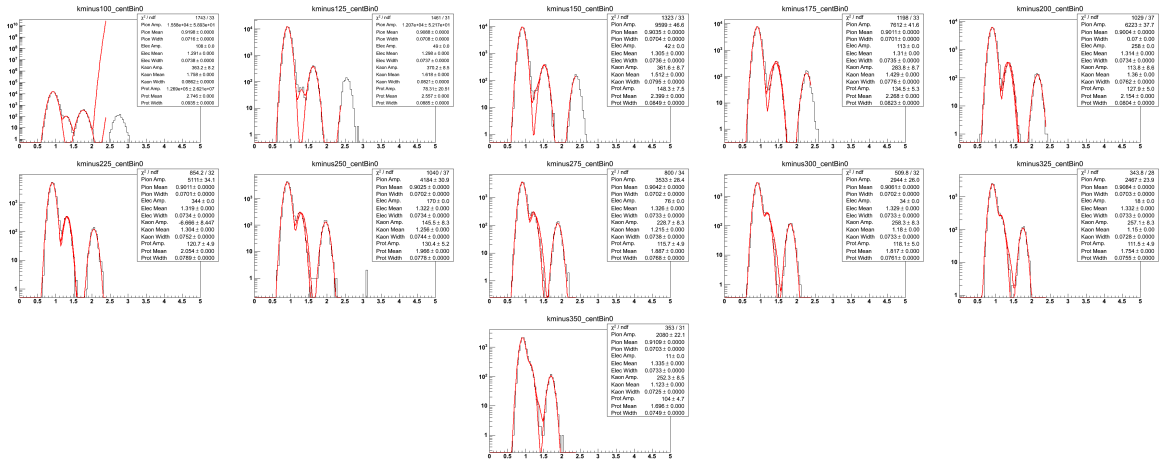

Figure A.7: Negative kaon TPC fits for 70%-80% central events Au+Au $\sqrt{s_{NN}} = 19.6$ GeV. These are organized in 25 MeV bins in $m_T - m_K$ in a rapidity window of 0.1 units around mid-rapidity, $|y| < 0.05$. The Gaussian fits, drawn in red, are in $\log(10^6 \times dE/dx)$ and are of the $m_T - m_K =$ 0.100 to 0.500 GeV/c^2 range. The track data are represented in the black histogram.

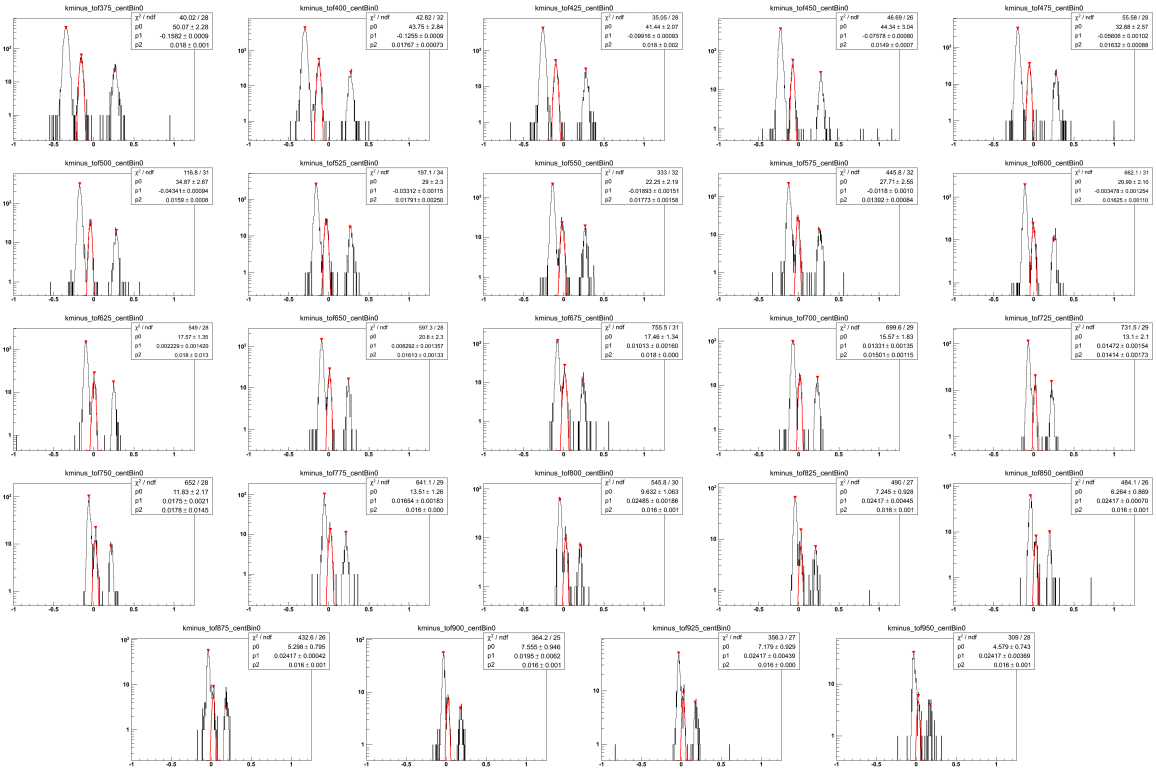

Figure A.8: Negative kaon TOF fits for 70%-80% central events Au+Au $\sqrt{s_{NN}} = 19.6$ GeV. These are organized in 25 MeV bins in $m_T - m_K$ in a rapidity window of 0.1 units around mid-rapidity, $|y| < 0.05$. The Gaussian fits, drawn in red, are in $\beta^{-1}_{\text{expected}} - \beta^{-1}_{\text{measured}}$ and are of the $m_T - m_K =$ 0.350 to 1.0 GeV/c^2 range. The track data are represented in the black histogram.

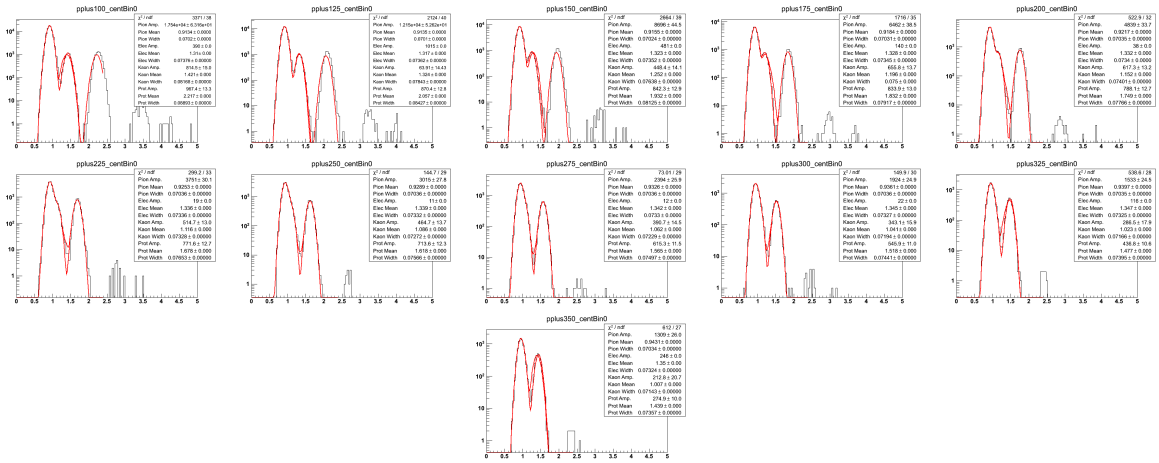

Figure A.9: Positive proton TPC fits for 70%-80% central events Au+Au $\sqrt{s_{NN}}$ = 19.6 GeV. These are organized in 25 MeV bins in $m_T - m_p$ in a rapidity window of 0.1 units around mid-rapidity, $|y| < 0.05$. The Gaussian fits, drawn in red, are in $\log(10^6 \times dE/dx)$ and are of the $m_T - m_p = 0.100$ to 0.500 GeV/c^2 range. The track data are represented in the black histogram.

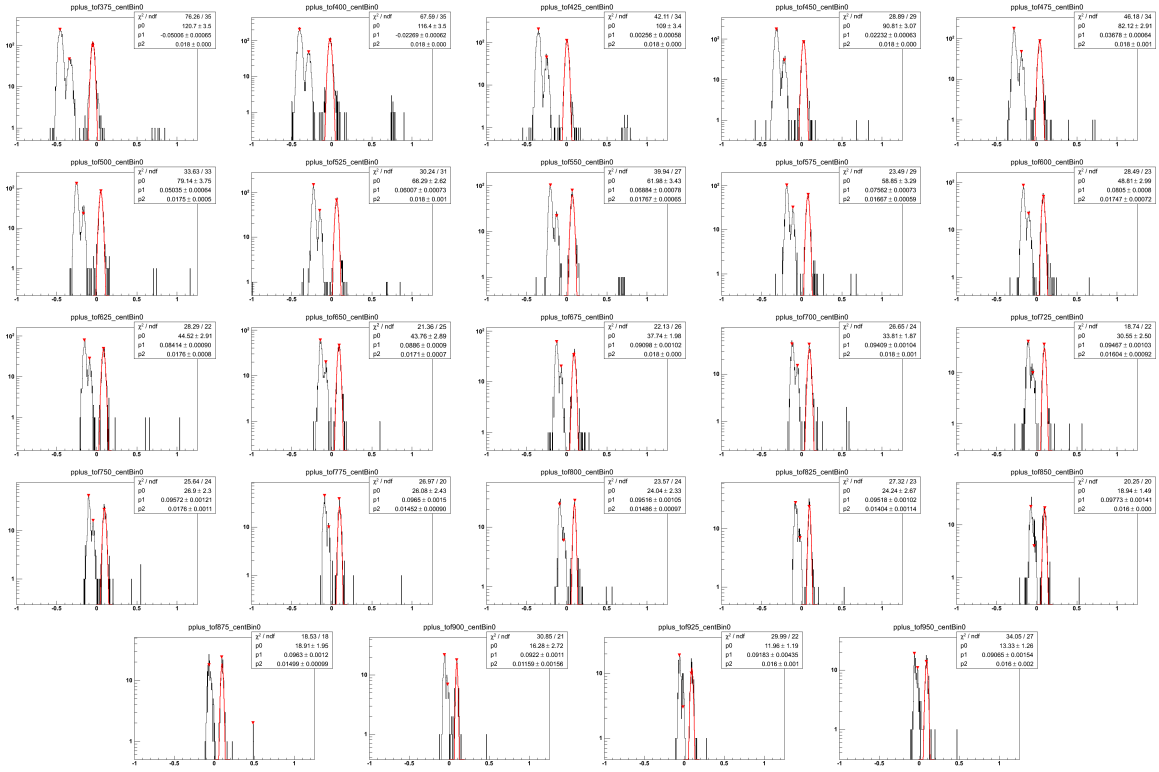

Figure A.10: Positive proton TOF fits for 70%-80% central events Au+Au $\sqrt{s_{NN}}$ = 19.6 GeV. These are organized in 25 MeV bins in $m_T - m_p$ in a rapidity window of 0.1 units around mid-rapidity, $|y| < 0.05$. The Gaussian fits, drawn in red, are in $\beta^{-1}_{\text{expected}} - \beta^{-1}_{\text{measured}}$ and are of the $m_T - m_p = 0.350$ to 1.0 GeV/c^2 range. The track data are represented in the black histogram.

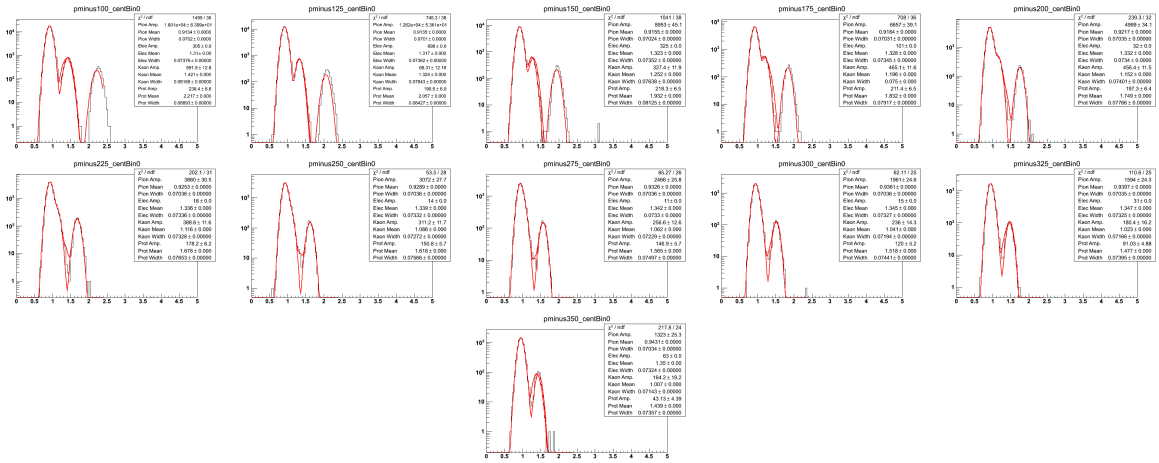

Figure A.11: Negative proton TPC fits for 70%-80% central events Au+Au $\sqrt{s_{NN}} = 19.6$ GeV. These are organized in 25 MeV bins in $m_T - m_p$ in a rapidity window of 0.1 units around mid-rapidity, $|y| < 0.05$. The Gaussian fits, drawn in red, are in $\log(10^6 \times dE/dx)$ and are of the $m_T - m_p = 0.100$ to 0.500 GeV/c^2 range. The track data are represented in the black histogram.

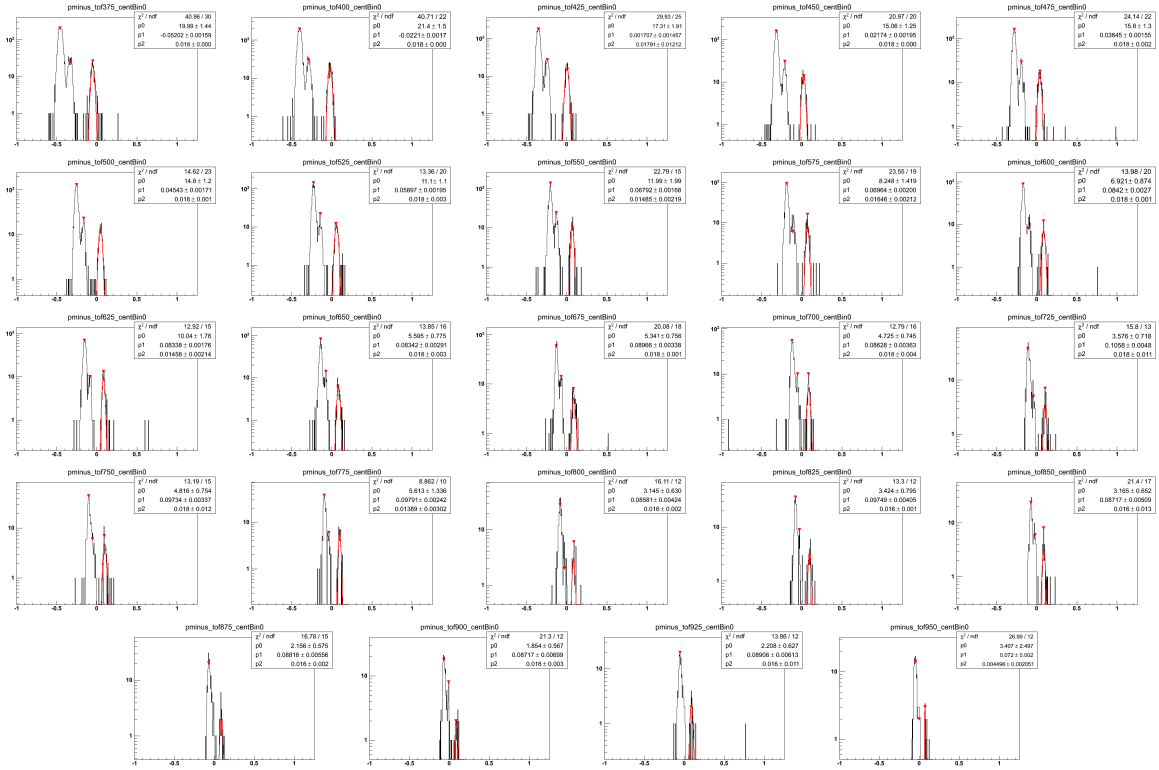

Figure A.12: Negative proton TOF fits for 70%-80% central events Au+Au $\sqrt{s_{NN}} = 19.6$ GeV. These are organized in 25 MeV bins in $m_T - m_p$ in a rapidity window of 0.1 units around mid-rapidity, $|y| < 0.05$. The Gaussian fits, drawn in red, are in $\beta^{-1}_{\text{expected}} - \beta^{-1}_{\text{measured}}$ and are of the $m_T - m_p = 0.350$ to 1.0 GeV/c^2 range. The track data are represented in the black histogram.

A.2 The 60%-70% Centrality Class

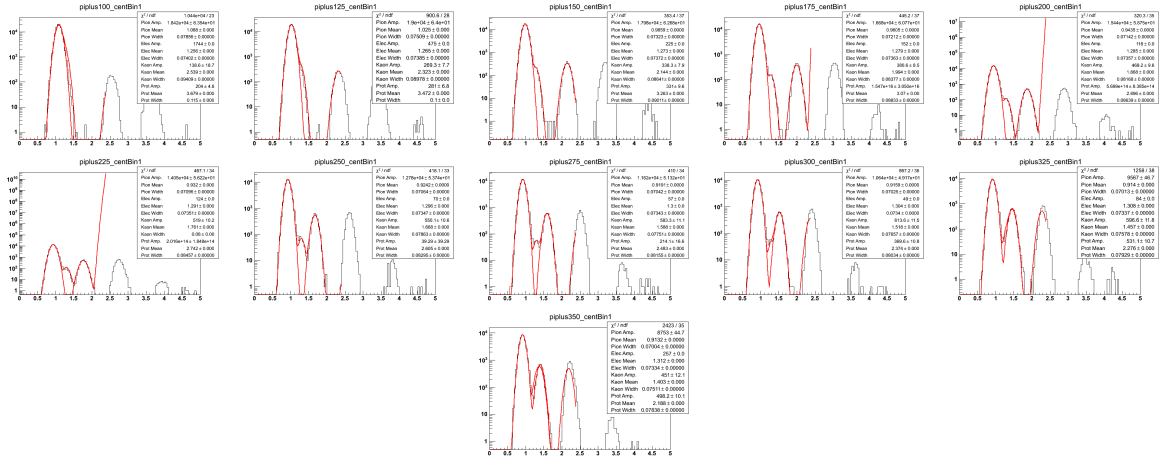

Figure A.13: Positive pion TPC fits for 60%-70% central events Au+Au $\sqrt{s_{NN}} = 19.6$ GeV. These are organized in 25 MeV bins in $m_T - m_\pi$ in a rapidity window of 0.1 units around mid-rapidity, $|y| < 0.05$. The Gaussian fits, drawn in red, are in $\log(10^6 \times dE/dx)$ and are of the $m_T - m_\pi =$ 0.100 to 0.500 GeV/c^2 range. The track data are represented in the black histogram.

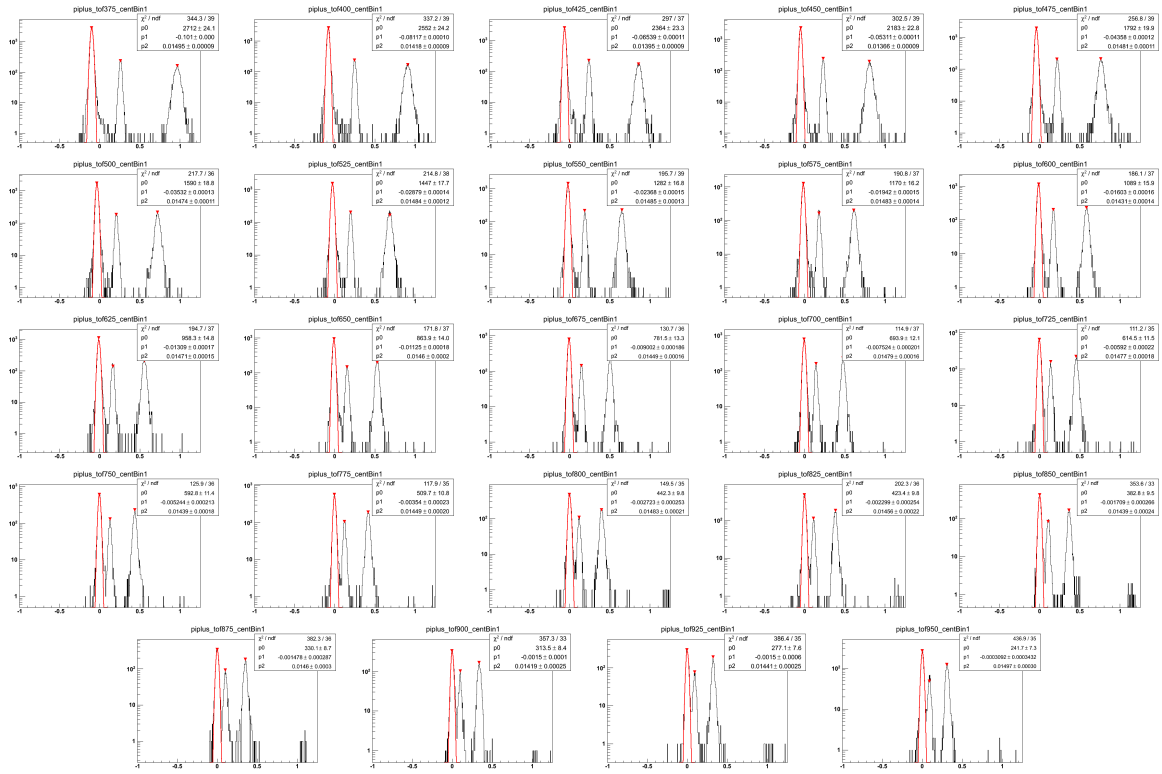

Figure A.14: Positive pion TOF fits for 60%-70% central events Au+Au $\sqrt{s_{NN}} = 19.6$ GeV. These are organized in 25 MeV bins in $m_T - m_\pi$ in a rapidity window of 0.1 units around mid-rapidity, $|y| < 0.05$. The Gaussian fits, drawn in red, are in $\beta^{-1}_{\text{expected}} - \beta^{-1}_{\text{measured}}$ and are of the $m_T - m_\pi = 0.350$ to 1.0 GeV/c^2 range. The track data are represented in the black histogram.

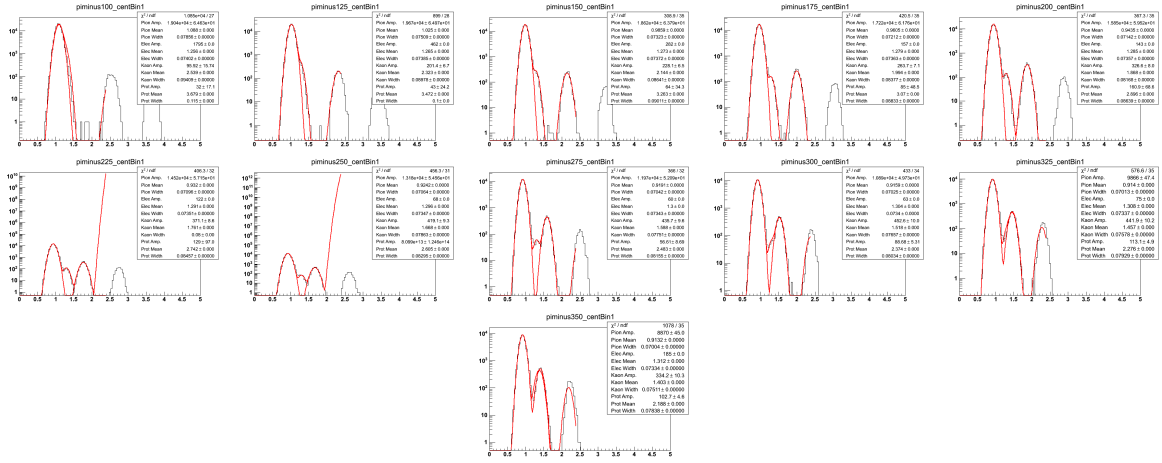

Figure A.15: Negative pion TPC fits for 60%-70% central events Au+Au $\sqrt{s_{NN}} = 19.6$ GeV. These are organized in 25 MeV bins in $m_T - m_\pi$ in a rapidity window of 0.1 units around mid-rapidity, $|y| < 0.05$. The Gaussian fits, drawn in red, are in $\log(10^6 \times dE/dx)$ and are of the $m_T - m_\pi = 0.100$ to 0.500 GeV/c^2 range. The track data are represented in the black histogram.

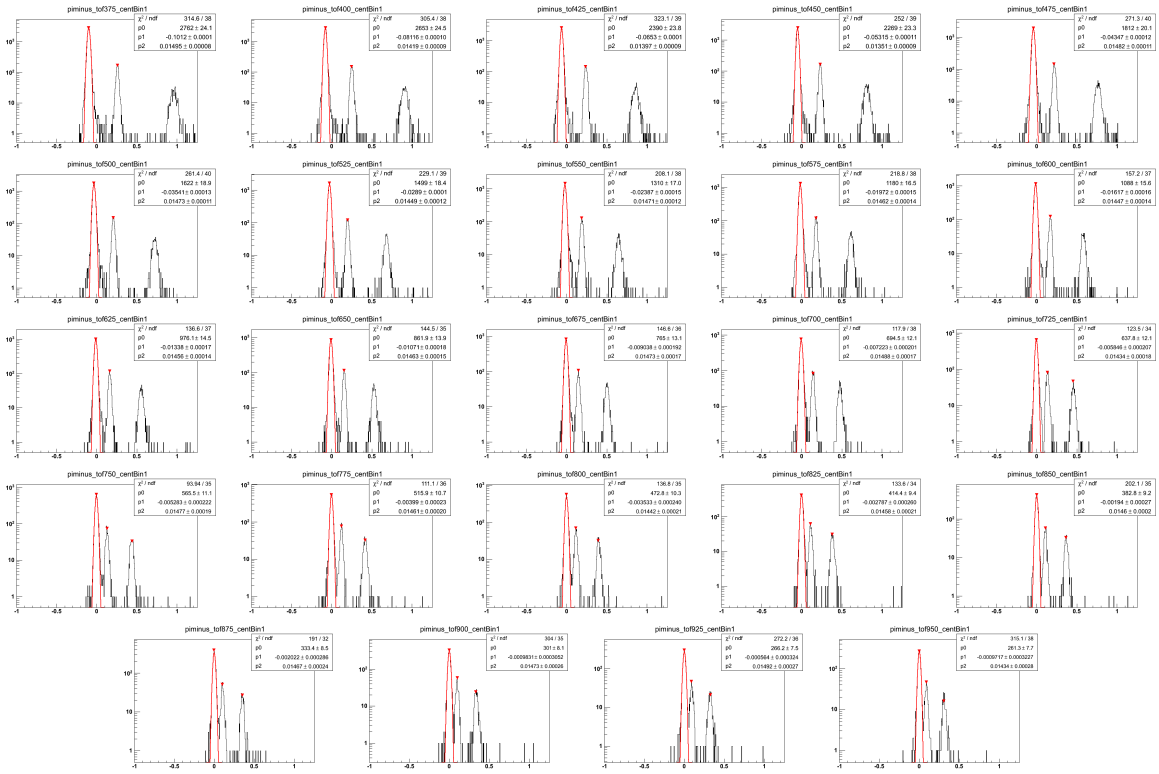

Figure A.16: Negative pion TOF fits for 60%-70% central events Au+Au $\sqrt{s_{NN}} = 19.6$ GeV. These are organized in 25 MeV bins in $m_T - m_\pi$ in a rapidity window of 0.1 units around mid-rapidity, $|y| < 0.05$. The Gaussian fits, drawn in red, are in $\beta^{-1}_{\text{expected}} - \beta^{-1}_{\text{measured}}$ and are of the $m_T - m_\pi = 0.350$ to 1.0 GeV/c^2 range. The track data are represented in the black histogram.

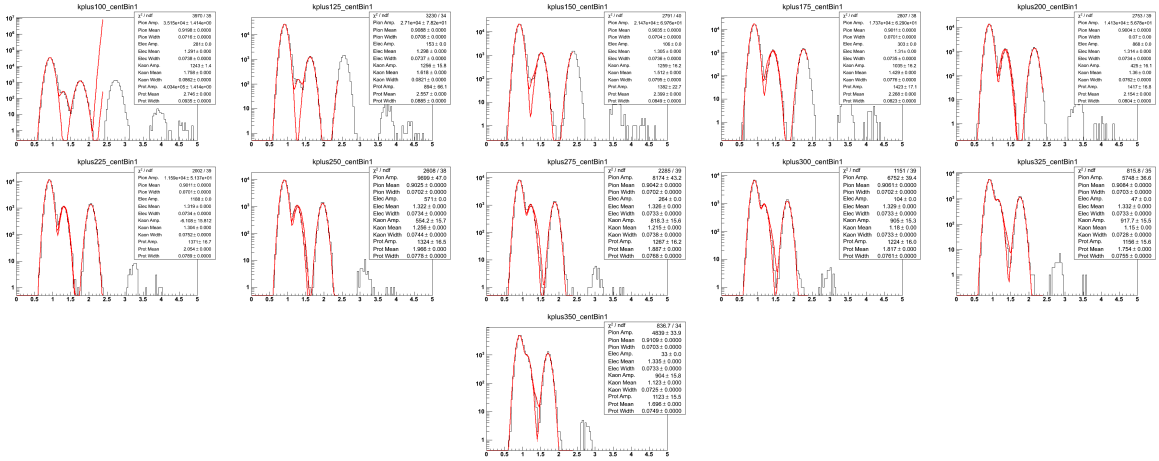

Figure A.17: Positive kaon TPC fits for 60%-70% central events Au+Au $\sqrt{s_{NN}} = 19.6$ GeV. These are organized in 25 MeV bins in $m_T - m_K$ in a rapidity window of 0.1 units around mid-rapidity, $|y| < 0.05$. The Gaussian fits, drawn in red, are in $\log(10^6 \times dE/dx)$ and are of the $m_T - m_K = 0.100$ to 0.500 GeV/c^2 range. The track data are represented in the black histogram.

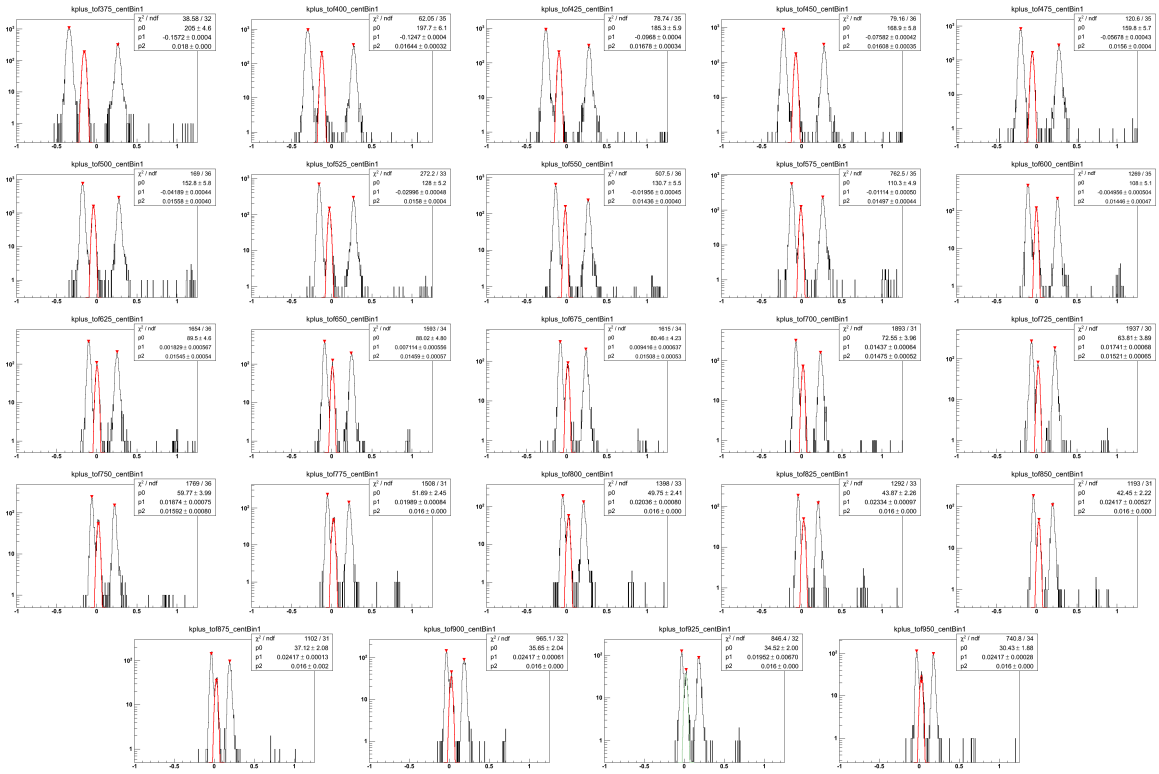

Figure A.18: Positive kaon TOF fits for 60%-70% central events Au+Au $\sqrt{s_{NN}} = 19.6$ GeV. These are organized in 25 MeV bins in $m_T - m_K$ in a rapidity window of 0.1 units around mid-rapidity, $|y| < 0.05$. The Gaussian fits, drawn in red, are in $\beta^{-1}_{\text{expected}} - \beta^{-1}_{\text{measured}}$ and are of the $m_T - m_K =$ 0.350 to 1.0 GeV/c^2 range. The track data are represented in the black histogram.

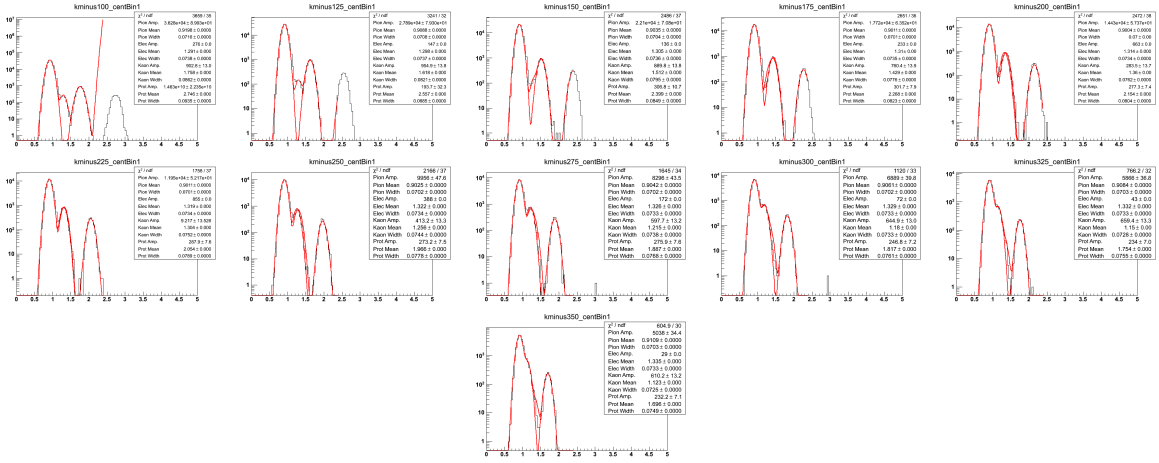

Figure A.19: Negative kaon TPC fits for 60%-70% central events Au+Au $\sqrt{s_{NN}} = 19.6$ GeV. These are organized in 25 MeV bins in $m_T - m_K$ in a rapidity window of 0.1 units around mid-rapidity, $|y| < 0.05$. The Gaussian fits, drawn in red, are in $\log(10^6 \times dE/dx)$ and are of the $m_T - m_K = 0.100$ to 0.500 GeV/c^2 range. The track data are represented in the black histogram.

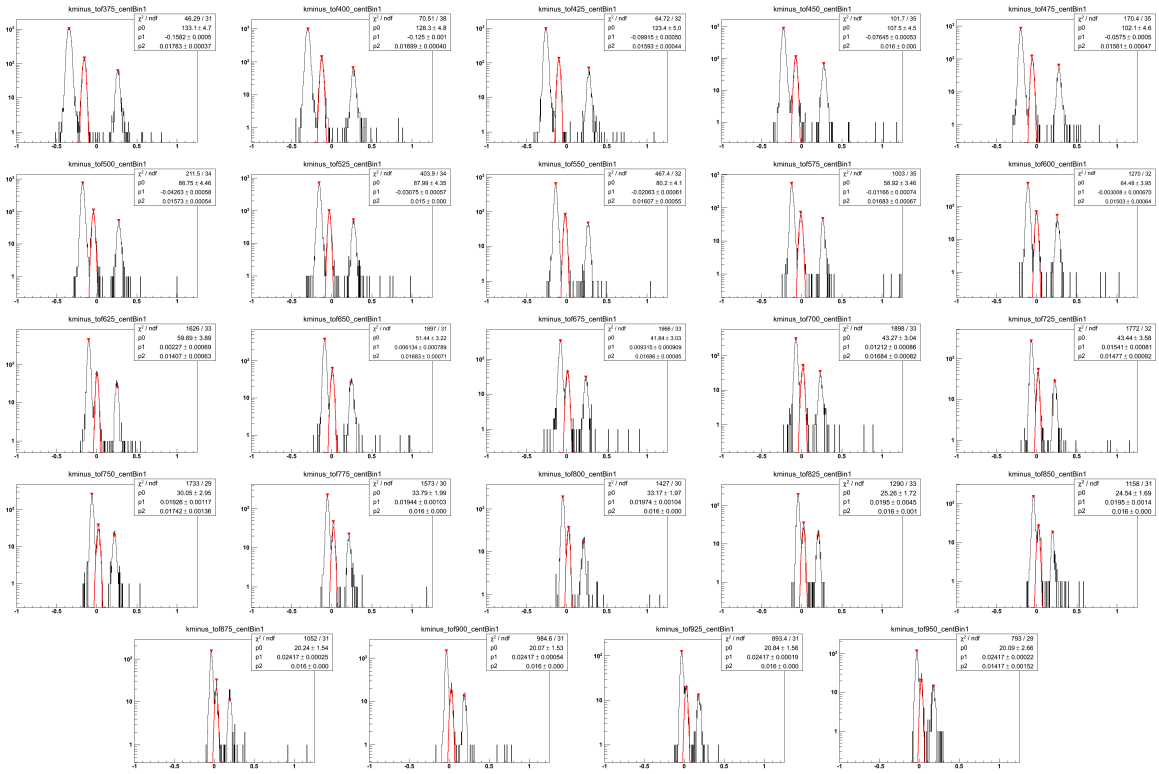

Figure A.20: Negative kaon TOF fits for 60%-70% central events Au+Au $\sqrt{s_{NN}} = 19.6$ GeV. These are organized in 25 MeV bins in $m_T - m_K$ in a rapidity window of 0.1 units around mid-rapidity, $|y| < 0.05$. The Gaussian fits, drawn in red, are in $\beta^{-1}_{\text{expected}} - \beta^{-1}_{\text{measured}}$ and are of the $m_T - m_K = 0.350$ to 1.0 GeV/c^2 range. The track data are represented in the black histogram.

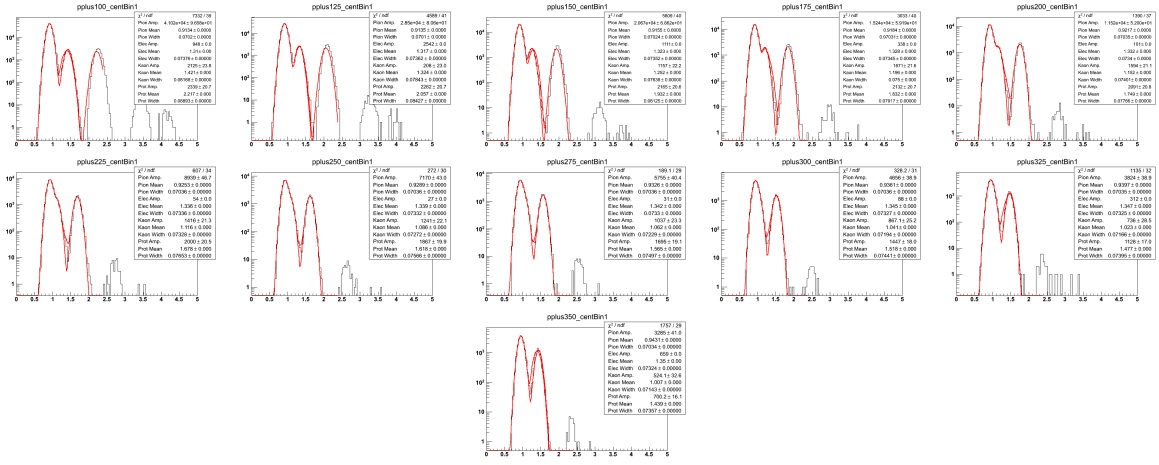

Figure A.21: Positive proton TPC fits for 60%-70% central events Au+Au $\sqrt{s_{NN}} = 19.6$ GeV. These are organized in 25 MeV bins in $m_T - m_p$ in a rapidity window of 0.1 units around mid-rapidity, $|y| < 0.05$. The Gaussian fits, drawn in red, are in $\log(10^6 \times dE/dx)$ and are of the $m_T - m_p = 0.100$ to 0.500 GeV/c^2 range. The track data are represented in the black histogram.

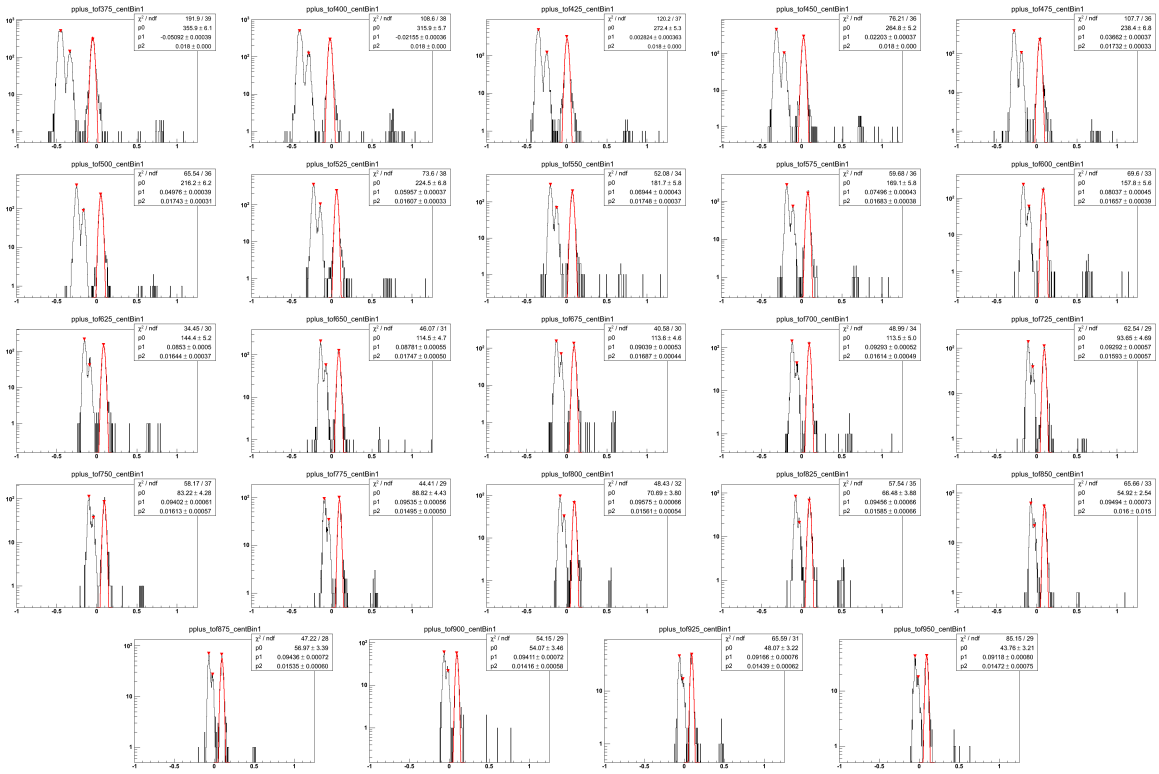

Figure A.22: Positive proton TOF fits for 60%-70% central events Au+Au $\sqrt{s_{NN}} = 19.6$ GeV. These are organized in 25 MeV bins in $m_T - m_p$ in a rapidity window of 0.1 units around mid-rapidity, $|y| < 0.05$. The Gaussian fits, drawn in red, are in $\beta^{-1}_{\text{expected}} - \beta^{-1}_{\text{measured}}$ and are of the $m_T - m_p = 0.350$ to 1.0 GeV/c^2 range. The track data are represented in the black histogram.

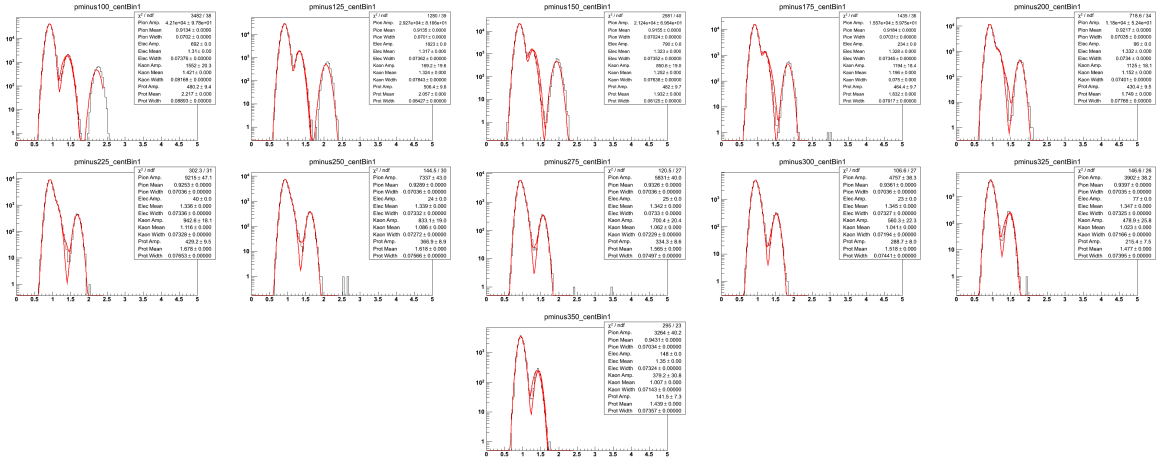

Figure A.23: Negative proton TPC fits for 60%-70% central events Au+Au $\sqrt{s_{NN}} = 19.6$ GeV. These are organized in 25 MeV bins in $m_T - m_p$ in a rapidity window of 0.1 units around mid-rapidity, $|y| < 0.05$. The Gaussian fits, drawn in red, are in $\log(10^6 \times dE/dx)$ and are of the $m_T - m_p = 0.100$ to 0.500 GeV/c^2 range. The track data are represented in the black histogram.

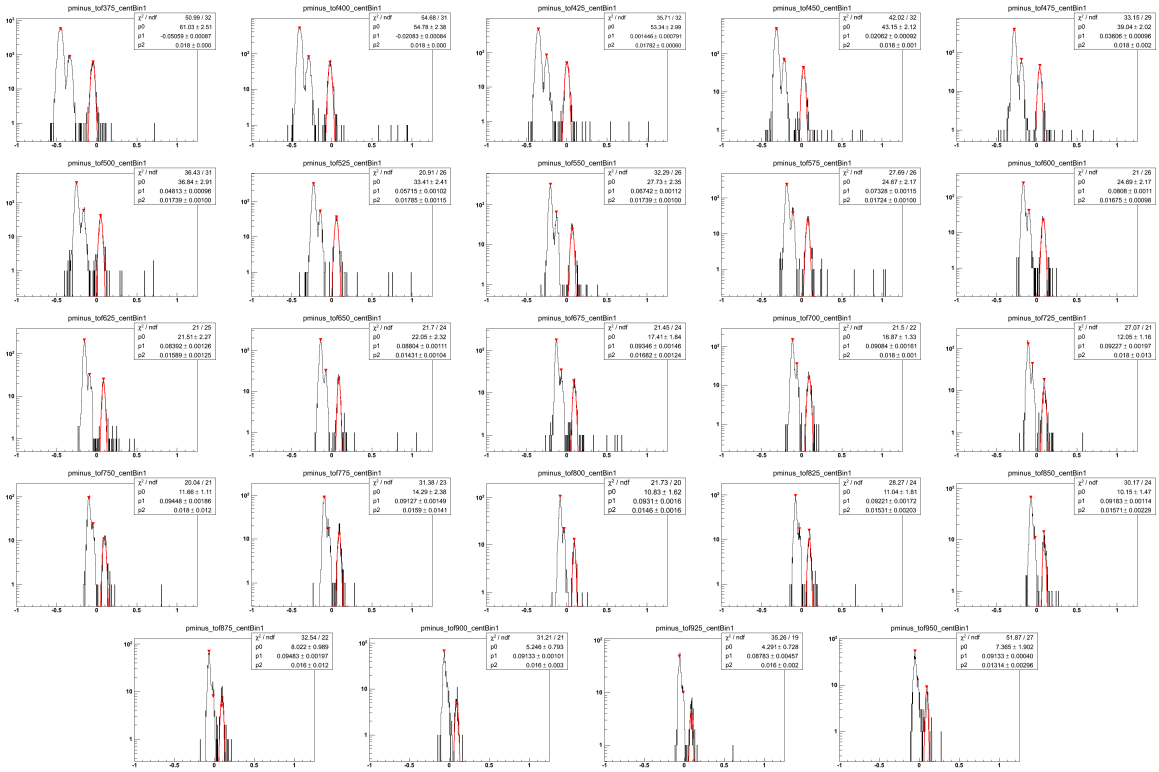

Figure A.24: Negative proton TOF fits for 60%-70% central events Au+Au $\sqrt{s_{NN}} = 19.6$ GeV. These are organized in 25 MeV bins in $m_T - m_p$ in a rapidity window of 0.1 units around mid-rapidity, $|y| < 0.05$. The Gaussian fits, drawn in red, are in $\beta^{-1}_{\text{expected}} - \beta^{-1}_{\text{measured}}$ and are of the $m_T - m_p = 0.350$ to 1.0 GeV/c^2 range. The track data are represented in the black histogram.

A.3 The 50%-60% Centrality Class

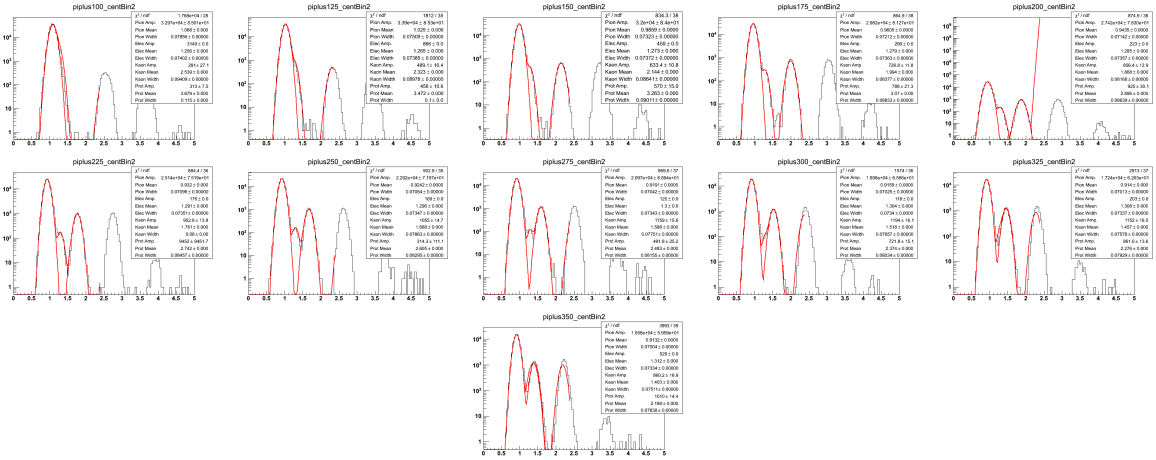

Figure A.25: Positive pion TPC fits for 50%-60% central events Au+Au $\sqrt{s_{NN}} = 19.6$ GeV. These are organized in 25 MeV bins in $m_T - m_\pi$ in a rapidity window of 0.1 units around mid-rapidity, $|y| < 0.05$. The Gaussian fits, drawn in red, are in $\log(10^6 \times dE/dx)$ and are of the $m_T - m_\pi =$ 0.100 to 0.500 GeV/c^2 range. The track data are represented in the black histogram.

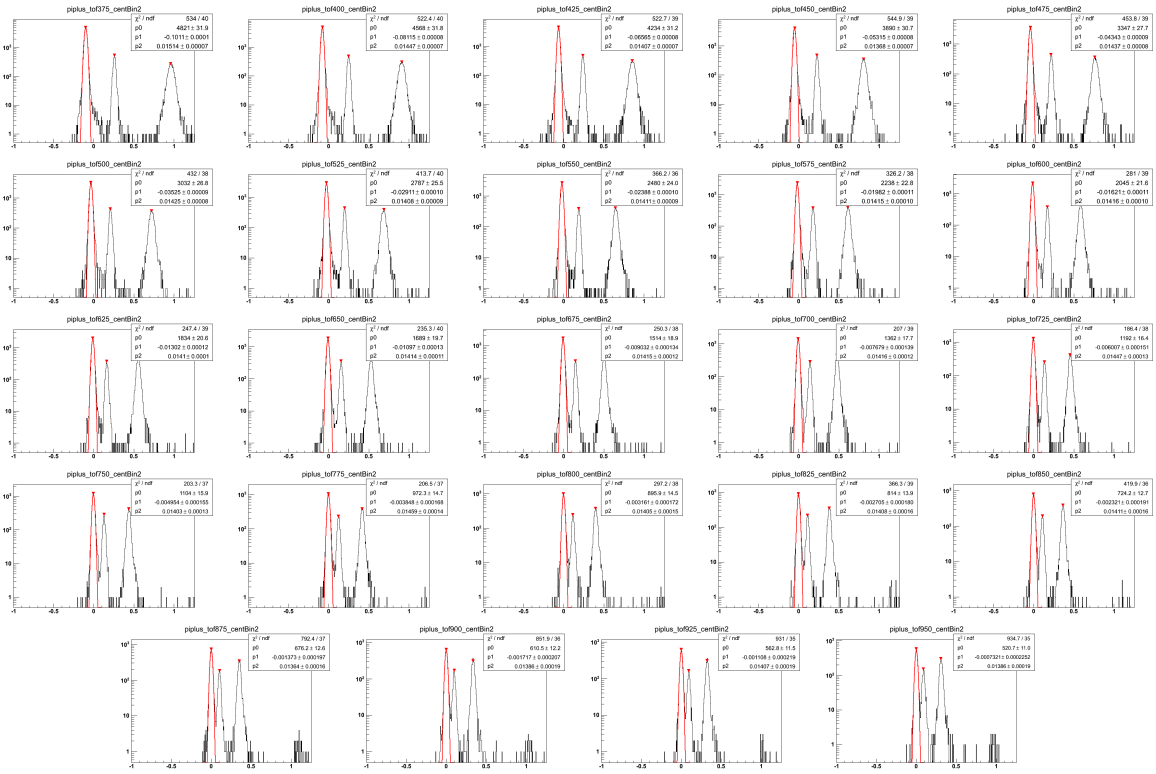

Figure A.26: Positive pion TOF fits for 50%-60% central events Au+Au $\sqrt{s_{NN}} = 19.6$ GeV. These are organized in 25 MeV bins in $m_T - m_\pi$ in a rapidity window of 0.1 units around mid-rapidity, $|y| < 0.05$. The Gaussian fits, drawn in red, are in $\beta^{-1}_{\text{expected}} - \beta^{-1}_{\text{measured}}$ and are of the $m_T - m_\pi = 0.350$ to 1.0 GeV/c^2 range. The track data are represented in the black histogram.

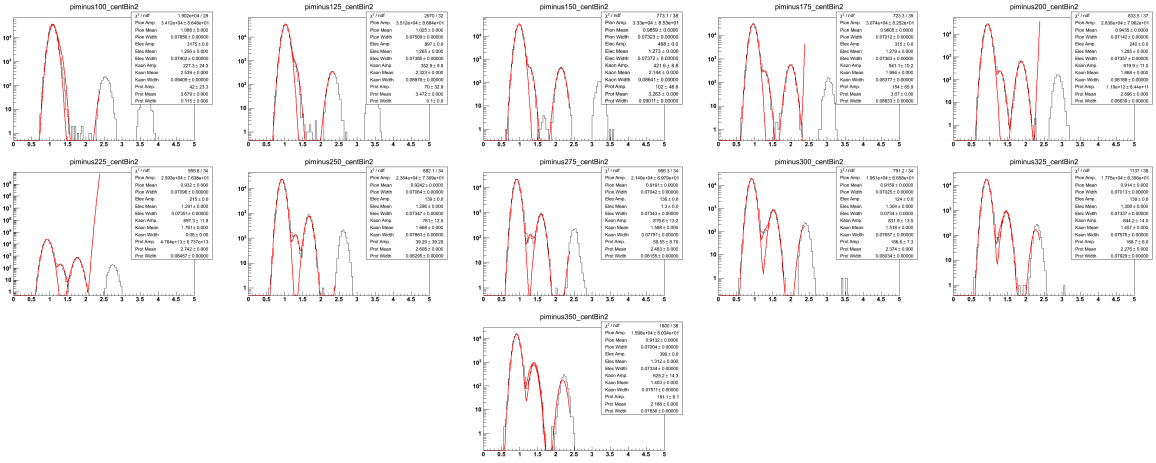

Figure A.27: Negative pion TPC fits for 50%-60% central events Au+Au $\sqrt{s_{NN}} = 19.6$ GeV. These are organized in 25 MeV bins in $m_T - m_\pi$ in a rapidity window of 0.1 units around mid-rapidity, $|y| < 0.05$. The Gaussian fits, drawn in red, are in $\log(10^6 \times dE/dx)$ and are of the $m_T - m_\pi = 0.100$ to 0.500 GeV/c^2 range. The track data are represented in the black histogram.

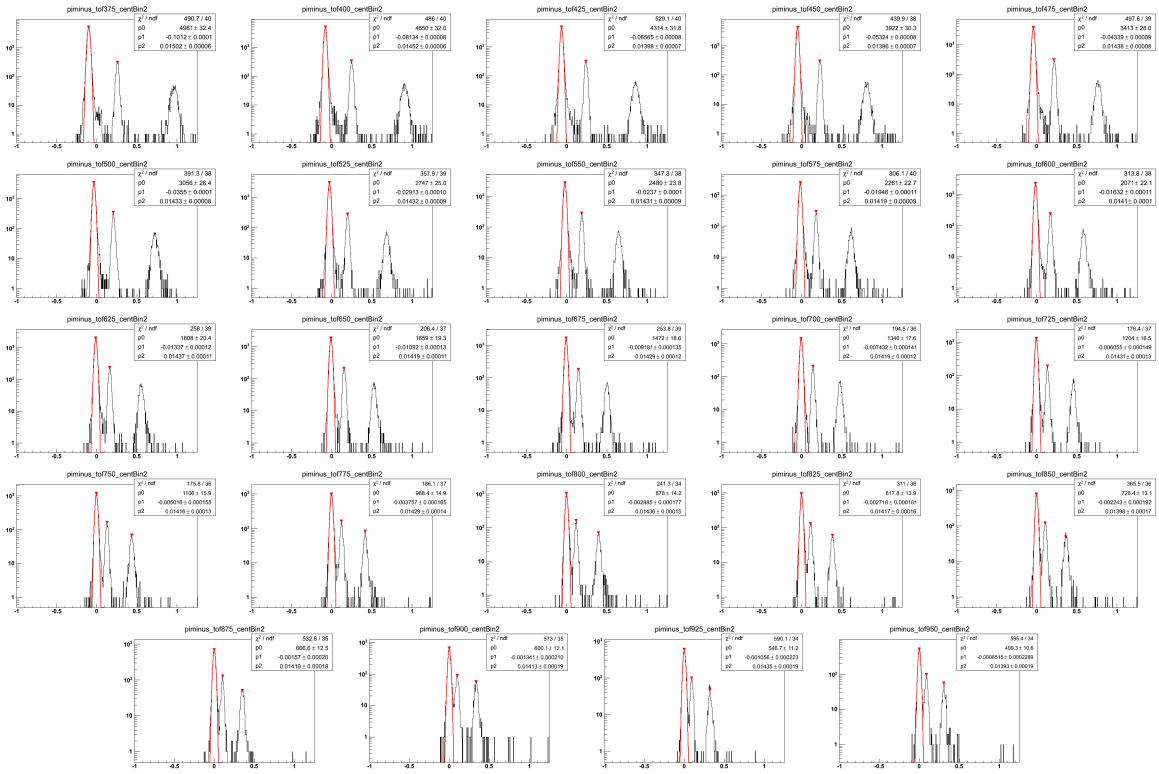

Figure A.28: Negative pion TOF fits for 50%-60% central events Au+Au $\sqrt{s_{NN}} = 19.6$ GeV. These are organized in 25 MeV bins in $m_T - m_\pi$ in a rapidity window of 0.1 units around mid-rapidity, $|y| < 0.05$. The Gaussian fits, drawn in red, are in $\beta^{-1}_{\text{expected}} - \beta^{-1}_{\text{measured}}$ and are of the $m_T - m_\pi = 0.350$ to 1.0 GeV/c^2 range. The track data are represented in the black histogram.

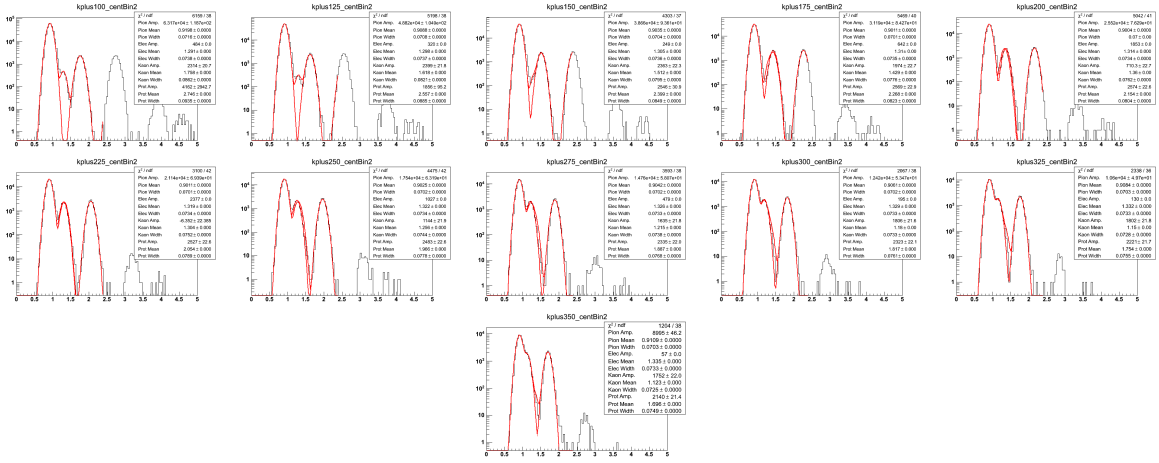

Figure A.29: Positive kaon TPC fits for 50%-60% central events Au+Au $\sqrt{s_{NN}} = 19.6$ GeV. These are organized in 25 MeV bins in $m_T - m_K$ in a rapidity window of 0.1 units around mid-rapidity, $|y| < 0.05$. The Gaussian fits, drawn in red, are in $\log(10^6 \times dE/dx)$ and are of the $m_T - m_K = 0.100$ to 0.500 GeV/c^2 range. The track data are represented in the black histogram.

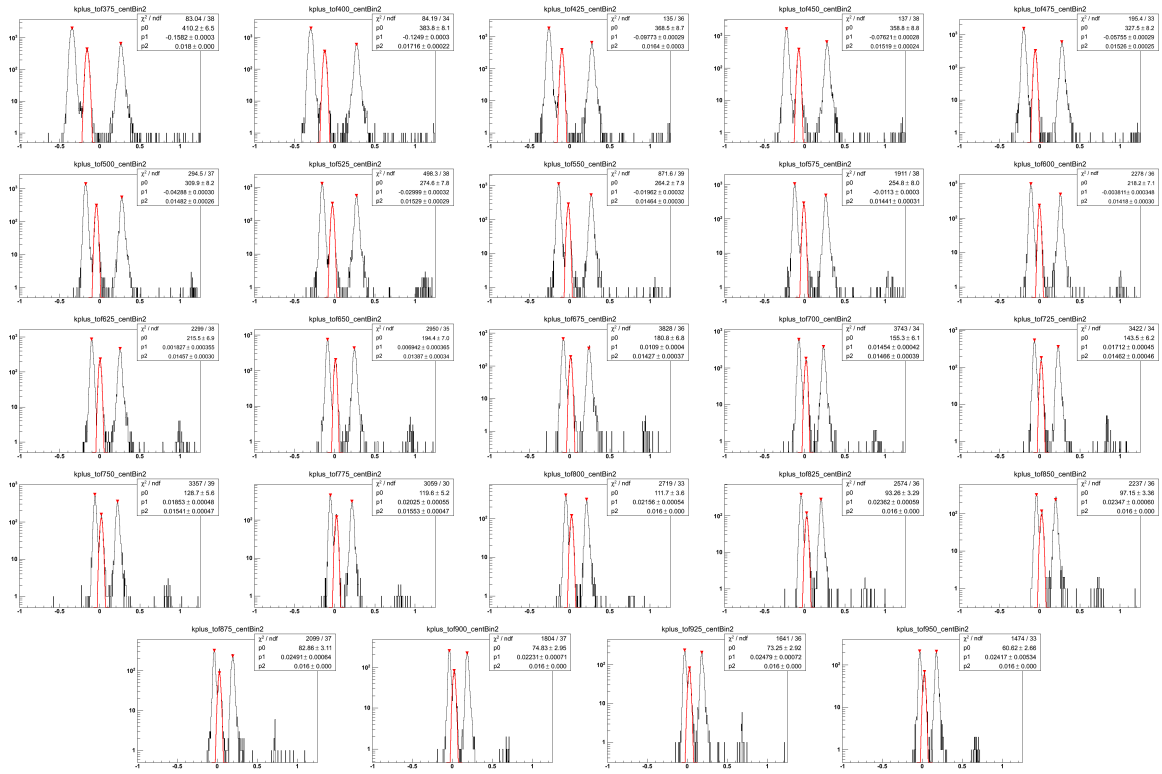

Figure A.30: Positive kaon TOF fits for 50%-60% central events Au+Au $\sqrt{s_{NN}} = 19.6$ GeV. These are organized in 25 MeV bins in $m_T - m_K$ in a rapidity window of 0.1 units around mid-rapidity, $|y| < 0.05$. The Gaussian fits, drawn in red, are in $\beta^{-1}_{\text{expected}} - \beta^{-1}_{\text{measured}}$ and are of the $m_T - m_K =$ 0.350 to 1.0 GeV/c^2 range. The track data are represented in the black histogram.

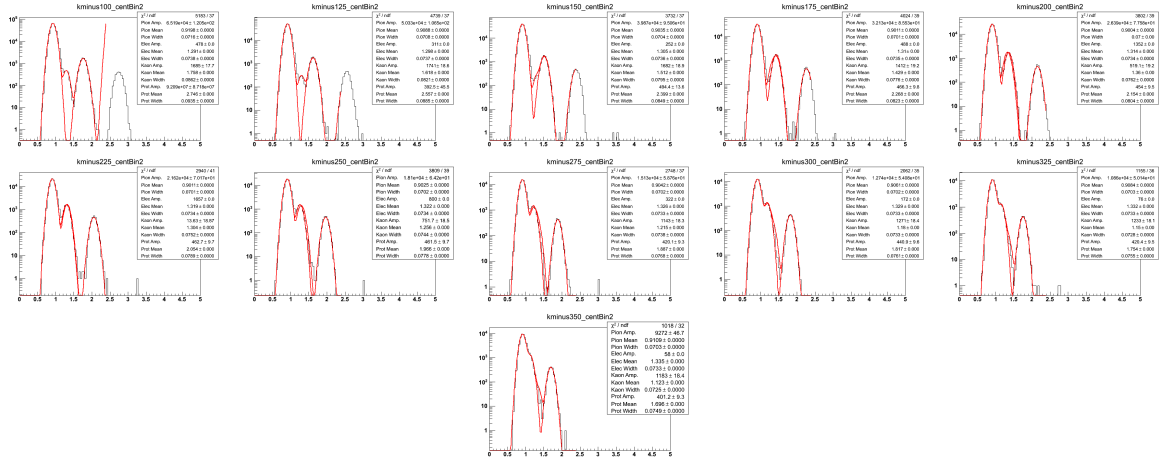

Figure A.31: Negative kaon TPC fits for 50%-60% central events Au+Au $\sqrt{s_{NN}} = 19.6$ GeV. These are organized in 25 MeV bins in $m_T - m_K$ in a rapidity window of 0.1 units around mid-rapidity, $|y| < 0.05$. The Gaussian fits, drawn in red, are in $\log(10^6 \times dE/dx)$ and are of the $m_T - m_K = 0.100$ to 0.500 GeV/c^2 range. The track data are represented in the black histogram.

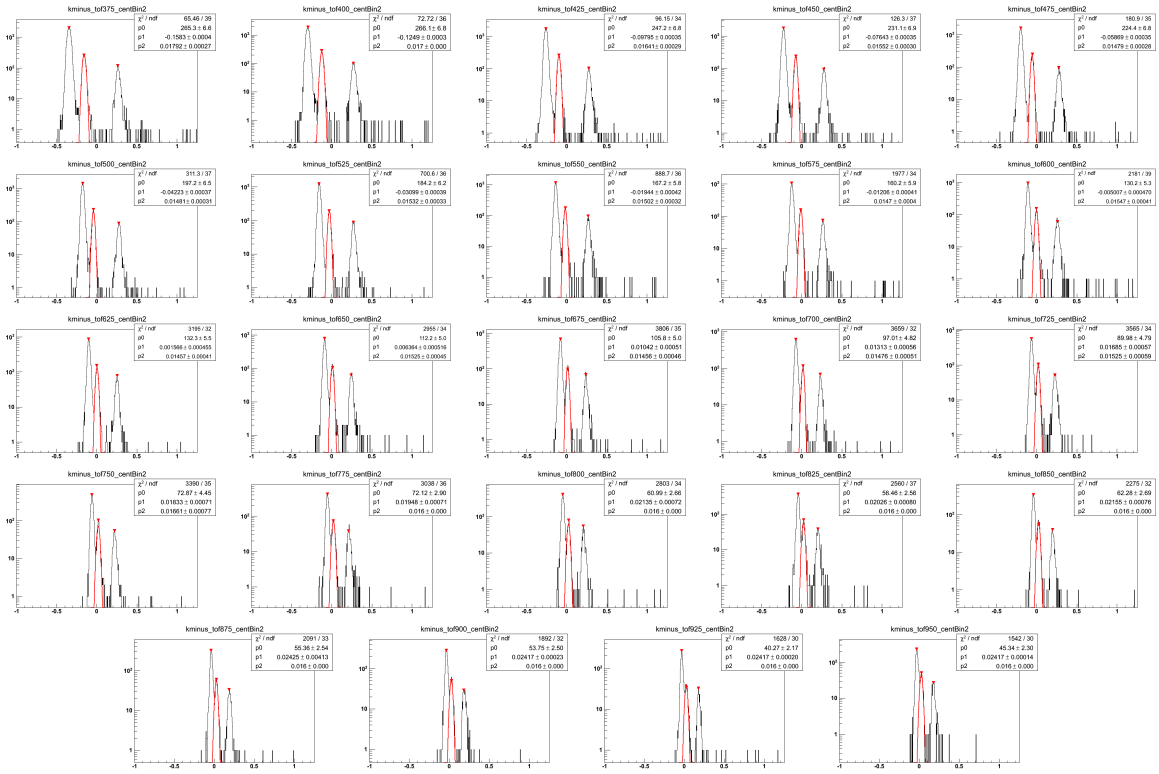

Figure A.32: Negative kaon TOF fits for 50%-60% central events Au+Au $\sqrt{s_{NN}} = 19.6$ GeV. These are organized in 25 MeV bins in $m_T - m_K$ in a rapidity window of 0.1 units around mid-rapidity, $|y| < 0.05$. The Gaussian fits, drawn in red, are in $\beta^{-1}_{\text{expected}} - \beta^{-1}_{\text{measured}}$ and are of the $m_T - m_K = 0.350$ to 1.0 GeV/c^2 range. The track data are represented in the black histogram.

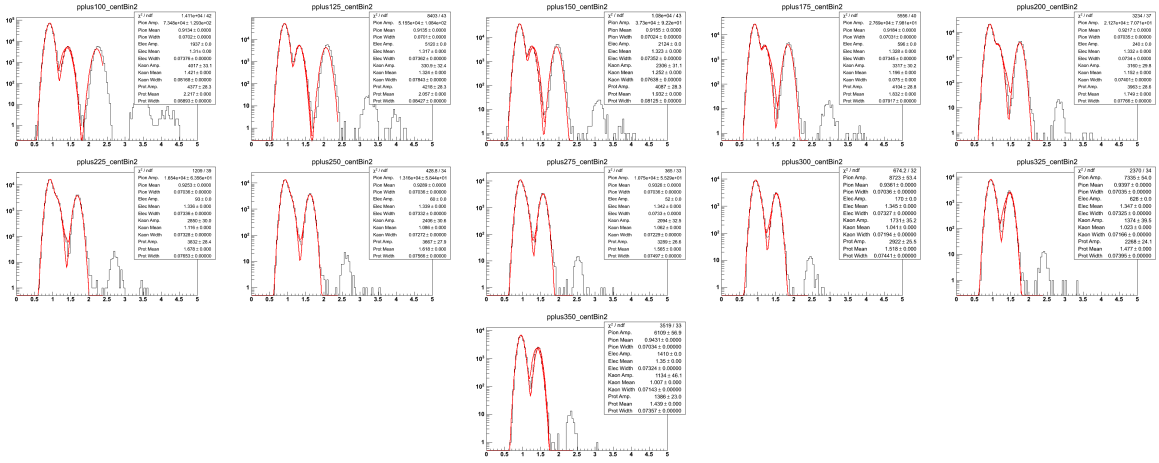

Figure A.33: Positive proton TPC fits for 50%-60% central events Au+Au $\sqrt{s_{NN}} = 19.6$ GeV. These are organized in 25 MeV bins in $m_T - m_p$ in a rapidity window of 0.1 units around mid-rapidity, $|y| < 0.05$. The Gaussian fits, drawn in red, are in $\log(10^6 \times dE/dx)$ and are of the $m_T - m_p = 0.100$ to 0.500 GeV/c^2 range. The track data are represented in the black histogram.

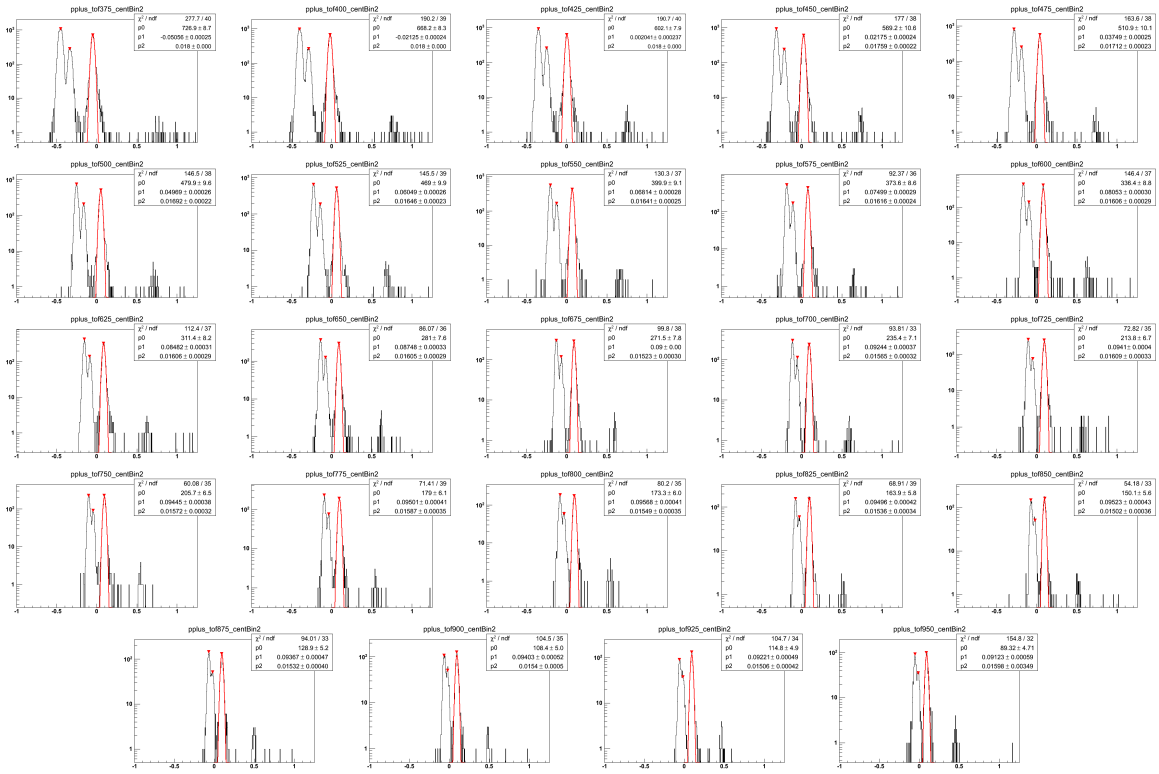

Figure A.34: Positive proton TOF fits for 50%-60% central events Au+Au $\sqrt{s_{NN}} = 19.6$ GeV. These are organized in 25 MeV bins in $m_T - m_p$ in a rapidity window of 0.1 units around mid-rapidity, $|y| < 0.05$. The Gaussian fits, drawn in red, are in $\beta^{-1}_{\text{expected}} - \beta^{-1}_{\text{measured}}$ and are of the $m_T - m_p = 0.350$ to 1.0 GeV/c^2 range. The track data are represented in the black histogram.

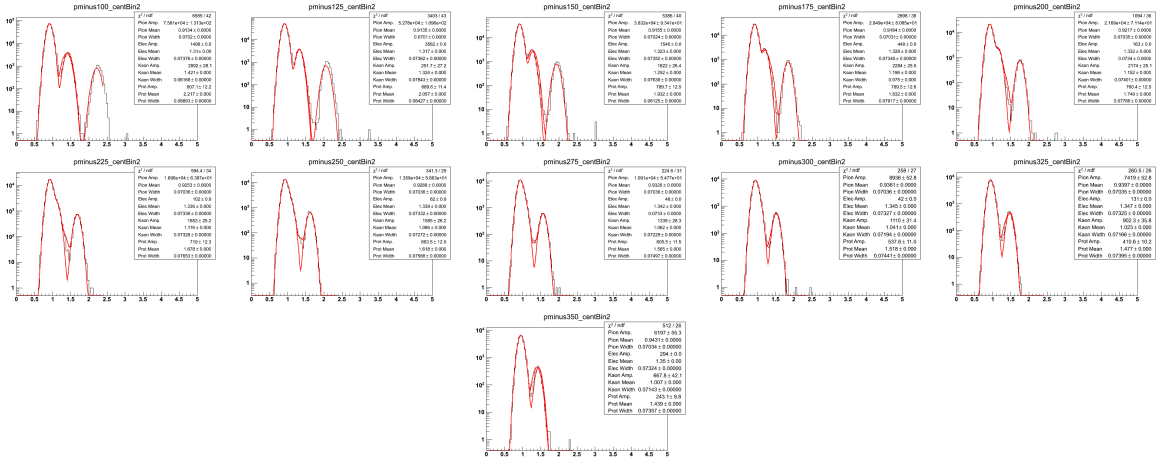

Figure A.35: Negative proton TPC fits for 50%-60% central events Au+Au $\sqrt{s_{NN}} = 19.6$ GeV. These are organized in 25 MeV bins in $m_T - m_p$ in a rapidity window of 0.1 units around mid-rapidity, $|y| < 0.05$. The Gaussian fits, drawn in red, are in $\log(10^6 \times dE/dx)$ and are of the $m_T - m_p = 0.100$ to 0.500 GeV/c^2 range. The track data are represented in the black histogram.

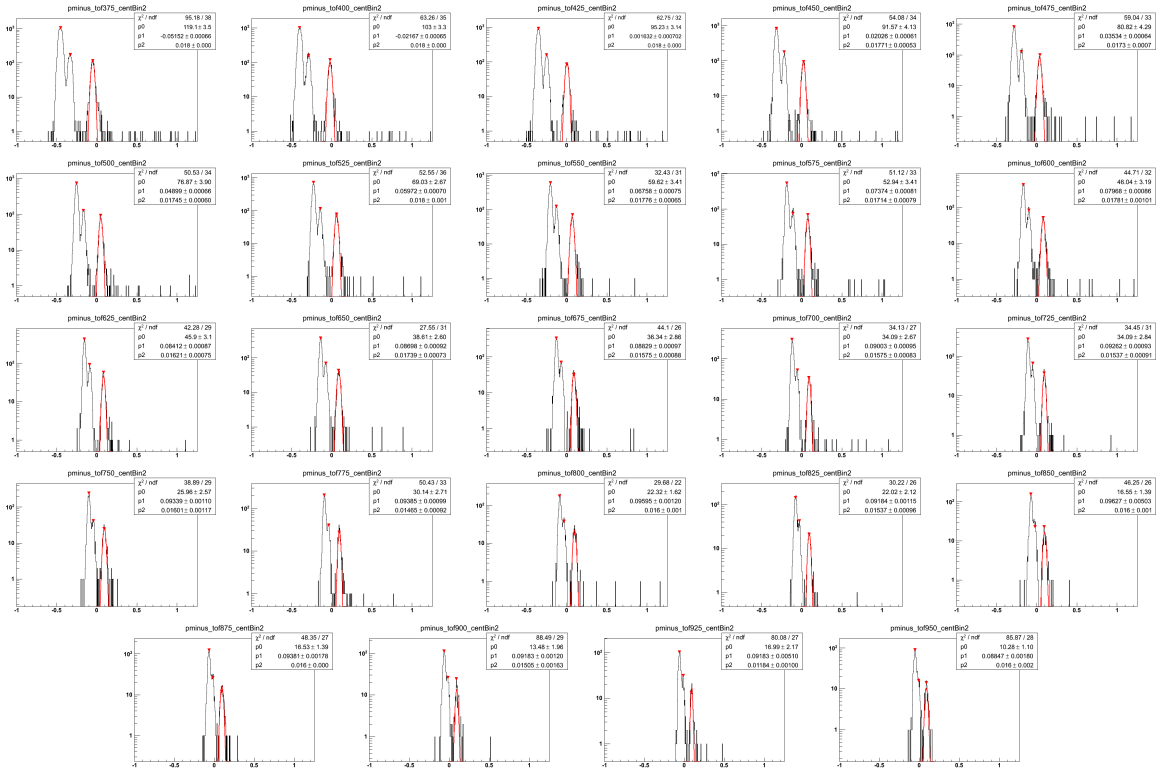

Figure A.36: Negative proton TOF fits for 50%-60% central events Au+Au $\sqrt{s_{NN}} = 19.6$ GeV. These are organized in 25 MeV bins in $m_T - m_p$ in a rapidity window of 0.1 units around mid-rapidity, $|y| < 0.05$. The Gaussian fits, drawn in red, are in $\beta^{-1}_{\text{expected}} - \beta^{-1}_{\text{measured}}$ and are of the $m_T - m_p = 0.350$ to 1.0 GeV/c^2 range. The track data are represented in the black histogram.

A.4 The 40%-50% Centrality Class

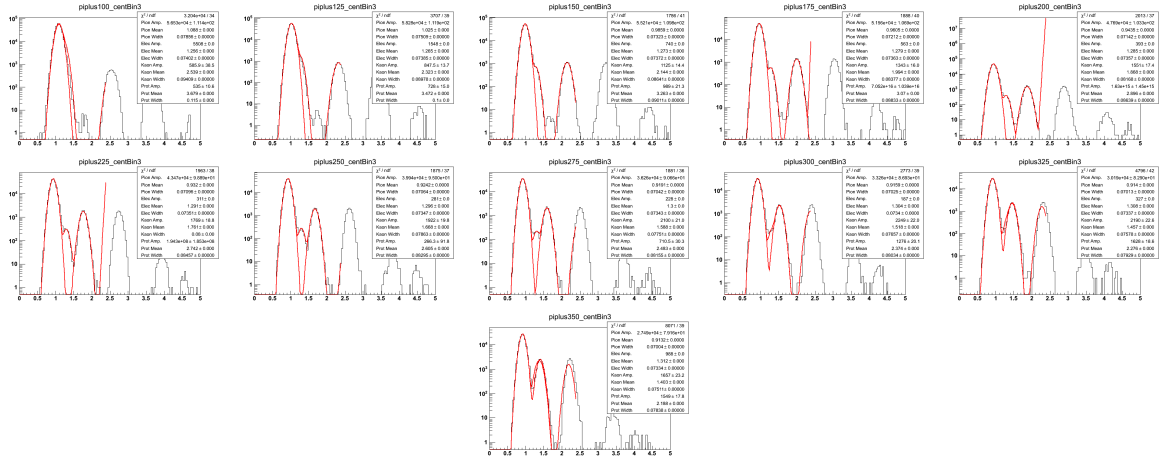

Figure A.37: Positive pion TPC fits for 40%-50% central events Au+Au $\sqrt{s_{NN}} = 19.6$ GeV. These are organized in 25 MeV bins in $m_T - m_\pi$ in a rapidity window of 0.1 units around mid-rapidity, $|y| < 0.05$. The Gaussian fits, drawn in red, are in $\log(10^6 \times dE/dx)$ and are of the $m_T - m_\pi =$ 0.100 to 0.500 GeV/c^2 range. The track data are represented in the black histogram.

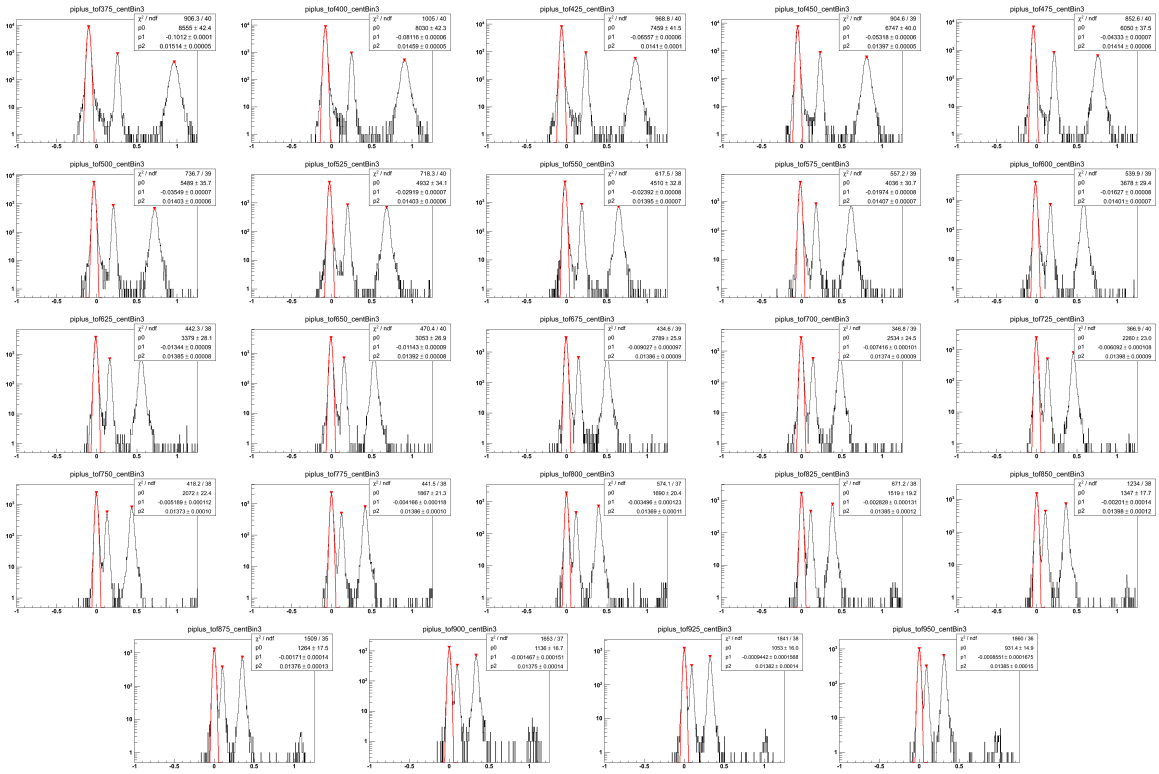

Figure A.38: Positive pion TOF fits for 40%-50% central events Au+Au $\sqrt{s_{NN}} = 19.6$ GeV. These are organized in 25 MeV bins in $m_T - m_\pi$ in a rapidity window of 0.1 units around mid-rapidity, $|y| < 0.05$. The Gaussian fits, drawn in red, are in $\beta^{-1}_{\text{expected}} - \beta^{-1}_{\text{measured}}$ and are of the $m_T - m_\pi = 0.350$ to 1.0 GeV/c^2 range. The track data are represented in the black histogram.

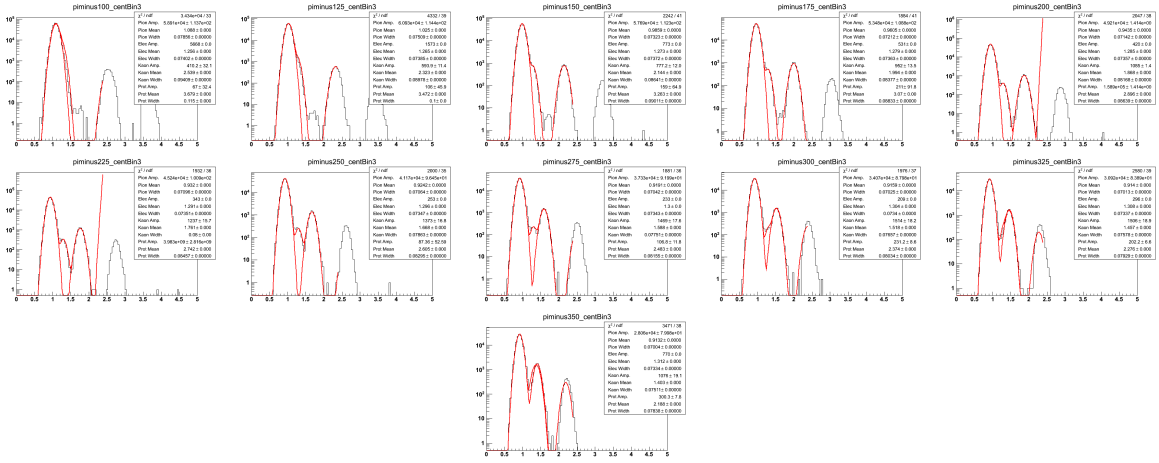

Figure A.39: Negative pion TPC fits for 40%-50% central events Au+Au $\sqrt{s_{NN}} = 19.6$ GeV. These are organized in 25 MeV bins in $m_T - m_\pi$ in a rapidity window of 0.1 units around mid-rapidity, $|y| < 0.05$. The Gaussian fits, drawn in red, are in $\log(10^6 \times dE/dx)$ and are of the $m_T - m_\pi = 0.100$ to 0.500 GeV/c^2 range. The track data are represented in the black histogram.

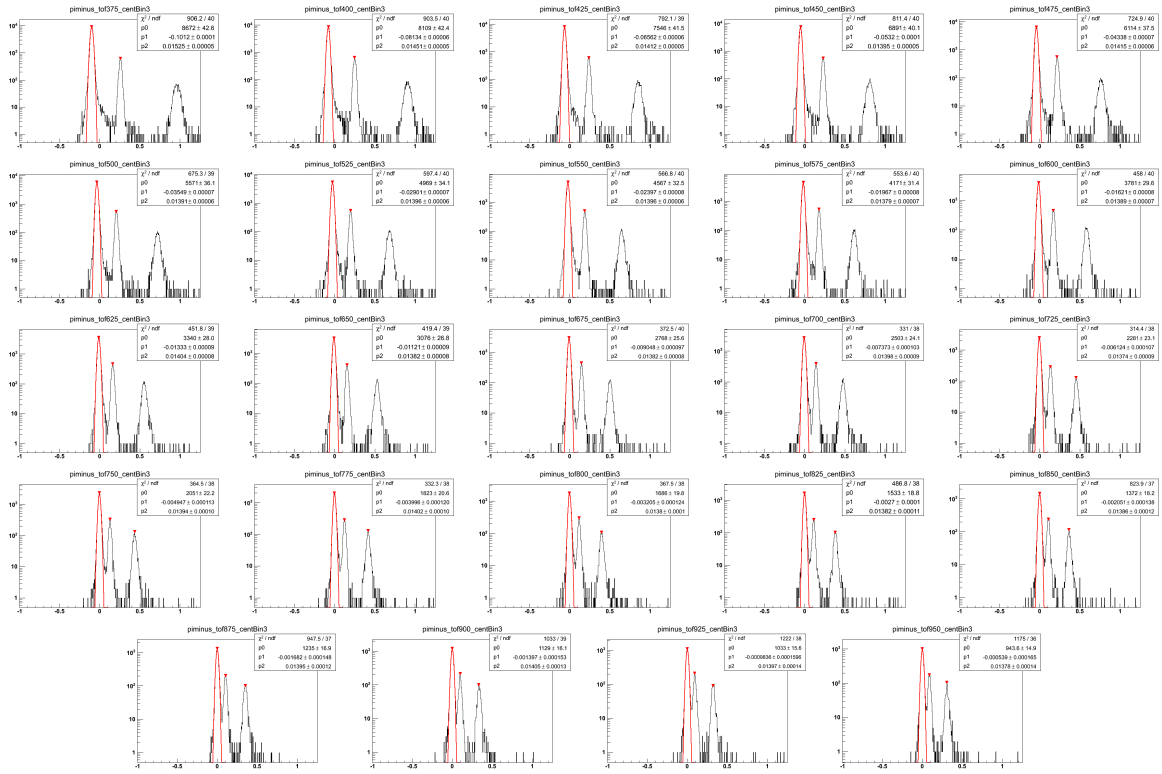

Figure A.40: Negative pion TOF fits for 40%-50% central events Au+Au $\sqrt{s_{NN}} = 19.6$ GeV. These are organized in 25 MeV bins in $m_T - m_\pi$ in a rapidity window of 0.1 units around mid-rapidity, $|y| < 0.05$. The Gaussian fits, drawn in red, are in $\beta^{-1}_{\text{expected}} - \beta^{-1}_{\text{measured}}$ and are of the $m_T - m_\pi = 0.350$ to 1.0 GeV/c^2 range. The track data are represented in the black histogram.

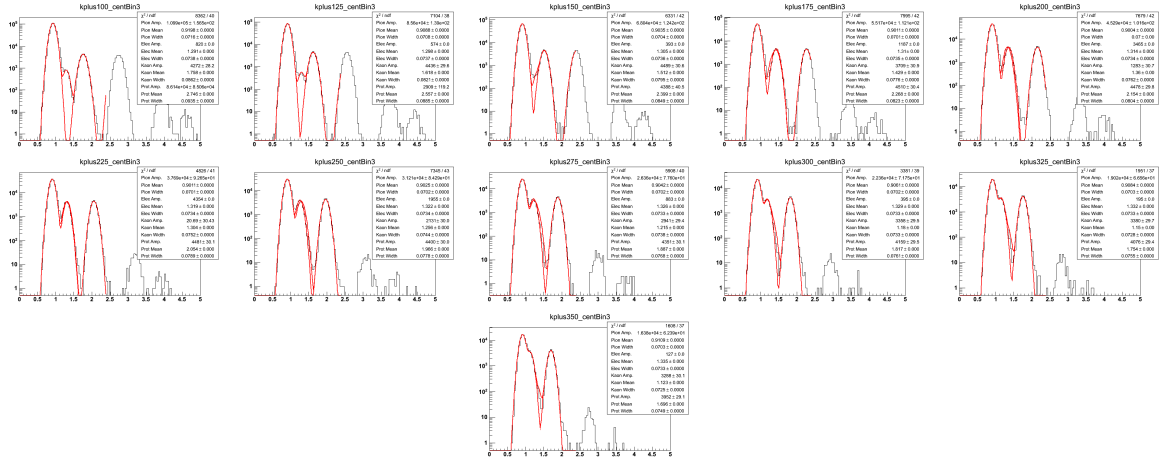

Figure A.41: Positive kaon TPC fits for 40%-50% central events Au+Au $\sqrt{s_{NN}} = 19.6$ GeV. These are organized in 25 MeV bins in $m_T - m_K$ in a rapidity window of 0.1 units around mid-rapidity, $|y| < 0.05$. The Gaussian fits, drawn in red, are in $\log(10^6 \times dE/dx)$ and are of the $m_T - m_K = 0.100$ to 0.500 GeV/c^2 range. The track data are represented in the black histogram.

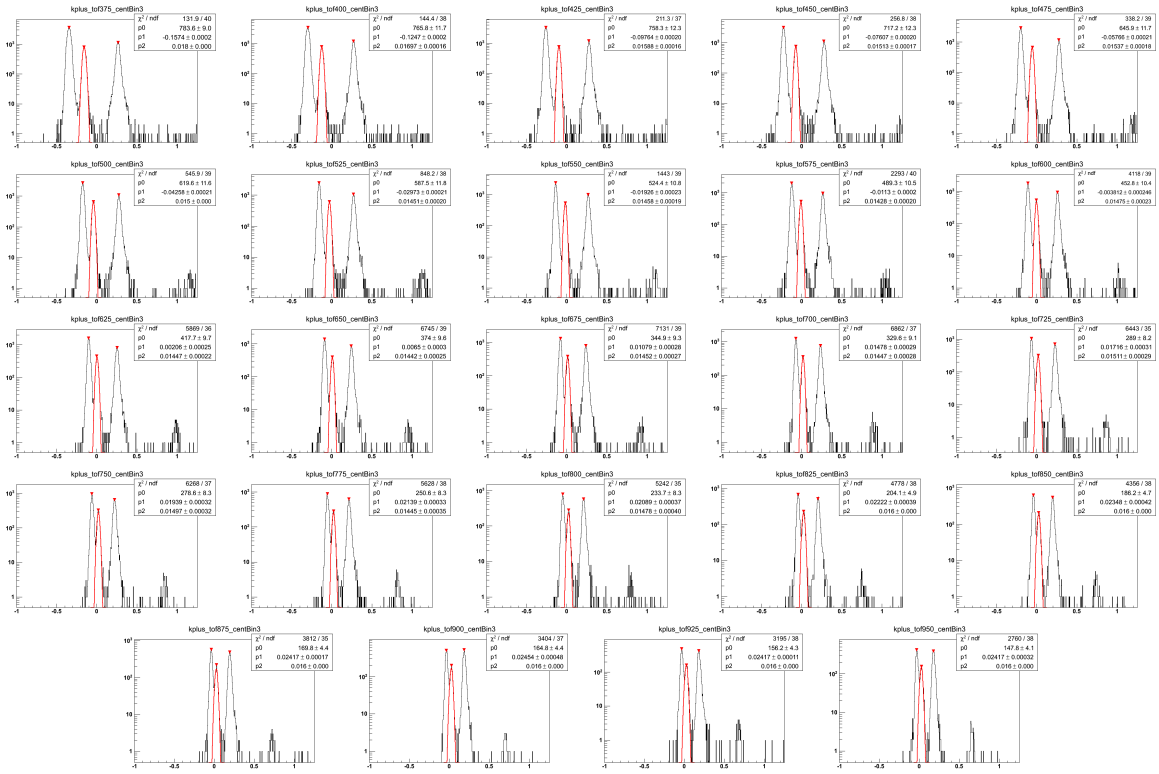

Figure A.42: Positive kaon TOF fits for 40%-50% central events Au+Au $\sqrt{s_{NN}} = 19.6$ GeV. These are organized in 25 MeV bins in $m_T - m_K$ in a rapidity window of 0.1 units around mid-rapidity, $|y| < 0.05$. The Gaussian fits, drawn in red, are in $\beta^{-1}_{\text{expected}} - \beta^{-1}_{\text{measured}}$ and are of the $m_T - m_K =$ 0.350 to 1.0 GeV/c^2 range. The track data are represented in the black histogram.

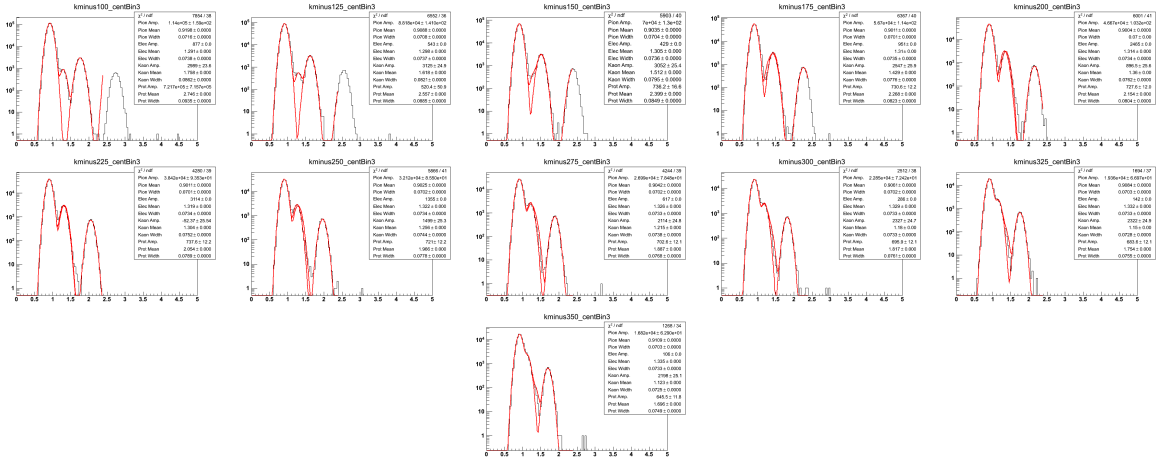

Figure A.43: Negative kaon TPC fits for 40%-50% central events Au+Au $\sqrt{s_{NN}} = 19.6$ GeV. These are organized in 25 MeV bins in $m_T - m_K$ in a rapidity window of 0.1 units around mid-rapidity, $|y| < 0.05$. The Gaussian fits, drawn in red, are in $\log(10^6 \times dE/dx)$ and are of the $m_T - m_K = 0.100$ to 0.500 GeV/c^2 range. The track data are represented in the black histogram.

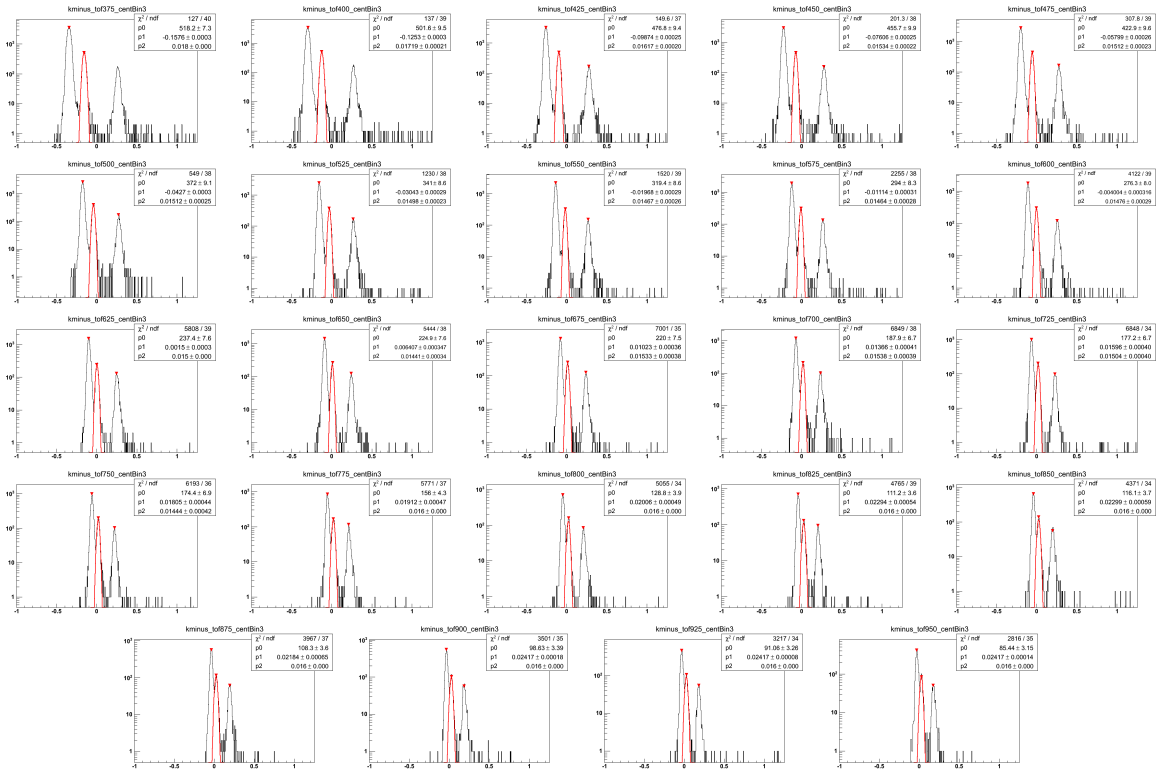

Figure A.44: Negative kaon TOF fits for 40%-50% central events Au+Au $\sqrt{s_{NN}} = 19.6$ GeV. These are organized in 25 MeV bins in $m_T - m_K$ in a rapidity window of 0.1 units around mid-rapidity, $|y| < 0.05$. The Gaussian fits, drawn in red, are in $\beta^{-1}_{\text{expected}} - \beta^{-1}_{\text{measured}}$ and are of the $m_T - m_K = 0.350$ to 1.0 GeV/c^2 range. The track data are represented in the black histogram.

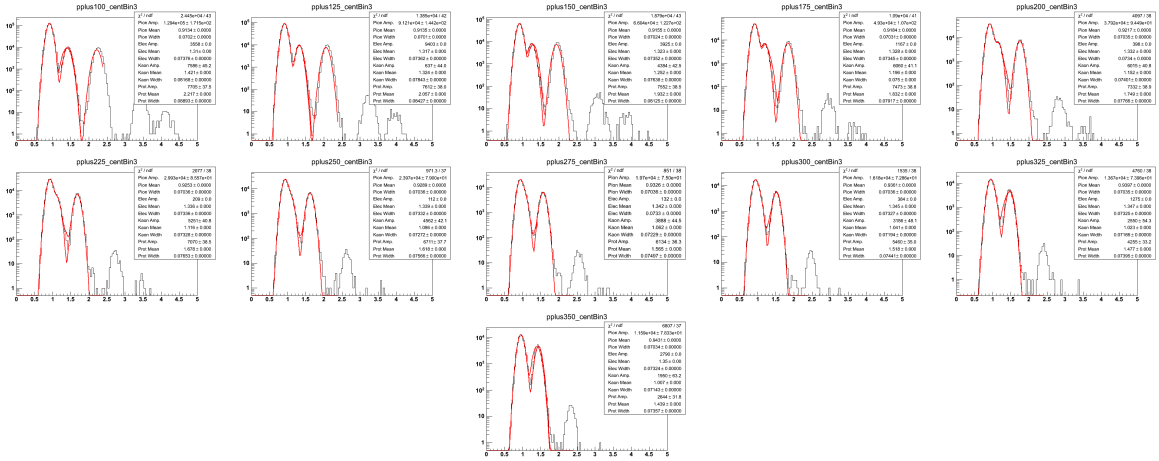

Figure A.45: Positive proton TPC fits for 40%-50% central events Au+Au $\sqrt{s_{NN}} = 19.6$ GeV. These are organized in 25 MeV bins in $m_T - m_p$ in a rapidity window of 0.1 units around mid-rapidity, $|y| < 0.05$. The Gaussian fits, drawn in red, are in $\log(10^6 \times dE/dx)$ and are of the $m_T - m_p = 0.100$ to 0.500 GeV/c^2 range. The track data are represented in the black histogram.

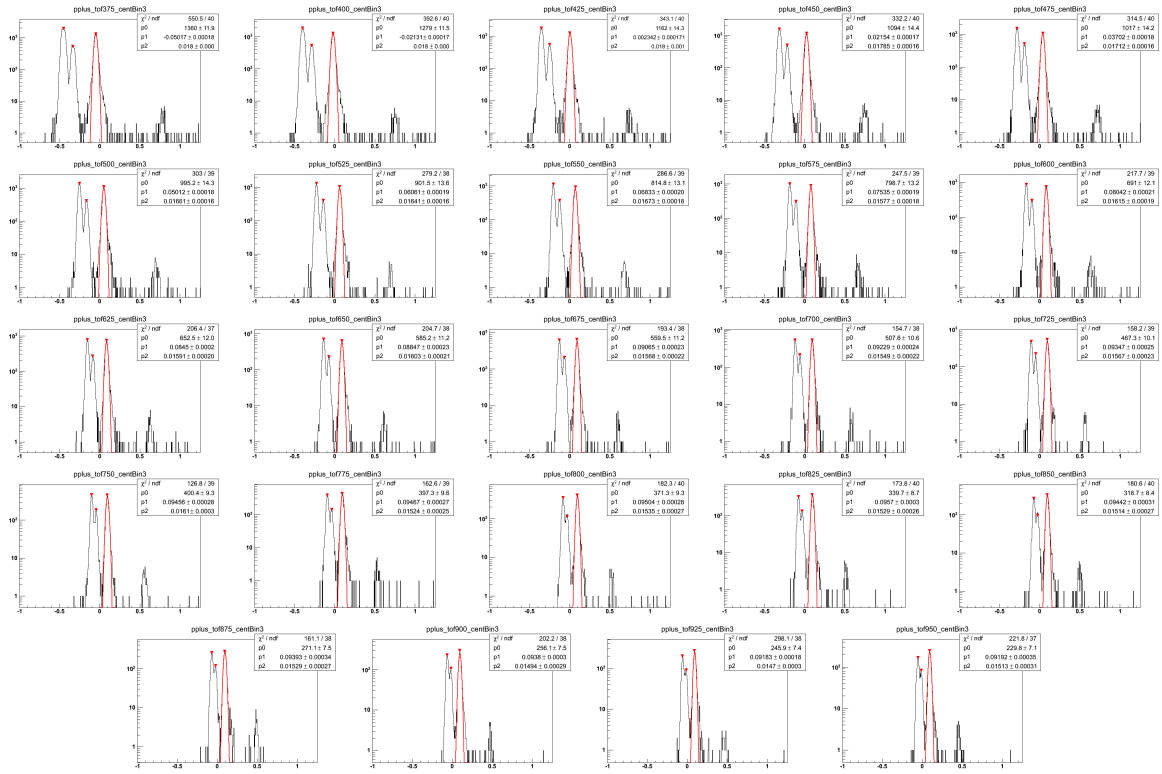

Figure A.46: Positive proton TOF fits for 40%-50% central events Au+Au $\sqrt{s_{NN}} = 19.6$ GeV. These are organized in 25 MeV bins in $m_T - m_p$ in a rapidity window of 0.1 units around mid-rapidity, $|y| < 0.05$. The Gaussian fits, drawn in red, are in $\beta^{-1}_{\text{expected}} - \beta^{-1}_{\text{measured}}$ and are of the $m_T - m_p = 0.350$ to 1.0 GeV/c^2 range. The track data are represented in the black histogram.

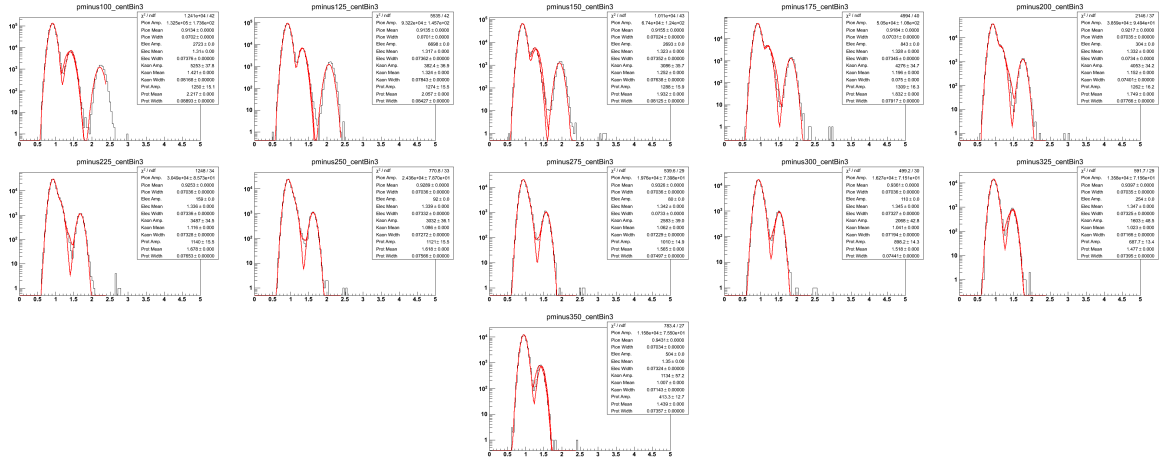

Figure A.47: Negative proton TPC fits for 40%-50% central events Au+Au $\sqrt{s_{NN}} = 19.6$ GeV. These are organized in 25 MeV bins in $m_T - m_p$ in a rapidity window of 0.1 units around mid-rapidity, $|y| < 0.05$. The Gaussian fits, drawn in red, are in $\log(10^6 \times dE/dx)$ and are of the $m_T - m_p = 0.100$ to 0.500 GeV/c^2 range. The track data are represented in the black histogram.

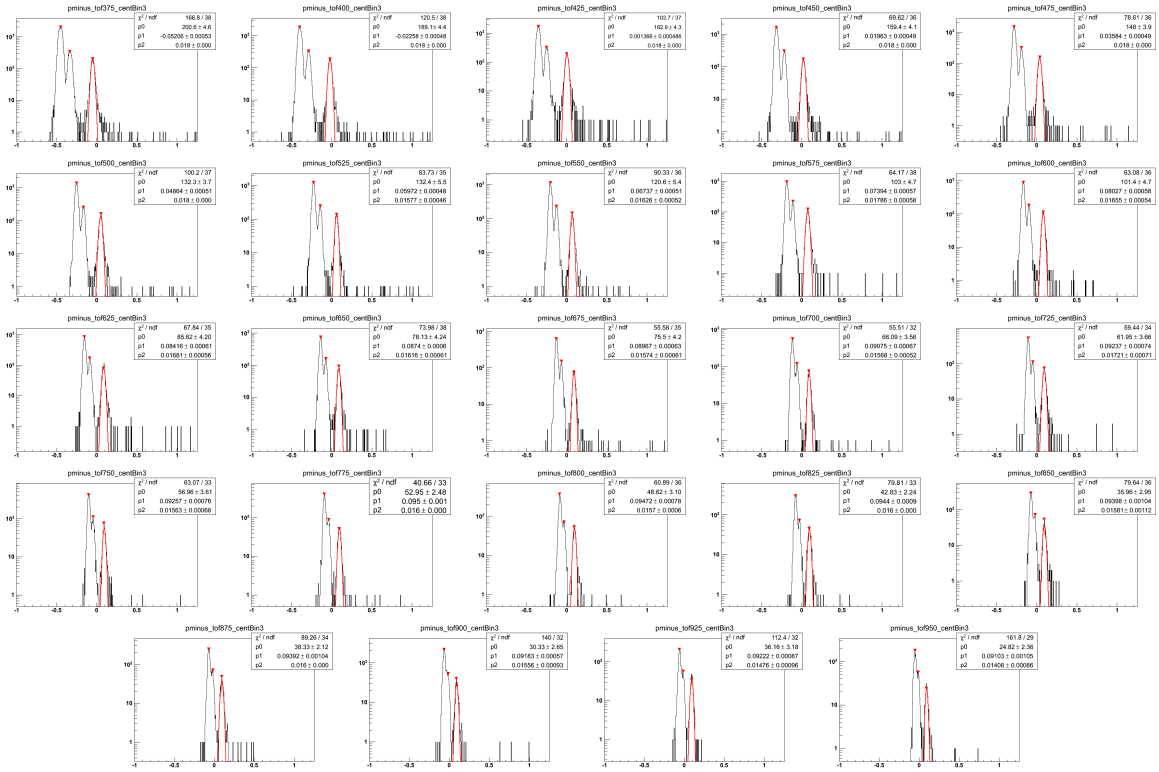

Figure A.48: Negative proton TOF fits for 40%-50% central events Au+Au $\sqrt{s_{NN}} = 19.6$ GeV. These are organized in 25 MeV bins in $m_T - m_p$ in a rapidity window of 0.1 units around mid-rapidity, $|y| < 0.05$. The Gaussian fits, drawn in red, are in $\beta^{-1}_{\text{expected}} - \beta^{-1}_{\text{measured}}$ and are of the $m_T - m_p = 0.350$ to 1.0 GeV/c^2 range. The track data are represented in the black histogram.

A.5 The 30%-40% Centrality Class

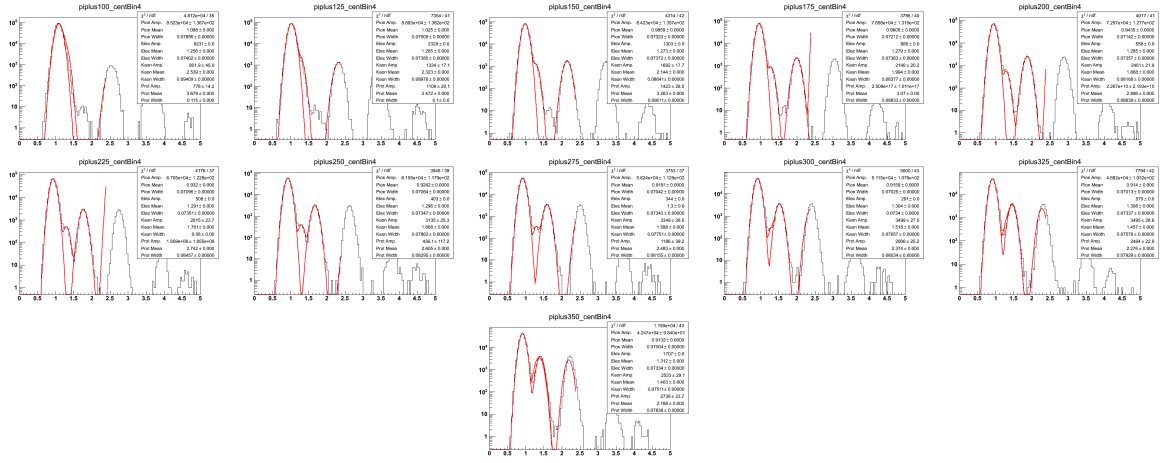

Figure A.49: Positive pion TPC fits for 30%-40% central events Au+Au $\sqrt{s_{NN}} = 19.6$ GeV. These are organized in 25 MeV bins in $m_T - m_\pi$ in a rapidity window of 0.1 units around mid-rapidity, $|y| < 0.05$. The Gaussian fits, drawn in red, are in $\log(10^6 \times dE/dx)$ and are of the $m_T - m_\pi =$ 0.100 to 0.500 GeV/c^2 range. The track data are represented in the black histogram.

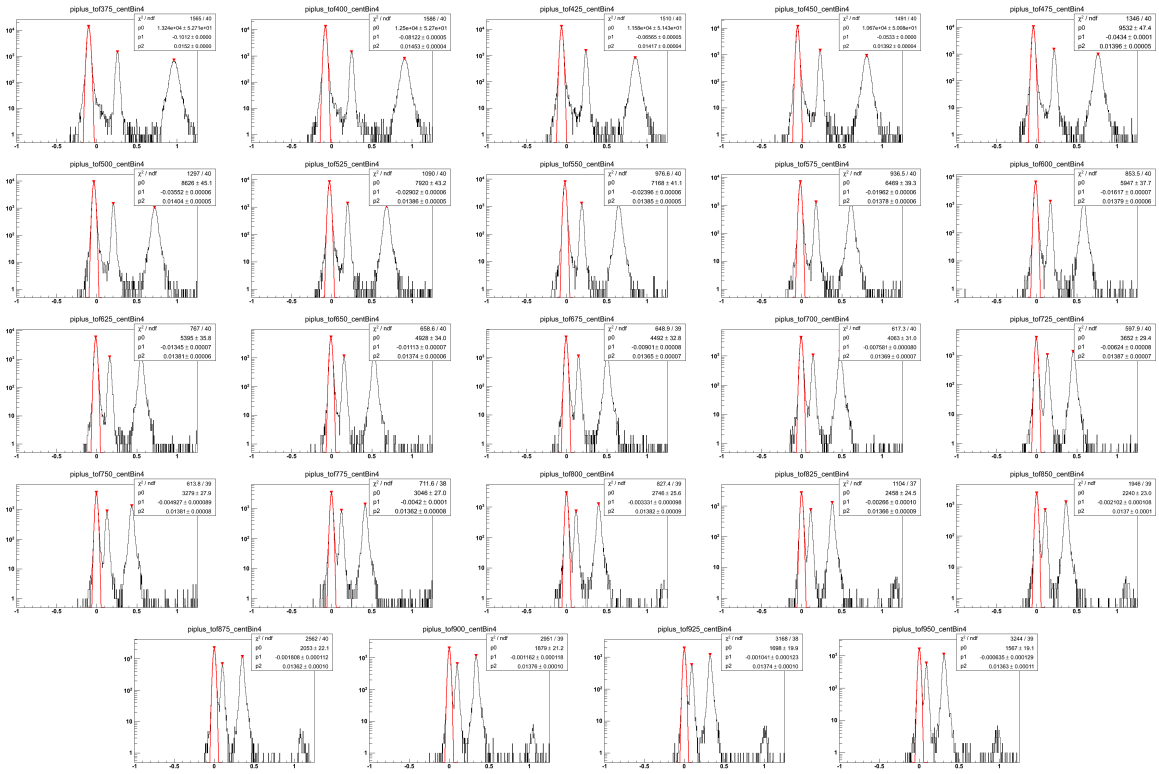

Figure A.50: Positive pion TOF fits for 30%-40% central events Au+Au $\sqrt{s_{NN}} = 19.6$ GeV. These are organized in 25 MeV bins in $m_T - m_\pi$ in a rapidity window of 0.1 units around mid-rapidity, $|y| < 0.05$. The Gaussian fits, drawn in red, are in $\beta^{-1}_{\text{expected}} - \beta^{-1}_{\text{measured}}$ and are of the $m_T - m_\pi = 0.350$ to 1.0 GeV/c^2 range. The track data are represented in the black histogram.

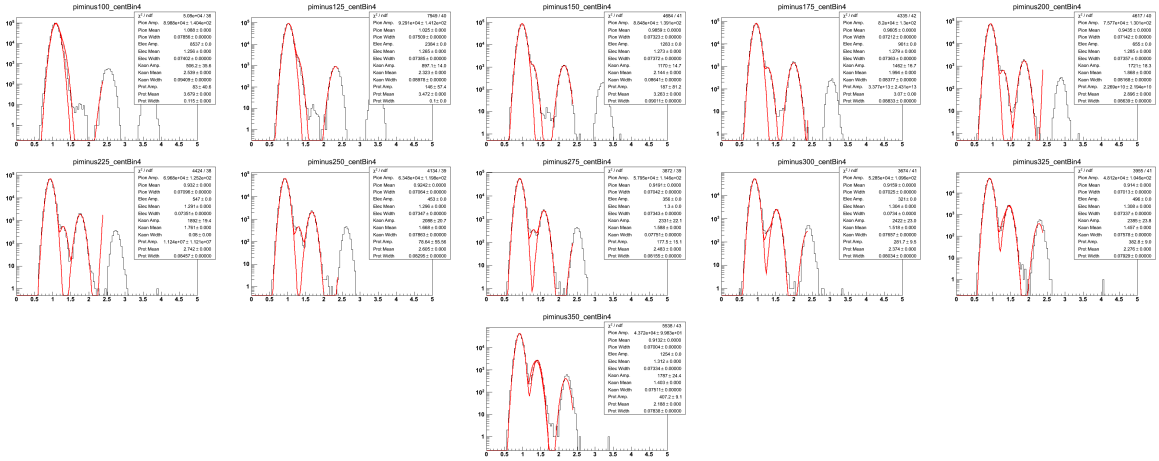

Figure A.51: Negative pion TPC fits for 30%-40% central events Au+Au $\sqrt{s_{NN}} = 19.6$ GeV. These are organized in 25 MeV bins in $m_T - m_\pi$ in a rapidity window of 0.1 units around mid-rapidity, $|y| < 0.05$. The Gaussian fits, drawn in red, are in $\log(10^6 \times dE/dx)$ and are of the $m_T - m_\pi = 0.100$ to 0.500 GeV/c^2 range. The track data are represented in the black histogram.

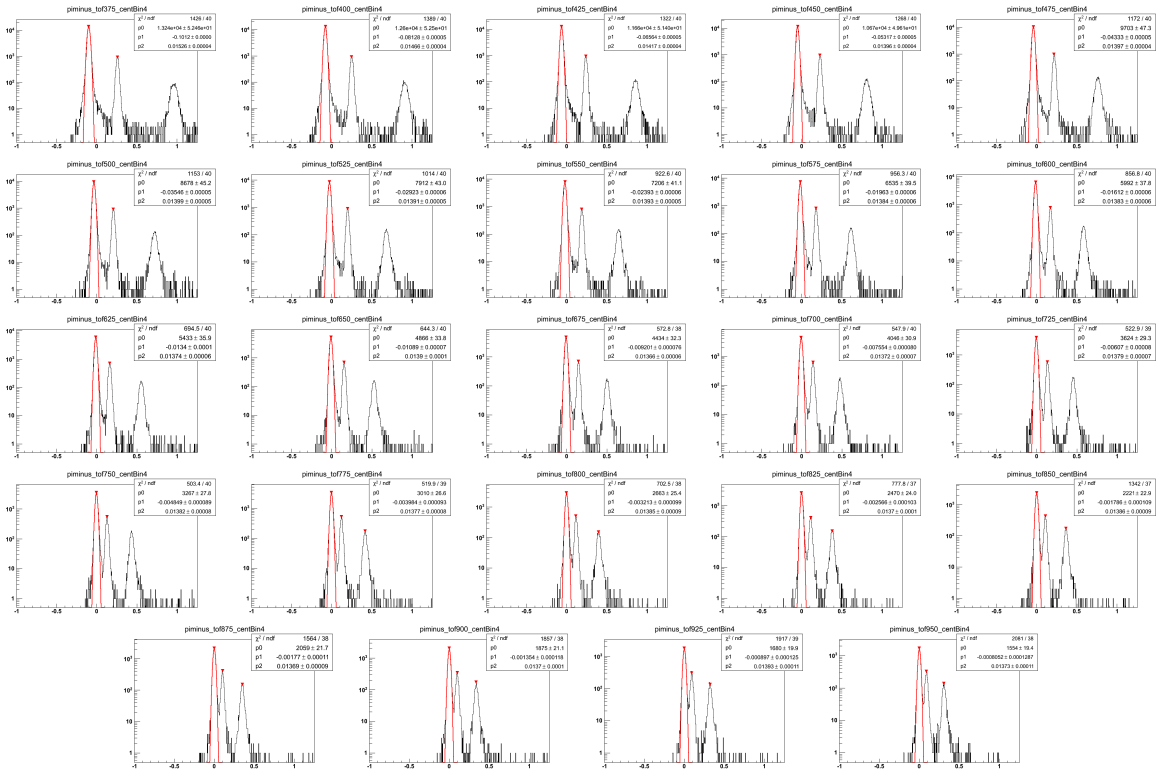

Figure A.52: Negative pion TOF fits for 30%-40% central events Au+Au $\sqrt{s_{NN}} = 19.6$ GeV. These are organized in 25 MeV bins in $m_T - m_\pi$ in a rapidity window of 0.1 units around mid-rapidity, $|y| < 0.05$. The Gaussian fits, drawn in red, are in $\beta^{-1}_{\text{expected}} - \beta^{-1}_{\text{measured}}$ and are of the $m_T - m_\pi = 0.350$ to 1.0 GeV/c^2 range. The track data are represented in the black histogram.

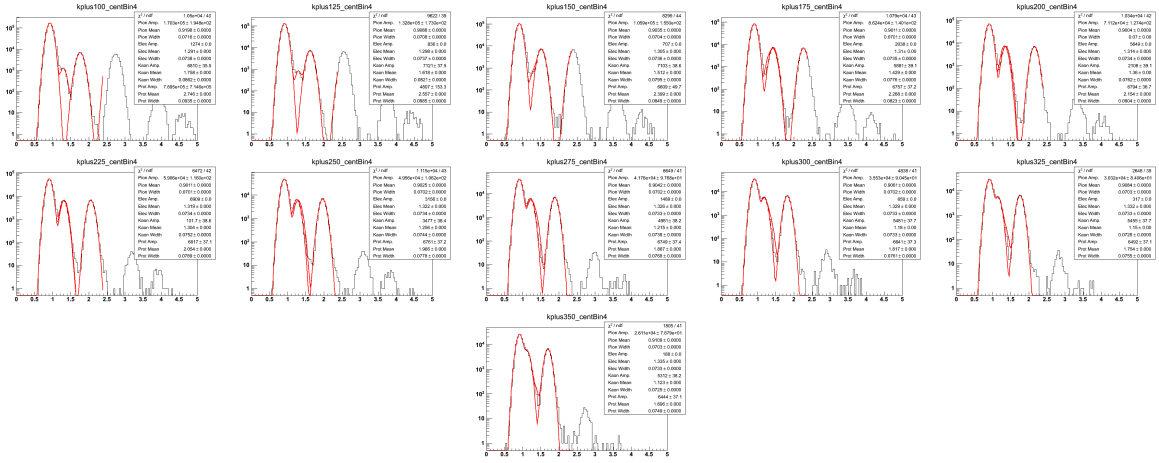

Figure A.53: Positive kaon TPC fits for 30%-40% central events Au+Au $\sqrt{s_{NN}} = 19.6$ GeV. These are organized in 25 MeV bins in $m_T - m_K$ in a rapidity window of 0.1 units around mid-rapidity, $|y| < 0.05$. The Gaussian fits, drawn in red, are in $\log(10^6 \times dE/dx)$ and are of the $m_T - m_K = 0.100$ to 0.500 GeV/c^2 range. The track data are represented in the black histogram.

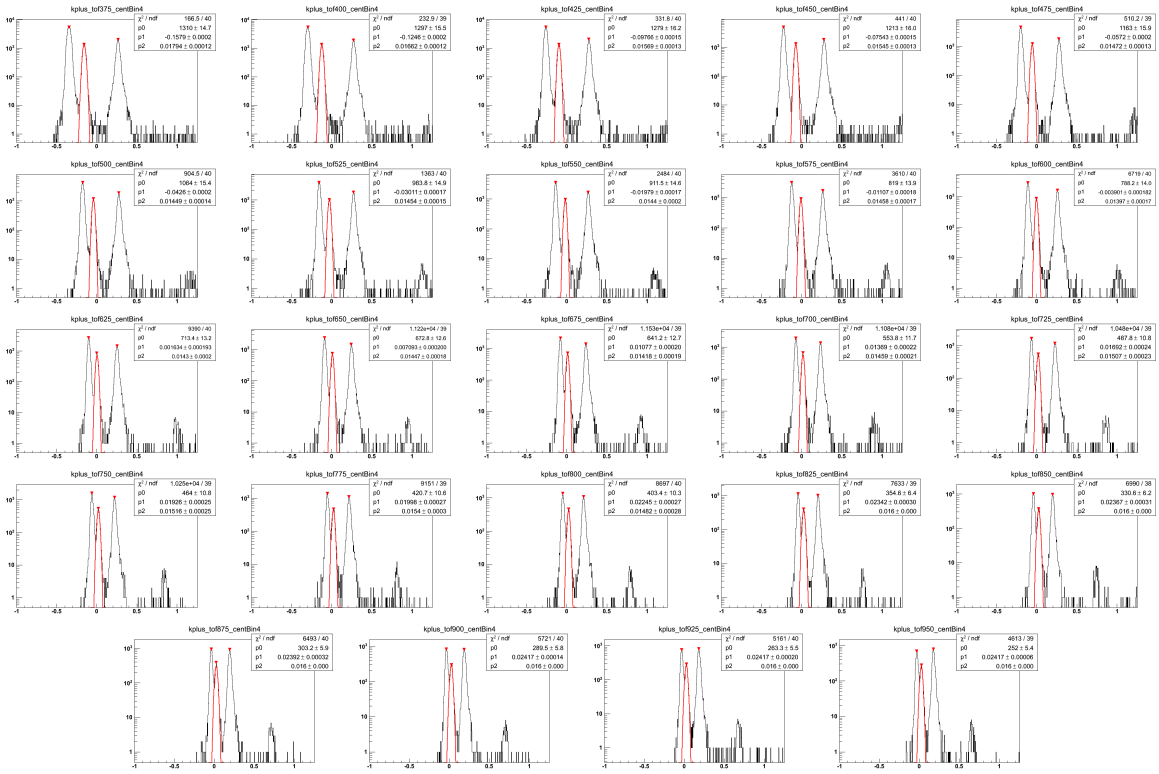

Figure A.54: Positive kaon TOF fits for 30%-40% central events Au+Au $\sqrt{s_{NN}} = 19.6$ GeV. These are organized in 25 MeV bins in $m_T - m_K$ in a rapidity window of 0.1 units around mid-rapidity, $|y| < 0.05$. The Gaussian fits, drawn in red, are in $\beta^{-1}_{\text{expected}} - \beta^{-1}_{\text{measured}}$ and are of the $m_T - m_K =$ 0.350 to 1.0 GeV/c^2 range. The track data are represented in the black histogram.

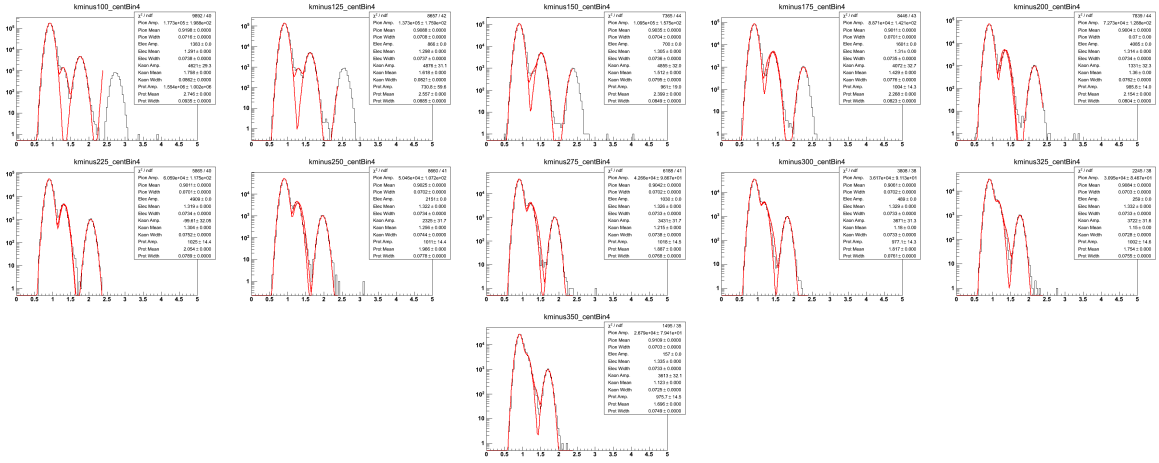

Figure A.55: Negative kaon TPC fits for 30%-40% central events Au+Au $\sqrt{s_{NN}} = 19.6$ GeV. These are organized in 25 MeV bins in $m_T - m_K$ in a rapidity window of 0.1 units around mid-rapidity, $|y| < 0.05$. The Gaussian fits, drawn in red, are in $\log(10^6 \times dE/dx)$ and are of the $m_T - m_K = 0.100$ to 0.500 GeV/c^2 range. The track data are represented in the black histogram.

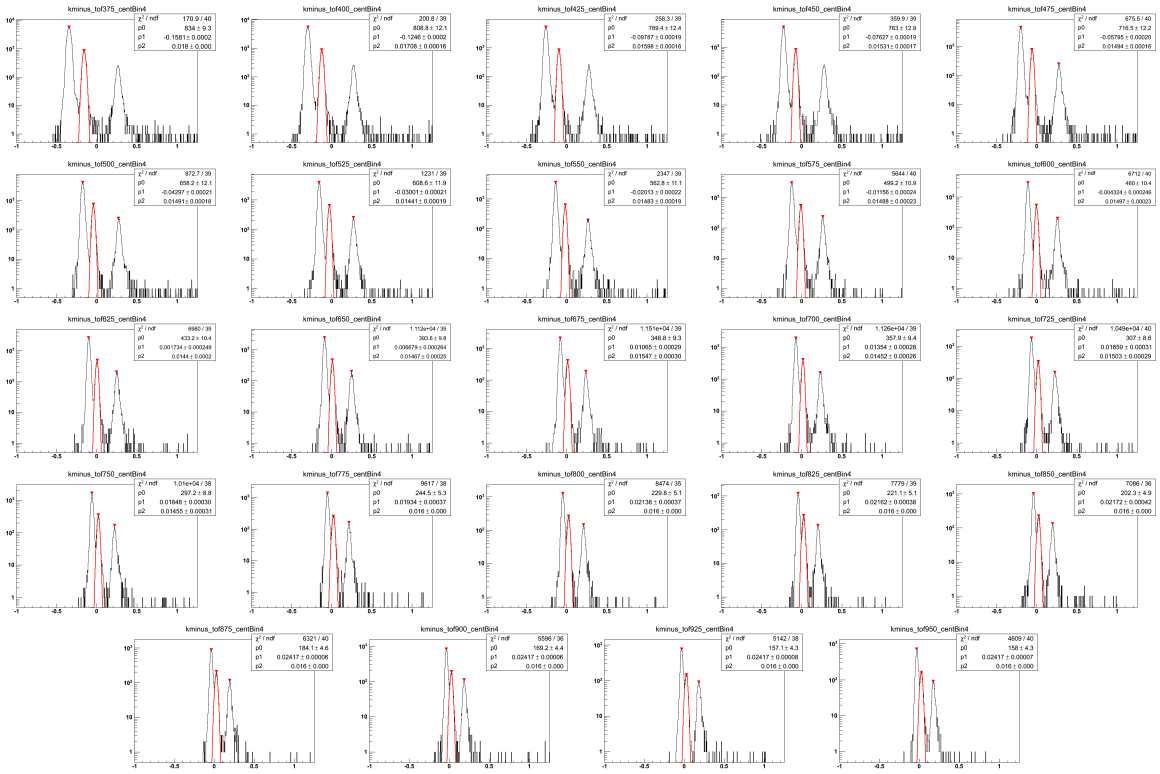

Figure A.56: Negative kaon TOF fits for 30%-40% central events Au+Au $\sqrt{s_{NN}} = 19.6$ GeV. These are organized in 25 MeV bins in $m_T - m_K$ in a rapidity window of 0.1 units around mid-rapidity, $|y| < 0.05$. The Gaussian fits, drawn in red, are in $\beta^{-1}_{\text{expected}} - \beta^{-1}_{\text{measured}}$ and are of the $m_T - m_K = 0.350$ to 1.0 GeV/c^2 range. The track data are represented in the black histogram.

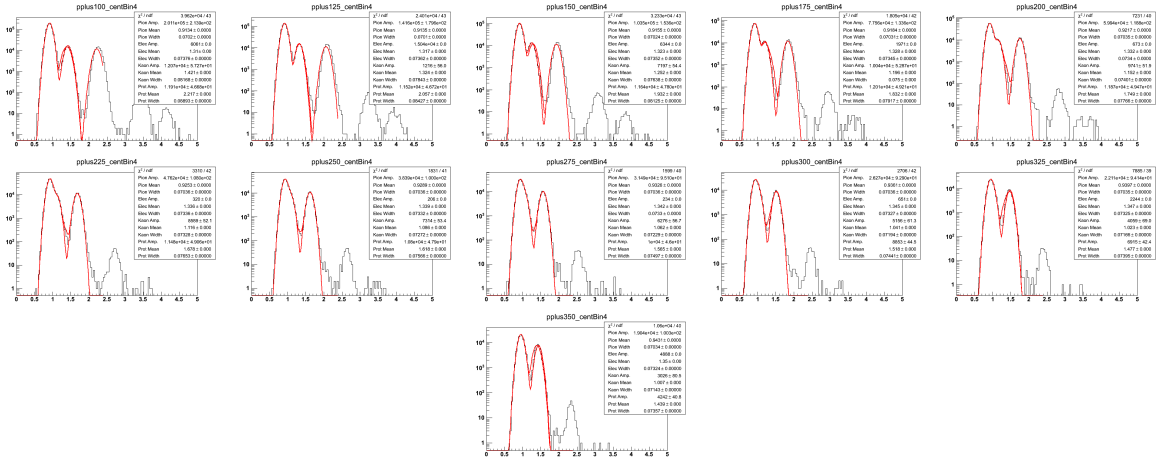

Figure A.57: Positive proton TPC fits for 30%-40% central events Au+Au $\sqrt{s_{NN}} = 19.6$ GeV. These are organized in 25 MeV bins in $m_T - m_p$ in a rapidity window of 0.1 units around mid-rapidity, $|y| < 0.05$. The Gaussian fits, drawn in red, are in $\log(10^6 \times dE/dx)$ and are of the $m_T - m_p = 0.100$ to 0.500 GeV/c^2 range. The track data are represented in the black histogram.

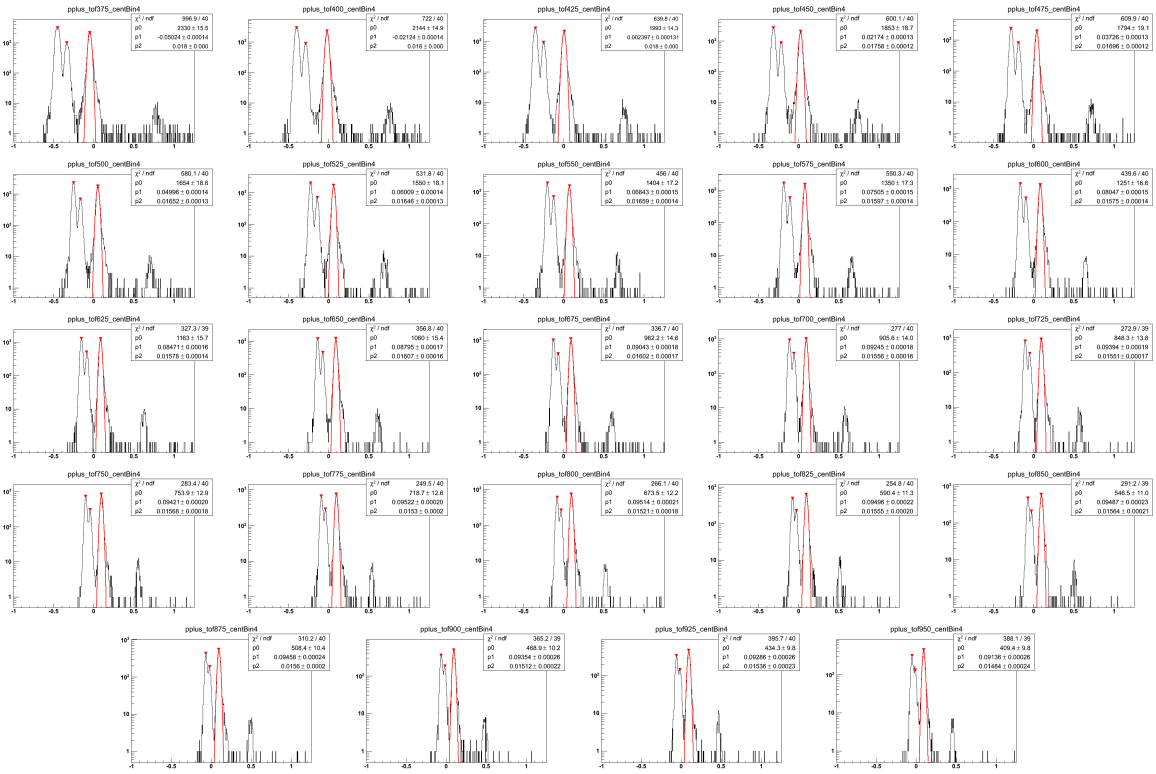

Figure A.58: Positive proton TOF fits for 30%-40% central events Au+Au $\sqrt{s_{NN}} = 19.6$ GeV. These are organized in 25 MeV bins in $m_T - m_p$ in a rapidity window of 0.1 units around mid-rapidity, $|y| < 0.05$. The Gaussian fits, drawn in red, are in $\beta^{-1}_{\text{expected}} - \beta^{-1}_{\text{measured}}$ and are of the $m_T - m_p = 0.350$ to 1.0 GeV/c^2 range. The track data are represented in the black histogram.

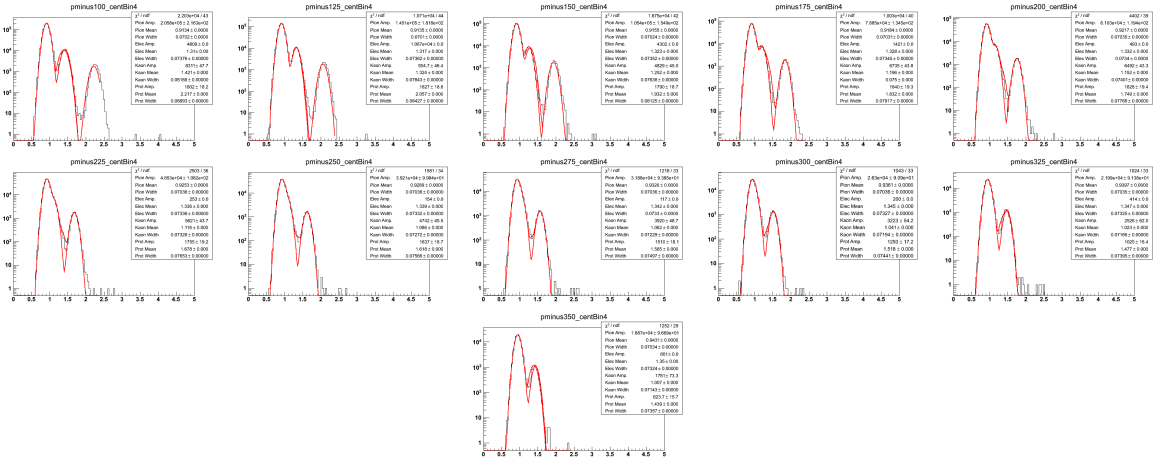

Figure A.59: Negative proton TPC fits for 30%-40% central events Au+Au $\sqrt{s_{NN}} = 19.6$ GeV. These are organized in 25 MeV bins in $m_T - m_p$ in a rapidity window of 0.1 units around mid-rapidity, $|y| < 0.05$. The Gaussian fits, drawn in red, are in $\log(10^6 \times dE/dx)$ and are of the $m_T - m_p = 0.100$ to 0.500 GeV/c^2 range. The track data are represented in the black histogram.

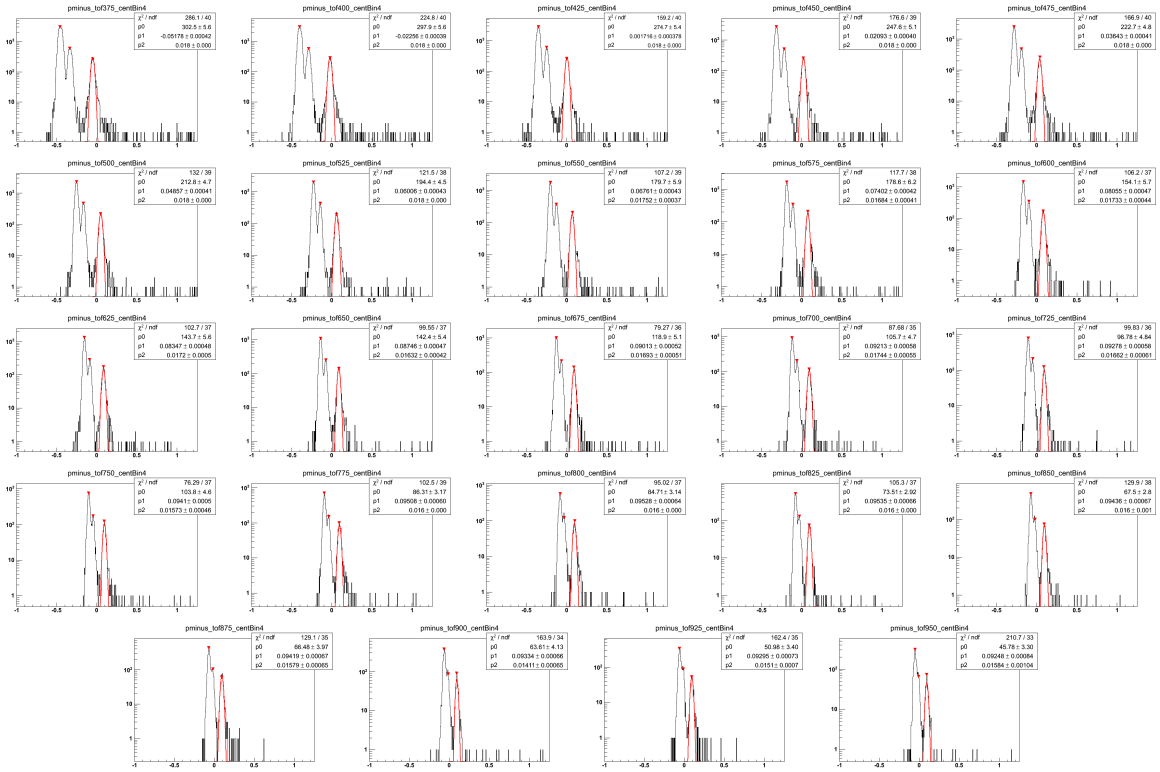

Figure A.60: Negative proton TOF fits for 30%-40% central events Au+Au $\sqrt{s_{NN}} = 19.6$ GeV. These are organized in 25 MeV bins in $m_T - m_p$ in a rapidity window of 0.1 units around mid-rapidity, $|y| < 0.05$. The Gaussian fits, drawn in red, are in $\beta^{-1}_{\text{expected}} - \beta^{-1}_{\text{measured}}$ and are of the $m_T - m_p = 0.350$ to 1.0 GeV/c^2 range. The track data are represented in the black histogram.

A.6 The 20%-30% Centrality Class

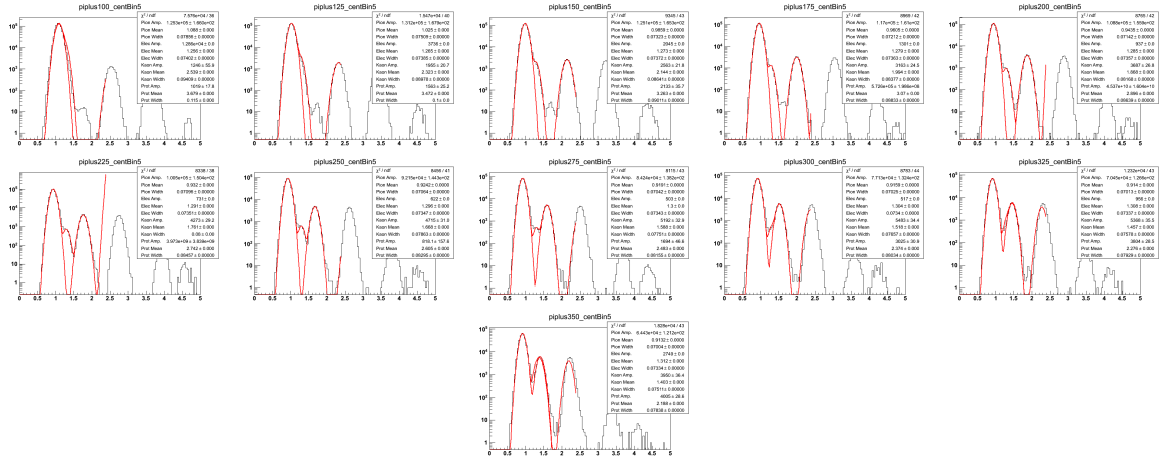

Figure A.61: Positive pion TPC fits for 20%-30% central events Au+Au $\sqrt{s_{NN}} = 19.6$ GeV. These are organized in 25 MeV bins in $m_T - m_\pi$ in a rapidity window of 0.1 units around mid-rapidity, $|y| < 0.05$. The Gaussian fits, drawn in red, are in $\log(10^6 \times dE/dx)$ and are of the $m_T - m_\pi =$ 0.100 to 0.500 GeV/c^2 range. The track data are represented in the black histogram.

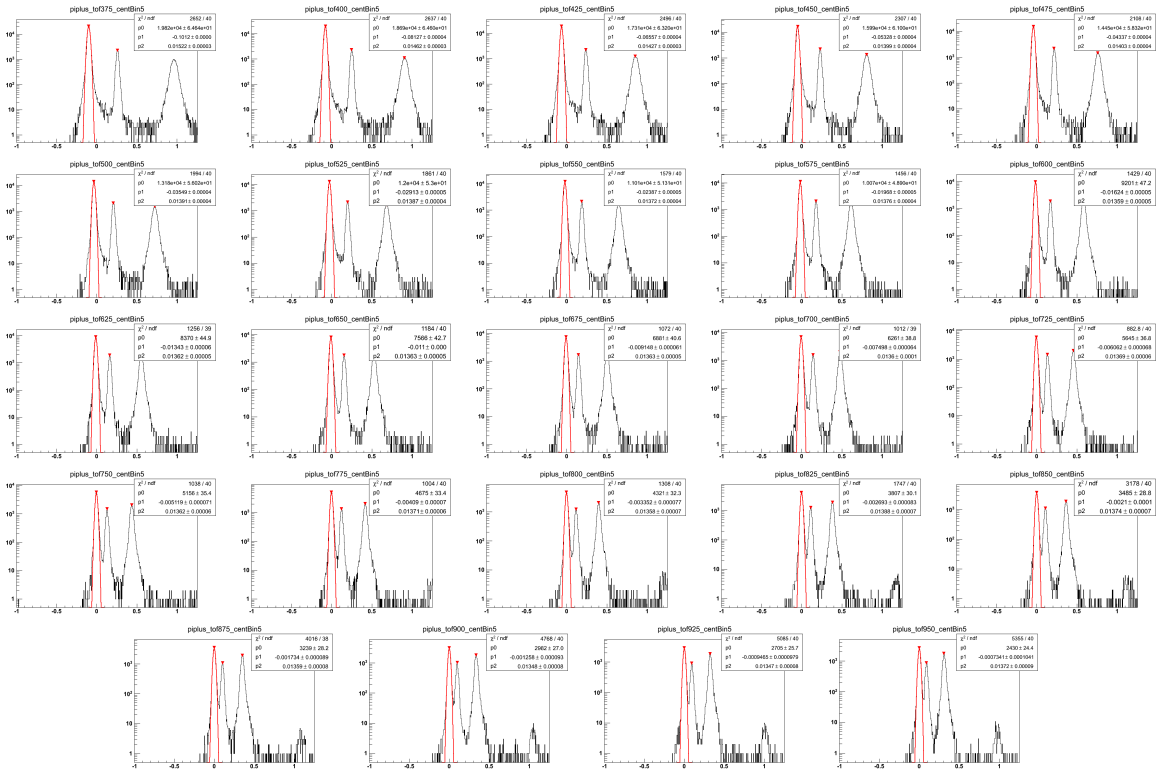

Figure A.62: Positive pion TOF fits for 20%-30% central events Au+Au $\sqrt{s_{NN}} = 19.6$ GeV. These are organized in 25 MeV bins in $m_T - m_\pi$ in a rapidity window of 0.1 units around mid-rapidity, $|y| < 0.05$. The Gaussian fits, drawn in red, are in $\beta^{-1}_{\text{expected}} - \beta^{-1}_{\text{measured}}$ and are of the $m_T - m_\pi = 0.350$ to 1.0 GeV/c^2 range. The track data are represented in the black histogram.

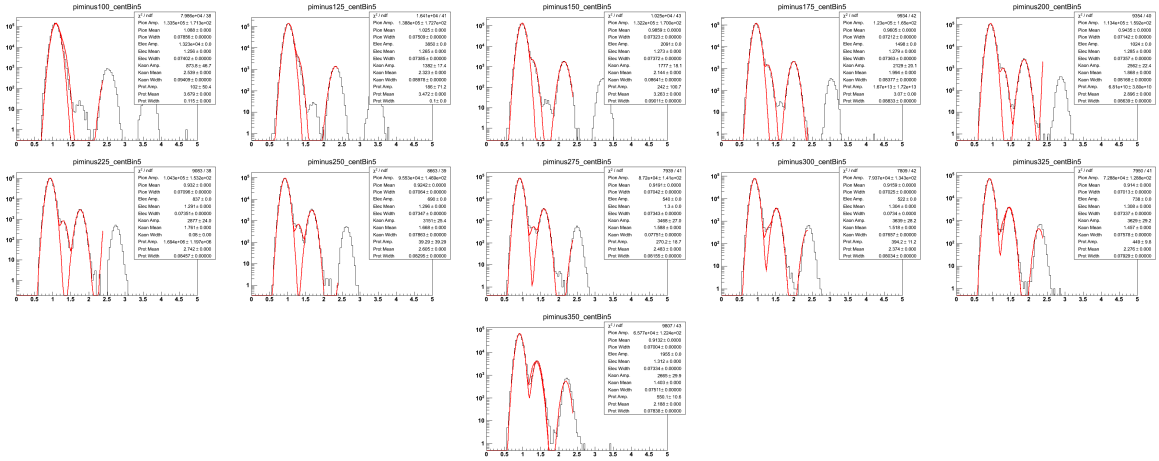

Figure A.63: Negative pion TPC fits for 20%-30% central events Au+Au $\sqrt{s_{NN}} = 19.6$ GeV. These are organized in 25 MeV bins in $m_T - m_\pi$ in a rapidity window of 0.1 units around mid-rapidity, $|y| < 0.05$. The Gaussian fits, drawn in red, are in $\log(10^6 \times dE/dx)$ and are of the $m_T - m_\pi = 0.100$ to 0.500 GeV/c^2 range. The track data are represented in the black histogram.

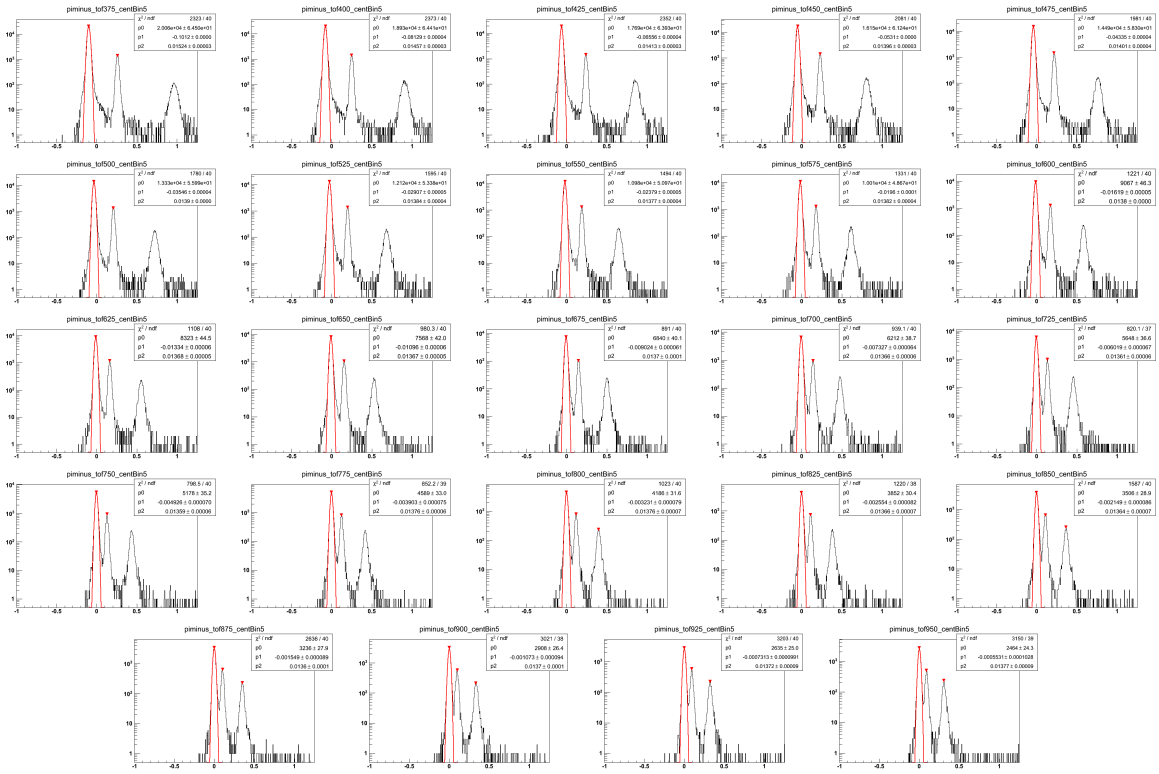

Figure A.64: Negative pion TOF fits for 20%-30% central events Au+Au $\sqrt{s_{NN}} = 19.6$ GeV. These are organized in 25 MeV bins in $m_T - m_\pi$ in a rapidity window of 0.1 units around mid-rapidity, $|y| < 0.05$. The Gaussian fits, drawn in red, are in $\beta^{-1}_{\text{expected}} - \beta^{-1}_{\text{measured}}$ and are of the $m_T - m_\pi = 0.350$ to 1.0 GeV/c^2 range. The track data are represented in the black histogram.

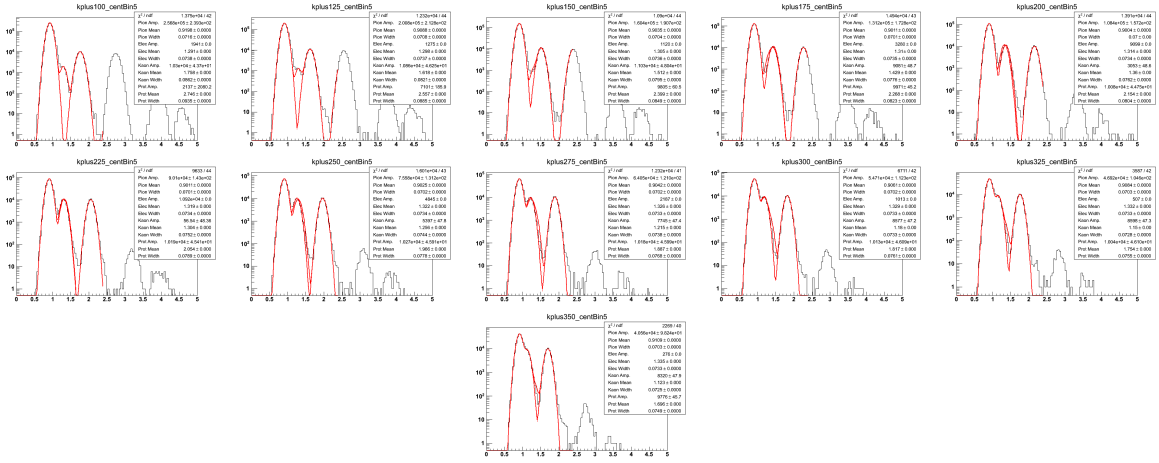

Figure A.65: Positive kaon TPC fits for 20%-30% central events Au+Au $\sqrt{s_{NN}} = 19.6$ GeV. These are organized in 25 MeV bins in $m_T - m_K$ in a rapidity window of 0.1 units around mid-rapidity, $|y| < 0.05$. The Gaussian fits, drawn in red, are in $\log(10^6 \times dE/dx)$ and are of the $m_T - m_K = 0.100$ to 0.500 GeV/c^2 range. The track data are represented in the black histogram.

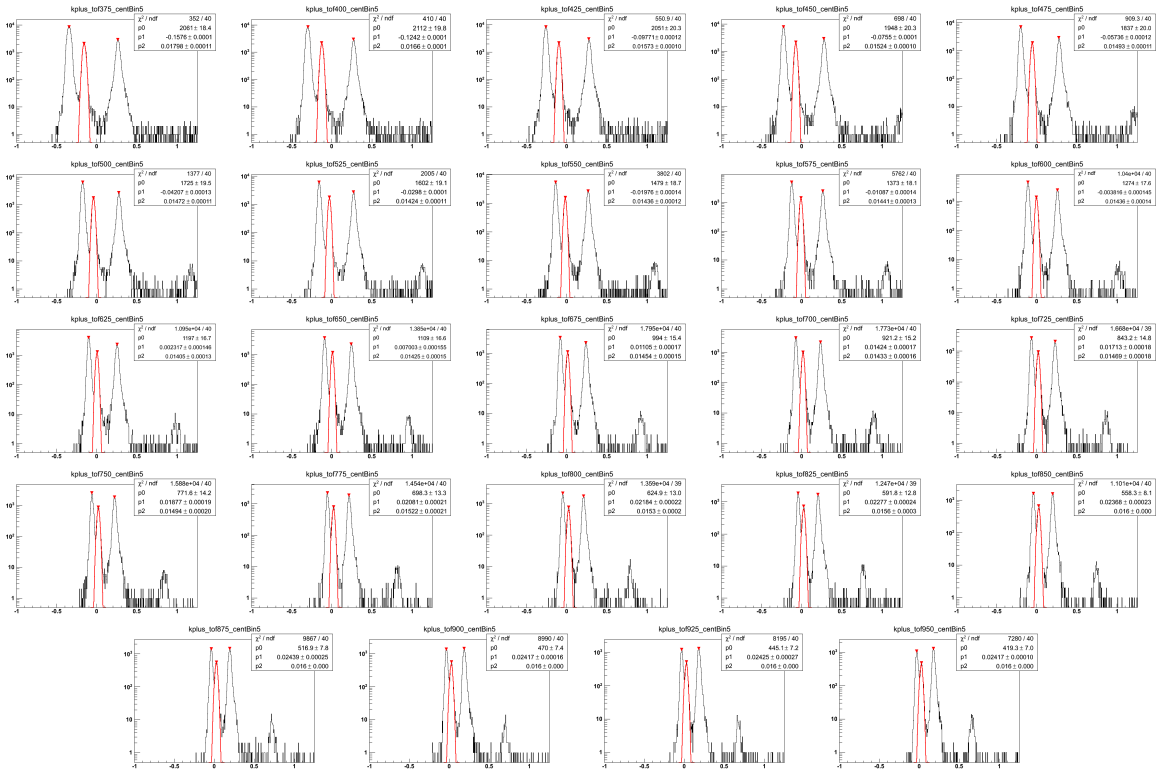

Figure A.66: Positive kaon TOF fits for 20%-30% central events Au+Au $\sqrt{s_{NN}} = 19.6$ GeV. These are organized in 25 MeV bins in $m_T - m_K$ in a rapidity window of 0.1 units around mid-rapidity, $|y| < 0.05$. The Gaussian fits, drawn in red, are in $\beta^{-1}_{\text{expected}} - \beta^{-1}_{\text{measured}}$ and are of the $m_T - m_K =$ 0.350 to 1.0 GeV/c^2 range. The track data are represented in the black histogram.

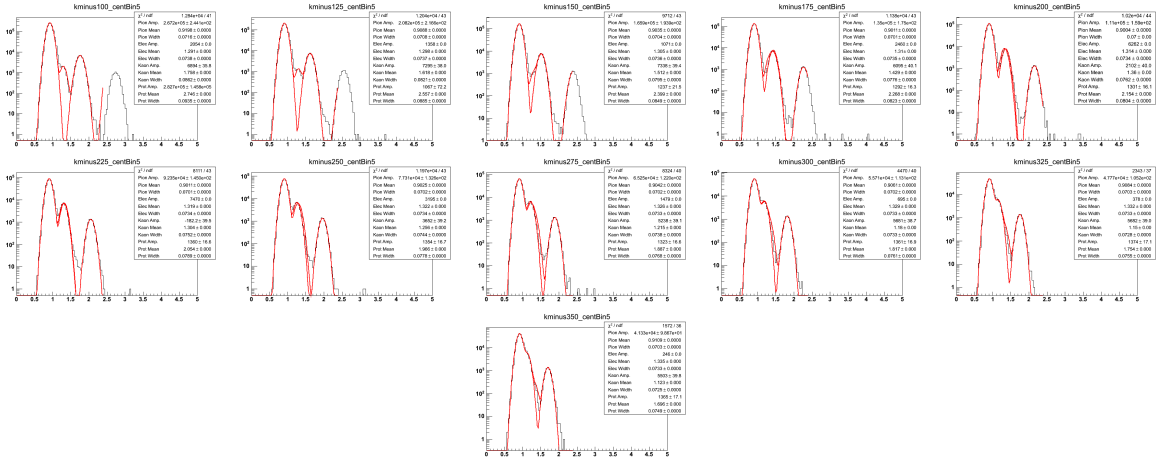

Figure A.67: Negative kaon TPC fits for 20%-30% central events Au+Au $\sqrt{s_{NN}} = 19.6$ GeV. These are organized in 25 MeV bins in $m_T - m_K$ in a rapidity window of 0.1 units around mid-rapidity, $|y| < 0.05$. The Gaussian fits, drawn in red, are in $\log(10^6 \times dE/dx)$ and are of the $m_T - m_K = 0.100$ to 0.500 GeV/c^2 range. The track data are represented in the black histogram.

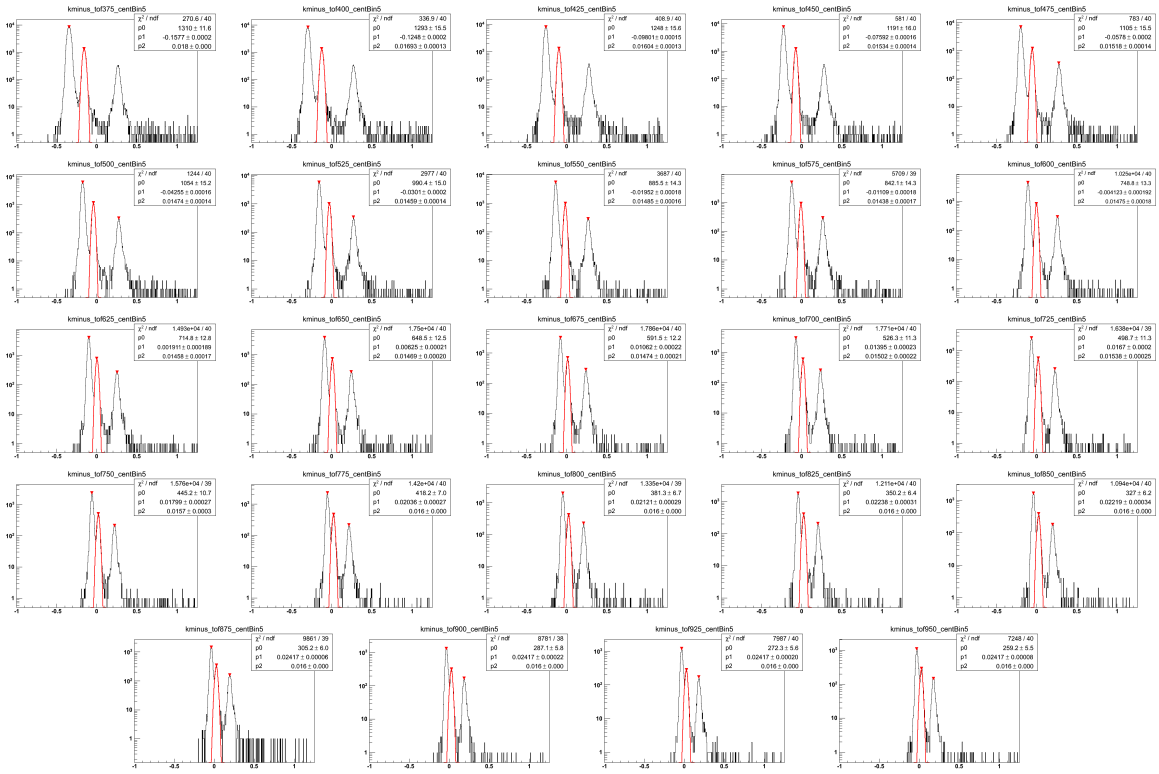

Figure A.68: Negative kaon TOF fits for 20%-30% central events Au+Au $\sqrt{s_{NN}} = 19.6$ GeV. These are organized in 25 MeV bins in $m_T - m_K$ in a rapidity window of 0.1 units around mid-rapidity, $|y| < 0.05$. The Gaussian fits, drawn in red, are in $\beta^{-1}_{\text{expected}} - \beta^{-1}_{\text{measured}}$ and are of the $m_T - m_K = 0.350$ to 1.0 GeV/c^2 range. The track data are represented in the black histogram.

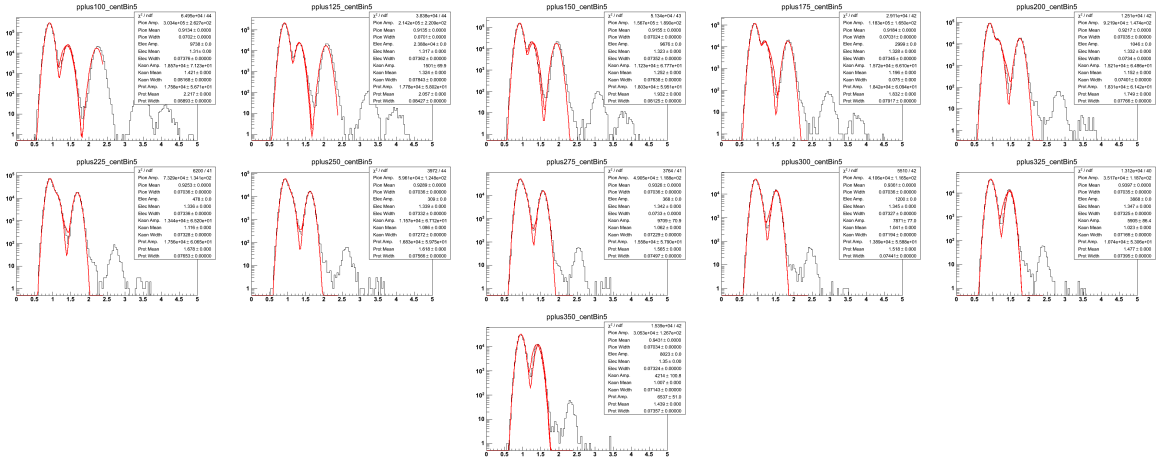

Figure A.69: Positive proton TPC fits for 20%-30% central events Au+Au $\sqrt{s_{NN}} = 19.6$ GeV. These are organized in 25 MeV bins in $m_T - m_p$ in a rapidity window of 0.1 units around mid-rapidity, $|y| < 0.05$. The Gaussian fits, drawn in red, are in $\log(10^6 \times dE/dx)$ and are of the $m_T - m_p = 0.100$ to 0.500 GeV/c^2 range. The track data are represented in the black histogram.

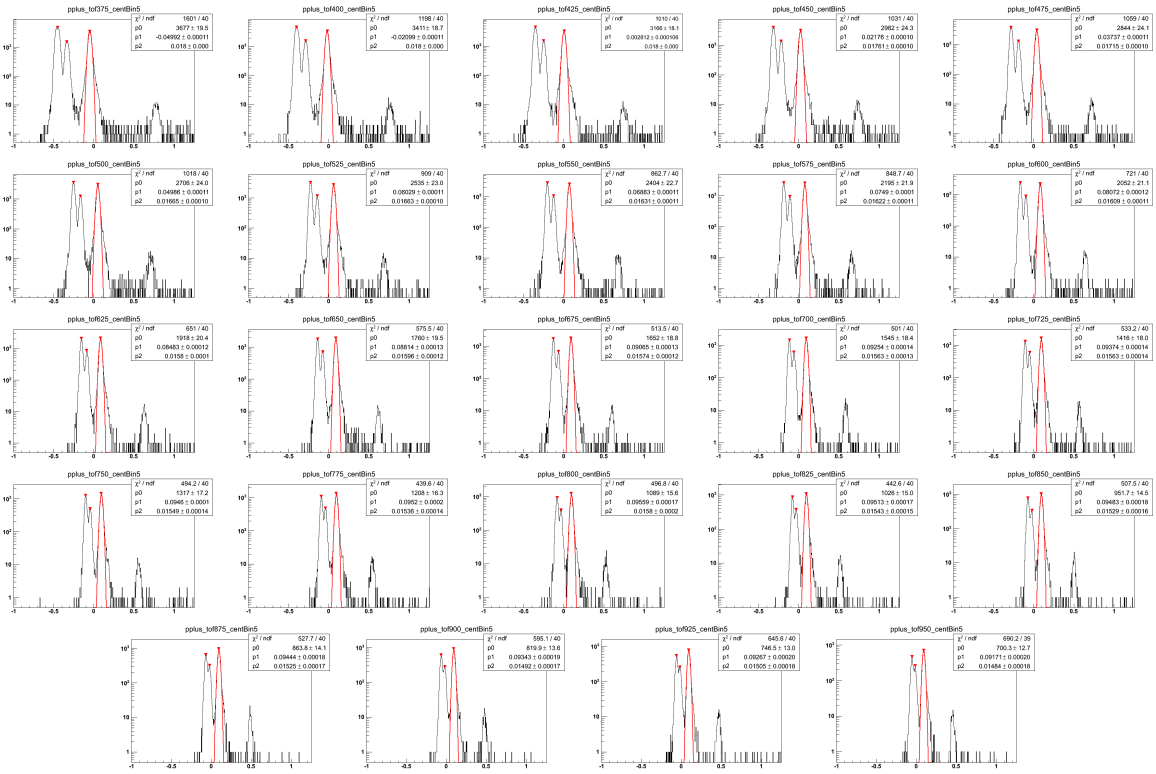

Figure A.70: Positive proton TOF fits for 20%-30% central events Au+Au $\sqrt{s_{NN}} = 19.6$ GeV. These are organized in 25 MeV bins in $m_T - m_p$ in a rapidity window of 0.1 units around mid-rapidity, $|y| < 0.05$. The Gaussian fits, drawn in red, are in $\beta^{-1}_{\text{expected}} - \beta^{-1}_{\text{measured}}$ and are of the $m_T - m_p = 0.350$ to 1.0 GeV/c^2 range. The track data are represented in the black histogram.

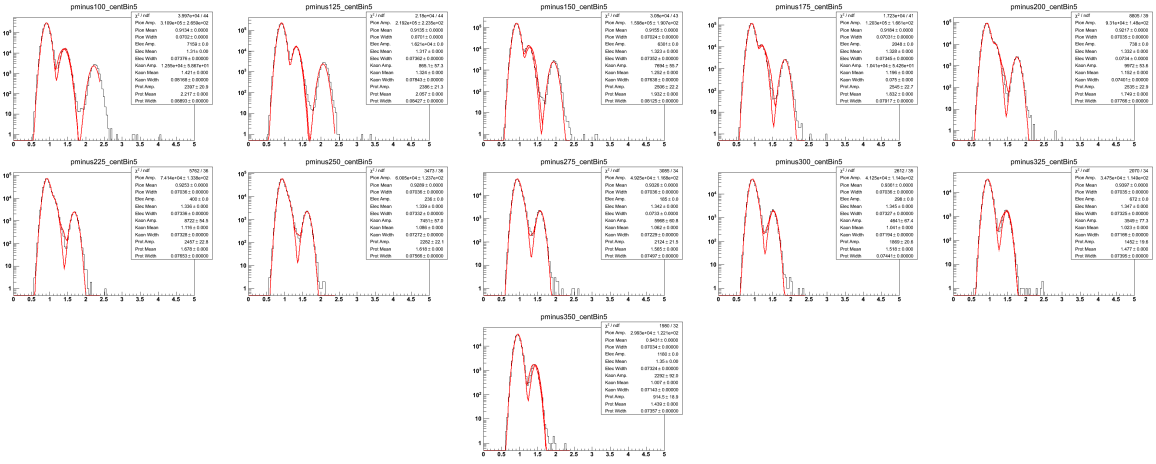

Figure A.71: Negative proton TPC fits for 20%-30% central events Au+Au $\sqrt{s_{NN}} = 19.6$ GeV. These are organized in 25 MeV bins in $m_T - m_p$ in a rapidity window of 0.1 units around mid-rapidity, $|y| < 0.05$. The Gaussian fits, drawn in red, are in $\log(10^6 \times dE/dx)$ and are of the $m_T - m_p = 0.100$ to 0.500 GeV/c^2 range. The track data are represented in the black histogram.

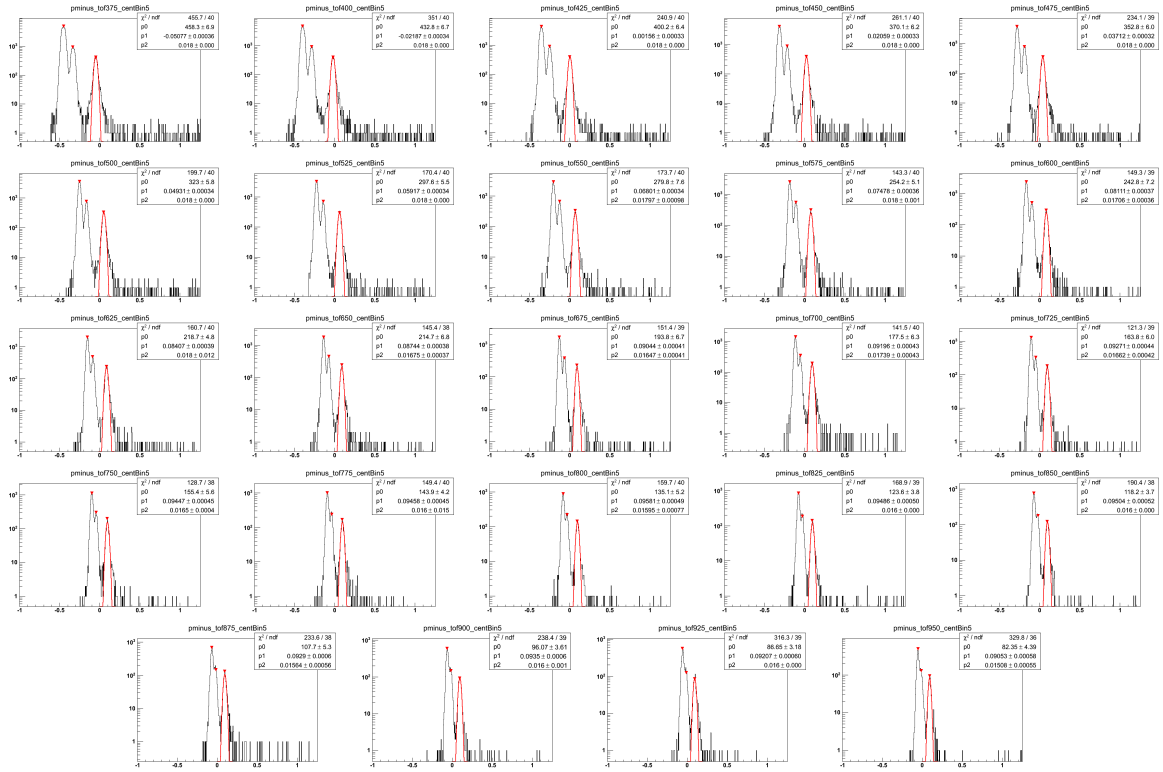

Figure A.72: Negative proton TOF fits for 20%-30% central events Au+Au $\sqrt{s_{NN}} = 19.6$ GeV. These are organized in 25 MeV bins in $m_T - m_p$ in a rapidity window of 0.1 units around mid-rapidity, $|y| < 0.05$. The Gaussian fits, drawn in red, are in $\beta^{-1}_{\text{expected}} - \beta^{-1}_{\text{measured}}$ and are of the $m_T - m_p = 0.350$ to 1.0 GeV/c^2 range. The track data are represented in the black histogram.

A.7 The 10%-20% Centrality Class

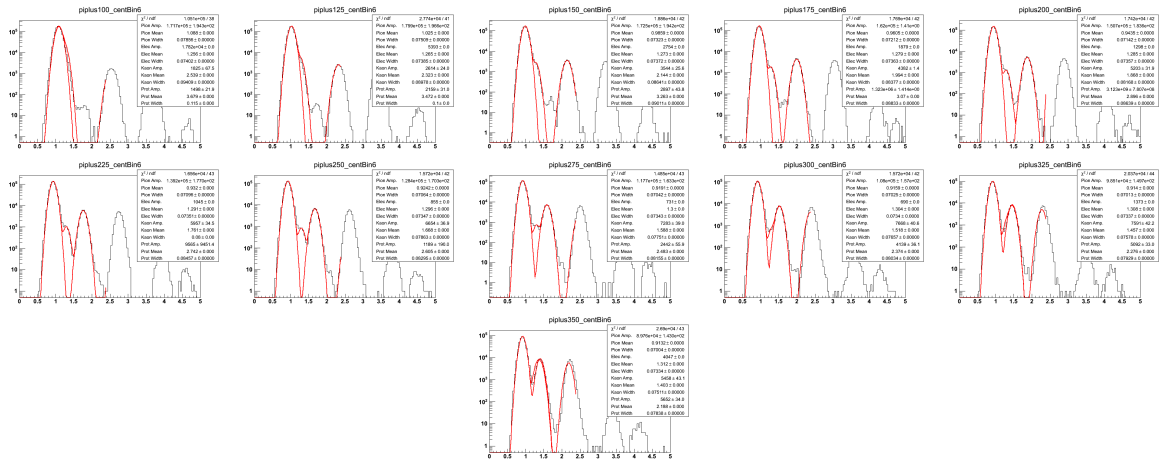

Figure A.73: Positive pion TPC fits for 10%-20% central events Au+Au $\sqrt{s_{NN}} = 19.6$ GeV. These are organized in 25 MeV bins in $m_T - m_\pi$ in a rapidity window of 0.1 units around mid-rapidity, $|y| < 0.05$. The Gaussian fits, drawn in red, are in $\log(10^6 \times dE/dx)$ and are of the $m_T - m_\pi =$ 0.100 to 0.500 GeV/c^2 range. The track data are represented in the black histogram.

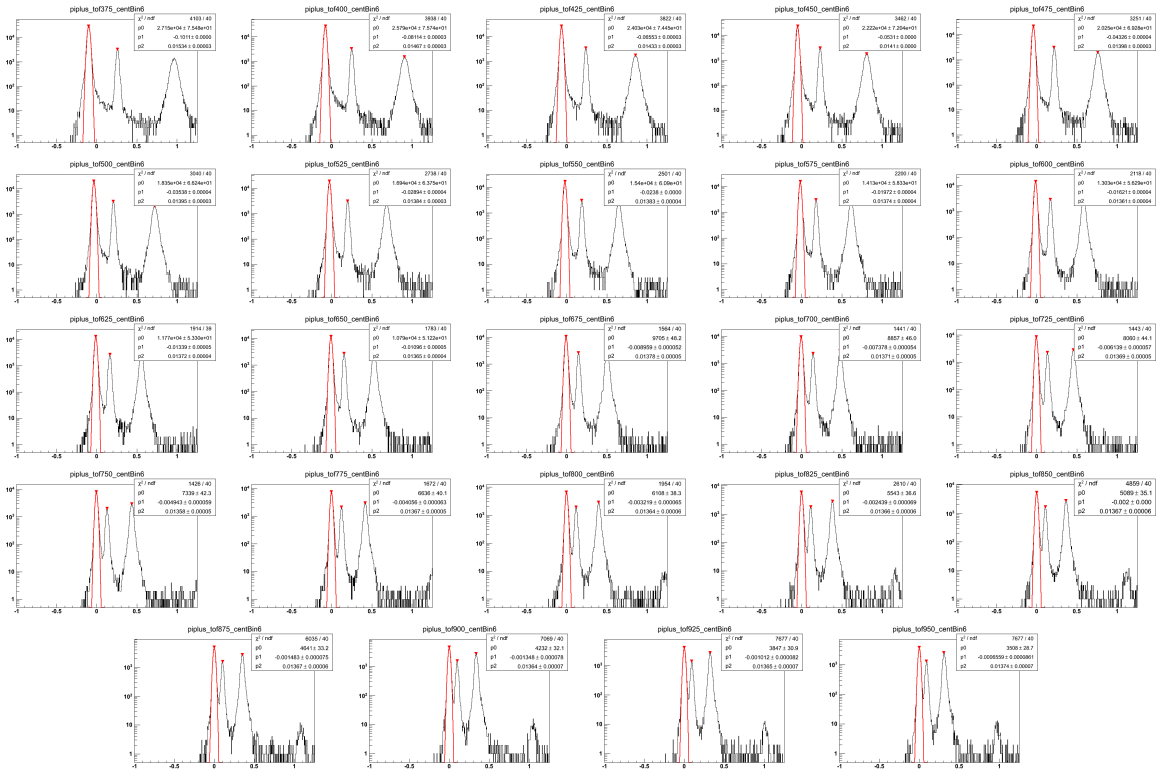

Figure A.74: Positive pion TOF fits for 10%-20% central events Au+Au $\sqrt{s_{NN}} = 19.6$ GeV. These are organized in 25 MeV bins in $m_T - m_\pi$ in a rapidity window of 0.1 units around mid-rapidity, $|y| < 0.05$. The Gaussian fits, drawn in red, are in $\beta^{-1}_{\text{expected}} - \beta^{-1}_{\text{measured}}$ and are of the $m_T - m_\pi = 0.350$ to 1.0 GeV/c^2 range. The track data are represented in the black histogram.

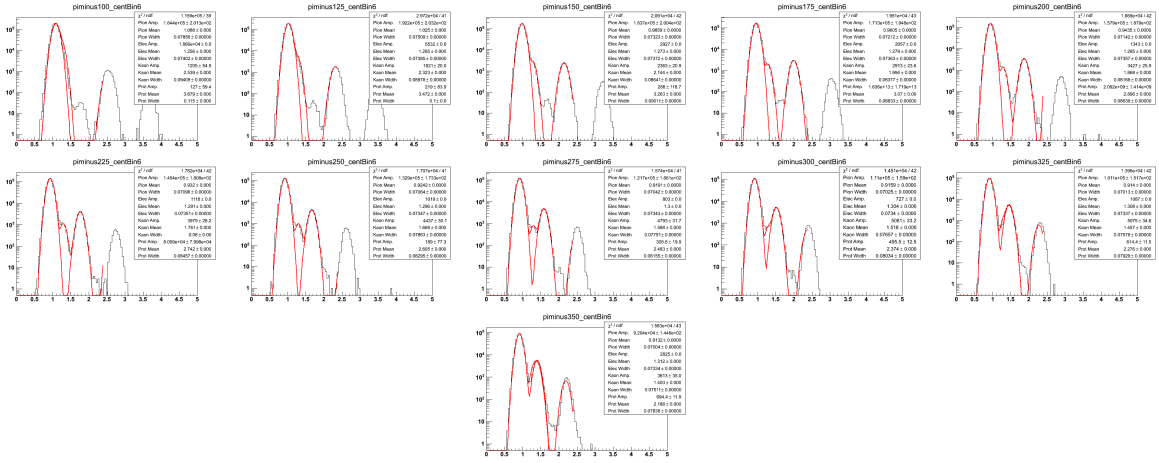

Figure A.75: Negative pion TPC fits for 10%-20% central events Au+Au $\sqrt{s_{NN}} = 19.6$ GeV. These are organized in 25 MeV bins in $m_T - m_\pi$ in a rapidity window of 0.1 units around mid-rapidity, $|y| < 0.05$. The Gaussian fits, drawn in red, are in $\log(10^6 \times dE/dx)$ and are of the $m_T - m_\pi = 0.100$ to 0.500 GeV/c^2 range. The track data are represented in the black histogram.

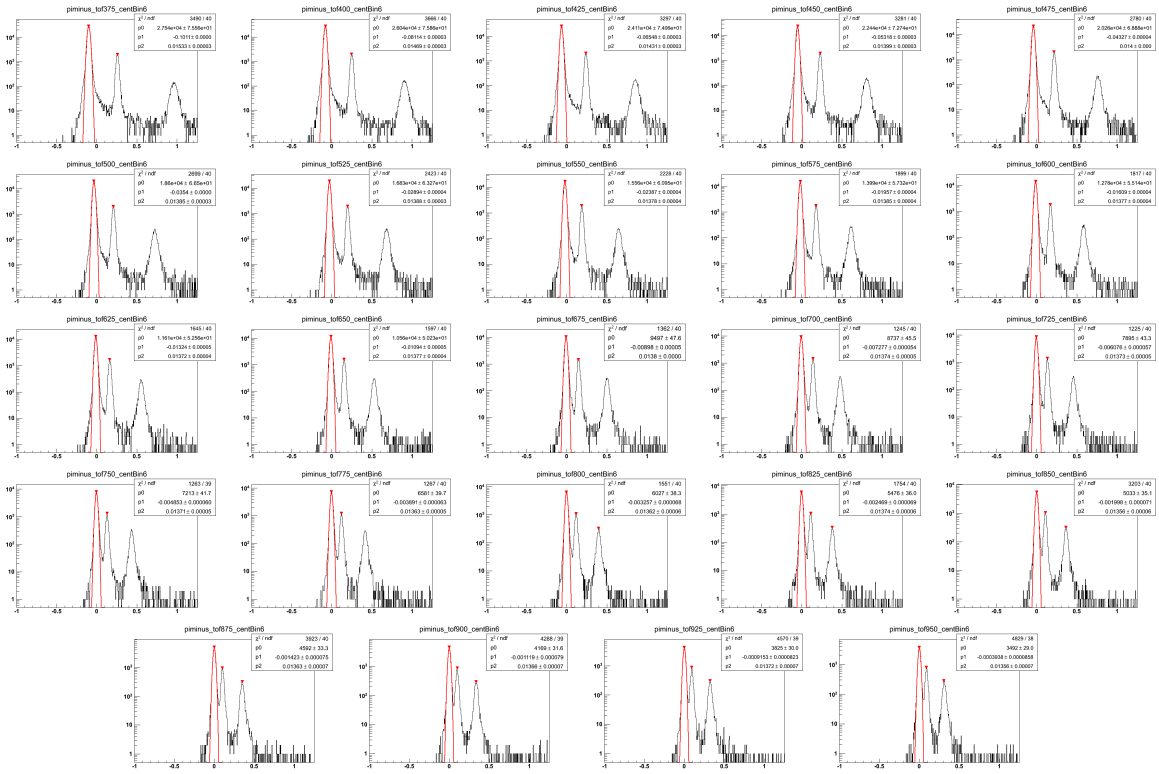

Figure A.76: Negative pion TOF fits for 10%-20% central events Au+Au $\sqrt{s_{NN}} = 19.6$ GeV. These are organized in 25 MeV bins in $m_T - m_\pi$ in a rapidity window of 0.1 units around mid-rapidity, $|y| < 0.05$. The Gaussian fits, drawn in red, are in $\beta^{-1}_{\text{expected}} - \beta^{-1}_{\text{measured}}$ and are of the $m_T - m_\pi = 0.350$ to 1.0 GeV/c^2 range. The track data are represented in the black histogram.

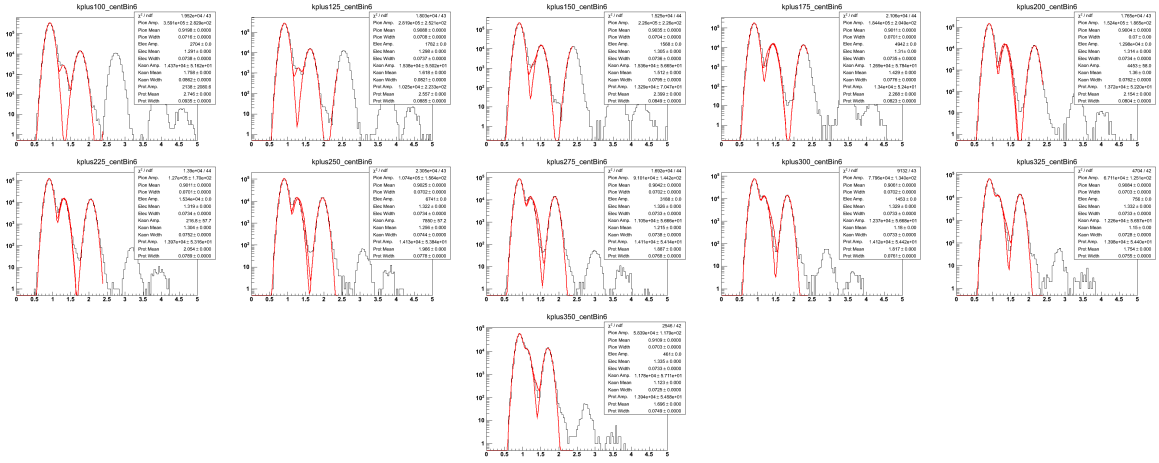

Figure A.77: Positive kaon TPC fits for 10%-20% central events Au+Au $\sqrt{s_{NN}} = 19.6$ GeV. These are organized in 25 MeV bins in $m_T - m_K$ in a rapidity window of 0.1 units around mid-rapidity, $|y| < 0.05$. The Gaussian fits, drawn in red, are in $\log(10^6 \times dE/dx)$ and are of the $m_T - m_K = 0.100$ to 0.500 GeV/c^2 range. The track data are represented in the black histogram.

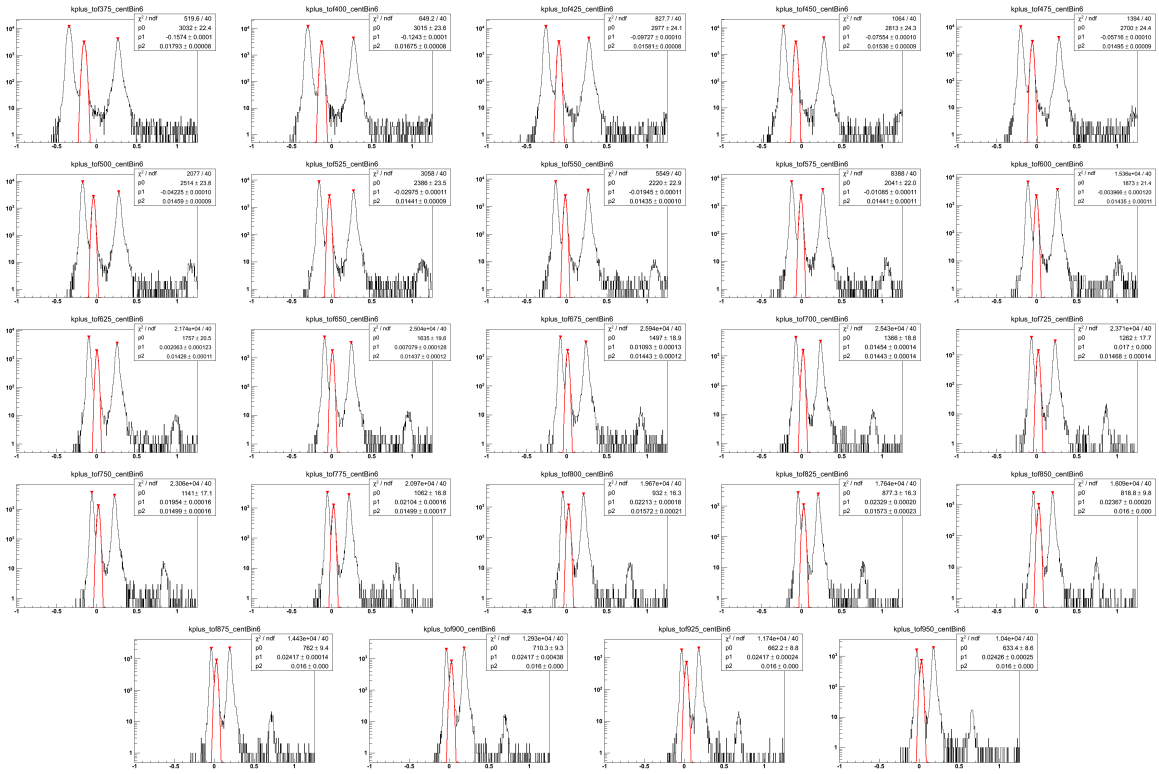

Figure A.78: Positive kaon TOF fits for 10%-20% central events Au+Au $\sqrt{s_{NN}} = 19.6$ GeV. These are organized in 25 MeV bins in $m_T - m_K$ in a rapidity window of 0.1 units around mid-rapidity, $|y| < 0.05$. The Gaussian fits, drawn in red, are in $\beta^{-1}_{\text{expected}} - \beta^{-1}_{\text{measured}}$ and are of the $m_T - m_K =$ 0.350 to 1.0 GeV/c^2 range. The track data are represented in the black histogram.

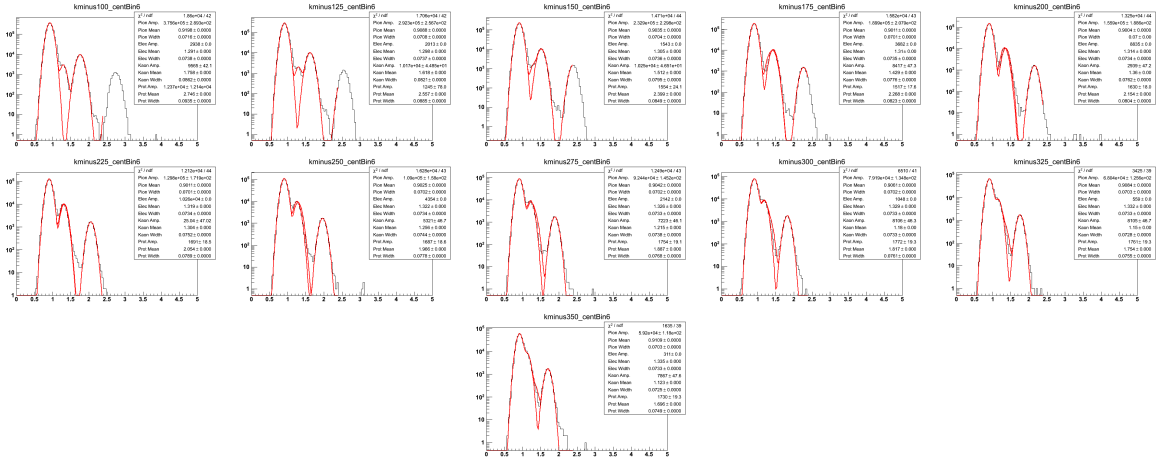

Figure A.79: Negative kaon TPC fits for 10%-20% central events Au+Au $\sqrt{s_{NN}} = 19.6$ GeV. These are organized in 25 MeV bins in $m_T - m_K$ in a rapidity window of 0.1 units around mid-rapidity, $|y| < 0.05$. The Gaussian fits, drawn in red, are in $\log(10^6 \times dE/dx)$ and are of the $m_T - m_K = 0.100$ to 0.500 GeV/c^2 range. The track data are represented in the black histogram.

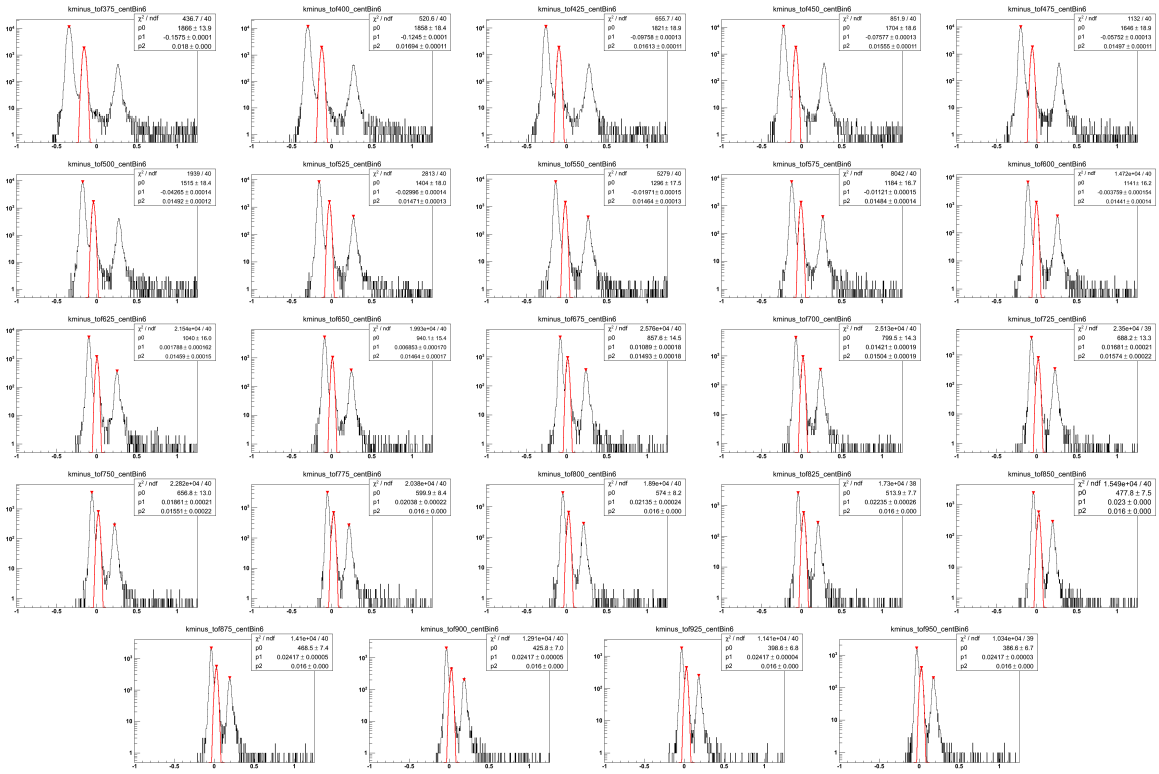

Figure A.80: Negative kaon TOF fits for 10%-20% central events Au+Au $\sqrt{s_{NN}} = 19.6$ GeV. These are organized in 25 MeV bins in $m_T - m_K$ in a rapidity window of 0.1 units around mid-rapidity, $|y| < 0.05$. The Gaussian fits, drawn in red, are in $\beta^{-1}_{\text{expected}} - \beta^{-1}_{\text{measured}}$ and are of the $m_T - m_K = 0.350$ to 1.0 GeV/c^2 range. The track data are represented in the black histogram.

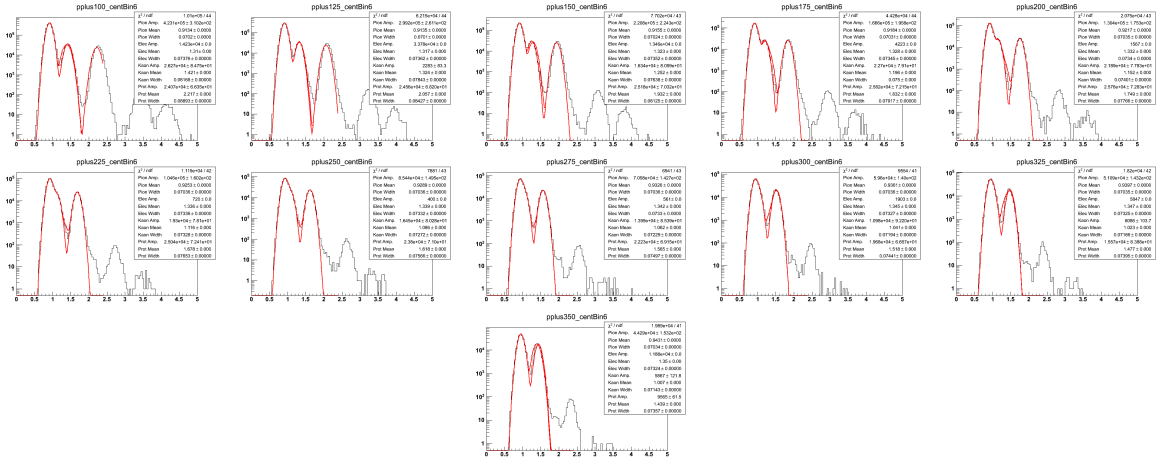

Figure A.81: Positive proton TPC fits for 10%-20% central events Au+Au $\sqrt{s_{NN}} = 19.6$ GeV. These are organized in 25 MeV bins in $m_T - m_p$ in a rapidity window of 0.1 units around mid-rapidity, $|y| < 0.05$. The Gaussian fits, drawn in red, are in $\log(10^6 \times dE/dx)$ and are of the $m_T - m_p = 0.100$ to 0.500 GeV/c^2 range. The track data are represented in the black histogram.

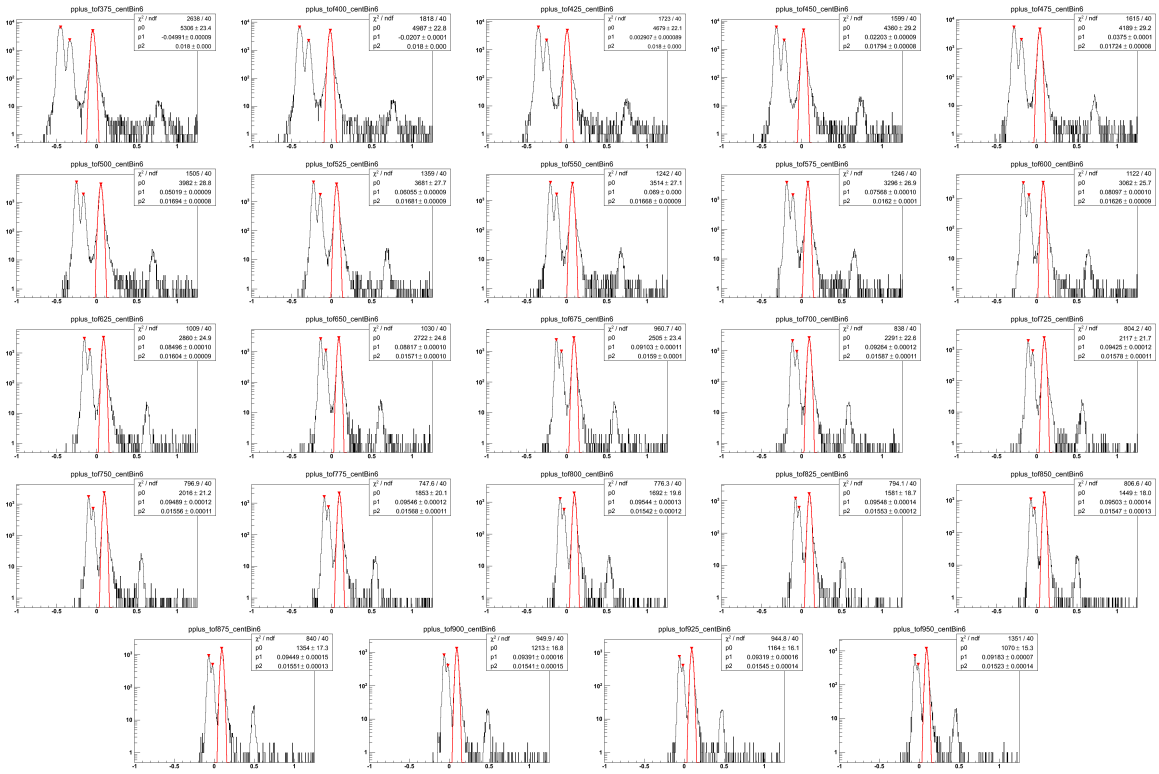

Figure A.82: Positive proton TOF fits for 10%-20% central events Au+Au $\sqrt{s_{NN}} = 19.6$ GeV. These are organized in 25 MeV bins in $m_T - m_p$ in a rapidity window of 0.1 units around mid-rapidity, $|y| < 0.05$. The Gaussian fits, drawn in red, are in $\beta^{-1}_{\text{expected}} - \beta^{-1}_{\text{measured}}$ and are of the $m_T - m_p = 0.350$ to 1.0 GeV/c^2 range. The track data are represented in the black histogram.

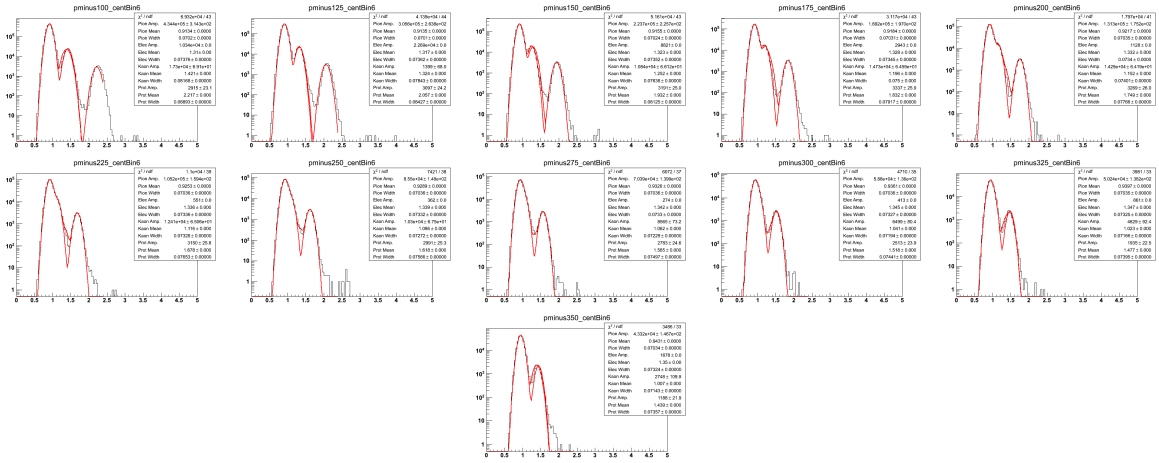

Figure A.83: Negative proton TPC fits for 10%-20% central events Au+Au $\sqrt{s_{NN}} = 19.6$ GeV. These are organized in 25 MeV bins in $m_T - m_p$ in a rapidity window of 0.1 units around mid-rapidity, $|y| < 0.05$. The Gaussian fits, drawn in red, are in $\log(10^6 \times dE/dx)$ and are of the $m_T - m_p = 0.100$ to 0.500 GeV/c^2 range. The track data are represented in the black histogram.

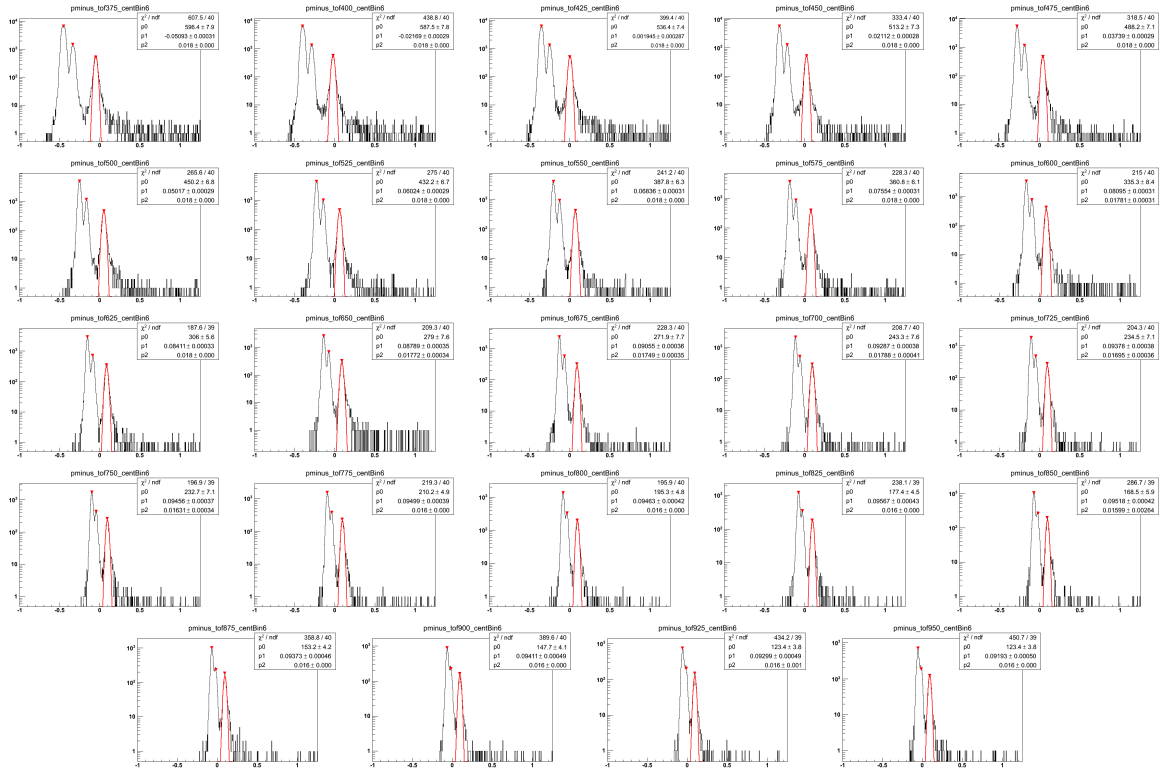

Figure A.84: Negative proton TOF fits for 10%-20% central events Au+Au $\sqrt{s_{NN}} = 19.6$ GeV. These are organized in 25 MeV bins in $m_T - m_p$ in a rapidity window of 0.1 units around mid-rapidity, $|y| < 0.05$. The Gaussian fits, drawn in red, are in $\beta^{-1}_{\text{expected}} - \beta^{-1}_{\text{measured}}$ and are of the $m_T - m_p = 0.350$ to 1.0 GeV/c^2 range. The track data are represented in the black histogram.

A.8 The 5%-10% Centrality Class

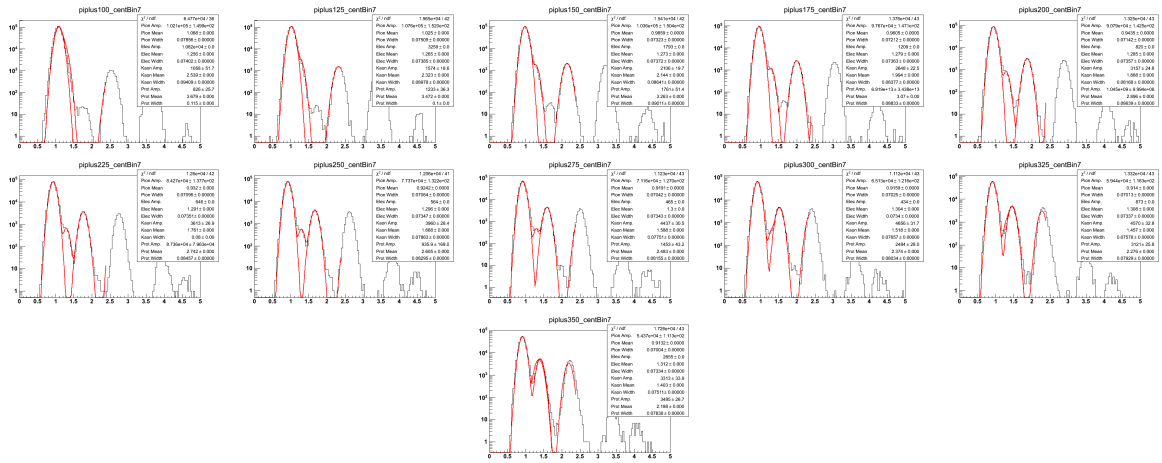

Figure A.85: Positive pion TPC fits for 5%-10% central events Au+Au $\sqrt{s_{NN}} = 19.6$ GeV. These are organized in 25 MeV bins in $m_T - m_\pi$ in a rapidity window of 0.1 units around mid-rapidity, $|y| < 0.05$. The Gaussian fits, drawn in red, are in $\log(10^6 \times dE/dx)$ and are of the $m_T - m_\pi =$ 0.100 to 0.500 GeV/c^2 range. The track data are represented in the black histogram.

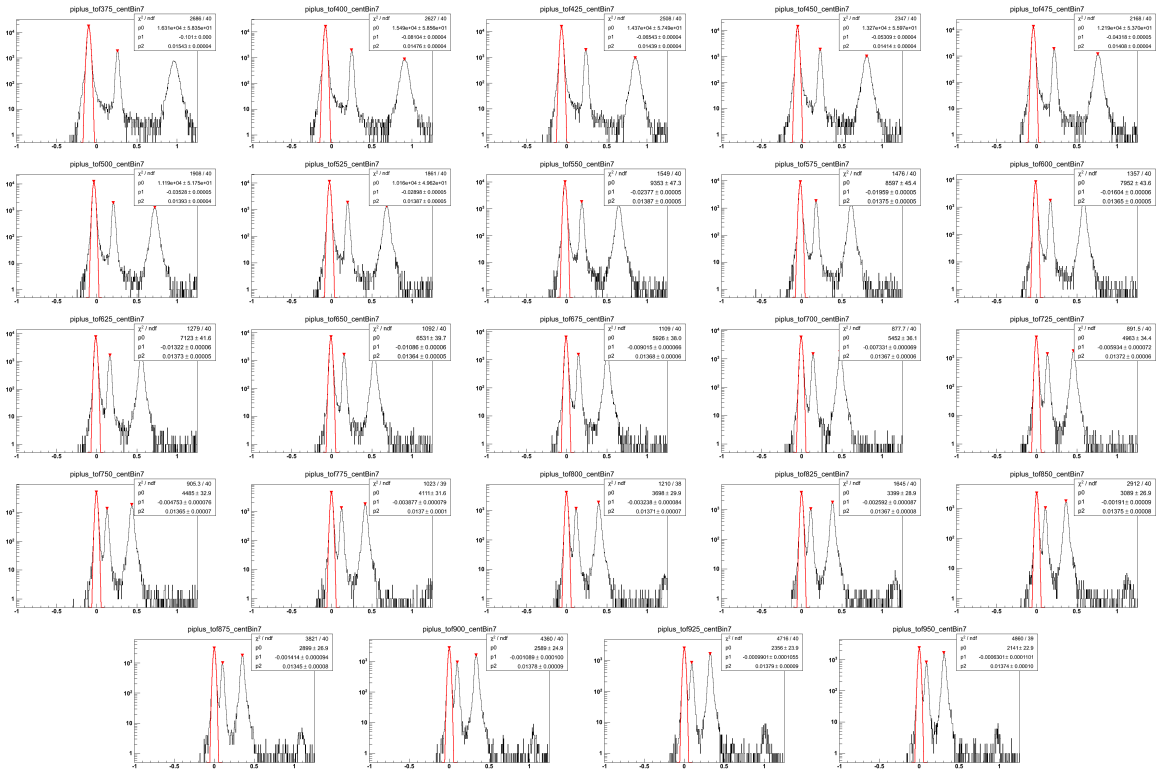

Figure A.86: Positive pion TOF fits for 5%-10% central events Au+Au $\sqrt{s_{NN}} = 19.6$ GeV. These are organized in 25 MeV bins in $m_T - m_\pi$ in a rapidity window of 0.1 units around mid-rapidity, $|y| < 0.05$. The Gaussian fits, drawn in red, are in $\beta^{-1}_{\text{expected}} - \beta^{-1}_{\text{measured}}$ and are of the $m_T - m_\pi = 0.350$ to 1.0 GeV/c^2 range. The track data are represented in the black histogram.

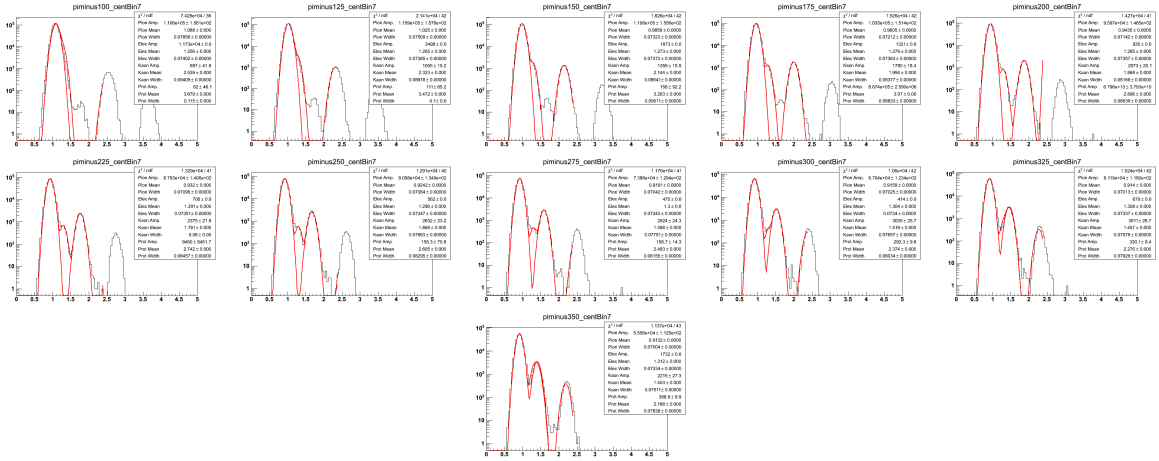

Figure A.87: Negative pion TPC fits for 5%-10% central events Au+Au $\sqrt{s_{NN}} = 19.6$ GeV. These are organized in 25 MeV bins in $m_T - m_\pi$ in a rapidity window of 0.1 units around mid-rapidity, $|y| < 0.05$. The Gaussian fits, drawn in red, are in $\log(10^6 \times dE/dx)$ and are of the $m_T - m_\pi = 0.100$ to 0.500 GeV/c^2 range. The track data are represented in the black histogram.

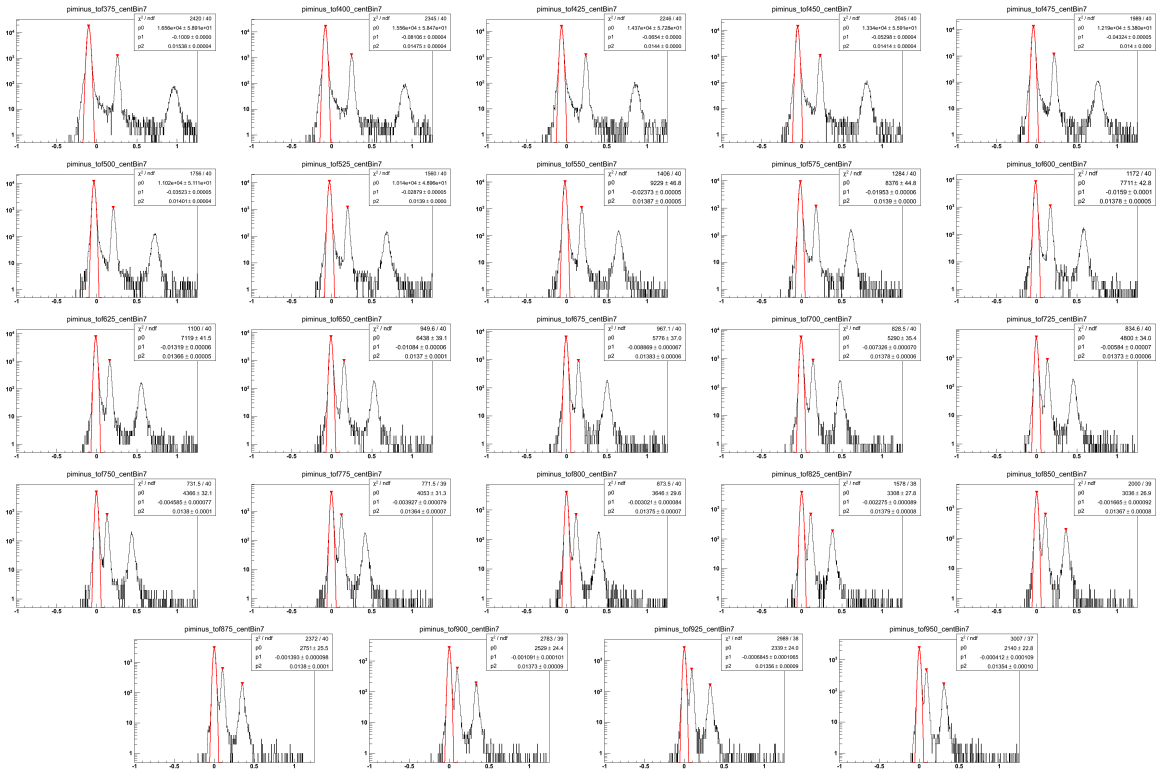

Figure A.88: Negative pion TOF fits for 5%-10% central events Au+Au $\sqrt{s_{NN}} = 19.6$ GeV. These are organized in 25 MeV bins in $m_T - m_\pi$ in a rapidity window of 0.1 units around mid-rapidity, $|y| < 0.05$. The Gaussian fits, drawn in red, are in $\beta^{-1}_{\text{expected}} - \beta^{-1}_{\text{measured}}$ and are of the $m_T - m_\pi =$ 0.350 to 1.0 GeV/c^2 range. The track data are represented in the black histogram.

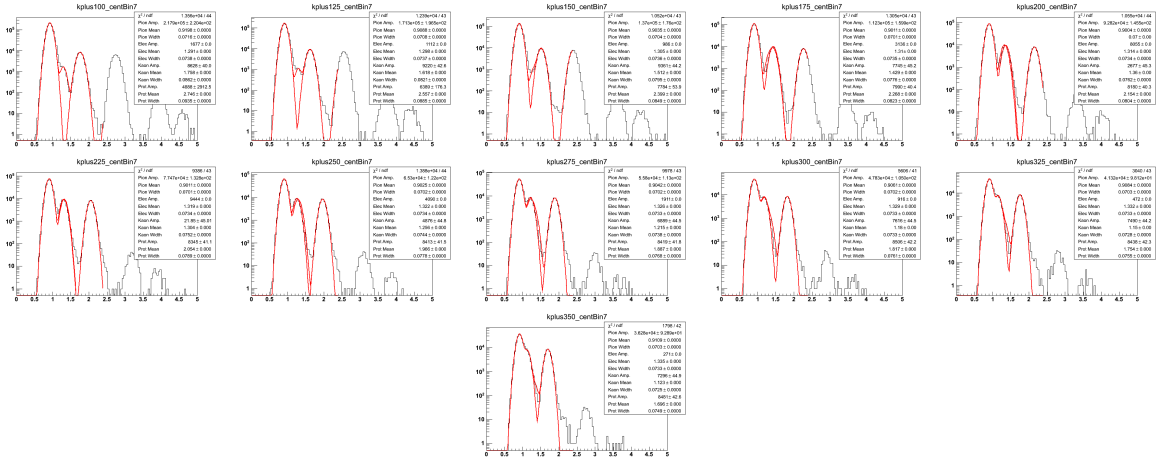

Figure A.89: Positive kaon TPC fits for 5%-10% central events Au+Au $\sqrt{s_{NN}} = 19.6$ GeV. These are organized in 25 MeV bins in $m_T - m_K$ in a rapidity window of 0.1 units around mid-rapidity, $|y| < 0.05$. The Gaussian fits, drawn in red, are in $\log(10^6 \times dE/dx)$ and are of the $m_T - m_K =$ 0.100 to 0.500 GeV/c^2 range. The track data are represented in the black histogram.

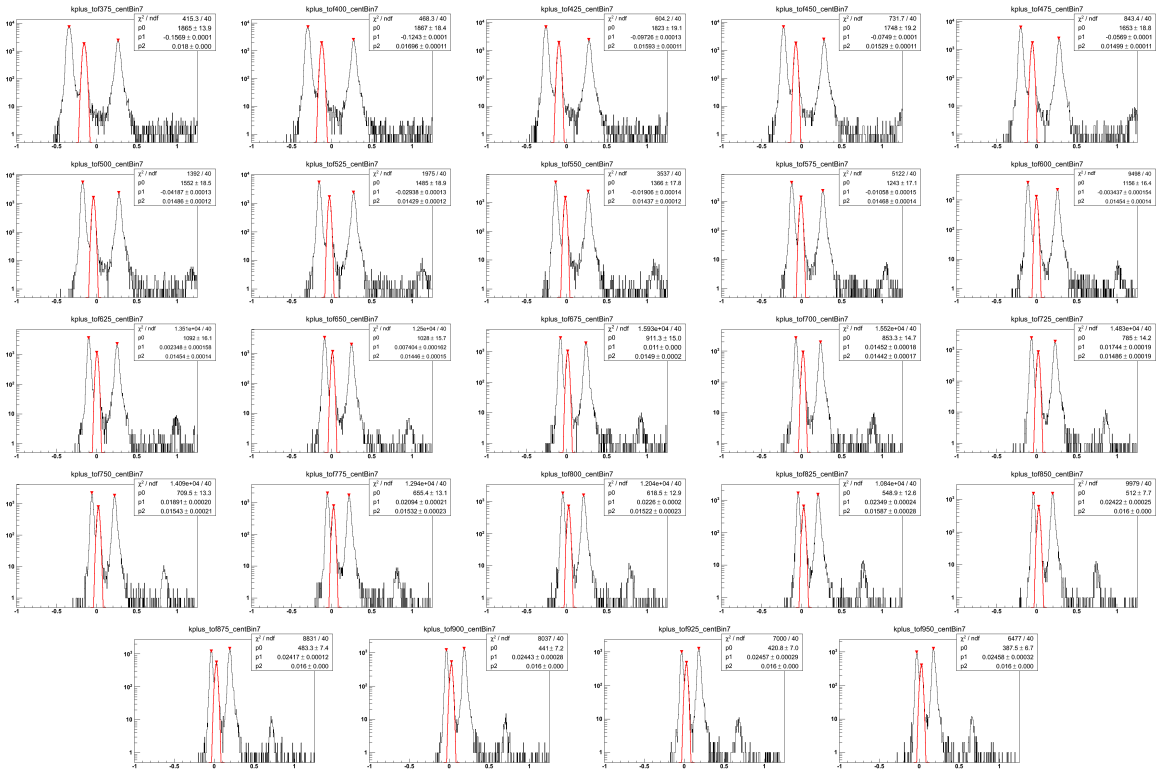

Figure A.90: Positive kaon TOF fits for 5%-10% central events Au+Au $\sqrt{s_{NN}} = 19.6$ GeV. These are organized in 25 MeV bins in $m_T - m_K$ in a rapidity window of 0.1 units around mid-rapidity, $|y| < 0.05$. The Gaussian fits, drawn in red, are in $\beta^{-1}_{\text{expected}} - \beta^{-1}_{\text{measured}}$ and are of the $m_T - m_K =$ 0.350 to 1.0 GeV/c^2 range. The track data are represented in the black histogram.

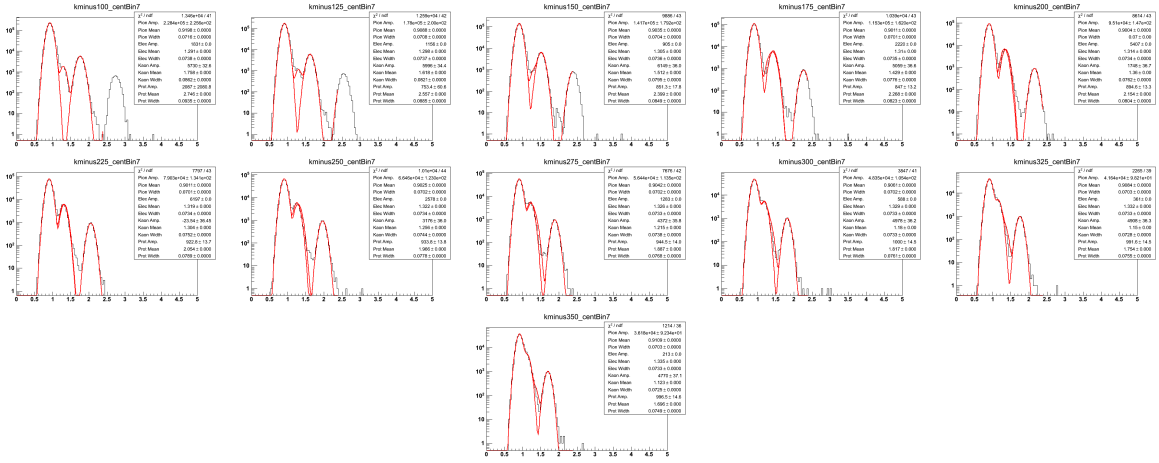

Figure A.91: Negative kaon TPC fits for 5%-10% central events Au+Au $\sqrt{s_{NN}} = 19.6$ GeV. These are organized in 25 MeV bins in $m_T - m_K$ in a rapidity window of 0.1 units around mid-rapidity, $|y| < 0.05$. The Gaussian fits, drawn in red, are in $\log(10^6 \times dE/dx)$ and are of the $m_T - m_K =$ 0.100 to 0.500 GeV/c^2 range. The track data are represented in the black histogram.

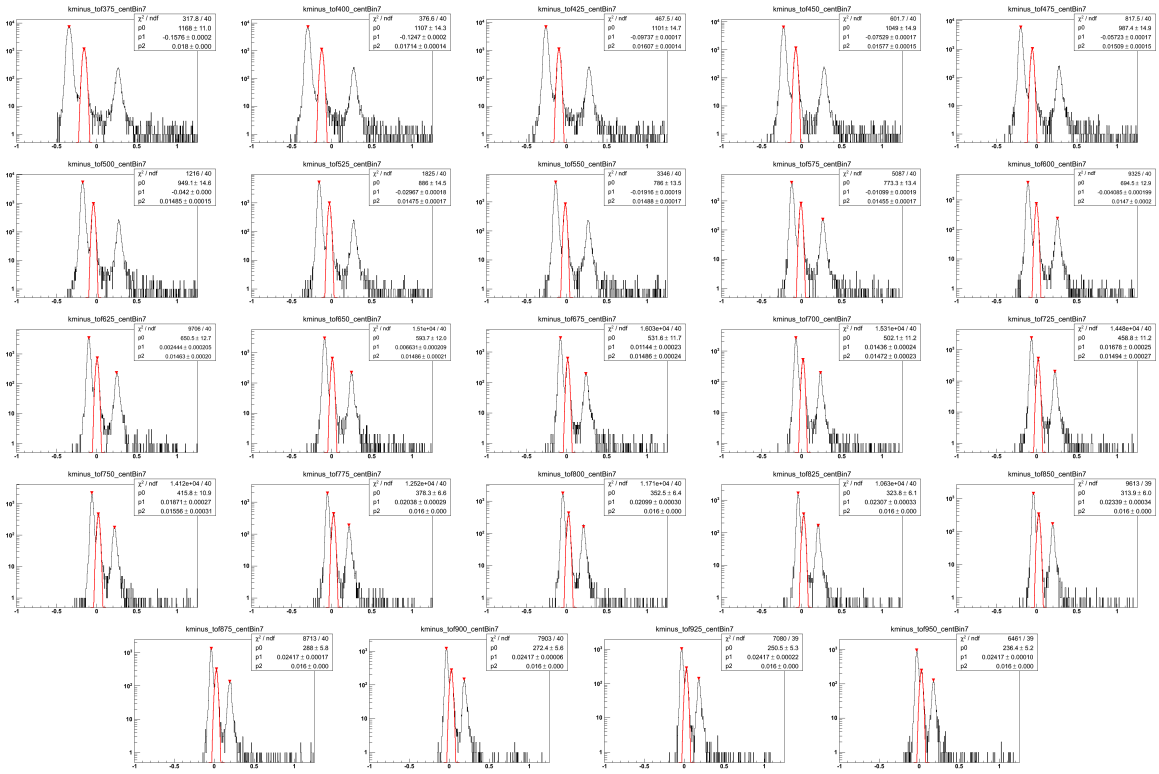

Figure A.92: Negative kaon TOF fits for 5%-10% central events Au+Au $\sqrt{s_{NN}} = 19.6$ GeV. These are organized in 25 MeV bins in $m_T - m_K$ in a rapidity window of 0.1 units around mid-rapidity, $|y| < 0.05$. The Gaussian fits, drawn in red, are in $\beta^{-1}_{\text{expected}} - \beta^{-1}_{\text{measured}}$ and are of the $m_T - m_K =$ 0.350 to 1.0 GeV/c^2 range. The track data are represented in the black histogram.

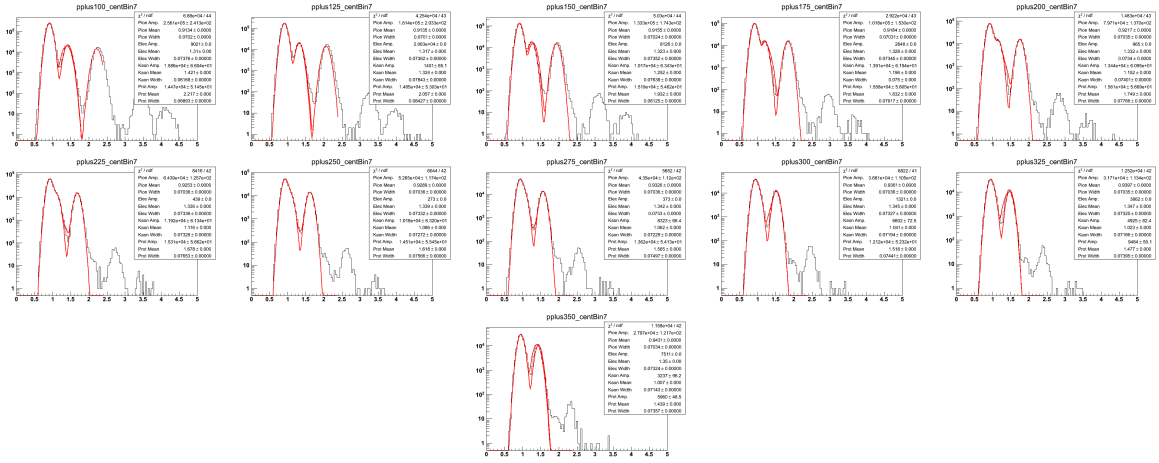

Figure A.93: Positive proton TPC fits for 5%-10% central events Au+Au $\sqrt{s_{NN}} = 19.6$ GeV. These are organized in 25 MeV bins in $m_T - m_p$ in a rapidity window of 0.1 units around mid-rapidity, $|y| < 0.05$. The Gaussian fits, drawn in red, are in $\log(10^6 \times dE/dx)$ and are of the $m_T - m_p = 0.100$ to 0.500 GeV/c^2 range. The track data are represented in the black histogram.

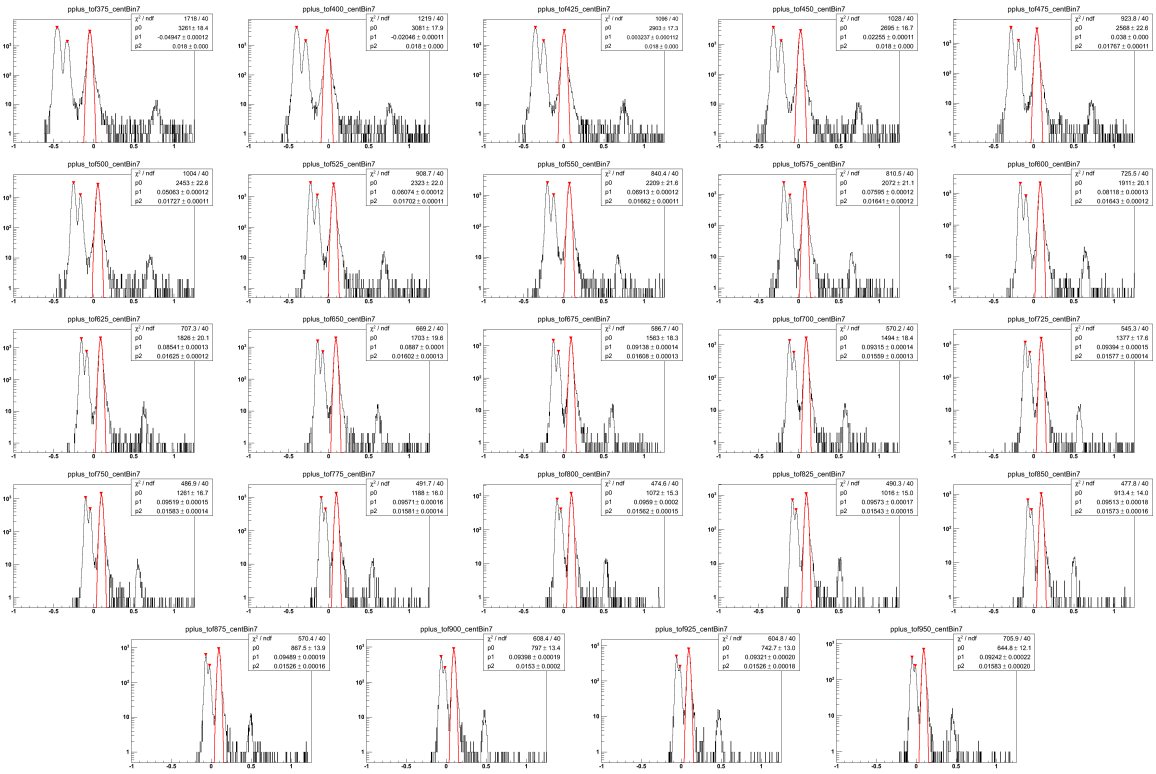

Figure A.94: Positive proton TOF fits for 5%-10% central events Au+Au $\sqrt{s_{NN}} = 19.6$ GeV. These are organized in 25 MeV bins in $m_T - m_p$ in a rapidity window of 0.1 units around mid-rapidity, $|y| < 0.05$. The Gaussian fits, drawn in red, are in $\beta^{-1}_{\text{expected}} - \beta^{-1}_{\text{measured}}$ and are of the $m_T - m_p = 0.350$ to 1.0 GeV/c^2 range. The track data are represented in the black histogram.

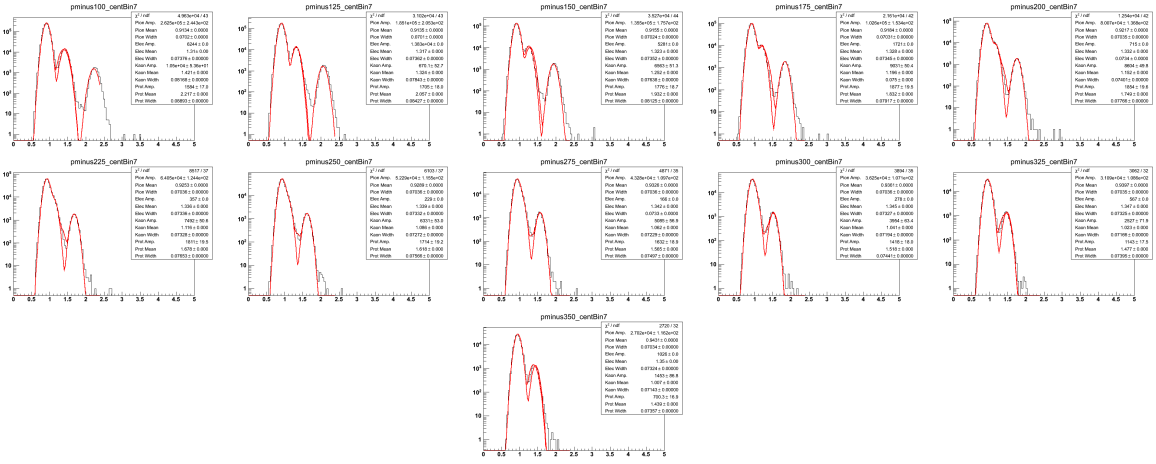

Figure A.95: Negative proton TPC fits for 5%-10% central events Au+Au $\sqrt{s_{NN}} = 19.6$ GeV. These are organized in 25 MeV bins in $m_T - m_p$ in a rapidity window of 0.1 units around mid-rapidity, $|y| < 0.05$. The Gaussian fits, drawn in red, are in $\log(10^6 \times dE/dx)$ and are of the $m_T - m_p = 0.100$ to 0.500 GeV/c^2 range. The track data are represented in the black histogram.

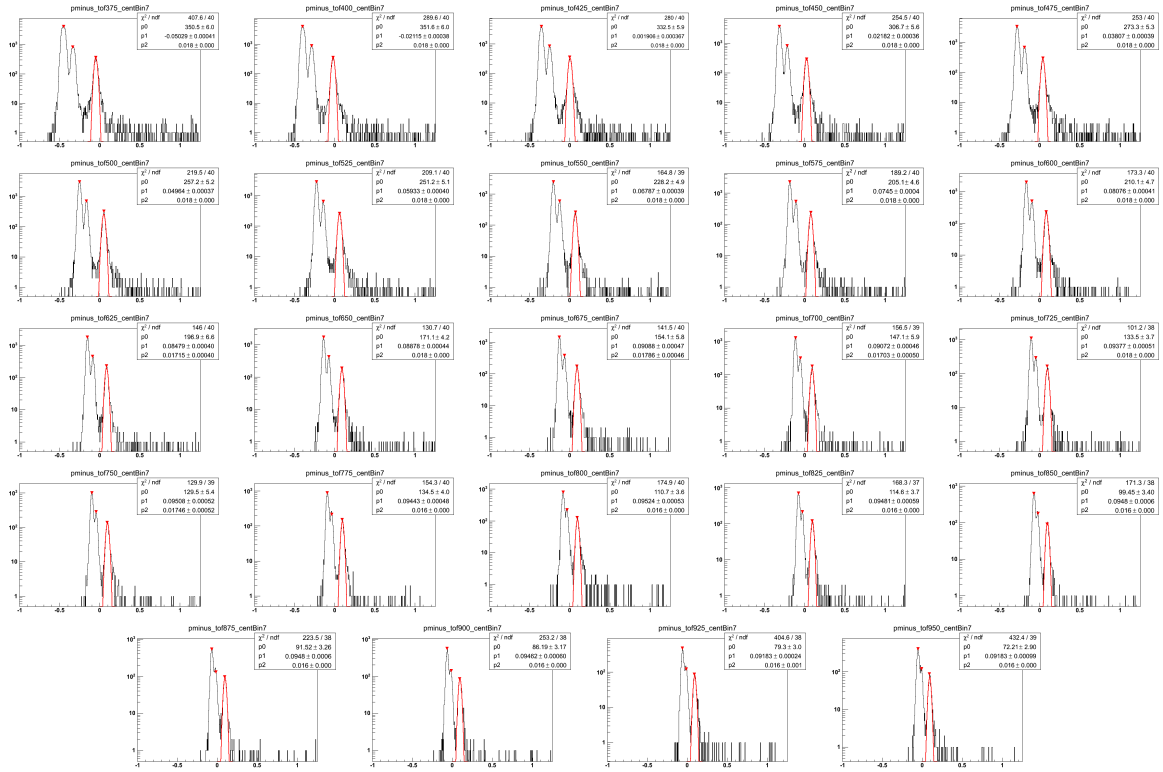

Figure A.96: Negative proton TOF fits for 5%-10% central events Au+Au $\sqrt{s_{NN}}$ = 19.6 GeV. These are organized in 25 MeV bins in $m_T - m_p$ in a rapidity window of 0.1 units around mid-rapidity, $|y| < 0.05$. The Gaussian fits, drawn in red, are in $\beta^{-1}_{\text{expected}} - \beta^{-1}_{\text{measured}}$ and are of the $m_T - m_p = 0.350$ to 1.0 GeV/c^2 range. The track data are represented in the black histogram.

A.9 The 0%-5% Centrality Class

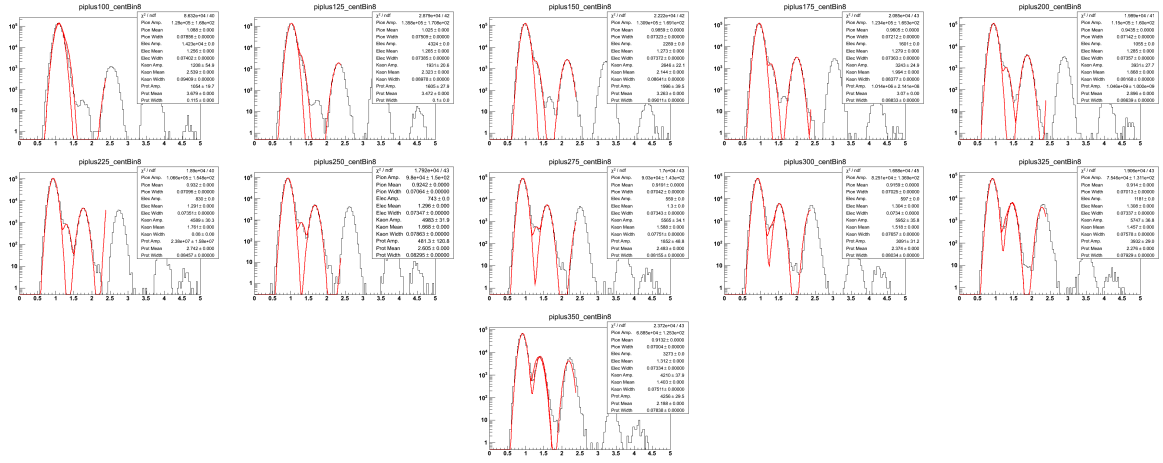

Figure A.97: Positive pion TPC fits for 0%-5% central events Au+Au $\sqrt{s_{NN}} = 19.6$ GeV. These are organized in 25 MeV bins in $m_T - m_\pi$ in a rapidity window of 0.1 units around mid-rapidity, $|y| < 0.05$. The Gaussian fits, drawn in red, are in $\log(10^6 \times dE/dx)$ and are of the $m_T - m_\pi =$ 0.100 to 0.500 GeV/c^2 range. The track data are represented in the black histogram.

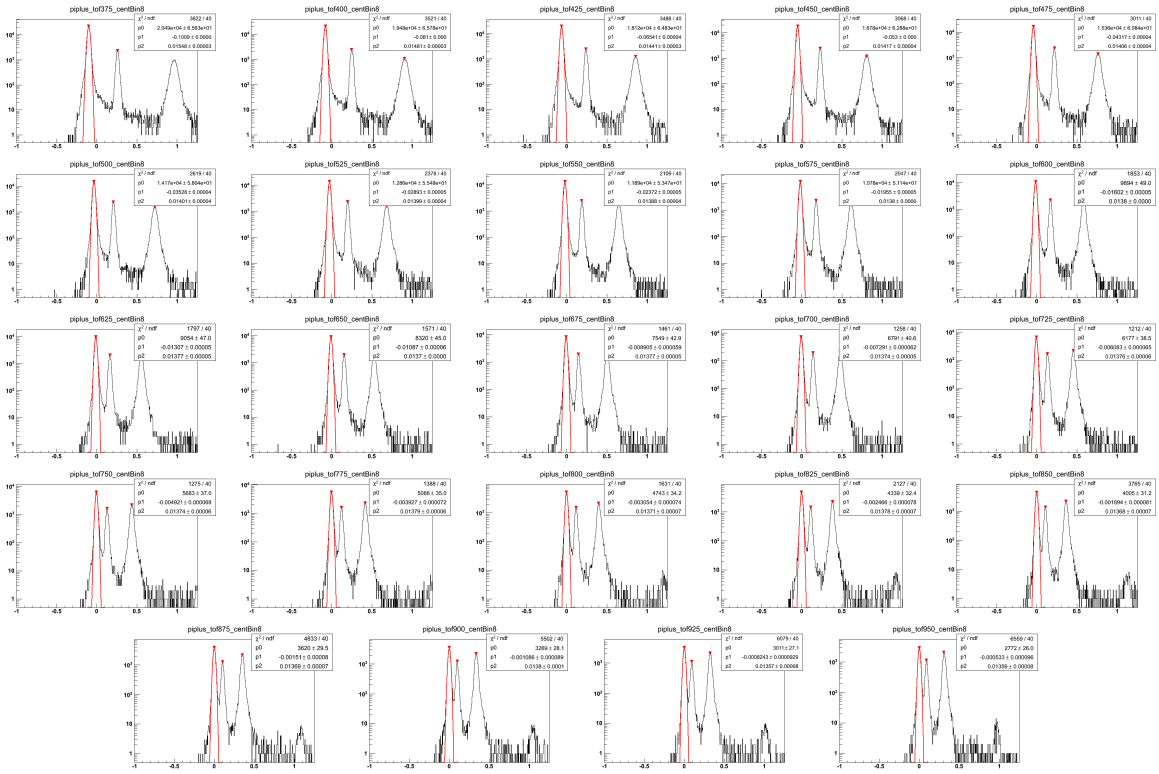

Figure A.98: Positive pion TOF fits for 0%-5% central events Au+Au $\sqrt{s_{NN}} = 19.6$ GeV. These are organized in 25 MeV bins in $m_T - m_\pi$ in a rapidity window of 0.1 units around mid-rapidity, $|y| < 0.05$. The Gaussian fits, drawn in red, are in $\beta^{-1}_{\text{expected}} - \beta^{-1}_{\text{measured}}$ and are of the $m_T - m_\pi = 0.350$ to 1.0 GeV/c^2 range. The track data are represented in the black histogram.

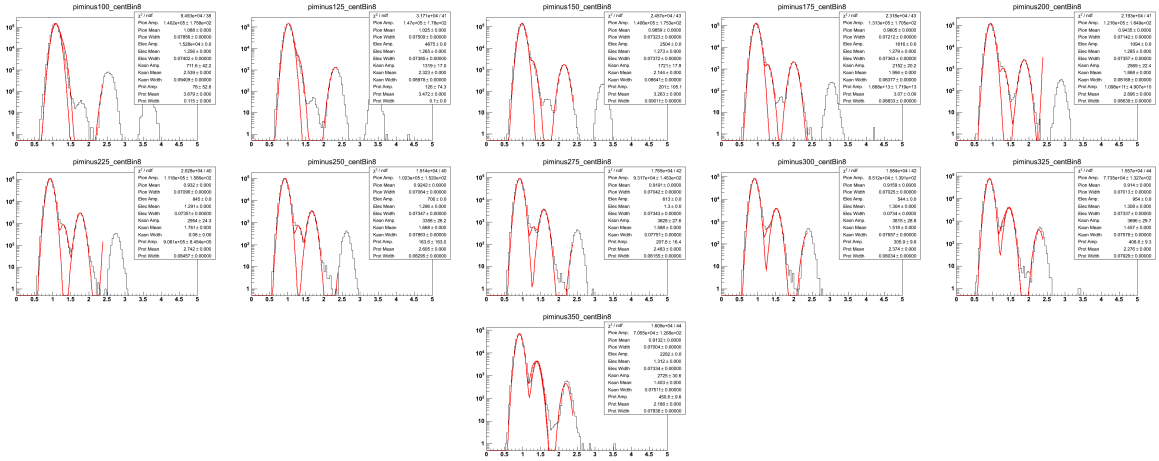

Figure A.99: Negative pion TPC fits for 0%-5% central events Au+Au $\sqrt{s_{NN}} = 19.6$ GeV. These are organized in 25 MeV bins in $m_T - m_\pi$ in a rapidity window of 0.1 units around mid-rapidity, $|y| < 0.05$. The Gaussian fits, drawn in red, are in $\log(10^6 \times dE/dx)$ and are of the $m_T - m_\pi = 0.100$ to 0.500 GeV/c^2 range. The track data are represented in the black histogram.

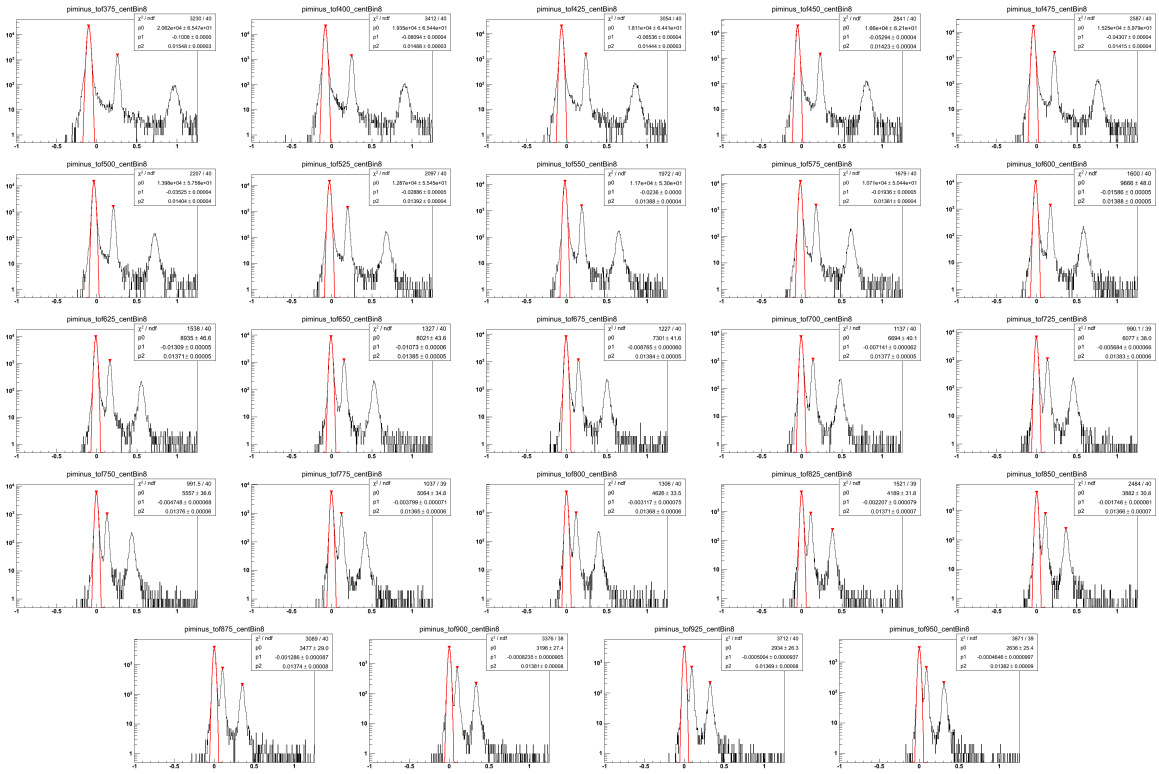

Figure A.100: Negative pion TOF fits for 0%-5% central events Au+Au $\sqrt{s_{NN}} = 19.6$ GeV. These are organized in 25 MeV bins in $m_T - m_\pi$ in a rapidity window of 0.1 units around mid-rapidity, $|y| < 0.05$. The Gaussian fits, drawn in red, are in $\beta^{-1}_{\text{expected}} - \beta^{-1}_{\text{measured}}$ and are of the $m_T - m_\pi = 0.350$ to 1.0 GeV/c^2 range. The track data are represented in the black histogram.

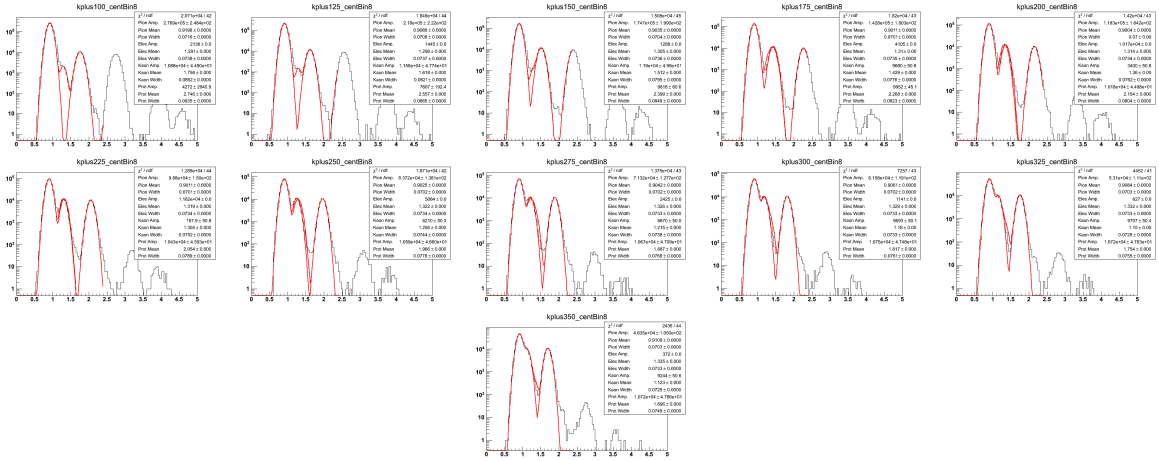

Figure A.101: Positive kaon TPC fits for 0%-5% central events Au+Au $\sqrt{s_{NN}} = 19.6$ GeV. These are organized in 25 MeV bins in $m_T - m_K$ in a rapidity window of 0.1 units around mid-rapidity, $|y| < 0.05$. The Gaussian fits, drawn in red, are in $\log(10^6 \times dE/dx)$ and are of the $m_T - m_K = 0.100$ to 0.500 GeV/c^2 range. The track data are represented in the black histogram.

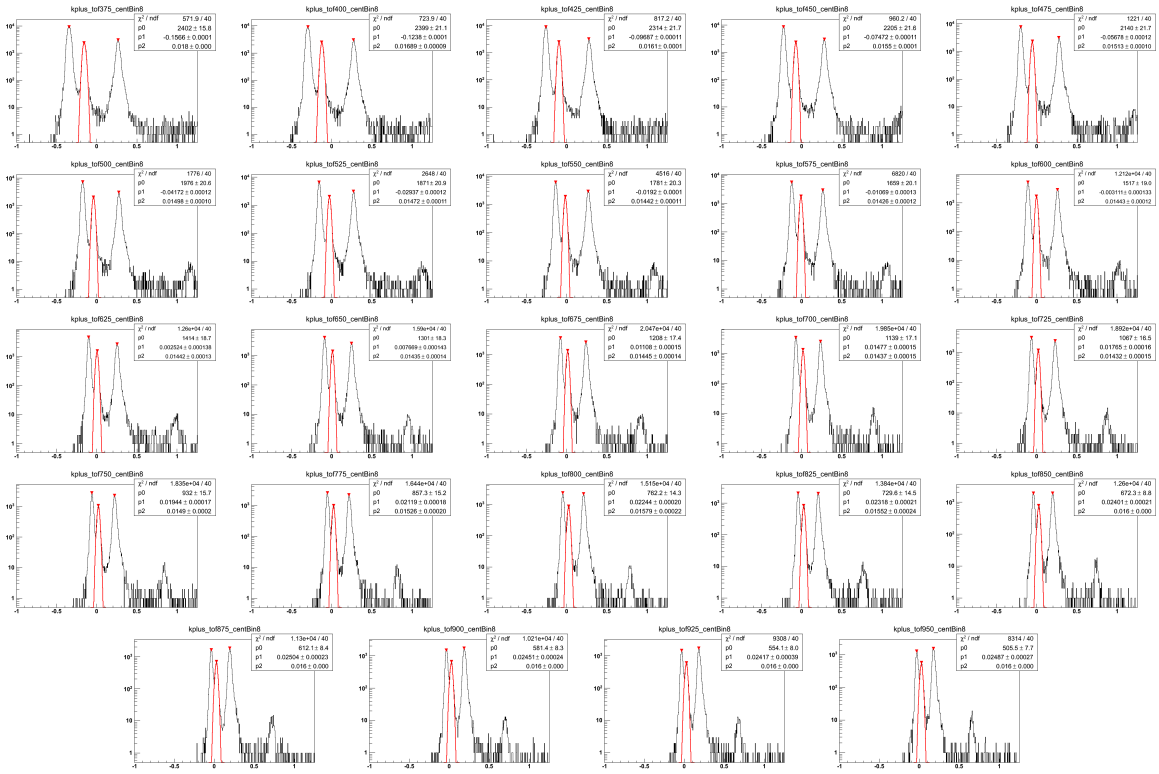

Figure A.102: Positive kaon TOF fits for 0%-5% central events Au+Au $\sqrt{s_{NN}} = 19.6$ GeV. These are organized in 25 MeV bins in $m_T - m_K$ in a rapidity window of 0.1 units around mid-rapidity, $|y| < 0.05$. The Gaussian fits, drawn in red, are in $\beta^{-1}_{\text{expected}} - \beta^{-1}_{\text{measured}}$ and are of the $m_T - m_K =$ 0.350 to 1.0 GeV/c^2 range. The track data are represented in the black histogram.

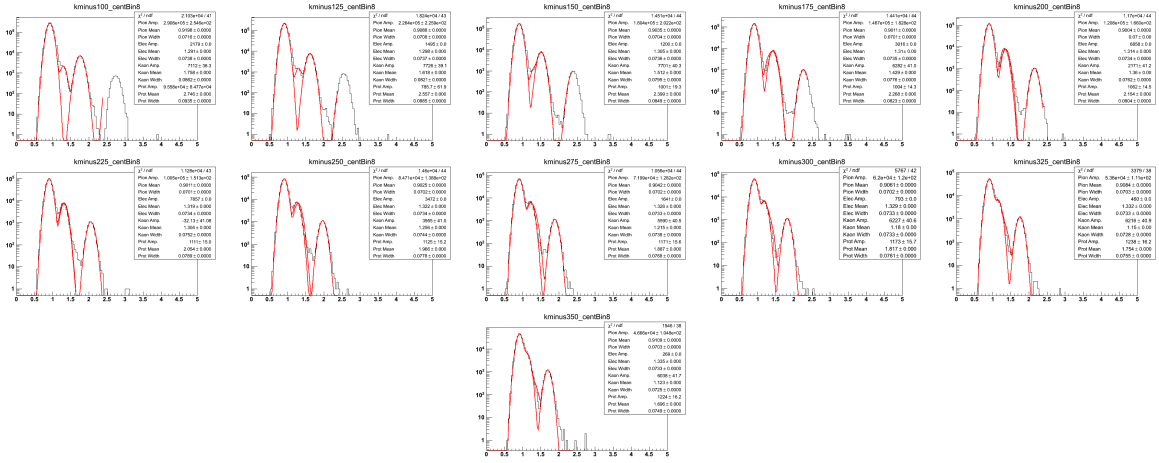

Figure A.103: Negative kaon TPC fits for 0%-5% central events Au+Au $\sqrt{s_{NN}} = 19.6$ GeV. These are organized in 25 MeV bins in $m_T - m_K$ in a rapidity window of 0.1 units around mid-rapidity, $|y| < 0.05$. The Gaussian fits, drawn in red, are in $\log(10^6 \times dE/dx)$ and are of the $m_T - m_K =$ 0.100 to 0.500 GeV/c^2 range. The track data are represented in the black histogram.

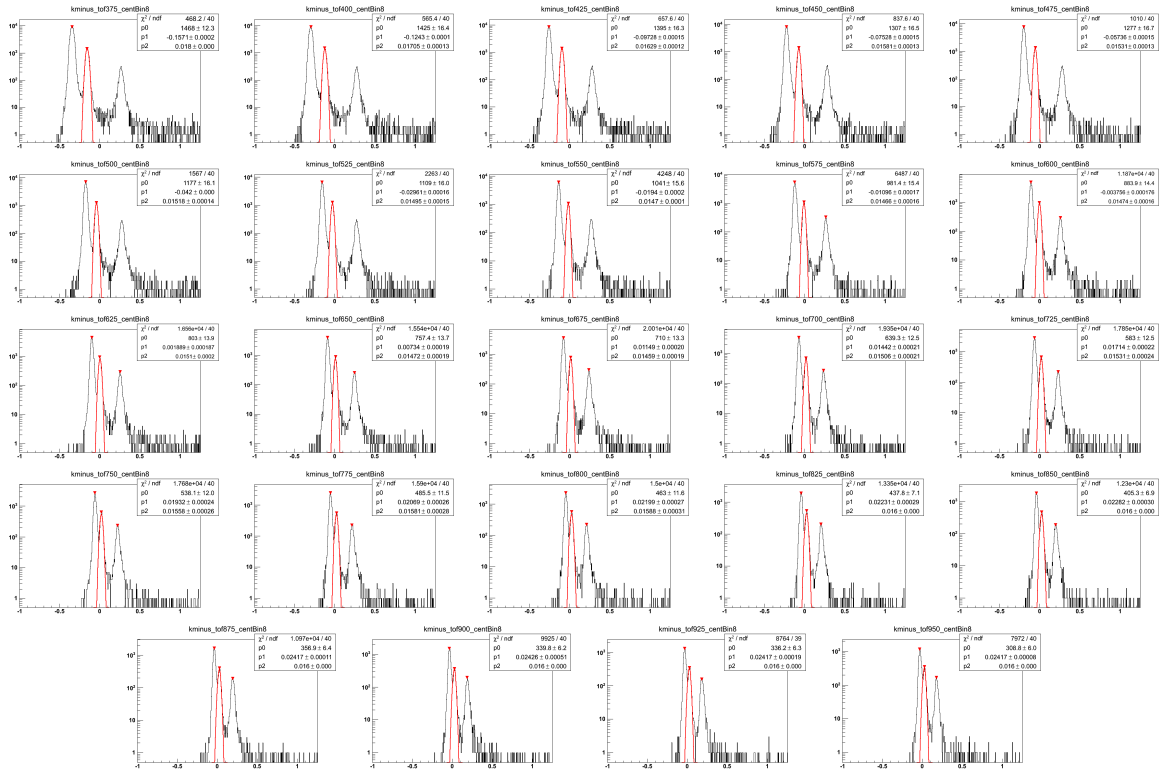

Figure A.104: Negative kaon TOF fits for 0%-5% central events Au+Au $\sqrt{s_{NN}} = 19.6$ GeV. These are organized in 25 MeV bins in $m_T - m_K$ in a rapidity window of 0.1 units around mid-rapidity, $|y| < 0.05$. The Gaussian fits, drawn in red, are in $\beta^{-1}_{\text{expected}} - \beta^{-1}_{\text{measured}}$ and are of the $m_T - m_K =$ 0.350 to 1.0 GeV/c^2 range. The track data are represented in the black histogram.

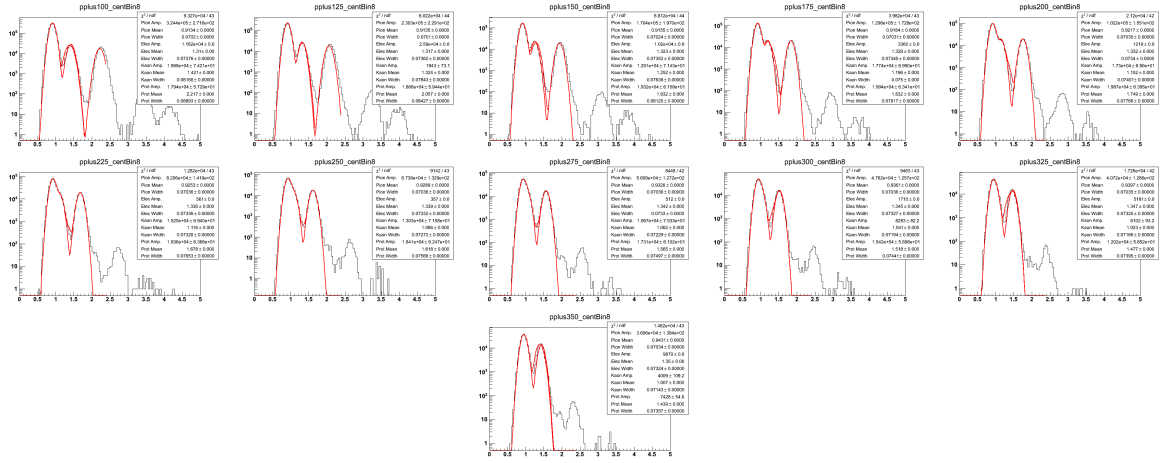

Figure A.105: Positive proton TPC fits for 0%-5% central events Au+Au $\sqrt{s_{NN}} = 19.6$ GeV. These are organized in 25 MeV bins in $m_T - m_p$ in a rapidity window of 0.1 units around mid-rapidity, $|y| < 0.05$. The Gaussian fits, drawn in red, are in $\log(10^6 \times dE/dx)$ and are of the $m_T - m_p = 0.100$ to 0.500 GeV/c^2 range. The track data are represented in the black histogram.

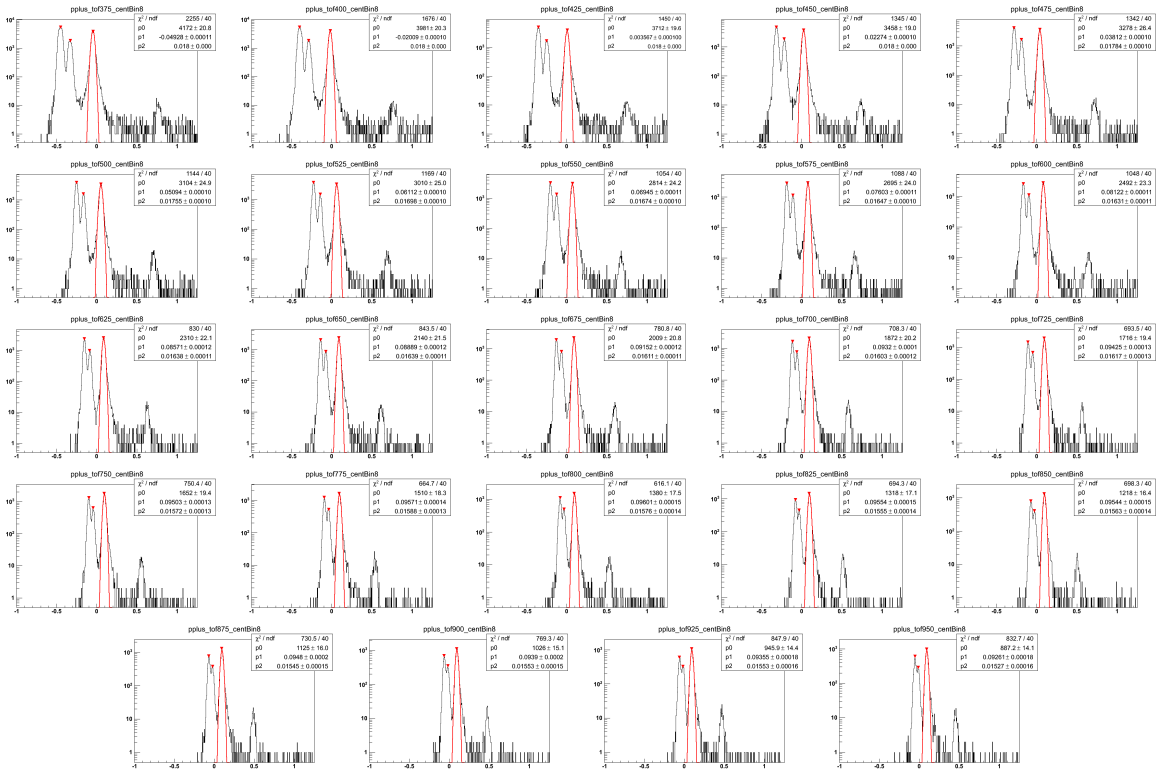

Figure A.106: Positive proton TOF fits for 0%-5% central events Au+Au $\sqrt{s_{NN}} = 19.6$ GeV. These are organized in 25 MeV bins in $m_T - m_p$ in a rapidity window of 0.1 units around mid-rapidity, $|y| < 0.05$. The Gaussian fits, drawn in red, are in $\beta^{-1}_{\text{expected}} - \beta^{-1}_{\text{measured}}$ and are of the $m_T - m_p = 0.350$ to 1.0 GeV/c^2 range. The track data are represented in the black histogram.

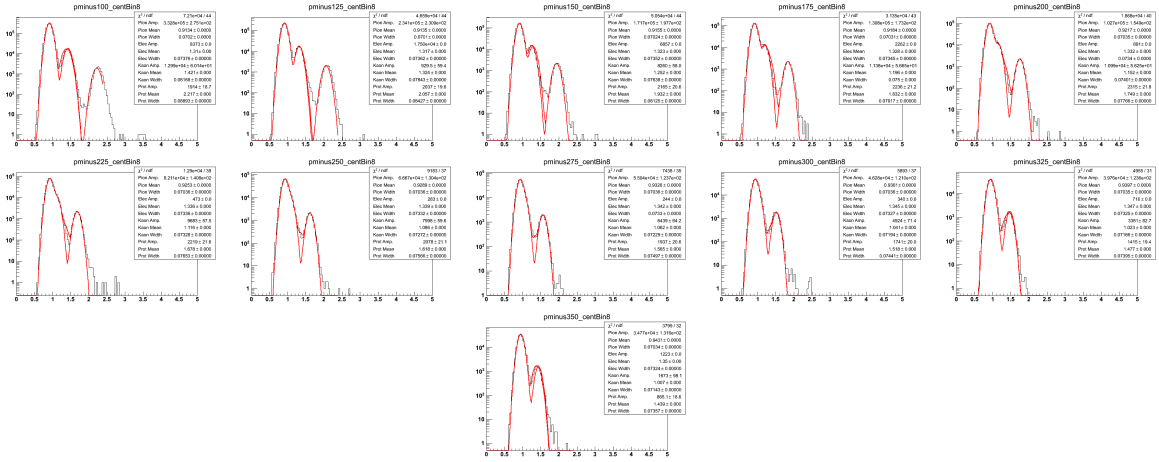

Figure A.107: Negative proton TPC fits for 0%-5% central events Au+Au $\sqrt{s_{NN}} = 19.6$ GeV. These are organized in 25 MeV bins in $m_T - m_p$ in a rapidity window of 0.1 units around mid-rapidity, $|y| < 0.05$. The Gaussian fits, drawn in red, are in $\log(10^6 \times dE/dx)$ and are of the $m_T - m_p = 0.100$ to 0.500 GeV/c^2 range. The track data are represented in the black histogram.

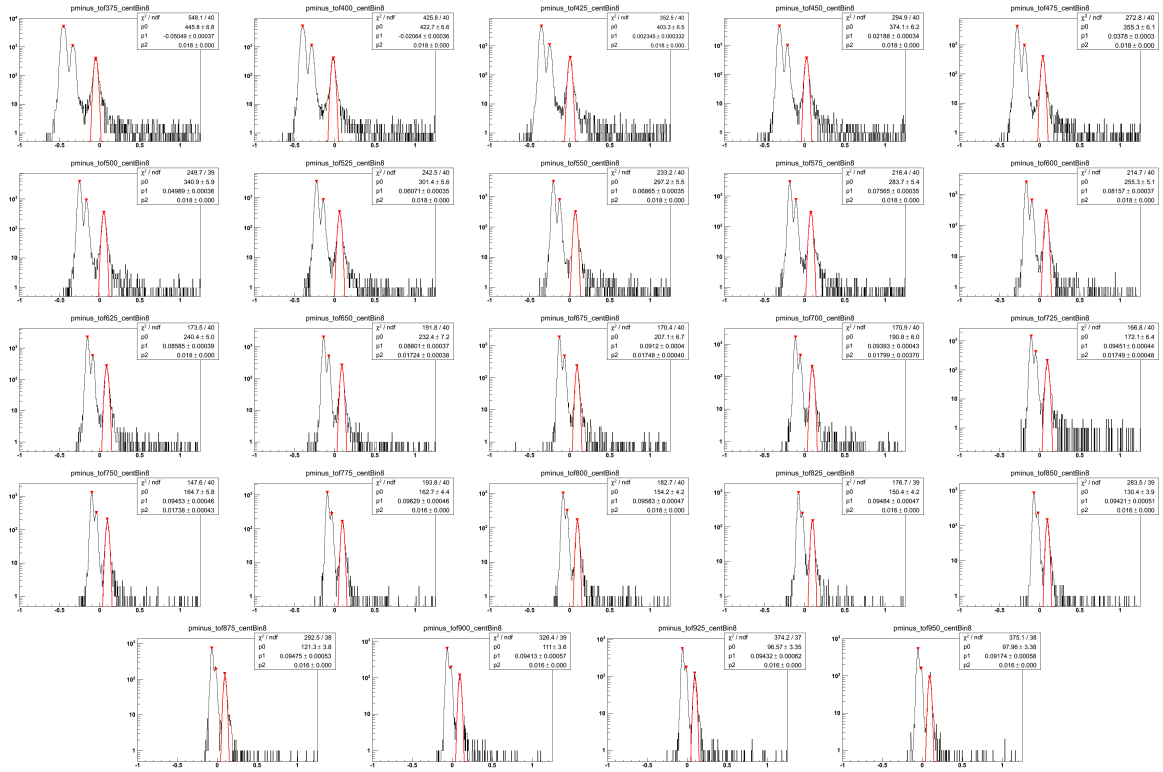

Figure A.108: Negative proton TOF fits for 0%-5% central events Au+Au $\sqrt{s_{NN}} = 19.6$ GeV. These are organized in 25 MeV bins in $m_T - m_p$ in a rapidity window of 0.1 units around mid-rapidity, $|y| < 0.05$. The Gaussian fits, drawn in red, are in $\beta^{-1}_{\text{expected}} - \beta^{-1}_{\text{measured}}$ and are of the $m_T - m_p = 0.350$ to 1.0 GeV/c^2 range. The track data are represented in the black histogram.

Appendix B

Global Properties of Nucleus-Nucleus Collisions

Nucleus-nucleus collisions, $A + A$, have three main stages of evolution, discussed in Chapter 2. These stages each have signatures which survive hadronization and are the signals pulled from all data sets. Discussed in this Appendix are the experimental observables measured by particle detectors relating to the theory of the collision.

In the final stage of the collision, hadronization and chemical and kinetic freeze-out occur. In the subsequent hot hadronic gas phase following hadronization, global observables can provide information regarding the initial parameters of the collision. The particle detectors discussed in Chapter 3 collect data on the total number of produced particles (or tracks in the STAR case), specific particle charge, velocity/momentum, position, and energy loss. From kinematic equations and geometry other properties of the collision are determined.

B.1 The Glauber Model

One of the first parameters to determine, outside of specifics to a particular particle, is what class of events one is analyzing. What kind of collision occurred? Central, or peripheral? By answering this type of question, the feasibility of certain analyses on that class of event becomes apparent (meaning, in glancing collisions, an Υ production analysis would be unreasonably difficult). Determining the impact parameter, or the centrality, of the collision

is not by measuring the distance between the centers of each nuclei, but rather through the Glauber Model [33, 34, 185].

Collision geometry plays an important role due to the dependence of the total cross section on the size of the colliding nuclei. Figure B.1 displays the range of overlap that two colliding nuclei may achieve. A peripheral, or least central collision is represented in (a) while a central, or least peripheral, collision is displayed in (b). The Glauber model takes advantage of this relation to predict, based on the number of participating (or "wounded") nucleons, how many particles will be produced and detected for a given impact parameter. A simplified model does this by assuming each nucleon is a hard sphere populating the nucleus according to the Woods-Saxon nuclear density distribution,

$$\rho(r) = \rho_0/(1 + e^{(r-R)/z}) \qquad , \tag{B.1}$$

where ρ_0 is the density in the central region of the nucleus, R is the mean electromagnetic radius of the nucleus (typically the radius when $\rho = \frac{1}{2}\rho_0$), and z describes the surface layer thickness. At RHIC, however, due to the capability of colliding many differing species of nuclei, the Fermi distribution is used [185]:

$$\rho(r) = \rho_0 \frac{1 + w(r/R)^2}{1 + \exp(\frac{r-R}{a})} \tag{B.2}$$

where ρ_0 corresponds to the central nuclear density, R corresponds to the radius of the nucleus, a is the skin depth, and w corresponds to deviations from a spherical nuclear shape. Note for ^{197}Au, $w = 0$ and reduces to the Woods-Saxon distribution. Additionally, the model needs the nucleon-nucleon cross-section which PYTHIA [177] [178] typically estimates from $\sim$ 32 mb to $\sim$ 42 at the range of RHIC energies [185]. This cross section constitutes the only beam-energy dependent variable in the Glauber model which is nontrivial [185]. From there, the analytical Glauber model utilizes the optical-limit approximation [176] [175] for the collision of two nucleons in each of the colliding nuclei. When two nucleons are determined

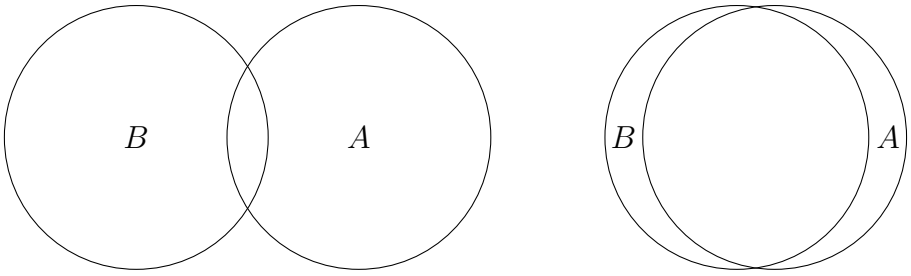

Figure B.1: Different overlap areas of colliding nuclei in (a) a more peripheral collision as the overlap region is smaller compared to (b) a more central collision since the overlap region is very large.

to collide, those nucleons are assumed to have sufficient momentum to continue essentially undeflected as the nuclei pass through each other and to move independently in the nucleus. Thus they count toward the total number of participating nucleons. The probability that a collision between nucleons will occur diminishes with the number of collisions in which a particular nucleon had already been a participant.

The Glauber Monte Carlo method is quite a bit simpler to obtain the geometrical quantities of interest, namely $N_{\rm part}$ and $N_{\rm coll}$. The distribution of nucleons is given as the Fermi distribution for each nuclei in the collision, and then a random impact parameter is chosen. The nuclear collisions are treated as independent binary collisions of nucleons, meaning no dependence of the inelastic nucleon-nucleon cross section on the number of collisions a particular nucleon has participated in perviously. A collision between nucleons occurs when their two-dimensional area (calculated either via a Gaussian distribution or the inelastic cross section) perpendicular to the beam axis overlaps. The averages of the geometrical quantities are then obtained via the repetition of many collisions at these differing impact parameters.

Once the number of participants and the number of collisions are determined via simulation these quantities translate to experimental observables entirely dependent on the experiment and collision system. Typically, to translate between experiment and Glauber, an experimental centrality class distribution is mapped to a similar centrality class distri-

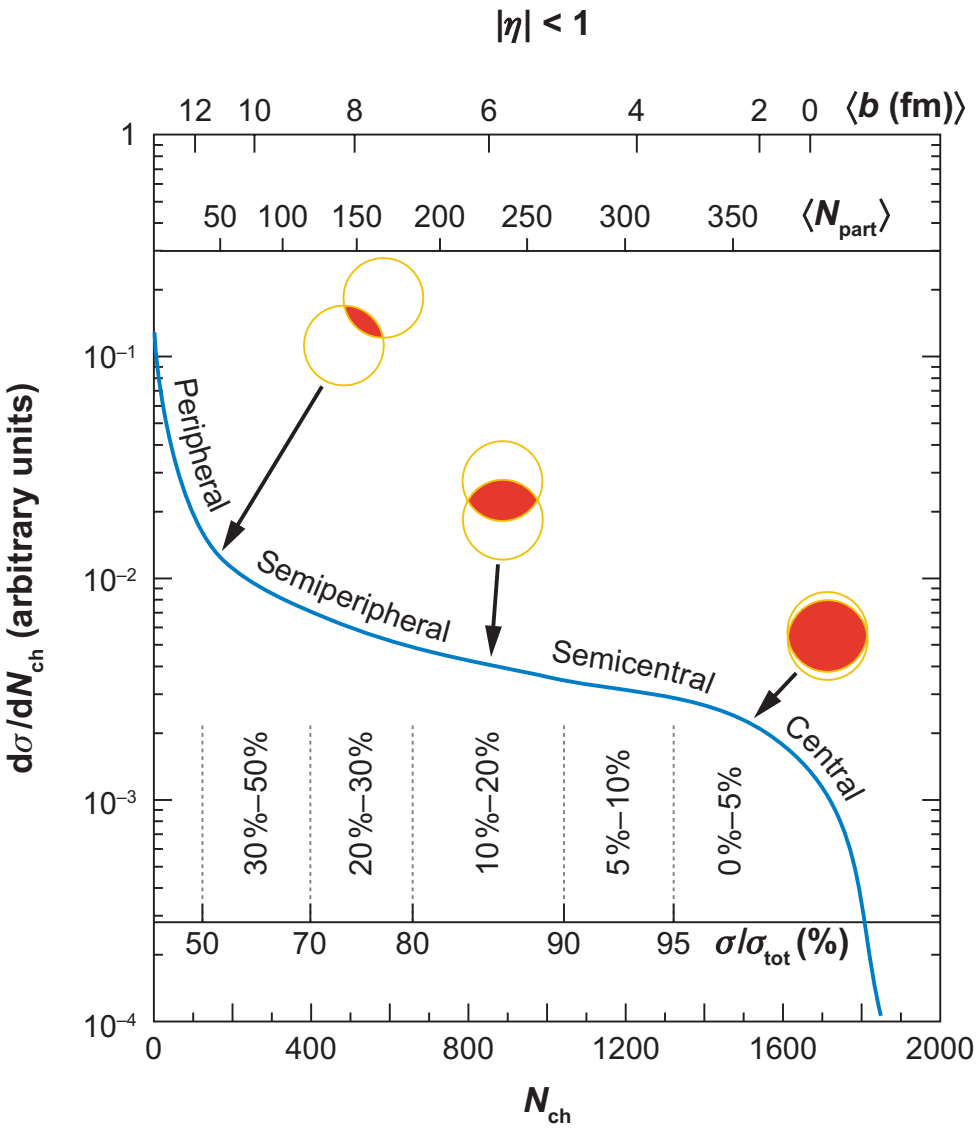

Figure B.2: Taken from Reference [185]. An illustrated example of the correlation of the final-state-observable total inclusive charged-particle multiplicity $N_{\rm ch}$ with Glauber-calculated quantities (b, $N_{\rm part}$). The plotted distribution and various values are illustrative and not actual measurements (T. Ullrich, private communication).

bution from Glauber by equating the mean values from the same centrality class in each distribution. This mapping relies on the basic assumption that the particle multiplicity is a monotonic function of the impact parameter, b, see Figure B.2. The smaller the impact parameter or more central the collision, the larger the number of produced particles we expect (right-hand region of the schematic), while the larger the impact parameter or more peripheral the collision, the smaller the expected number of produced particles (left-hand region of

the plot). Centrality classes are defined as a fraction of the total number of events in a distribution of the experimental and Glauber per-event charged particle multiplicity. A sample binning is given by the dashed lines. The geometric quantities then are calculated for each centrality class of the Glauber distribution. This Glauber mapping thus provides a relation between the number of experimentally-observed charged particles and the (experimentally unmeasurable) impact parameter, b.

References

[1] M. Gyulassy, J Phys. G: Nucl. Part. Phys., S911(2004)

[2] J. Adams *et al.* (STAR Collaboration), Phys. Rev. Lett. **91**, 072304 (2003)

[3] C. Adler *et al.* (STAR Collaboration), Phys. Rev. Lett. **90**, 082302 (2003)

[4] J. W. Harris and B. Muller, Annu. Rev. Nucl. Part. Sci. **46**, 71 (1996)

[5] M. Asakawa and K. Yazaki, Nucl. Phys. A **504**, 668 (1989)

[6] F. R. Brown *et al.*, Phys. Rev. Lett. **65**, 2491 (1990)

[7] U. Heinz and G. Kestin, Eur. Phys. J. Special Topics **155**, 75 (2008)

[8] D. H. Rischke, Prog. Part. Nucl. Phys. **52**, 197 (2004)

[9] C. Alt *et al.* (NA49 Collaboration), Phys. Rev. C **77**, 024903 (2008)

[10] Z. Fodor and S. D. Katz, JHEP **0404**, 050 (2004), hep-lat/0402006, `http://arxiv.org/abs/hep-lat/0402006`

[11] R. V. Gavai and S. Gupta, Phys. Rev. D **71**, 114014 (2005), hep-lat/0412035, `http://arxiv.org/abs/hep-lat/0412035`

[12] F. Karsch, C. R. Allton, S. Ejiri, S. J. Hands, O. Kaczmarek, E. Laermann, and C. Schmidt, Nucl. Phys. Proc. Suppl. **129**, 614 (2004), hep-lat/0309116, `http://arxiv.org/abs/hep-lat/0309116`

[13] P. de Forcrand and O. Philipsen, JHEP **01**, 077 (2007), hep-lat/0607017, `http://arxiv.org/abs/hep-lat/0607017`

[14] Z. Fodor and S. D. Katz, "The phase diagram of quantum chromodynamics," (08 2009), arXiv:0908.3341[hep-ph], 0908.3341, http://arxiv.org/abs/0908.3341

[15] R. V. Gavai and S. Gupta, Phys. Rev. D **78**, 114503 (2008), 0806.2233, http://arxiv.org/abs/0806.2233

[16] C. Schmidt, for RBC-Bielefeld, and H. Collaborations, Nucl. Phys. A **820**, 41c (10 2009), 0810.4024, http://arxiv.org/abs/0810.4024

[17] E. L. Bratkovskaya, M. Bleicher, A. Dumitru, K. Paech, M. Reiter, S. Soff, H. Stöcker, H. Weber, M. van Leeuwen, and W. Cassing, "Review of qgp signatures - ideas versus observables," (2004), arXiv:nucl-th/0401031, nucl-th/0401031, http://arxiv.org/abs/nucl-th/0401031

[18] E. Shuryak, "Interactions between hadrons are strongly modified near the qcd (tri)critical point," (2005), arXiv:hep-ph/0504048, hep-ph/0504048, http://arxiv.org/abs/hep-ph/0504048

[19] M. Gazdzicki, M. I. Gorenstein, and S. Mrowczynski, Phys. Lett. B **585**, 115 (2004), hep-ph/0304052, http://arxiv.org/abs/hep-ph/0304052

[20] M. I. Gorenstein, M. Gazdzicki, and O. S. Zozulya, Phys. Lett. B **585**, 237 (2004), hep-ph/0309142, http://arxiv.org/abs/hep-ph/0309142

[21] P. Kolb *et al.*, Phys. Rev. C **62**, 054909 (2000)

[22] J.-Y. Ollitrault *et al.*, Physical Review D **46**, 229 (1992)

[23] M. Stephanov *et al.*, Physical Review Letters **102**, 032301 (2009)

[24] S. Ejiri, F. Karsch, and K. Redlich, Physics Letters B **633**, 275 (2006), ISSN 0370-2693, http://www.sciencedirect.com/science/article/pii/S0370269305017521

[25] M. Asakawa", Physical Review Letters **101**, 2302 (2008)

[26] M. Stephanov, K. Rajagopal, and E. Shuryak, Phys. Rev. D **60**, 4028 (1999)

[27] M. Gazdzicki, Z. Fodor, and G. Vesztergombi, *Study of Hadron Production in Hadron-Nucleus and Nucleus-Nucleus Collisions at the CERN SPS*, Tech. Rep. SPSC-P-330. CERN-SPSC-2006-034 (CERN, Geneva, 2006)

[28] D. Cebra (for the STAR Collaboration), "Charged hadron results from au+au at 19.6 gev," (03 2009), arXiv:0903.4702[nucl-ex], 0903.4702, `http://arxiv.org/abs/0903.4702`

[29] L. Kumar (for the STAR Collaboration), J. Phys. G: Nucl. Part. Phys. **36**, 064066 (12 2009), 0812.4099, `http://arxiv.org/abs/0812.4099`

[30] B. I. Abelev *et al.* (STAR Collaboration), Phys. Rev. C **81**, 024911 (Feb 2010), `http://link.aps.org/doi/10.1103/PhysRevC.81.024911`

[31] M. M. Aggarwal *et al.* (STAR Collaboration), "An experimental exploration of the qcd phase diagram: The search for the critical point and the onset of de-confinement," (July 2010), arXiv:1007.2613 [nucl-ex]

[32] A. Bialas, M. Bleszynski, and W. Czyz, Nucl. Phys. B **111**, 461 (1976)

[33] R. J. Glauber and G. Matthiae, Nucl. Phys. B **21**, 135 (1970)

[34] R. J. Glauber, Nucl. Phys. A **774**, 3 (2006)

[35] L. Adamczyk *et al.* (STAR Collaboration), *RHIC Beam Use Request For Runs 14 and 15*, Tech. Rep. (Brookhaven National Laboratory, 2013) `www.c-ad.bnl.gov/esfd/RMEM_14/star_bur_2014.pdf`

[36] N. Cabibbo and G. Parisi, Phys. Lett. B, 67(1975)

[37] J. C. Collins and M. J. Perry, Phys. Rev. Lett. **34**, 1353 (1975)

[38] E. V. Shuryak, Phys. Lett. B **78**, 150 (1978)

[39] J. Beringer *et al.* (Particle Data Group), Phys. Rev. D **86**, 010001 (2012)

[40] K. Wilson, Phys. Rev. D **10**, 2445 (1974)

[41] R. Vogt, *Ultrarelativistic Heavy-Ion Collisions* (Elsevier, Amsterdam, 2007)

[42] F. Karsch, "Recent lattice results on finite temperature and density qcd, part i," ArXiv:[hep-lat]0711.0656

[43] F. Karsch, "Recent lattice results on finite temperature and density qcd, part ii," ArXiv:[hep-lat]0711.0661

[44] I. Montav and G. Munster, *Quantum Fields on a Lattice* (Cambridge University Press, Cambridge, 1994)

[45] F. Karsch, in *Lecture Notes In Physics*, Vol. 583, edited by W. Plessas and L. Mathelitsch (Springer, Berlin, 2002) pp. 209–249

[46] H. J. Rothe, in *Lecture Notes In Physics*, Vol. 59 (World Scientific, Singapore, 1997)

[47] F. Karsch and E. Laermann, in *Quark Gluon Plasma 3*, edited by R. C. Hwa and X.-N. Wang (World Scientific, Singapore, 2004) pp. 1–59

[48] L. D. McLerran and B. Svetitsky, Phys. Lett. B **98**, 195 (1981)

[49] L. D. McLerran and B. Svetitsky, Phys. Rev. D **24**, 450 (1981)

[50] J. Kuti, J. Polónyi, and K. Szlachányi, Phys. Lett. B **98**, 199 (1981)

[51] F. Karsch and E. Laermann, Phys. Rev. D **50**, 6954 (1994)

[52] F. Karsch, E. Laermann, and A. Peikert, Phys. Lett. B **478**, 447 (2000)

[53] J. Bartke, *Introduction to Relativistic Heavy Ion Physics* (World Scientific Co. Pte. Ltd., 2009)

[54] R. Raitio, Nucl. Phys. A **418**, 539c (1984)

[55] U. Heinz, "Concepts of heavy ion physics," (2004), cERN Yellow Report

[56] A. Bialas, M. Chojnacki, and W. Florkowski, J. Phys. G: Nucl. Part. Phys. **35**, 104073 (2008)

[57] J. Rafelski, Phys. Rept. **88**, 331 (1982)

[58] P. Koch, B. Muller, and J. Rafelski, Phys. Rept. **142**, 167 (1986)

[59] A. Tounsi and K. Redlich, "Strangeness enhancement and canonical suppression," (November 2001), arXiv:hep-ph/0111159

[60] T. Matsui and H. Satz, Phys. Lett. B **178**, 416 (1985)

[61] F. Karsch, E. Laermann, and A. Peikert, Nucl. Phys. Proc. Suppl. **94**, 411 (2001)

[62] L. Kluberg and H. Satz, "Color deconfinement and charmonium production in nuclear collisions," (January 2009), arXiv:0901.3831v1

[63] R. Chatterjee, L. Bhattacharya, and D. K. Srivastava, Lect. Notes Phys. **785**, 219 (2010)

[64] J. Alam, B. Sinha, and S. Raha, Phys. Rept. **273**, 243 (1996)

[65] J. Kapusta, P. Lichard, and D. Seibert, Phys. Rev. D **44**, 2774 (1991)

[66] J. Kapusta, P. Lichard, and D. Seibert, Phys. Rev. D **47**, 4171 (1993)

[67] M. M. Aggarwal *et al.* (WA98 Collaboration), Phys. Rev. Lett. **85**, 3595 (2000)

[68] S. S. Adler *et al.* (PHENIX Collaboration), Phys. Rev. Lett. **94**, 232301 (2005)

[69] C. Y. Wong, *Introduction of High Energy Heavy Ion Collisions* (World Scientific, Singapore, 1994)

[70] G. Agakichiev *et al.* (CERES Collaboration), Eur. Phys. J. C **41**, 475 (2005)

[71] D. Adamova *et al.* (NA45 Collaboration), Phys. Rev. Lett. **91**, 042301 (2003)

[72] R. Arnaldi *et al.* (NA60 Collaboration), Phys. Rev. Lett. **96**, 162302 (2006)

[73] C. Adler *et al.* (STAR Collaboration), Phys. Rev. Lett. **87**, 182301 (2001)

[74] C. Adler *et al.* (STAR Collaboration), Phys. Rev. Lett. **89**, 132301 (2002)

[75] C. Adler *et al.* (STAR Collaboration), Phys. Rev. Lett. **90**, 032301 (2003)

[76] S. Esumi *et al.* (PHENIX Collaboration), Nucl. Phys. A **715**, 599 (2003)

[77] S. S. Adler *et al.* (PHENIX Collaboration), Phys. Rev. Lett. **91**, 182301 (2001)

[78] (09 2014), `http://www.quantumdiaries.org/wp-content/uploads/2011/02/FlowPr.jpg`

[79] P. Huovinen, P. F. Kolb, U. Heinz, P. Ruuskanen, and S. A. Voloshin, Phys. Lett. B **503**, 58 (2001)

[80] D. Teaney, J. Lauret, and E. V. Shuryak, "A hydrodynamic description of heavy ion collisions at the sps and rhic," (2001), arXiv:nucl-th/0110037

[81] S. Voloshin and Y. Zhang, Z. Phys. C **70**, 665 (1996)

[82] A. M. Poskanzer and S. A. Voloshin, Phys. Rev. C **58**, 1671 (1998)

[83] T. Hirano, N. van der Kolk, and A. Bilandzic, Lect. Notes Phys. **785**, 139 (2010)

[84] E. Schnedermann, J. Sollfrank, and U. Heinz, Phys. Rev. C **48**, 2462 (1993)

[85] P. J. Siemens and J. O. Rasmussen, Phys. Rev. Lett. **42**, 880 (1979)

[86] L. V. Bravina, N. S. Amelin, L. P. Csernai, P. Levai, and D. Strottman, Nucl. Phys. A **566**, 461c (1994)

[87] L. V. Bravina, L. P. Csernai, P. Levai, and D. Strottman, Phys. Rev. C **50**, 2161 (1994)

[88] D. H. Rischke, Y. Puersuen, J. A. Maruhn, H. Stoecker, and W. Greiner, "The phase transition to the quark-gluon plasma and its effect on hydrodynamic flow," (1995), cU-TP-695, arXiv:nucl-th/9505014

[89] L. P. Csernai and D. Rohrich, Phys. Lett. B **458**, 454 (1999)

[90] A. Adare *et al.* (PHENIX Collaboration), Phys. Rev. Lett. **98**, 162301 (2007)

[91] A. Capella and E. G. Ferreiro, Phys. Rev. C **75**, 024905 (2007)

[92] C. Alt *et al.* (NA49 Collaboration), Phys. Rev. C **68**, 034903 (2003)

[93] J. Adams *et al.* (STAR Collaboration), Phys. Rev. Lett. **95**, 122301 (2005)

[94] J. Adams *et al.* (STAR Collaboration), Phys. Rev. Lett. **92**, 052302 (2004)

[95] H. Sorge, Phys. Rev. Lett. **82**, 2048 (1999)

[96] J. Adams *et al.* (STAR Collaboration), Phys. Rev. Lett. **92**, 182301 (2004)

[97] S. Sakai (for the PHENIX Collaboration), J Phys. G: Nucl. Part. Phys. **32**, S551 (2006)

[98] J. Adams *et al.* (STAR Collaboration), Nucl. Phys. A **757**, 102 (2005)

[99] D. Hardtke *et al.* (STAR Collaboration), Nucl. Phys. A **715**, 272 (2003)

[100] S. Chatrchyan *et al.*, Phys. Rev. C **87** (2013)

[101] J. D. Björken, Phys. Rev. D **27**, 140 (1983)

[102] W. Florkowski and W. Broniowski, Acta Phys. Polon. B **35**, 2895 (2004)

[103] F. Retiere and M. A. Lisa, "Observable implications of geometrical and dynamical aspects of freeze-out in heavy ion collisions," ArXiv:nucl-th/0312024

[104] W. Broniowski and W. Florkowski, Phys. Rev. Lett. **87**, 272302 (2001)

[105] W. Broniowski and W. Florkowski, Phys. Rev. C **65**, 064905 (2002)

[106] C. Hoehne *et al.* (NA49 Collaboration), Nucl. Phys. A **774**, 35 (2006)

[107] M. Gazdzicki and M. I. Gorenstein, Acta Phys. Polon. B **30**, 2705 (1999)

[108] M. I. Gorenstein, M. Gazdzicki, and K. A. Bugaev, Phys. Lett. B **567**, 175 (2003)

[109] H. Peterson and M. Bleicher, "Longitudinal flow and onset of deconfinement," Nucl-th/0611001

[110] E. Fermi, Prog. Theor. Phys. **5**, 570 (1950)

[111] M. Gazdzicki, Z. Phys. C **66**, 659 (1995)

[112] A. Rustamov, Cent. Eur. J. Phys **10**, 1267 (2012)

[113] L. D. Landau, Izv. Akad. Nauk **17**, 51 (1953)

[114] E. V. Shuryak, Yad. Fiz. **16**, 395 (1972)

[115] G. Baym and P. Braun-Munzinger, Nucl. Phys. A **610**, 286c (1996)

[116] W. Beneson *et al.*, Phys. Rev. Lett. **43**, 683 (1979)

[117] K. L. Wolf *et al.*, Phys. Rev. Lett. **42**, 1448 (1979)

[118] S. Nagamiya *et al.*, Phys. Rev. C **24**, 971 (1981)

[119] K. L. Wolf *et al.*, Phys. Rev. C **26**, 2572 (1982)

[120] M. Gonin *et al.* (E802/E866), Nucl. Phys. A **566**, 601c (1994)

[121] F. Videbaek *et al.* (E866), Nucl. Phys. A **590**, 249c (1995)

[122] L. Ahle *et al.* (E802 Collaboration), Nucl. Phys. A **610**, 139c (1996)

[123] L. Ahle *et al.*, Phys. Rev. C **57**, R466 (1998)

[124] C. Muentz, Acta Phys. Polon. B **29**, 3253 (1998)

[125] K. H. Ackermann *et al.*, Nucl. Instr. Meth. A **499**, 624 (2003)

[126] J. M. Landgraf *et al.*, Nucl. Instr. Meth. A. **499**, 762 (2003)

[127] M. Beddo *et al.*, Nucl. Instr. Meth. A **499**, 725 (2003)

[128] C. E. Allgower *et al.*, Nucl. Instr. Meth. A **499**, 740 (2003)

[129] M. Anderson *et al.*, Nucl. Instr. Meth. A **499**, 679 (2003)

[130] K. H. Ackermann *et al.*, Nucl. Instr. Meth. A **499**, 713 (2003)

[131] L. Kotchenda *et al.*, Nucl. Instr. Meth. A **499**, 703 (2003)

[132] H. S. Matis *et al.*, Nucl. Instr. Meth. A **499**, 802 (2003)

[133] J. Abele *et al.*, Nucl. Instr. Meth. A **499**, 692 (2003)

[134] C. Adler *et al.*, Nucl. Instr. Meth. A **499**, 778 (2003)

[135] A. Braem *et al.*, Nucl. Instr. Meth. A **499**, 720 (2003)

[136] M. M. Aggarwal *et al.*, Nucl. Instr. Meth. A **499**, 751 (2003)

[137] D. Reichhold *et al.*, Nucl. Instr. Meth. A **499**, 792 (2003)

[138] L. Arnold *et al.*, Nucl. Instr. Meth. A **499**, 652 (2003)

[139] R. Bellwied *et al.*, Nucl. Instr. Meth. A **499**, 640 (2003)

[140] M. Anderson, Nucl. Instr. Meth. A **499**, 659 (2003)

[141] F. S. Bieser, Nucl. Instr. Meth. A **499**, 766 (2003)

[142] F. Bergsma *et al.*, Nucl. Instr. Meth. A **499**, 633 (2003)

[143] A. Schmah (for the STAR Collaboration), J. Phys. G: Nucl. Part. Phys. **38**, 124049 (2011)

[144] (September 2014), `http://www.star.bnl.gov/public/imagelib/collisions2001/`

[145] S. Margetis and D. Cebra, *Main Vertex Reconstruction in STAR*, Tech. Rep. 89 (STAR Note, http://drupal.star.bnl.gov/ST AR/starnotes/public/sn0089, 1994)

[146] H. Bichsel, *Energy loss in thin layers of argon*, Tech. Rep. 418 (STAR Note, http://www.star.bnl.gov/star/starlib/doc/www/sno/ice/sn0418.html, 2000)

[147] H. Bichsel, *Comparison of Bethe-Bloch and Bichsel Functions*, Tech. Rep. 439 (STAR Note, http://www.star.bnl.gov/star/starlib/doc/www/sno/ice/sn0439.html, 2001)

[148] W. J. Llope *et al.*, Nucl. Instr. Meth. A **522**, 252 (2004)

[149] E. C. Zeballos *et al.*, Nucl. Instr. Meth. A **374**, 132 (1996)

[150] M. C. S. Williams *et al.*, Nucl. Instr. Meth. A **478**, 183 (2002)

[151] B. Bonner *et al.*, Nucl. Instr. Meth. A **508**, 181 (2003)

[152] L. Ruan, *Pion, Kaon, Proton and Antiproton Spectra in d+Au and p+p Collisions at* $\sqrt{s_{NN}} = 200$ *GeV at the Relativistic Heavy Ion Collider*, Ph.D. thesis, University of Science and Technology of China (September 2004)

[153] (September 2014), `https://www.star.bnl.gov/public/bbc/geom/front_view.html`

[154] C. Adler, A. Denisov, E. Garcia, M. Murray, H. Stroebele, and S. White, Nucl. Instr. Meth. A **470**, 488 (2001)

[155] A. J. Baltz, C. Chasman, and S. N. White, Nucl. Instr. Meth. A **417**, 1 (1998)

[156] H. Appelhauser *et al.* (NA49 Collaboration), Eur. Phys. J. A **2** (1998)

[157] R. Reed *et al.*, J. Phys.: Conf. Ser. **219**, 032020 (2010)

[158] K. S. Krane, *Introductory Nuclear Physics* (John Wiley and Sons, 1988)

[159] S. A. Bass *et al.*, Prog. Part. Nucl. Phys. **41**, 225 (1998)

[160] M. Bleicher *et al.*, J. Phys. G: Nucl. Part. Phys. **25**, 1859 (1999)

[161] J. Engelage *et al.*, *STAR Trigger-DAQ Interface Specification Version 1.4*, STAR

[162] A. Wagner *et al.* (KaoS Collaboration), Phys. Lett. B **420**, 20 (1998)

[163] M. Heffner, *Hadron Spectra in Au+Au Collisions at the BNL AGS*, Ph.D. thesis, University of California, Davis (2000)

[164] J. L. Klay *et al.* (E895 Collaboration), Phys. Rev. C **68**, 054905 (2003)

[165] L. Ahle *et al.* (E866 and E917 Collaborations), Phys. Lett. B **476**, 1 (2000)

[166] I. G. Beardon *et al.* (NA44 Collaboration), Phys. Rev. C **66**, 044907 (2002)

[167] H. Boggild *et al.* (NA44 Collaboration), Phys. Lett. B **372**, 339 (1996)

[168] S. V. Afanasiev *et al.* (NA49 Collaboration), Phys. Rev. C **66**, 054902 (2002)

[169] M. M. Aggarwal *et al.* (WA98 Collaboration), Phys. Rev. C **67**, 014906 (2003)

[170] M. M. Aggarwal (WA98 Collaboration), Eur. Phys. J. C **48**, 343 (2006)

[171] D. Pelte *et al.* (FoPi Collaboration), Z. Phys. A **357**, 215 (1997)

[172] W. Reisdorf *et al.* (FoPi Collaboration), Nucl. Phys. A **781**, 459 (2007)

[173] F. Retiere *et al.* (WA98 Collaboration), Nucl. Phys. A **681**, 149c (2001)

[174] L. Rosselet *et al.* (WA98 Collaboration), Nucl. Phys. A **698**, 647c (2002)

[175] T. Wibig and D. Sobczynska, J. Phys. G **24**, 2037 (1998)

[176] J. Chauvin, D. Bebrun, A. Lounis, and M. Buenerd, Phys. Rev. C **28**, 1970 (1983)

[177] T. Sjostrand, S. Mrenna, and P. Z. Skands, JHEP **0605** (2006)

[178] J. P. Guillaud and A. Sobol, *Simulation of diffractive and non-diffractive processes at the LHC energy with the PYTHIA and PHOJET MC event generators.*, Tech. Rep. LAPP-EXP 2004–06 (CNRS Tech. Rep., CNRS, Paris, France, 2004)

[179] P. Braun-Munzinger *et al.*, Nucl. Phys. A **697**, 902 (2002)

[180] E. V. Shuryak, PoSCPOD2006:026(2006)

[181] U. Heinz and A. Kuhlman, Phys. Rev. Lett. **94**, 132301 (2005)

[182] *The Physics of the Quark Gluon Plasma*, edited by S. Sarkar, H. Satz, and B. Sinha (Springer, Heidelberg, 2010)

[183] B. Muller, *The Physics of the Quark Gluon Plasma* (Springer, Heidelberg, 1985)

[184] R. C. Hwa, *Quark Gluon Plasma*, Vol. 1, 2 (World Scientific, 1990 and 1995)

[185] M. Miller *et al.*, Annu. Rev. Nucl. Part. Sci. **57**, 205 (2007)

[186] L. Kumar, *Identified Particle Production, Fluctuations and Correlations Studies in Heavy Ion Collisions at RHIC Energies*, Ph.D. thesis, Panjab University (2009)